Oxidation and its effect on the Fatigue Properties of the Nickel Based Superalloy RR1000

David Thomas Stephen Lewis
(MEng *Hons.*)

Submitted to Swansea University in partial fulfilment of the requirements for the Degree of Doctor of Engineering

Swansea University

2020

Abstract

As temperatures within the aero engine increase, oxidation will begin to have a greater effect on the high temperature materials. How this damage will affect the mechanical properties of the high pressure turbine rotor material i.e. nickel superalloy RR1000, must be understood. In this study an attempt was made to understand how the oxides form and the effect they will have on the fatigue performance of the alloy. Initial thermal exposures were undertaken under no-load and tensile and compressive loads in order to determine the variation in oxide characteristics. Subsequent thermal exposures were undertaken to determine the effect oxidation has on the fatigue lives of the nickel-based superalloy. The oxide morphologies were the same throughout, but the application of an external load caused increased reaction rates, with compressive loads causing greater rate increase than tensile. Methodologies were determined using forms of the Arrhenius relationship to numerically compare the oxidation reaction. Tensile and compressive oxidation asymmetry was believed to be related to the mechano-chemical nature of the reaction. The pre-fatigue thermal exposures initially caused a considerable reduction in the fatigue lives with increasing oxidation. However, the longest exposure time resulted in an S-N curve that lay between the shortest and mid length exposures. A range of analyses were undertaken to determine the presence of any relevant mechanisms that caused this unexpected life improvement. It was found that few of the mechanisms investigated were likely to have an effect on the change in life. The exceptions were; reduction in dislocation movement and crack deflection as a result of a recrystallised zone at the surface, changes in the tertiary γ' size, variation in hardness of different regions due to a γ' depleted plastic zone and a hard ceramic oxide, and reduced initiations due to the presence of a 'healing' chromium oxide scale. Notch fatigue tests were performed to determine the importance of the findings to components in service and it was found that the notch acted as the cause of crack initiation, effectively mitigating against the effects of the oxidation damage.

Declarations

This work has not previously been accepted in substance for any degree and is not being concurrently submitted in candidature for any degree.

Signed .....[redacted].....

Date .....29/07/2020.....

Statements

This thesis is the result of my own investigations, except where otherwise stated.

Other sources are acknowledged by footnotes giving explicit references. A bibliography is appended.

Signed ...[redacted].....

Date .....29/07/2020.....

I hereby give consent for my thesis, if accepted, to be available for photocopying and for inter-library loans after expiry of a bar on access approved by the Swansea University.

Signed ....[redacted].....

Date .....29/07/2020.....

Contents

Acknowledgements

I would like to thank my academic supervisor Prof. Mark Whittaker for his continued support throughout my project after I was unexpectantly unloaded on him part way through. He took up the mantle, and has never been short of a sarcastic quip to lighten any situation.

Thank you to Rolls-Royce plc. and the Engineering and Physical Sciences Research Council for sponsoring me throughout this project and providing the material and funding needed to complete the work.

I would also like to thank all those in the Institute of Structural Materials for making my time with you so memorable, and at times, extremely enjoyable. I have truly made some lifelong friends. This thesis is the result of the efforts of a wide range of people, even if just with a word of advice or a dedication of time to help me learn something new. Special thanks go to Steve Jordan, for repeatedly taking time to show me how things work and answering my often stupid questions. I would still be testing if it were not for you.

Thanks go to my friends and family for supporting me all the way through this at often very tedious process. To my kids, you were the most terrible distraction, and I loved every minute of it. Most importantly, thanks go to my wonderful wife Delyth, for supporting me and always being there to talk things through, be it work, or just anything else at all. Without you, I wouldn't have come this far.

List of Tables

List of Figures

Abbreviations

RR – Rolls-Royce plc.
TET – Turbine Entry Temperature
FCC – Face Centered Cubic
γ – Gamma Matrix
γ' – Gamma prime
SEM – Scanning Electron Microscope
TEM – Transmission Electron Microscopy
STEM – Scanning Transmission Electron Microscopy
SAD – Selected Area Diffraction
FEG – Field Emission Gun
EDS – Energy Dispersive X-ray Spectroscopy
EBSD – Electron Backscatter Diffraction
HP – High Pressure
SE – Secondary Electron
BSE – Backscatter Electron
TGA – Thermogravimetric Analysis
SPT – Small Punch Tensile
LCF – Low Cycle Fatigue
TMF – Thermo-mechanical Fatigue
SAGBO – Stress assisted grain boundary oxidation
FG – Fine Grain
CG – Coarse Grain
HIP – Hot Isostatic Press
STOP – Standard Test Operating Procedure

1 Introduction

As the requirements of the jet engine have evolved, the functionality required from critical rotating disc components has increased. Application specific, nickel based superalloys have been developed to fill this need [1]; RR1000, a Rolls Royce plc. (RR) designed powder metallurgy nickel based superalloy, is currently used in RR turbofan jet engines as a turbine disc material.

As turbine entry temperatures are increasing in a continuing battle to improve the operational efficiencies of the aero-engine, high temperature damage mechanisms are becoming of greater significance. One of these damage mechanisms is oxidation, the reaction that will occur through increasing the oxidation state of the material by formation of metallic oxide compounds.

It is the aim of this study to better understand the morphology and rates of formation of the oxidation products of the alloy across a range of temperatures and surface conditions. A model is sought that will aid in quantifying the oxidation damage mechanism, in order that it can be compared across variants of the alloy and any number of other alloys.

Following from this, it was hoped to gain a more comprehensive understanding of complex mechanism of thermo-mechanical oxidation; how applied stress in both the compressive and tensile regimes affects the oxidation characteristics. This is a more accurate representation of the oxidation conditions of the alloy in service. An attempt to quantify the effect of the thermo-mechanical oxidation reaction is undertaken alongside the thermal exposure methodology for direct comparison.

Finally, a scheme of work was sought that would enable for an initial understanding into the influence oxidation damage produces on the fatigue lives of the material, encompassing different test methods and analytical techniques to understand the significance of any outcomes.

For the ease of the reader, the study has been split into two main sections; that dedicated to the oxidation study and that to the fatigue testing programme. Literature reviews, experimental methods and results/ discussions have been undertaken for each section separately, in order that the study is more coherent. A short initial study was

also performed into the aero-engine to better appreciate the reasoning behind the research, and also the alloy composition and processing in order to better comprehend the various outcomes that will be derived in the analysis. A common discussion and conclusions section has then been performed, drawing all threads together.

2 Literature Review

2.1 The Aero Engine

The gas turbine is simply a heat engine that is used to convert chemical to rotational kinetic energy, which can then provide useful work; in the case of the aircraft engine gas turbine, this useful work is thrust. The gas turbine operates on the same cycle as any heat engine; intake, compression, combustion and expansion. In a simple turbojet engine, like that shown in Figure 1, air is drawn in through the intake, compressed in the compressor through a number of stages, before entering the combustion chamber. Fuel is then added and the mixture is burned, forcing the mixture with high energy through the turbine section and out through the exhaust. The high energy exhaust is what provides the engine with thrust; the turbine section uses energy from the exhaust stream to rotate the shaft, providing energy for the compression process.

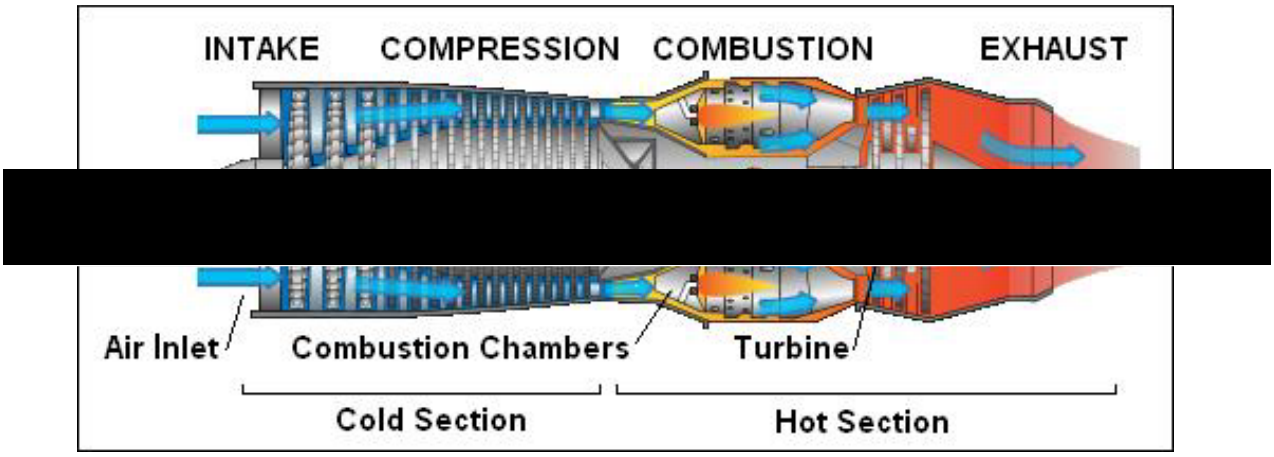

Figure 1: Turbojet Engine [2]

There are many different types of aero engine, but they all operate on the same basic principle as the turbojet. As a general rule the turbojet is used for military jet propulsion aircraft, turboprops are used for propeller driven aircraft and turboshaft engines are used for helicopters, marine propulsion and industrial power generation, and the turbo fan is used for large commercial aircraft (although true for most cases there are some exceptions). The turbofan is the engine of most importance to the

project as the material being investigated is only in use in large commercial turbofan engines.

2.1.1 Turbofan

A turbofan engine can be thought of as a turbojet engine at the core, with a ducted fan unit, usually located at the fore section of the engine, with the addition of an air bypass section, which will usually surround the core as shown in Figure 2.

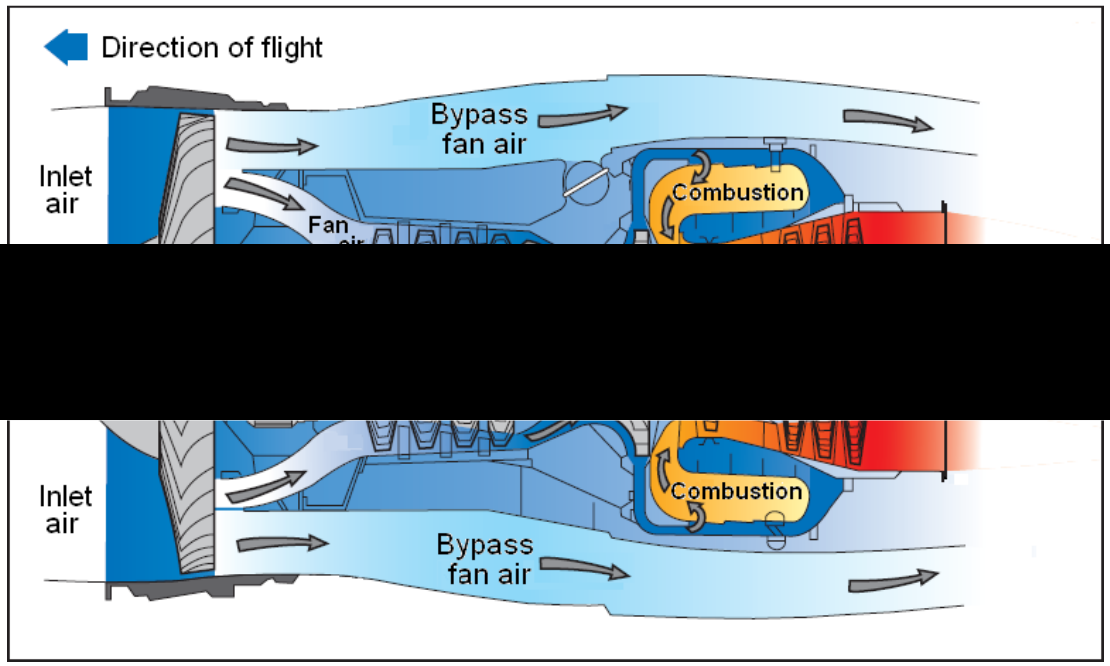

Figure 2: Turbofan Engine [3]

The fan will usually be driven by the low pressure turbine and will increase the velocity of the air entering the engine; it can be considered a low pressure compressor stage. A substantial amount of the fan air will not pass through the core of the engine but will be directed, with increased velocity through the bypass section, directly to and increasing the thrust of the jet stream [4]. The current Trent 1000 engine has a bypass ratio of between 10.8 and 11; this will improve specific fuel consumption and propulsive efficiency. However, this bypass increases the size of the engine, and the manoeuvrability is decreased in comparison to that of a turbojet.

2.1.2 Turbine Discs

The turbine disc is a component used to "locate and retain the rotating blades enabling the circumferential force produced by them to be transmitted to the compressor through the central shafts" [5]. The turbine disc will experience a range of temperatures and stresses; at the bore it is approximately 300°C with high stresses, and at the rim it will experience high temperatures and relatively low stresses. These differences will create stress and thermal gradients across the disc [6]. It is categorised as a critical component, as its failure would likely lead to loss of life.

The original design for the turbine disc was optimised for high burst strengths, as it was believed that this was the key requirement; however, the design is now based more on fatigue damage tolerance and extending creep life [1]. Aircraft engines are designed so that if a component was to become loose it would, where possible, be contained within the engine casing, minimising the potential for damage to the fuselage. However, due to the mass and angular momentum experienced by the rotating disc, this containment is not possible; this results in the need for a very reliable component. With the requirement for safety also comes the need for precision manufacturing to produce the disc to tight tolerances to reduce gaps where possible and minimise friction; this is especially important at the fir tree route fittings, where the turbine blade attaches to the disc, i.e. ±10μm. These factors combined, make the design of the turbine disc a complex and important task.

In many gas turbine engines for commercial and military aircraft, the turbine disc will be made from one of a large range of nickel-base superalloys, which have been developed specifically for the high-strength, complex mechanical properties required. Many methods have been developed to produce the best mechanical properties from; the alloying combination, advanced alloying methods such as powder metallurgy, and processing such as hot isostatic pressing and shot peening. The combination of new methods for heat treatments & processing, and complex combinations of elements in the alloys has allowed for an increase in rotational speeds and higher turbine entry temperatures (TETs), leading to greater operational efficiencies. However, with the constant requirement for greater efficiency, the mechanical properties of these materials need to be continuously investigated for their applicability for greater

stresses and temperatures. If the existing materials are found to be unsuitable, a new alloy or novel processing method may be required.

2.2 Nickel and its Alloys

Nickel (Ni) is a metal that forms the base of many of the superalloys currently utilised by the aerospace industry [7]. Nickel based alloys are common in many industries for a wide range of applications. Nickel has a face centred cubic (FCC) crystalline structure, which is a close packed cubic structure meaning it will form strong, ductile materials [8]. Primarily nickel atoms with small additions of γ forming elements form a disordered FCC γ matrix; this is the name for the continuous FCC austenitic phase [9], the structure of which can be seen in Figure 3. The diagram is simplified and states only Ni and Al, however, any of the γ forming elements can be randomly arranged throughout the structure. It is a dense alloy system compared to many of the alloys used within the aero engine, at approximately 8900kg/m^3 at room temperature, dropping to approximately 8300 kg/m^3 at its melting point at approximately 1450°C. Nickel is resistant to corrosion in comparison to other aerospace metals; however oxidation is rapid at high temperatures. The preferential formation of a protective oxide film layer on the surface, which limits further oxidation, provides a great advantage to its use at these high temperatures. Of fundamental importance to its use throughout the materials science industry, nickel will form alloys readily.

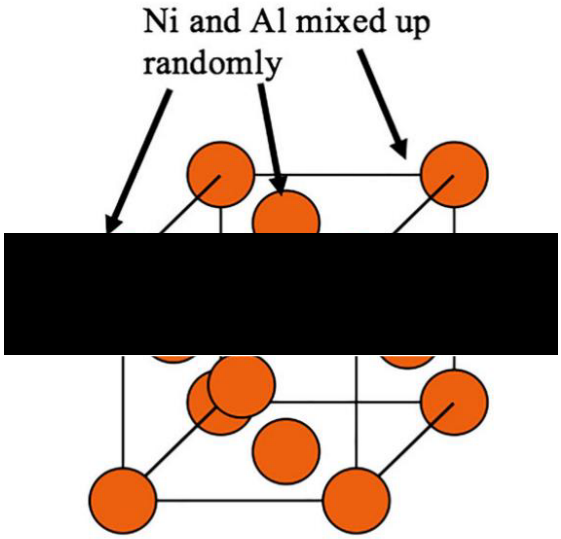

Figure 3: Crystal structure of the FCC γ phase [10]

Nickel is often alloyed with chromium, cobalt, molybdenum, aluminium, titanium and many other elements [11]. As with any alloying, it is the aim to produce a material suitable for a specific task. The nickel components in an aero engine require corrosion resistance, creep resistance, good ductility and high strength and hardness properties. This can be achieved in several ways including; solid solution strengthening, precipitation hardening and grain size control; these can all be achieved through alloying. The cobalt, molybdenum and tungsten provide the solid solution strengthening, the aluminium and titanium provide the precipitation hardening in the form of a γ' phase, with carbon and boron increasing strength and ductility through the formation of carbides and borides [12]. It is a very complex process to design a new alloy; an element may be added for certain properties, but other characteristics may be unfavourable e.g. titanium is used to increase hardness, but oxidises rapidly at high temperatures leading to embrittlement [13]. The name superalloys given to these alloy systems was earned due to their impressive creep performance at high temperatures and their ability to maintain their strength and operate in conditions close to their melting temperature. The impressive creep properties of different forms and variants of the superalloys can be seen in Figure 4, indicating the improvement of the alloys over time through alloying and processing methods.

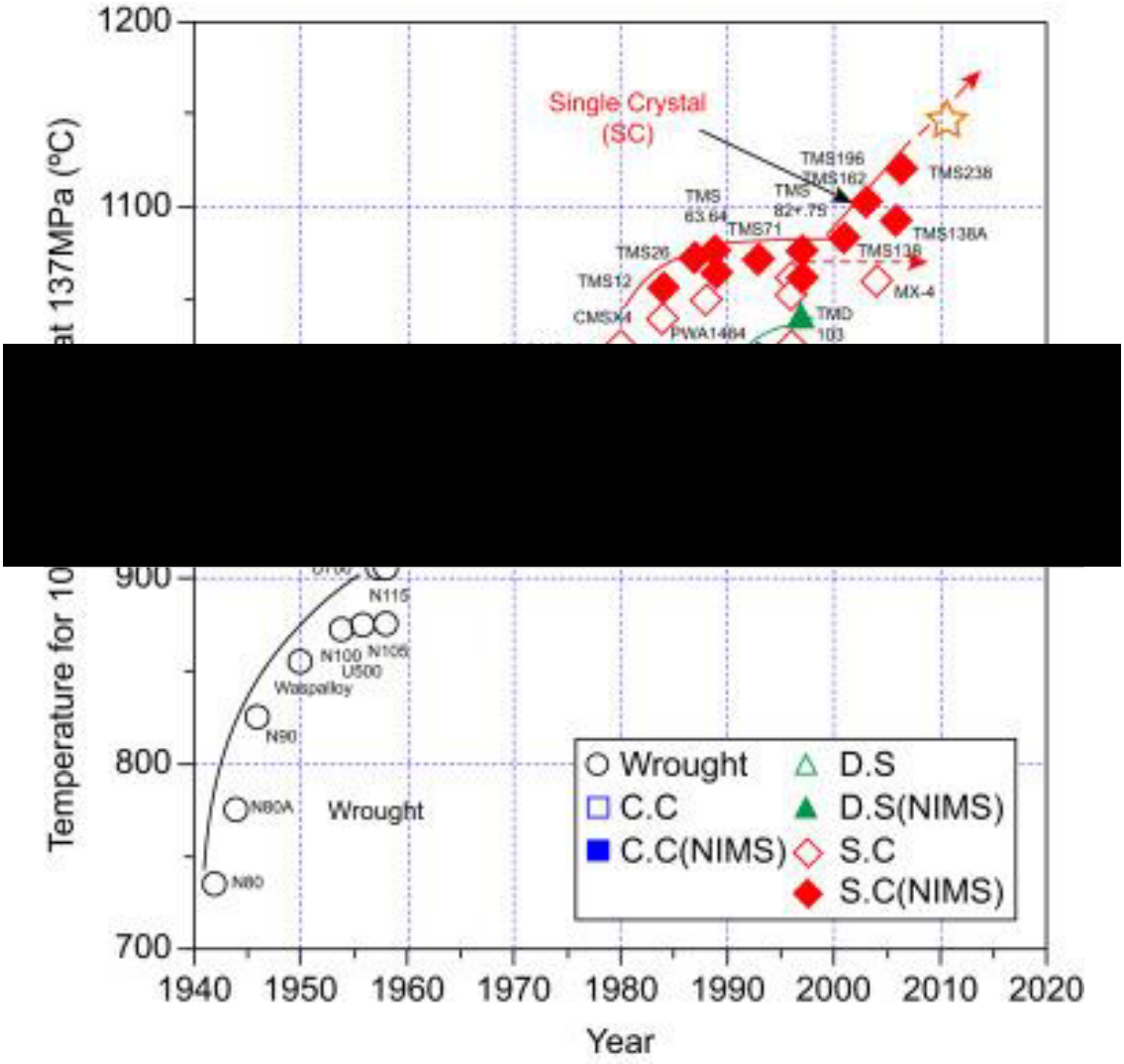

Figure 4: Progressive improvements in temperature capabilities of the superalloys [14]

2.2.1 RR1000

RR1000 is a Ni-based superalloy that was designed for application as a high-pressure turbine disc material to meet the requirements of the Trent 1000 engine, which was developed for use on the Boeing 787 aircraft. The increasing turbine entry temperature (TET) and rotational stresses of these new engines determined the need for a new alloy that could withstand these challenging conditions.

RR1000 is a powder metallurgy alloy that is formed using forging and heat treatments, and is utilised in both a fine (5-10µm) or coarse grain (32-45µm) structure [15]–[17]. These different microstructures will provide very different properties; coarse grain for enhanced creep resistance and fine grain for improved fatigue life. Dual microstructure

turbine disks are currently in operation, with finer grain near the disc bore and coarse grains at the rim. The alloy contains a high volume fraction of the γ' phase in 3 forms; primary, secondary and tertiary, all of which improve the alloy's mechanical properties in different ways. It is an extremely important contributor to the strength and hardness of RR1000.

The chemical composition of RR1000 can be seen in Table 1.

Table 1: Composition of RR1000 in wt. %

Ni	Cr	Co	Mo	Al	Ti	Ta	Hf	Zr	C	B
Bal.	15.0	18.5	5.0	3.0	3.6	2.0	0.5	0.06	0.027	0.015

Each element is added as it is believed that it will provide an advantageous characteristic to the alloy;

Nickel: forms the gamma matrix.

Chromium: Added for oxidation resistance properties and will form strengthening carbides.

Cobalt: Gamma matrix stabiliser and has good high temperature properties

Molybdenum: Good high temperature properties as it has a high melting temperature and will form carbides

Aluminium: Gamma prime former

Titanium: Gamma prime and carbide forming element

Tantalum: Gamma prime and carbide forming element.

Hafnium: Carbide former

Zirconium: Good high temperature properties due to its high melting temperature

Carbon: Good high temperature properties and base element of carbides.

Boron: Good high temperature properties and base element of borides

2.2.1.1 γ' (Gamma prime)

γ' is a precipitate phase coherent within the alloy's γ matrix, as it has a very similar crystal structure, as shown in Figure 5.

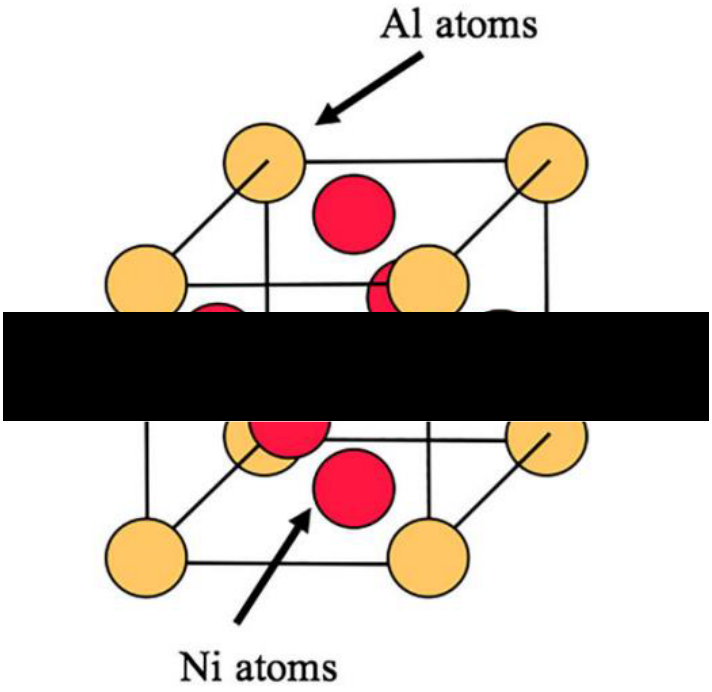

Figure 5: Ordered crystal structure of the FCC γ' phase [10]

A list of the γ' volume fractions of a number of nickel superalloys can be seen in Table 2, taken from research by Mitchell et al. (2004) [18], Jahangiri et al. (2012) [19] and Reed [11].

Table 2: γ' volume fractions for a number of nickel based superalloys

Alloy	Nimonic 105	IN939	RR1000	U720	CMSX-4
Approx. γ' volume fraction	45%	35%	47%	47%	70%

It is rich in elements such as titanium and aluminium and is the principal strengthening phase in Ni-based superalloys and has the form [Ni_3(Ti,Al)] [20]. The distribution, size

and volume fraction of γ' precipitates will directly impact the mechanical properties of an alloy [17]. The yield strength is a function of the inter-particle distance [21]; a volume fraction close to 50% will produce “excellent fatigue performance and damage tolerance, and good creep resistance” [22], which is why it is favoured for polycrystals and 70% produces favourable creep properties such as those needed in single crystals e.g. CMSX-4. The strengthening mechanism is derived from the interactions of dislocations within the material and the precipitate particles [21]. The primary γ' is the largest of the γ' precipitates (1-2μm) and is present in the alloy before the sub γ'-solvus heat treatment; they are commonly found at the grain boundaries, but can also sometimes be found within the grains. The grain boundary precipitates will restrict the grain growth to a fine grain size; when producing the RR1000 alloy with a coarse grain size, the material is heated above the γ' solvus to remove the restrictive primary γ' precipitates allowing the grains to continue growing through the heat treatment and cooling processes. The secondary and tertiary γ' precipitates are smaller than the primary at approximately 100-500nm and less than 50nm respectively and are stabilized during post forging heat treatments; they are only found within the grains [18], [23]. A micrograph of the forms of γ’ that will be present in RR1000 can be seen in Figure 6.

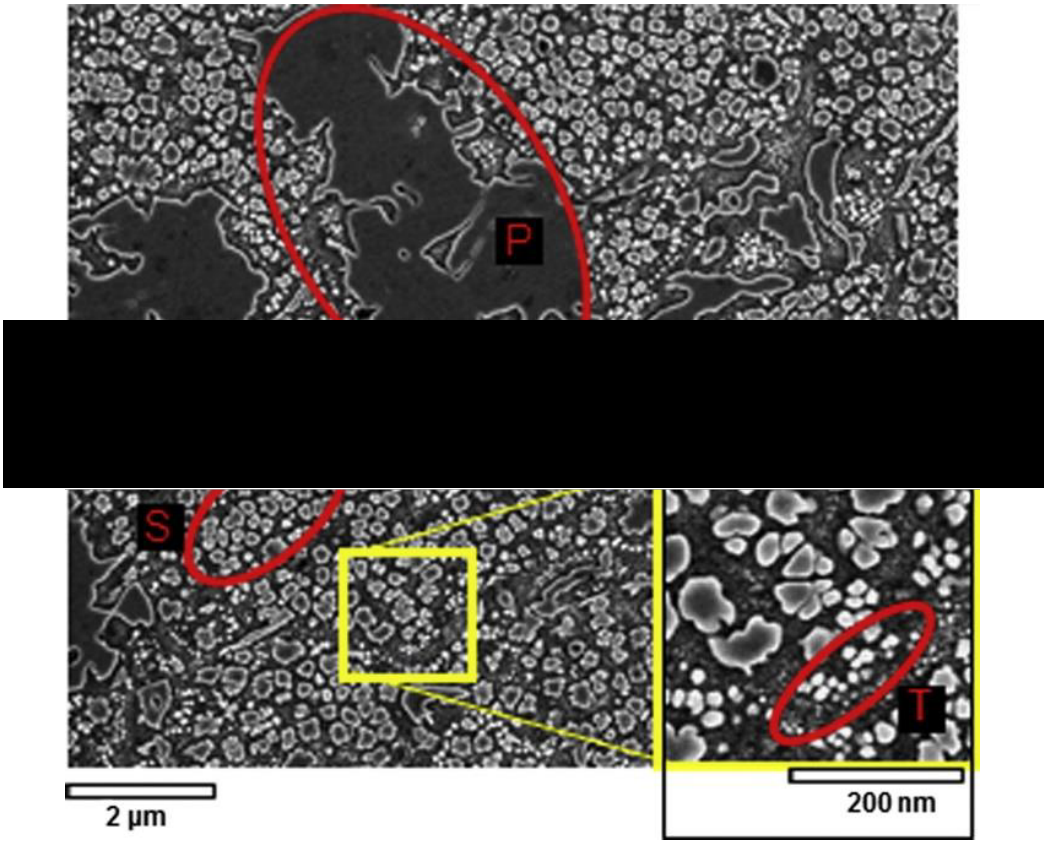

Figure 6: Gamma prime distributions in RR1000 where; P is primary, S is secondary and T is tertiary [17]

The γ' size and shape within the alloy is related to the post heat treatment cooling rate; initially the primary will form at the grain boundaries, subsequently the secondary γ' will form in the matrix within the grains, and finally with the tertiary γ' forming late in the cooling sequence, with an aging process to control the particle size for optimal mechanical properties [18]. The size and shape evolution of the γ' particles can be seen in Figure 7, which is a graphic used by Reed [11] based on research by Ricks [24].

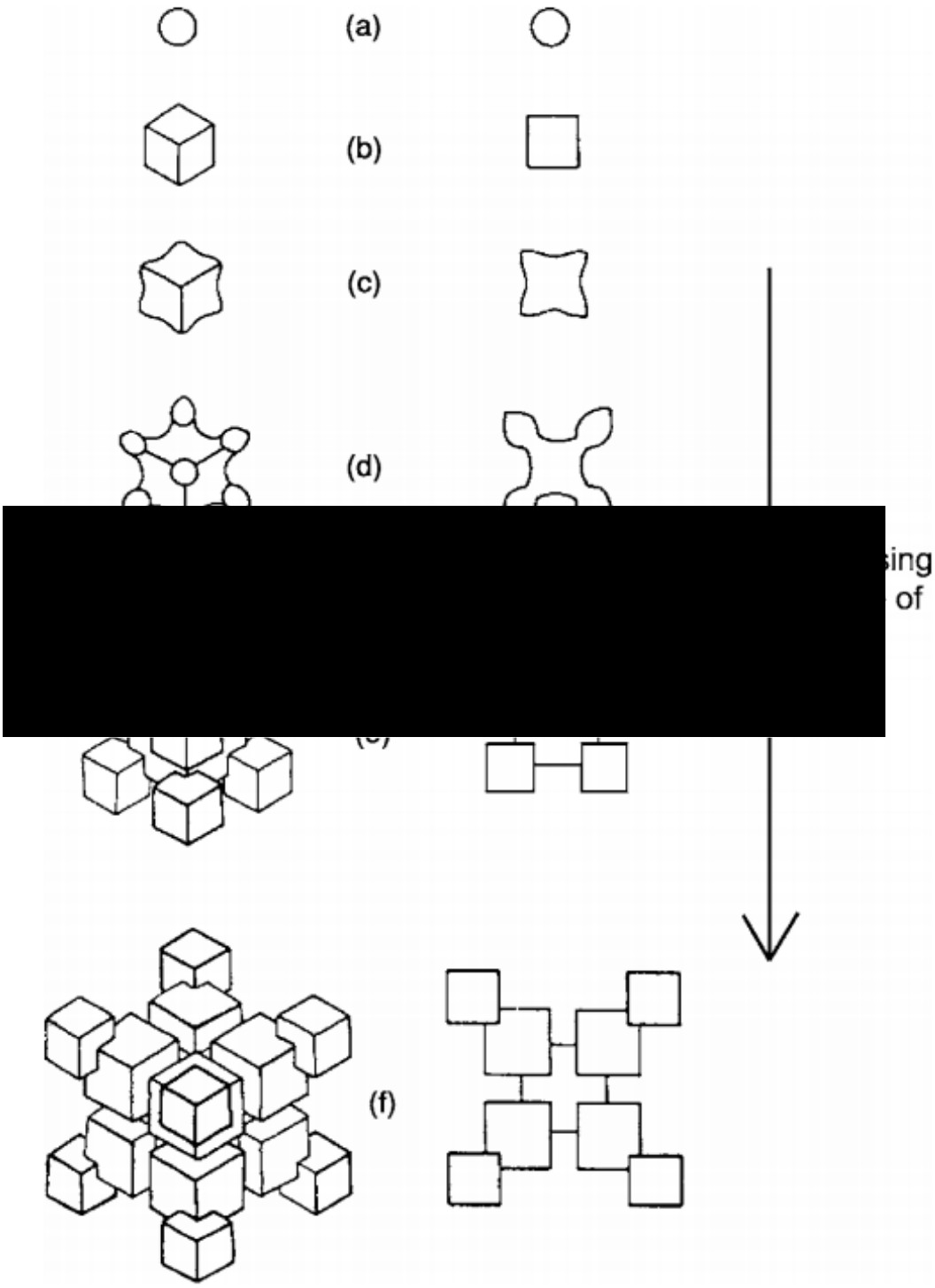

Figure 7: Diagram of evolution of γ' particles (left) <111> projection (right) <001> projection [11]

2.2.1.2 Carbide and Boride Phases

Similar to many other nickel based superalloys, RR1000 contains carbide and boride phases [25], [26]. The role of carbides and borides in nickel superalloys is controversial, however, it is now widely accepted that carbon and boron additions do improve the creep properties of the superalloys [11]. This is because they will primarily form at the grain boundaries of the γ matrix, inhibiting grain boundary sliding. Carbides and borides can be in the form MC, M_6C, $M_{23}C_6$ and M_5B_3, where M represents a metal; commonly chromium, hafnium, molybdenum, titanium and tantalum. The grain boundary carbides and borides in the nickel superalloy IN792 can be seen in Figure 8.

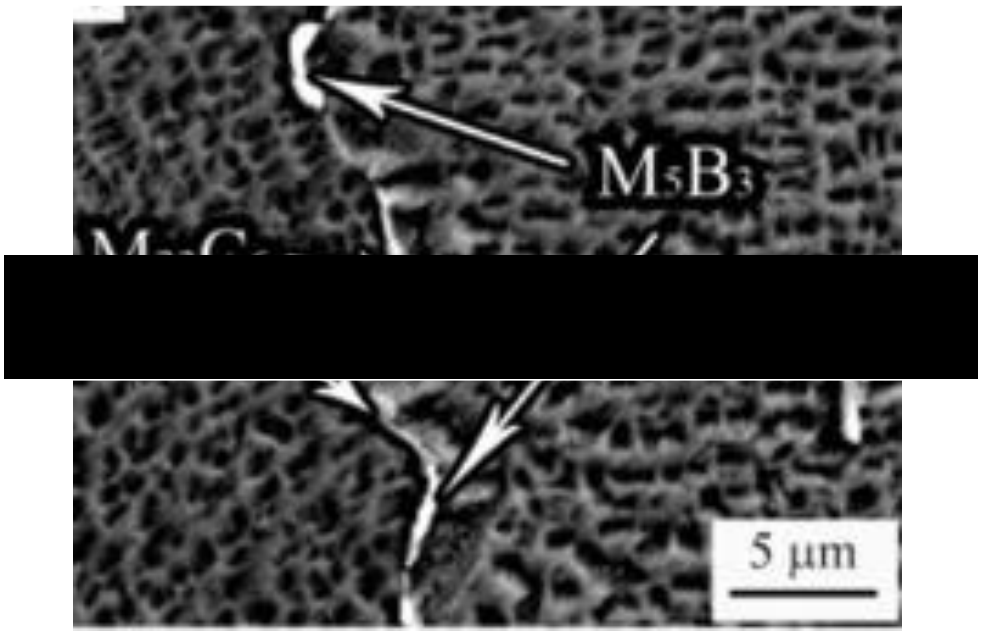

Figure 8: Carbides and borides in nickel based superalloy IN792 [27]

2.2.1.3 Mechanical Processing

The mechanical processing of RR1000 has developed beyond the conventional cast and wrought approach that was used extensively for other nickel based alloys for turbine disc applications, such as alloy 720Li. Due to difficulties in material processing; a powder metallurgy method has been adopted. The process route for the powder metallurgy process is described in Figure 9.

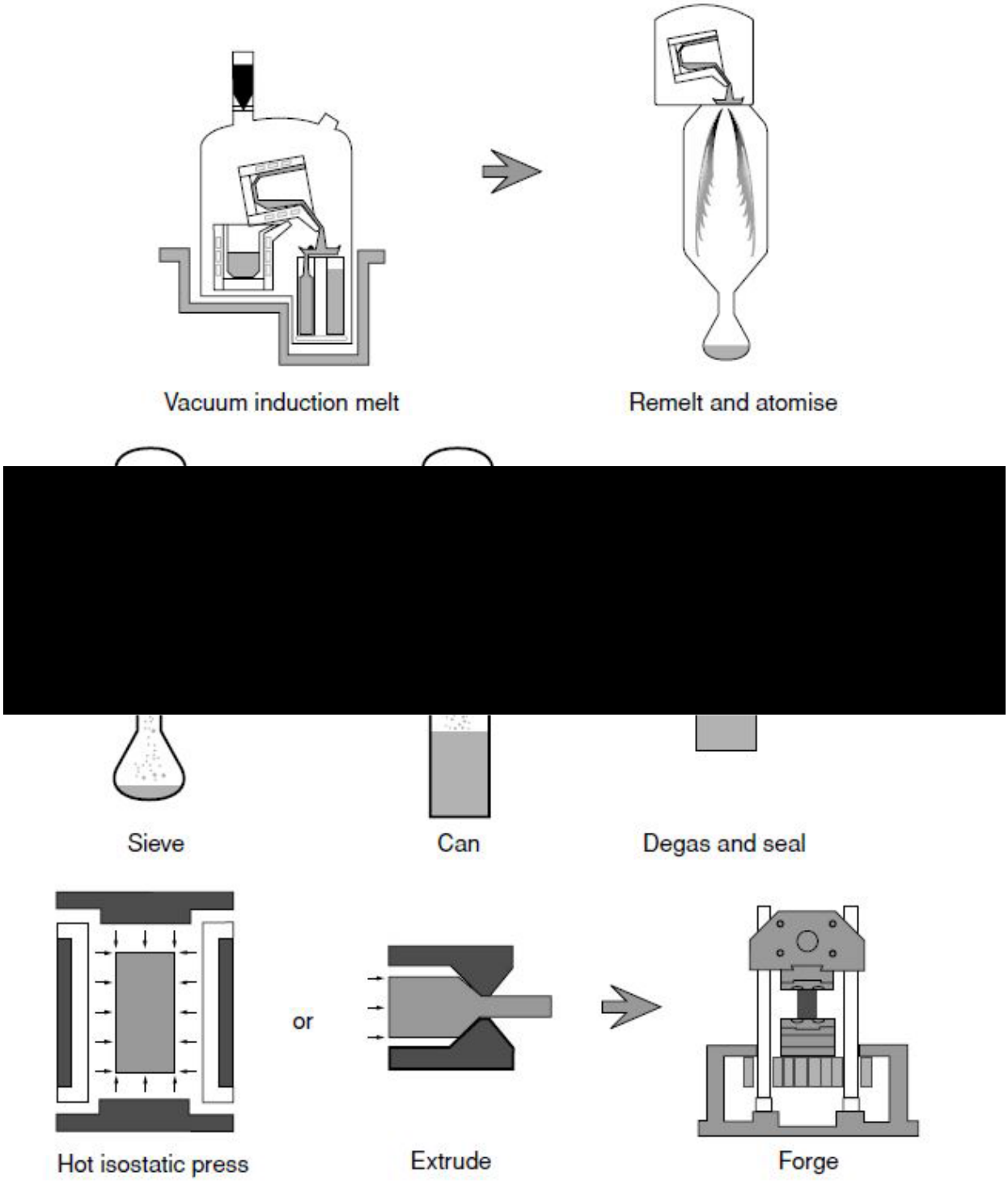

Figure 9: Processing route for powder metallurgy alloys [28]

The elements of the alloy are melted through the process of vacuum induction melting. The melting is performed under vacuum due to the reactivity of the metals. Vacuum induction melting is the preferred method of vacuum melting as it offers more control of the alloying composition and homogeneity [29]. The powder is then produced via atomisation: metal is heated to a molten state, broken up into small droplets and then solidified rapidly before they can recombine [30], using argon gas atomisation. High velocity argon gas is forced through a stream of molten metal breaking it up into small spheres and solidifying it; argon is used as it is extremely unreactive.

The powder then passes through a number of processes to prepare it for forging. Firstly, the powder is screened to ensure powder particles of approximately the same size are used in the billet forming. The particle size will have a massive effect on the processing and the final product. The powder is then blended, which aims at achieving uniform size and shape distribution of the particles within the powder. Next the powder is loaded into a container (canned), taking care to maintain the homogeneity of the powder, and the container is then degassed to remove absorbed gases and water vapour. The powder goes through the process of hot isostatic pressing (HIPing). During this stage the metal powder, is compressed using an inert gas at high pressure and high temperature. This forms the powder into a solid, ready for the extrusion process. The extrusion process is used to create billets of uniform diameter and length ready for forging.

This process route is used for the turbine discs as it is possible to achieve greater proportions of alloying additions, while avoiding the hot workability and segregation problems often associated with high alloy contents [31]. The alloys produced have a much greater likelihood of having an isotropic structure throughout the billet and therefore throughout the final component.

Turbine disc components have complex geometries and specialised microstructures. The forging processes to form them are multistage impacts using various closed dye preforms. Forging is a mechanical manufacturing process during which a material is shaped by the application of local compressive forces applied by another material, known as a hammer or a dye. The forging process will produce components with high strength compared to those formed through other manufacturing routes. Hot-forging is the processing route preferred for the formation of the turbine discs. The main

advantages provided by hot-forging are; the resultant reduction in porosity due to the compression, and the reduction or possible elimination of inclusions by their break-up and redistribution throughout the component [32]. The forgings are also preferable because they produce near net shape components, that require little or no machining [33].

The forging process can be optimised for a specific component. The variables defined for the process will alter the grain structure of the component; if these variables are optimised, a preferential structure can be formed.

Once the component is in its final geometry, shot peening is undertaken. Shot peening is a cold working process by which the surface of a component is work-hardened through the repeated impact of small metal spheres. The shot peening process is described in Figure 10.

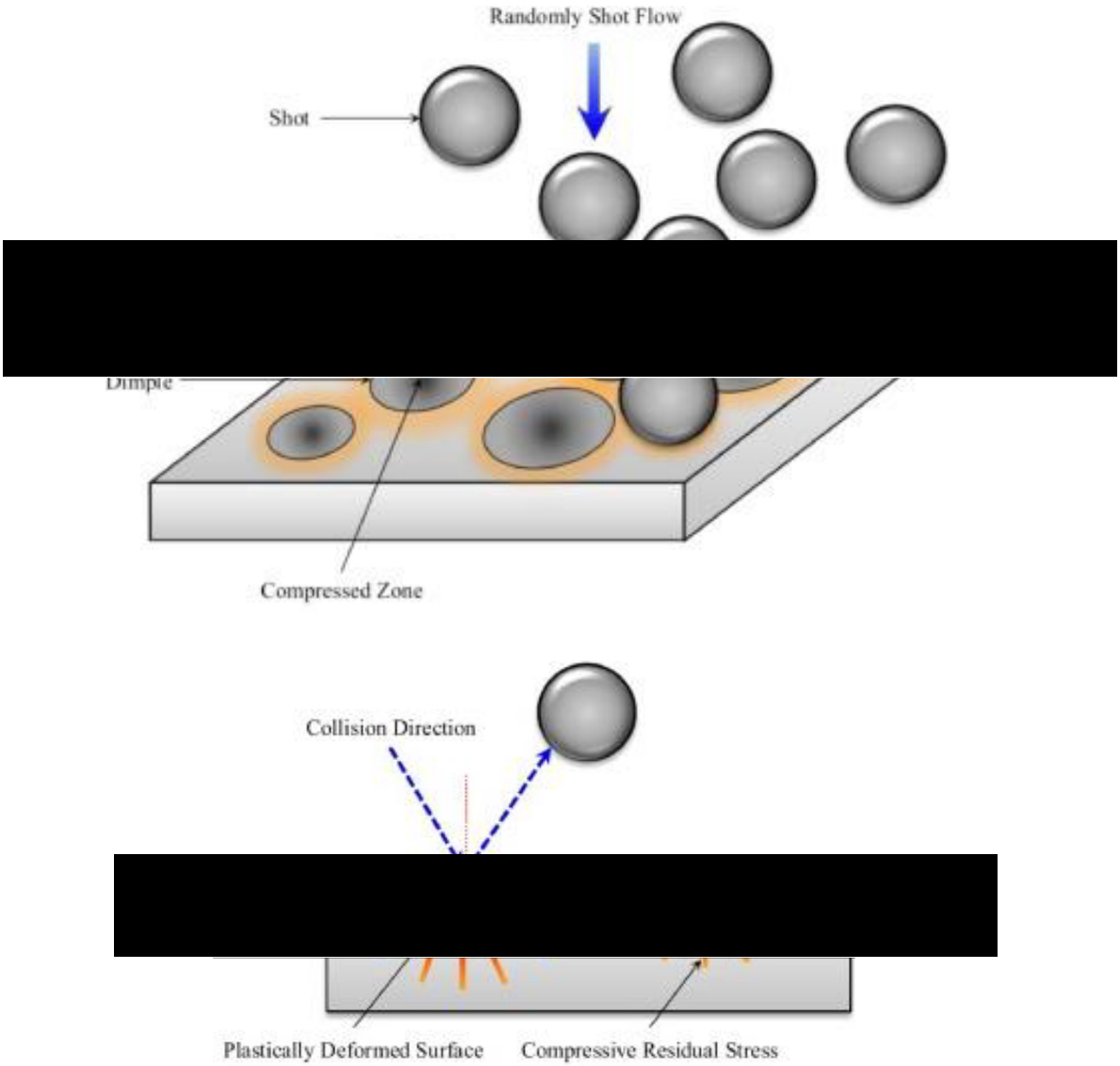

Figure 10: (top) the shot peening process (bottom) the plastic deformation made by shot peening [34]

After common machining processes it is likely that tensile residual stresses will remain at the surface; this residual stress will work to effectively raise the tensile loads experienced by a component. By applying a small compressive stress layer at the surface, these effects are mitigated, and the effects of initial tensile loading is further reduced [35], [36]. The compressive residual stress also acts to close microcracks from the surface and stop them from propagating. The overall result is a reduction in the rate of fatigue crack initiation.

These are a number of parameters that will affect the peening process [37]:

1. Component geometry
2. Material properties
3. Shot properties
    a. Size
    b. Velocity
    c. Angle of impingement
    d. Distance of nozzle from the surface
    e. Hardness of the shot (equal to or greater hardness than the material being peened)
4. Peening process parameters
    a. Coverage (ratio of peened surface to total area surface area)
    b. Intensity (represents the intensity of the peening and measured in Almen)

The current peening procedure used for the RR1000 turbine discs is: 110H/ 125-200%/ 6-8A where; the 110H is a measure of the hardness of the shot with a 125-200% coverage required at an intensity of 6-8A.

2.3 Oxidation

Practically all alloys of interest to the engineering and technology disciplines oxidise and corrode at elevated temperatures. However, the nature of reaction products and rates vary widely for different materials. The first work which expressly investigates high temperature oxidation is that of Tamman in 1920 [38]. It is highly desirable to be able to predict the forms and rates of oxidation and corrosion, and to do that it is vital to understand their mechanisms through investigation. Commonly this is in a laboratory environment, based on the operating conditions of components in service.

The term oxidation is used to describe any reaction that results in an increase in the oxidation state of a metal caused by the formation of an oxide compound, and is often referred to as dry corrosion or tarnishing. Oxidation at high temperatures can form molten or chemically unstable layers; however, more commonly it will form a non-metallic (ceramic) scale layer on the surface, which will prevent further oxidation by separating the material from the reactive gas [39].

Oxidation reactions can be thought of as occurring in three distinct phases. Initially, rapid oxidation reactions will occur with all alloy elements in contact with the gas (component surface) simultaneously. Subsequently, more thermodynamically stable oxide compounds will form replacing the less stable compounds that have already formed. Finally, a state of near equilibrium will be approached resulting in an effective steady state reaction. Alloys that have obtained wide use in the damaging high temperature environments are those that show lengthy periods of a slow steady state reaction.

Due to the complexities of the oxidation reaction and its effect on real world applications, a multidisciplinary approach is required. Materials science, chemistry and physical metallurgy provide the tools requisite to understand the reaction i.e. chemical kinetics, oxide properties and their effect on alloy phase constituents. Specific attention must be placed on the understanding of defect based diffusion mechanisms in polycrystalline materials. Equally, the effect of structural and compositional variations on the mechanical properties of different materials must be understood as it could play a pivotal role in the life of components.

In recent years there has been a remarkable increase in published research regarding high temperature corrosion. The understanding of oxide grain boundary diffusion has improved and the nature of chromium oxide and aluminium oxide scales and their ability to protect alloys from extensive oxidation is being developed.

The rate, extent and method of oxidation of a material are related to a number of factors including; the ability of the oxide to maintain a protective barrier, surface condition of the component, operating temperature and the time at temperature [40]–[48]. It has been found that the overall effects of oxidation on the life of the alloy RR1000 are detrimental, and have the potential to greatly reduce the life of a component [49], [50].

In this section, a review has been undertaken into the literature surrounding the areas of importance to an oxidation analysis. Firstly the oxidation reaction has been discussed, with care taken to understand the oxidation mechanisms. Secondly an understanding of the oxides that form during oxidation reactions and their ability to protect from further damage has been developed. Next, the methods of oxidation damage measurement have been evaluated in an effort to determine the best quantitative method to be used throughout this analysis. It was also deemed important to understand the effect of some basic properties on the oxidation rates of various alloy systems, therefore, surface condition, temperature and grain size were investigated. Penultimately, effort was made to determine any existing methods of comparing oxidation between different alloys. Finally a search was conducted to determine any work investigating thermo-mechanical oxidation; the effect of the addition of mechanical stress on the rate of oxidation.

2.3.1 Oxidation Reaction

Metal oxides will form according to Equation 1 [14]:

$$\frac{x}{y}M + \frac{1}{2}O_2 = \frac{1}{y}M_xO_y \qquad 1$$

Where:

M = reacting metal cations
O = oxygen anions

As such, for a reaction to occur, the metallic cations and oxide anions must come into contact. The processes will occur in three stages; the name of the reaction stage is the rate controlling factor during that phase of the process [51]:

1. Adsorption & nucleation
2. Thin film mechanism
3. Diffusion

To begin the reaction, oxygen gas must be chemisorbed onto the metal surface until an invisibly thin oxygen layer is formed. Oxygen will then dissolve into the substrate and the metallic oxides will nucleate, expanding laterally. The oxide nuclei will most likely originate at structural defects such as grain boundaries, impurities and dislocations due to their increased disorder [52]. The oxide islands that form from the nuclei will grow rapidly by surface diffusion of adsorbed oxygen until a thin film is formed. The oxidation rate then drops abruptly.

As per its name, the scale thickness during the thin film mechanism phase will be very small. There are many different theories suggesting how oxides grow, generally based around the Cabrera-Mott theory which applies for films up to 10nm thick. It suggests that electrons from the metal pass easily through the film by quantum tunnelling to reach the adsorbed oxygen at the oxide to gas interface and form oxygen anions. The electric field is strong enough to pull metallic cations through the film. The rate controlling step for this mechanism is the transfer of cations. As the film grows thicker

the field strength decreases and the mechanism changes to the diffusion stage [14], [52].

The final stage of the oxidation process will dominate once the thin film has thickened to the point where the thin film mechanism no longer dominates. Diffusion is the movement of atoms from an area of high concentration to an area of low concentration; diffusion in metals is described by Fick's laws. The rate of the oxidation reaction during this stage will be regulated by the ability of the oxide scale to impede the diffusion of oxygen into and the metal ions out of the substrate. A schematic of the growing oxide scale described by Young, 2016 [14] is shown in Figure 11.

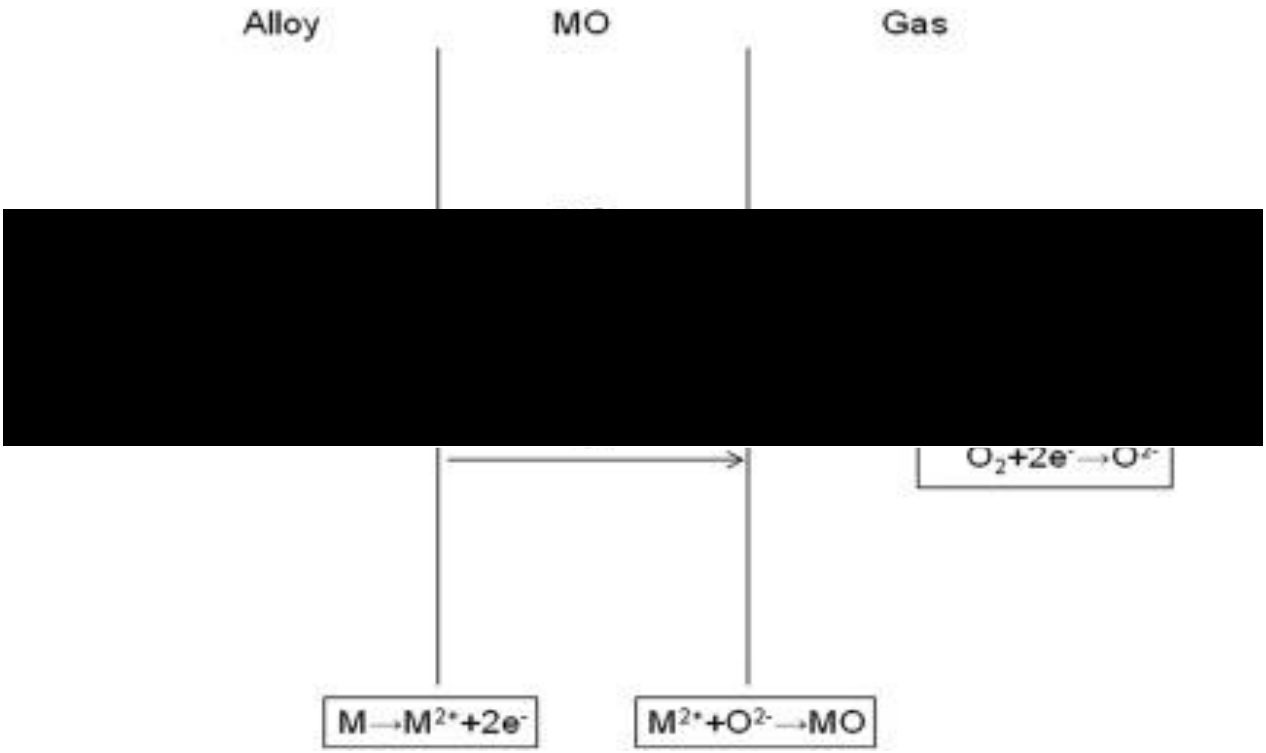

Figure 11: Reaction and transport process in the formation of the oxide scale [14]

The stages of scale growth are:

1. Oxidant delivery to the surface / gas interface.
2. Integration of the oxygen into the oxide scale.
3. Transport of the reacting metal to the substrate / scale interface.
4. Assimilation of the metal into the oxide scale.
5. Transfer of the metal and oxygen ions through the scale.

On an atomistic scale, the diffusion of the ions will be mediated by the presence of defects in the crystalline state. It should be noted that diffusion will be occurring constantly, even in pure metals, however, without a concentration gradient the net flow of the atoms is effectively zero.

The mechanism that will have the most effect on the rate of oxidation damage through the lifetime of most components will be solid-state diffusion [14], [53]; at this point the rate controlling factor will be the rate of solid-state diffusion through the oxide scale. Metal and oxygen ions will travel through the oxide layer to the oxide / gas interface and into the metal substrate from the oxide metal interface respectively. There are a number of diffusion mechanisms, the most common of which is a form of substitutional diffusion called vacancy diffusion. There are always a large number of vacancies in metallic crystal lattices and the jump distances are short making vacancy movement relatively easy. The mechanism of vacancy diffusion is presented in Figure 12.

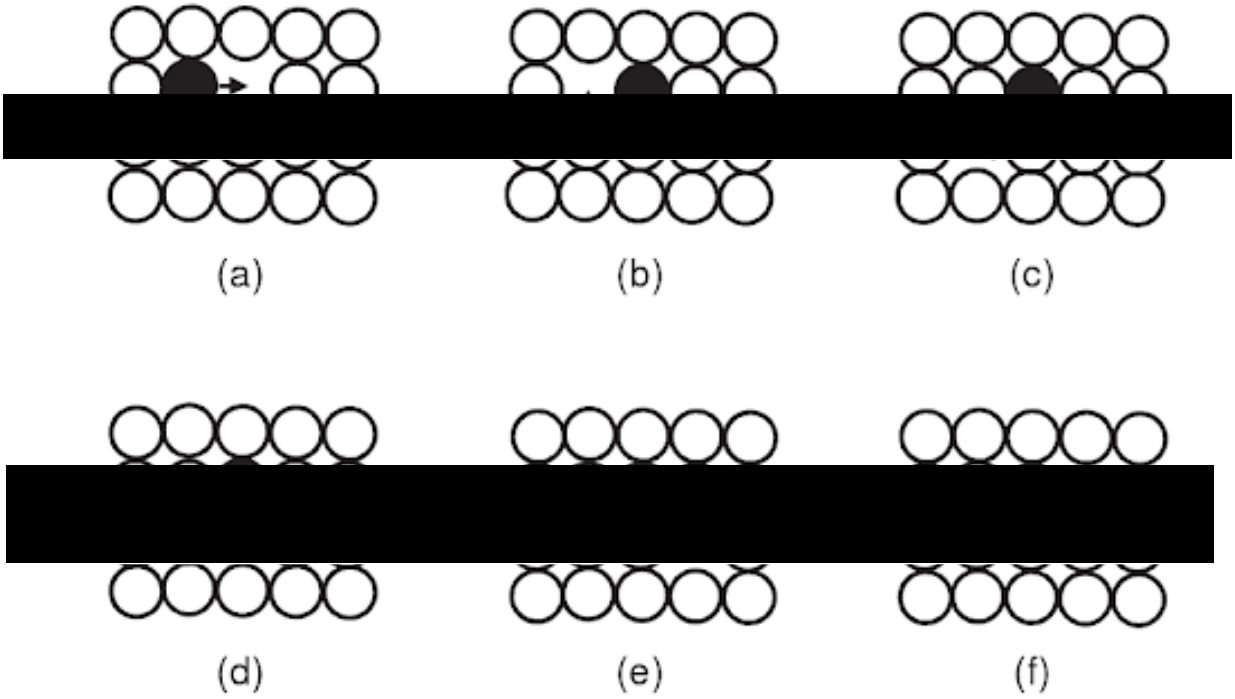

Figure 12: Vacancy diffusion mechanism [54]

For vacancy diffusion to occur the activation energy barrier must be overcome. A description of the role of activation energy in vacancy diffusion can be seen in Figure 13.

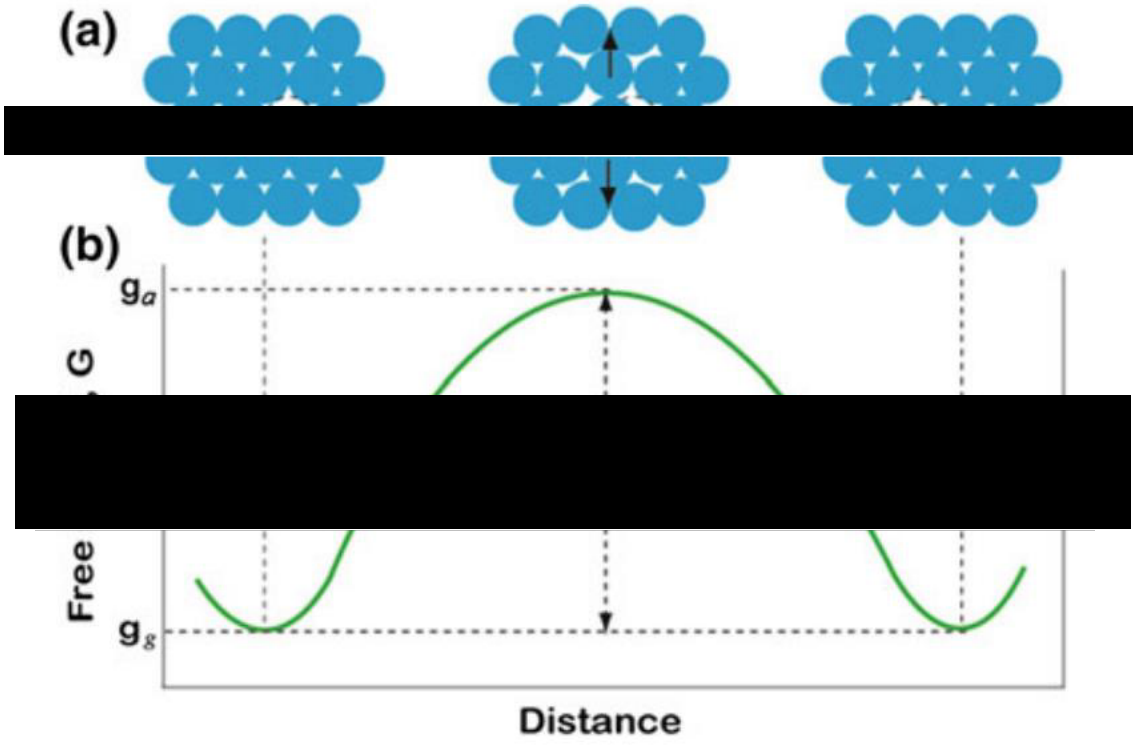

Figure 13: Activation energy barrier for vacancy diffusion (a) atomic movement correlated to (b) the free energy during the movement [55]

In the unlikely condition of only few vacancies being present in a material structure, they can be formed by a number of methods, including dislocation movement and pair annihilation, which will be caused by mechanical and thermal stresses in the material [56].

The method of diffusion for smaller atoms will often be through interstitial diffusion, meaning the atoms locate in the interstice between the larger atoms. Interstitial diffusion occurs though the movement of atoms between interstices sites with little displacement of the atoms in the crystal lattice. This will likely be the diffusion route for the oxygen ions as they would be sufficiently small compared to the metal ions [14], [54], [55], the mechanism of interstitial diffusion can be seen in Figure 14.

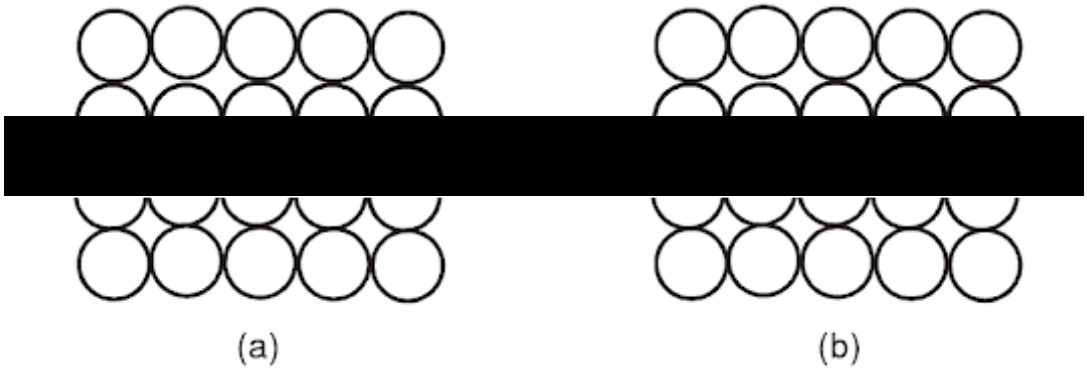

Figure 14: Interstitial diffusion mechanism [54]

Similar to the vacancy diffusion mechanism, the activation energy barrier must be overcome in order for interstitial diffusion to occur, as shown in Figure 15.

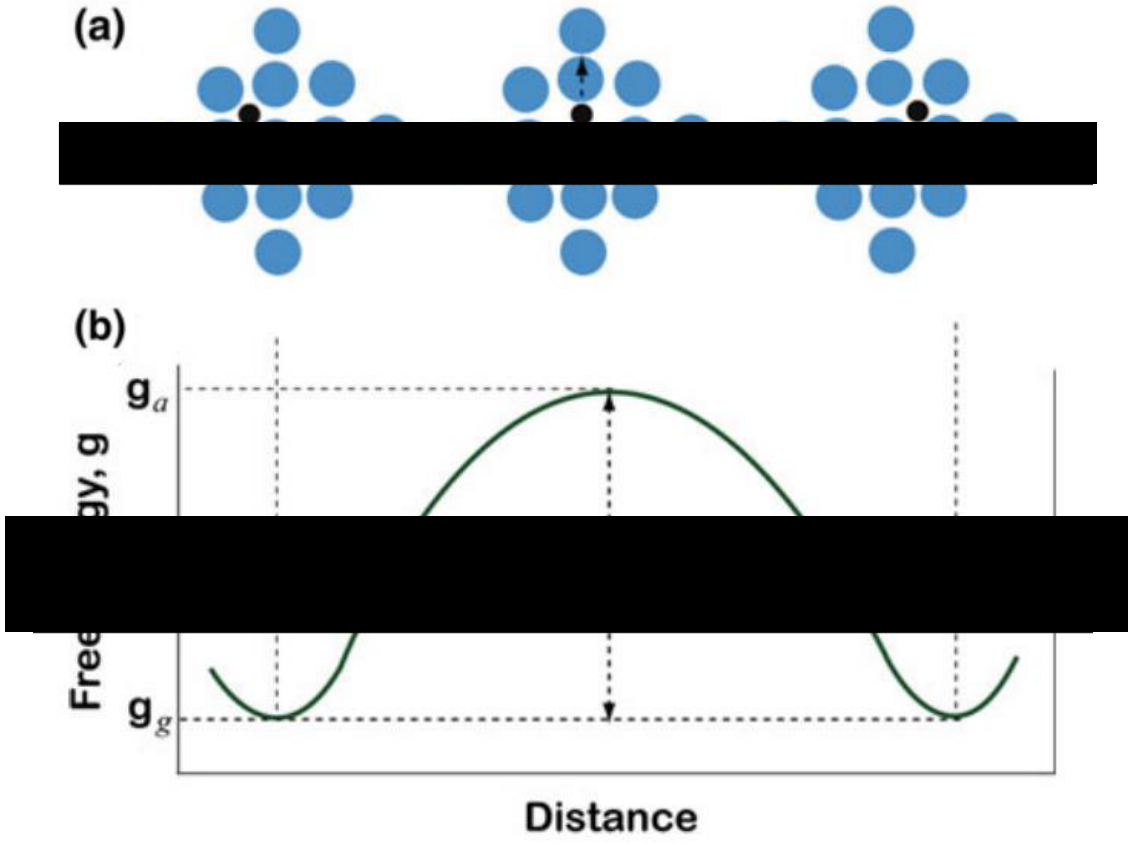

Figure 15: Activation energy barrier for interstitial diffusion (a) atomic movement correlated to (b) the free energy during the movement [55]

The activation energy barrier for diffusion of interstitial diffusion will be smaller than that of vacancy diffusion, because the atoms are smaller and will therefore require less distortion of the crystal lattice to jump to new locations.

The diffusion of atoms along ‘short circuits’ in a material, e.g. grain boundaries and phase boundaries is known a short-circuit diffusion. The reason that the activation energy of short-circuit diffusion is lower than lattice diffusion relates to the more disordered structures of the grain boundaries and line defects. A diagram showing the different types of short circuits in a polycrystalline material can be seen in Figure 16.

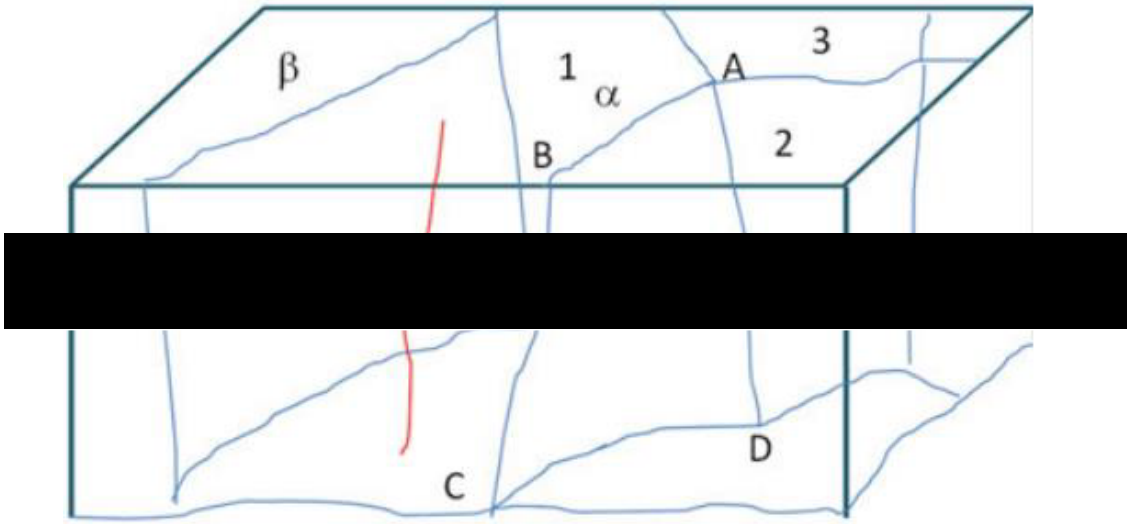

Figure 16: Schematic showing short-circuit paths in polycrystalline material [57]

Where:

- ρ is a dislocation line defect (pipe diffusion)
- ABCD represent grain boundaries (grain boundary diffusion)
- α & β show a phase boundary

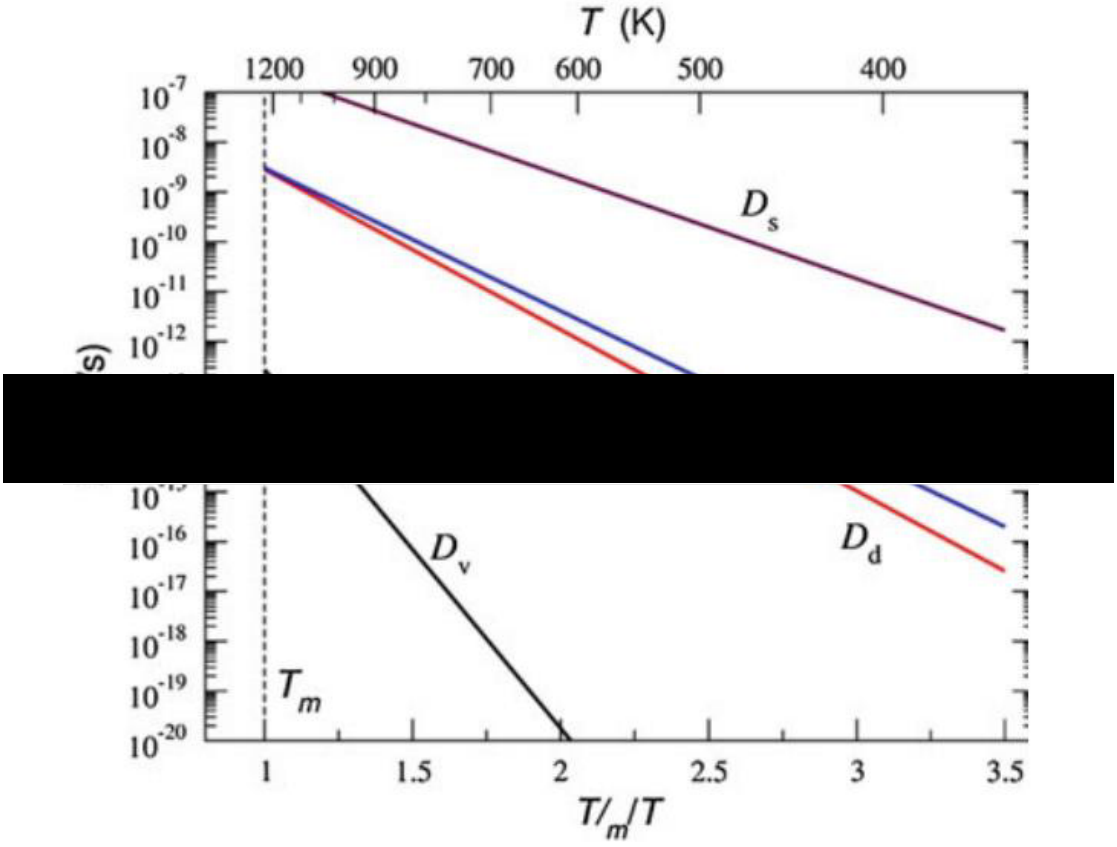

Figure 17: Experimental data on diffusion rates in Ag [57]: Vacancy diffusion – D_v [58], D_d – dislocation diffusion [59], D_{gb} – grain boundary diffusion [59], D_s – surface diffusion in vacuum [60]

There have also been a great many supporting studies describing the process of how short circuit transport occurs for anion and cation species [61]–[66], which supplement the work shown in Figure 17.

The reduction in energy of diffusion at grain boundaries explains why the oxidation processes in a wide variety of alloys commonly form oxides which penetrate the substrate along the grain boundaries as can be seen by the micrographs in Figure 18.

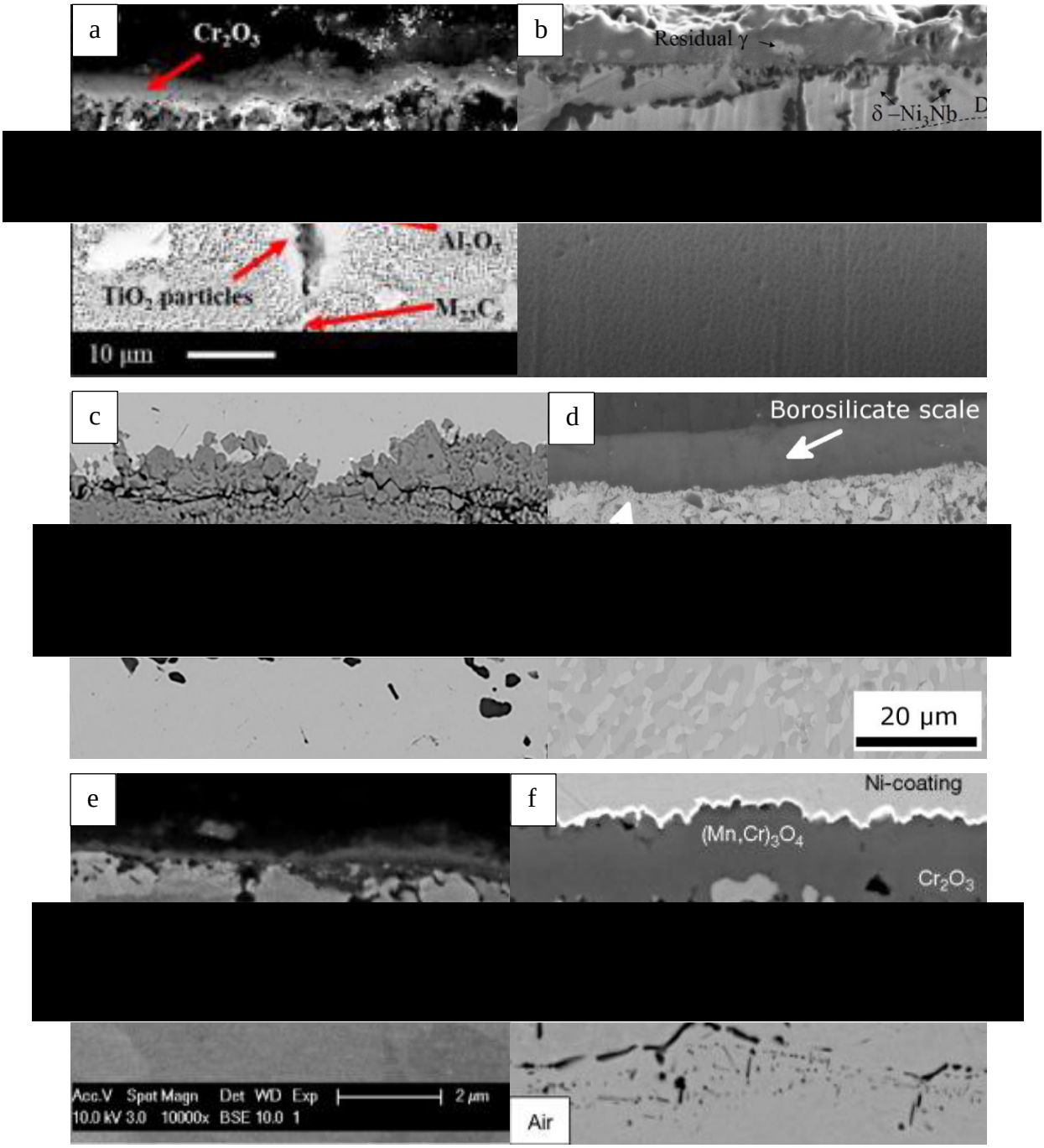

Figure 18: Oxide fingers formed in a number of alloys (a) Rene 80 [67] (b) V207J [68] (c) Refractory austenitic steel [69] (d) Mo50W20Si15B15 alloy [70] (e) RR1000 [71] (f) Croffer 22 [72]

It has been found that the grain sizes within the oxide scale can be very small [14]; however, it can vary greatly depending on composition and temperature of formation from sub-micron to tens of microns in diameter [73]. The sensitivity of the relationship between oxide scale size and time and temperature can be clearly seen in Figure 19.

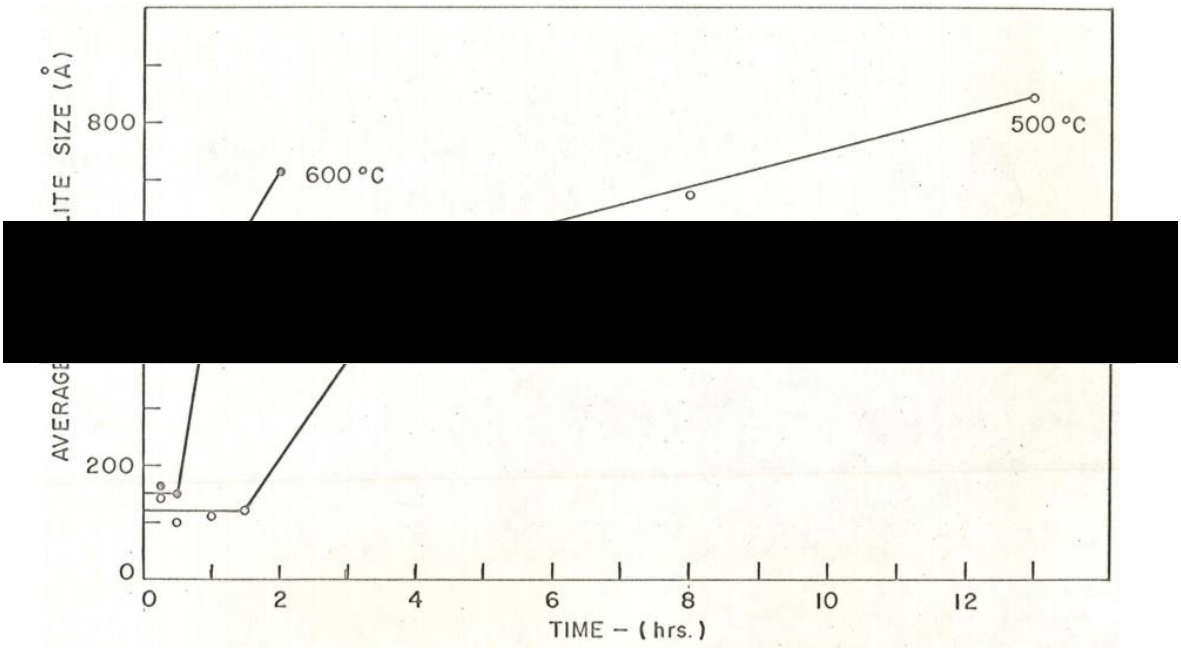

Figure 19: Average grain size in nickel oxide scales against time [74]

At lower temperatures (<800°C) the grain size of the scale will likely be smaller than that of the substrate meaning that short-circuit diffusion will be a driver of diffusion through the scale. However, given the larger substrate grain size in this case, there will likely be a mixed mode diffusion overall between atomic movement along lattice vacancies and along short-circuits; the effects of the vacancy diffusion mechanisms will have a dramatic increase in contribution at higher temperatures, as is indicated by Figure 17.

It was found that Σ3 boundaries have no effect on the oxidation rate, as they showed similar oxidation behaviours as the intra-granular region [75], which is an important consideration given the high volume of Σ3 boundaries found in the superalloys.

2.3.2 Pilling Bedworth Ratio

The mechanical properties of surface oxides are important as components in service may undergo damage from scratching, abrasion or most likely deformation due to loading. The ideal oxide scale would have high compressive strength, minimal epitaxial misfit, similar thermal expansion values and good adhesion to the underlying alloy in order to minimise spallation [76], [77]. Spallation is the process by which the oxide scale will break away from the surface of a larger solid body and can be produced by a variety of mechanisms, including impact, excessive corrosion, cavitation or weathering.

The ability of the scale to protect from further oxidation of the metal and avoid spallation is related to the ratio of volumes of metal to oxide; this is termed the Pilling Bedworth ratio [78]. If the ratio is lower than 1 the layer will be porous, and if the ratio is greater than 2, the oxide film can crack and flake off. Either of these cases will result in an unprotected surface, which will allow further oxidation of the metal. The ideal value for the ratio is between 1 and 2, where the properties of the base metal are similar to the properties of the oxide layer [79]. A graphical representation of the PB ratio can be seen in Figure 20.

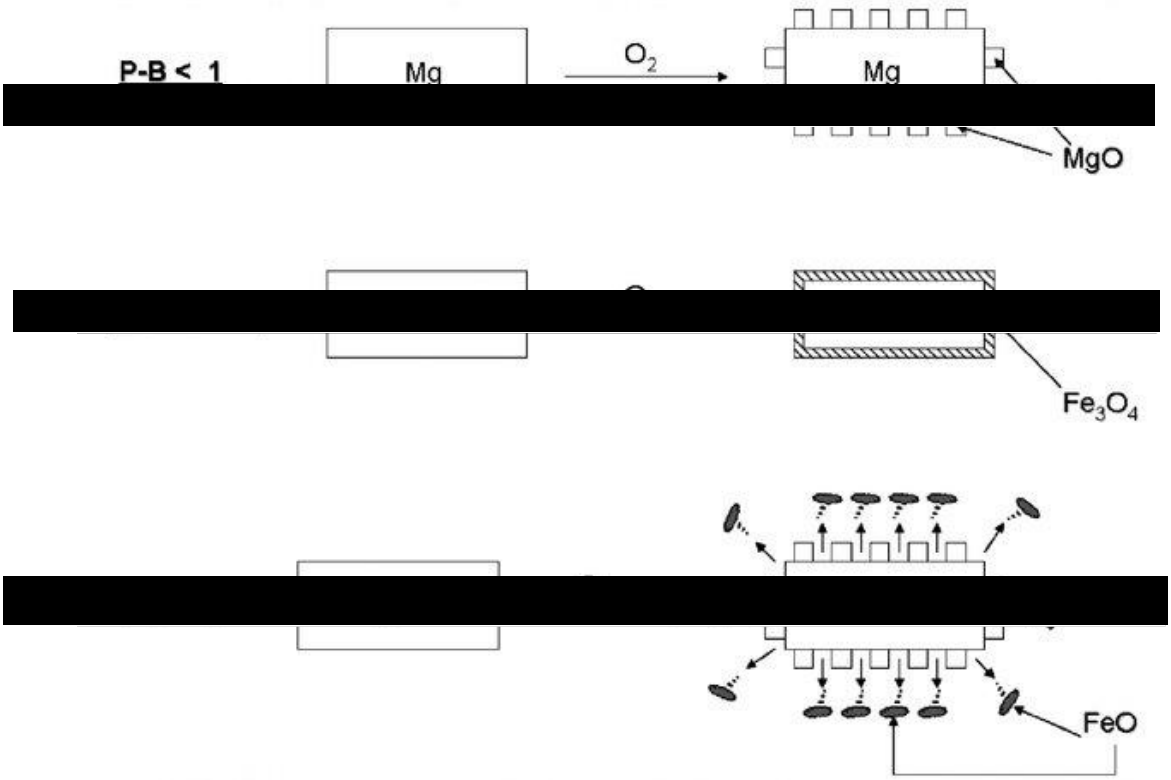

Figure 20: Schematic showing the relation between the PB ratio and the ability of a scale to prevent corrosion [80]

The Piling Bedworth values of some of the main oxide formers of RR1000 and other common metal oxides can be seen in Figure 21.

Oxide	*Pilling-Bedworth ratio (Oxide-metal volume ratio)*
K_2O	0.45
MgO	0.81
Na_2O	0.97
Al_2O_3	1.28
ThO_2	1.30
[redacted]	[redacted]
Fe_3O_4 (on α-Fe)	2.10
Fe_2O_3 (on α-Fe)	2.14
Ta_2O_5	2.5
Nb_2O_5	2.68
V_2O_5	3.19
WoO_3	3.3
$Fe_3Cr_2O_4$spinel (on Fe-9Cr alloy)	2.1
$FeCr_2O_4$ (on Fe-18Cr-8Ni)	2.1
Cr_2O_3 (on Fe-25Cr-20Ni)	2.1
Fe_3O_4 (on FeO)	1.2
Fe_2O_3(on Fe_3O_4)	1.02

Figure 21: Pilling-Bedworth ratio of several metals and their oxides [81]

There are a number of other factors that also affect the resistance provided by the film including; the level of film adherence, the thermal expansion coefficients for the 2 materials, and the mechanical properties of the oxide scale, meaning that the Piling Bedworth ratio is not the only consideration when determining the spallation risk of an alloy.

2.3.3 Oxide Growth in RR1000

Oxidation resistance can be increased in an alloy by the addition of elements that produce protective preferential oxide layers, such as chromium and aluminium that are used in a wide variety of alloys. For the nickel based superalloys, un-alloyed nickel will itself form a semi-protective nickel oxide scale when exposed to an oxidising gas; however, when alloyed, chromium oxide and aluminium oxide will commonly form preferentially to nickel oxide [7]. Different combinations of the oxidising elements will alter the oxide growth kinetics; however, generally they will result in a net reduction in the overall rate of oxide formation [45].

There has been some initial investigation into certain aspects of the oxidation of coarse and fine grain RR1000, primarily by Cruchley [45], [46], [49], [82], [83] and Foss [43], [84]. The research was focussed around the determination of the oxides present in the alloys and the way different elements affect the oxidation characteristics. Broadly speaking work has focussed on the coarse grain variants of the alloy with initial investigation undertaken into the oxidation characteristics of the fine grain variant such as; oxygen diffusivity determinations and some basic characterisation of the oxidation damage under thermal exposure and thermo-mechanical (compressive and tensile loads) conducted in a high partial pressure oxygen environment. Utilising a high partial pressure of oxygen will mean a great deal of results can be produced quickly; however, it will be less representative of the operating condition of the alloy in service.

Figure 22 is a diagram by Foss [84] based on his initial research into coarse grain RR1000 showing the features expected when inspecting oxidised RR1000.

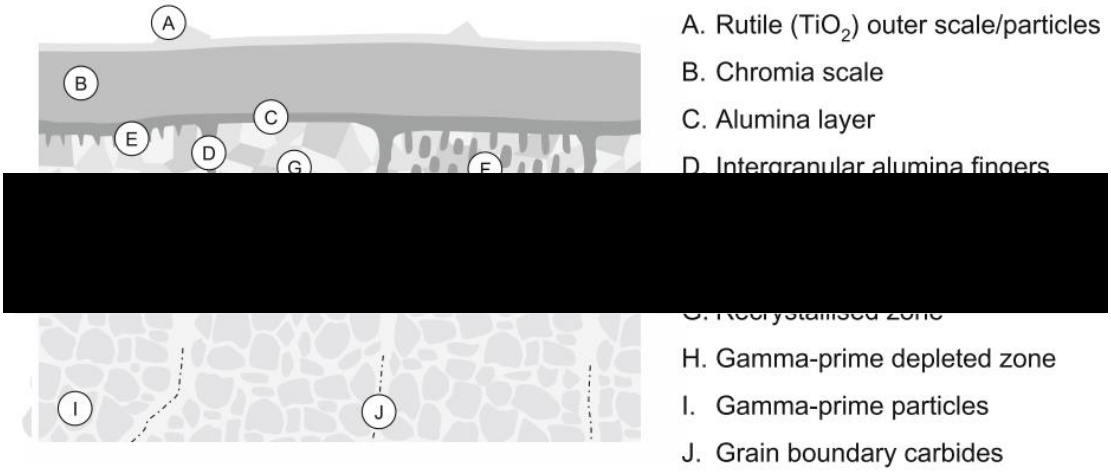

Figure 22: Representation of a micrograph showing predicted oxidation morphology [84]

It is possible that not all the characteristics shown would be present for all oxidised samples; however, most would be expected [84].

It is important to have an understanding of the various oxides that will form within RR1000; the protective oxides, the damaging oxides and those that have no apparent effect.

2.3.3.1 The Protective Oxides

Chromium and aluminium are used in many alloys for their ability to protect from extensive oxidation. The choice of these elements is based on the slow rate, at which their oxides form, and their chemical stability, which are significantly more favourable than iron, nickel and cobalt; their oxides will form preferentially to other alloying elements if kinetically possible. Silicon has also found some use and is widely available; however, due to the toughness and weldability reductions that come with the addition of useful volumes of silicon, it is often avoided.

The chromium oxide forms as a continuous scale layer on the surface of the alloy and provides a barrier, greatly reducing the rate of oxygen diffusion into the substrate, [45]. The scale has a very good adherence to the alloy and will likely stay attached to the alloy throughout thermal expansion and contraction. It is formed from the diffusion of chromium from $M_{23}C_6$ grain boundary carbides [85], [86], which will result in the deepest oxidation related damage that can be observed in RR1000, grain boundary carbide depletion. The depletion will lead to a reduction in the creep strength of the material [86] and can act as preferential crack initiation sites. An EDS map of a chromium oxide layer formed in coarse grain RR1000 variant can be in seen Figure 23.

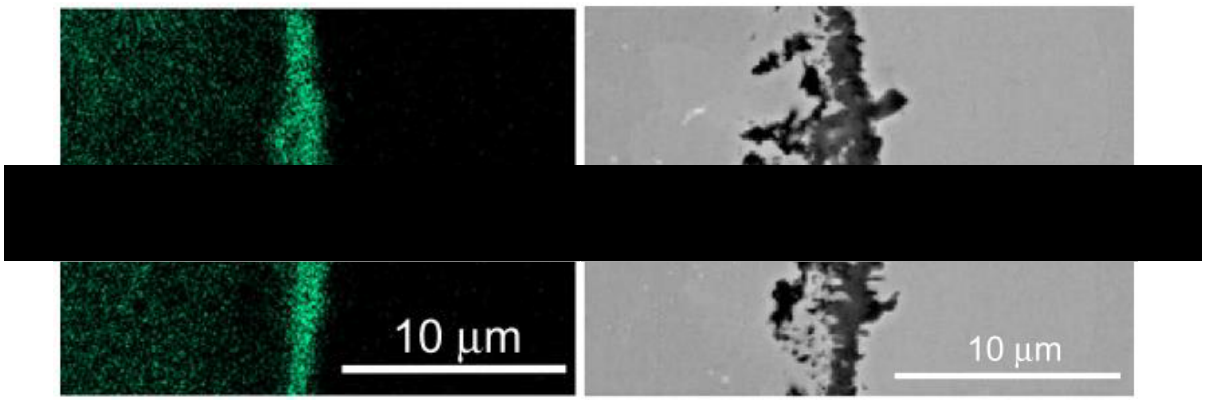

Figure 23: (left) EDS of the chromium oxide scale (right) corresponding micrograph [45]

Under conditions when an alloy element is selectively oxidised, but cannot reach the surface rapidly enough to form the scale, it will form an internal oxide. Internal

oxidation may occur as a result of the depletion of the primary oxidising element, or if multiple oxidation reactions take place simultaneously [87], as is the case with RR1000. A great deal of research has been conducted to determine the method of the internal oxidation reaction mechanism [88]–[90].

The aluminium oxide can form as a continuous layer with intergranular fingers or as intragranular islands [49], [82], [91], [92]. Aluminium oxide is the most protective and stable of the commonly utilised oxidation protection elements [93]. Aluminium oxide has favourable characteristics in preventing further oxidation as it forms a strong coherence to the substrate and reduces oxygen diffusion further into the substrate. The formation of aluminium oxide will lead to a 'γ' depleted zone' [45], [49], [82], [86], which will result in un-restricted grain growth, reduce the creep resistance of the material near the surface and reduced the hardness. Due to higher activation energy for diffusion of aluminium than chromium, aluminium oxide growth is more dependent on the presence of impurities than chromium oxide, meaning there is a greater amount of variation in the extent of formation of the aluminium oxides in operation [93]. An EDS map of the aluminium oxide layer and fingers formed in coarse grain RR1000 is pictured in Figure 24. The area of lower aluminium concentration below the aluminium fingers is indicative of the γ' depletion.

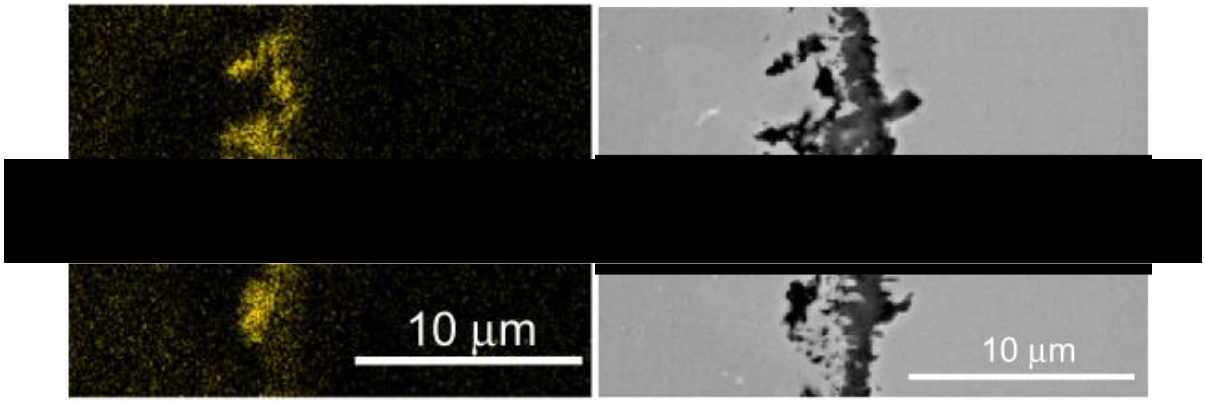

Figure 24: (left) EDS of the aluminium oxide (right) corresponding micrograph [45]

2.3.3.2 Other Oxides

Many of the other oxides that form in nickel based superalloys have a less favourable effect on the oxidation resistance of the material. Their inclusion in the alloys is based on other specific functions, and they cannot therefore be avoided. It is important to consider these oxides and determine if they influence the mechanical properties.

A great deal of research has been performed into the effect of titanium on oxidation [94]–[96]; titanium oxide particles form throughout the chromium oxide scale [45]. When titanium oxide forms it results in an increase in the level of oxidation, unlike aluminium oxide and chromium oxide which will reduce the rate of oxidation [13]. This is because the titanium oxide is brittle and is likely to break away exposing the substrate alloy to further oxidation. The titanium oxide forms inclusions within the protective chromium oxide layer that have been found to increase the chromium oxide layer thickness and chromium ion diffusion compared to alloys that contain no titanium [45], [91]. This will result in a comparative reduction of strength of the alloy, as the original alloy is damaged to a greater depth, and may lead to an increase in failure due to surface effects. Similar to the formation of the aluminium oxide, the titanium oxide formation will result in a gamma prime depleted zone [45], [49], [82], [86]. An EDS map of the titanium oxide doping formed in and above the chromium oxide scale in coarse grain RR1000 can be seen in Figure 25. Similar to the EDS map of aluminium, the area of lower concentration of titanium is an indication of the γ' depletion depth.

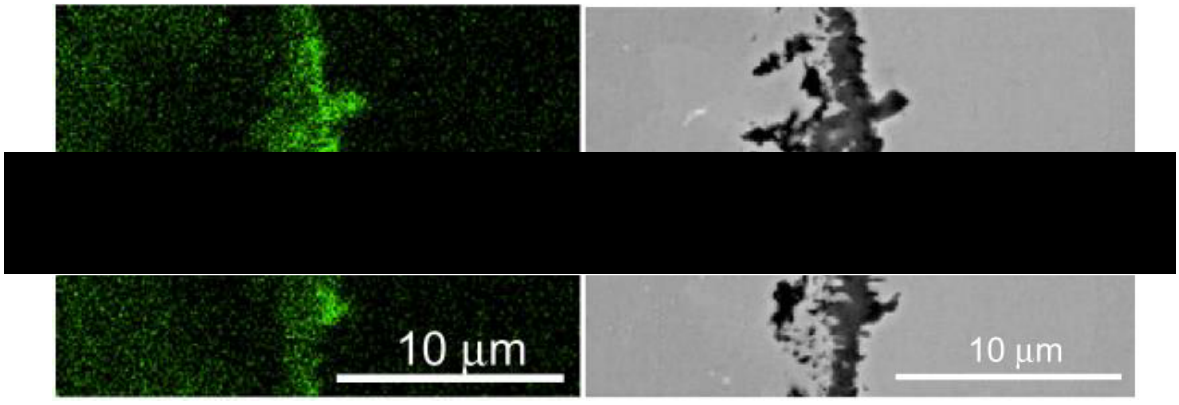

Figure 25: (left) EDS of the titanium oxide (right) corresponding micrograph [45]

Hafnium Oxide can be extremely detrimental to the life of a component as the phase that forms can be very brittle, but will most likely form inclusion clusters that will act as crack initiation sites due to decohesion with the matrix; therefore, minimising this possibility of their formation is greatly advantageous [97].

Refractory metals, such as molybdenum, niobium and tantalum are believed to impart a favourable effect on oxide rates due to their affinity for oxygen. The positive influence is however rendered less effective as the oxides formed result in a reduction in the diffusion rates of the protective chromium and aluminium atoms, leading to thinner, less protective scales and they also have low melting points [78], [94], [98], [99]. Their disadvantages are generally seen to be outweighed by their advantages, as they are extremely effective at forming γ' and carbide and boride precipitates, meaning their deleterious effects are largely ignored [100].

There are limited sources on the effect of cobalt oxide in nickel superalloys, other than research presented by Smialek and Meier (1987) [98], suggesting that at weight percentages lower than 5%, cobalt produces favourable cyclic oxidation resistance.

Boron and Carbon additions have been found to have a negative effect on the oxidation rates at high volume percentages. The borides that form at grain boundaries are found to be preferentially oxidised via diffusion along the grain boundaries leading to increased damage of the protective chromium oxide scale [78], [94]. The presence of high levels of carbon have also been found to increase the rates of cavitation and embrittlement in the superalloys [101], [102]. Due to the efficacy of grain boundary carbides and borides at slowing fatigue crack growth, these are still included in a range of superalloys, just in small weight percentages.

2.3.4 Oxide Measurement

There are two primary methods of analysing the extent of oxidation damage within a material; thermogravimetric analysis (TGA) measuring oxygen uptake and micrographic analyses to image the oxidation effects. TGA is the most common form of oxidation analysis [103]–[111] and there are two forms; interrupted thermal exposures with weighing of specimen before and after exposure, and the more accurate method using a specialised TGA system, with constant mass measurements taken throughout the exposure. Interrupted exposures are advantageous as they provide a specimen on which post analysis can be completed at each interrupted stage, and TGA systems are convenient, as a test provides a great deal of data from a small quantity of material. An example of a TGA setup can be seen in Figure 26.

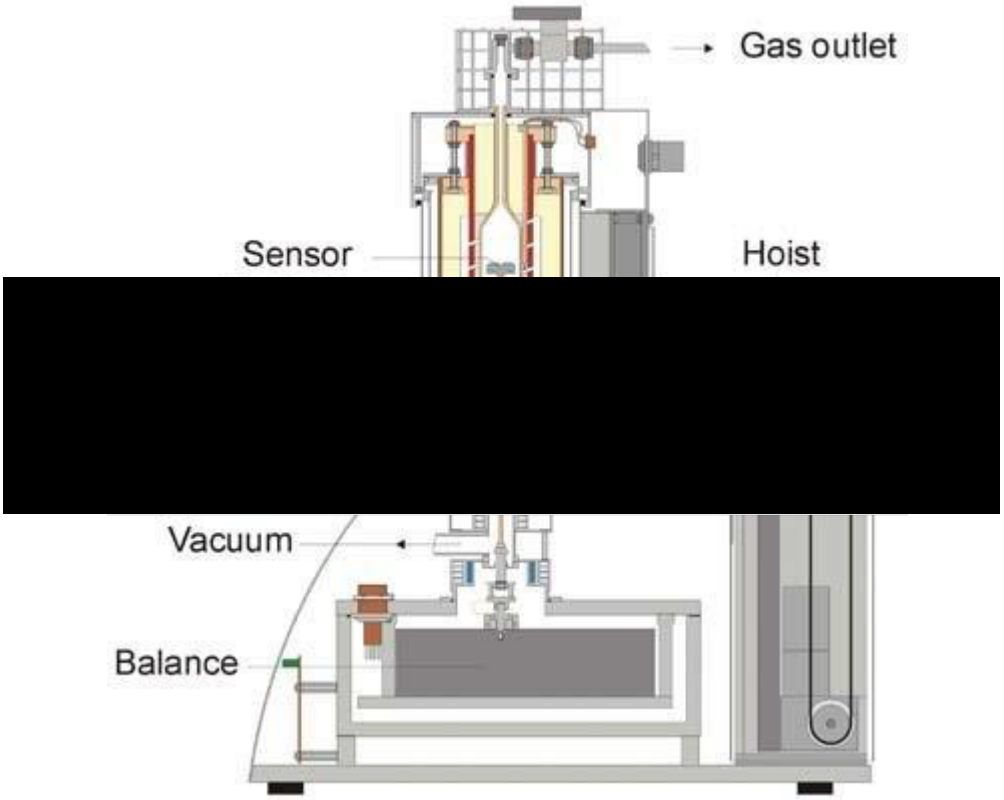

Figure 26: Schematic of a TGA system [112]

There are a couple of issues with TGA systems; they are complicated, expensive systems that are very sensitive so need to be highly isolated. It is not possible to

determine the rate and stage at which different oxides form, or monitor for the onset of any oxidation associated damage mechanisms e.g. phase changes or gamma prime depletion. This is where micrographic analysis is more useful. Recent attempts have been made to measure the oxides in a range of nickel based superalloys, primarily based around the method of focussed ion beam (FIB) milling [66], [84], [113]. An image of a FIBed surface of RR1000 used for oxidation analyses can be seen in Figure 27.

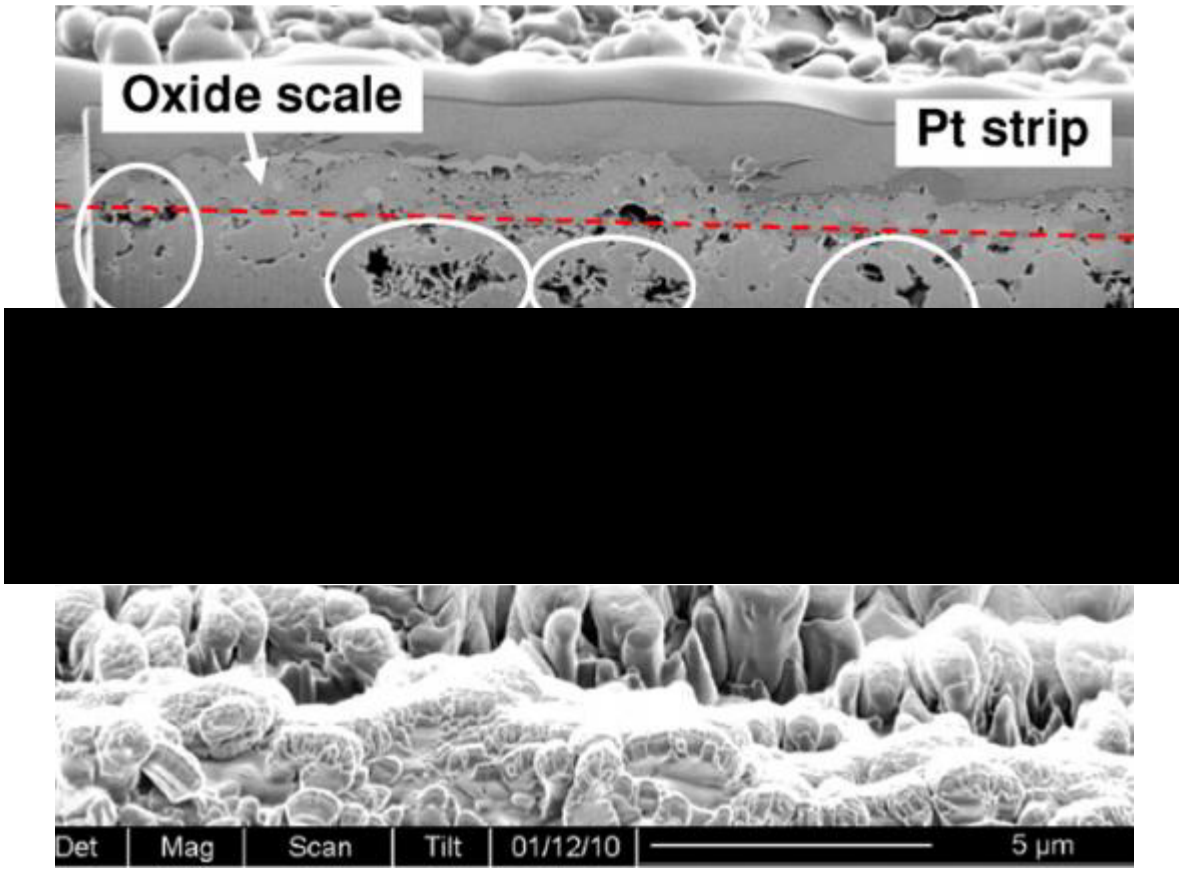

Figure 27: Focussed ion beam milled CG RR1000 for oxide analyses [114]

This method is very time intensive and requires a great deal of expensive equipment. Also, as the area of analysis following FIBing is so location dependant there is a good chance a feature of note may be missed.

Cross sectional analysis similar to that performed by Cao [115] and Cruchley [46] is seen as a more thorough way of analysing the oxides. By imaging the cross section of

a heat treated specimen it is possible to investigate the entire length or width for anomalies, and take measurements accordingly. This will still not be fool proof as a method of highlighting unusual features in the oxidised surface, it will however, reduce the risk of missing something compared to FIB analyses.

As can be seen in Figure 28, when compared to the oxidation measurements available from Figure 27, it is possible to localise the micrographic imaging more directly on the area of interest, therefore increasing the accuracy of oxide measurements.

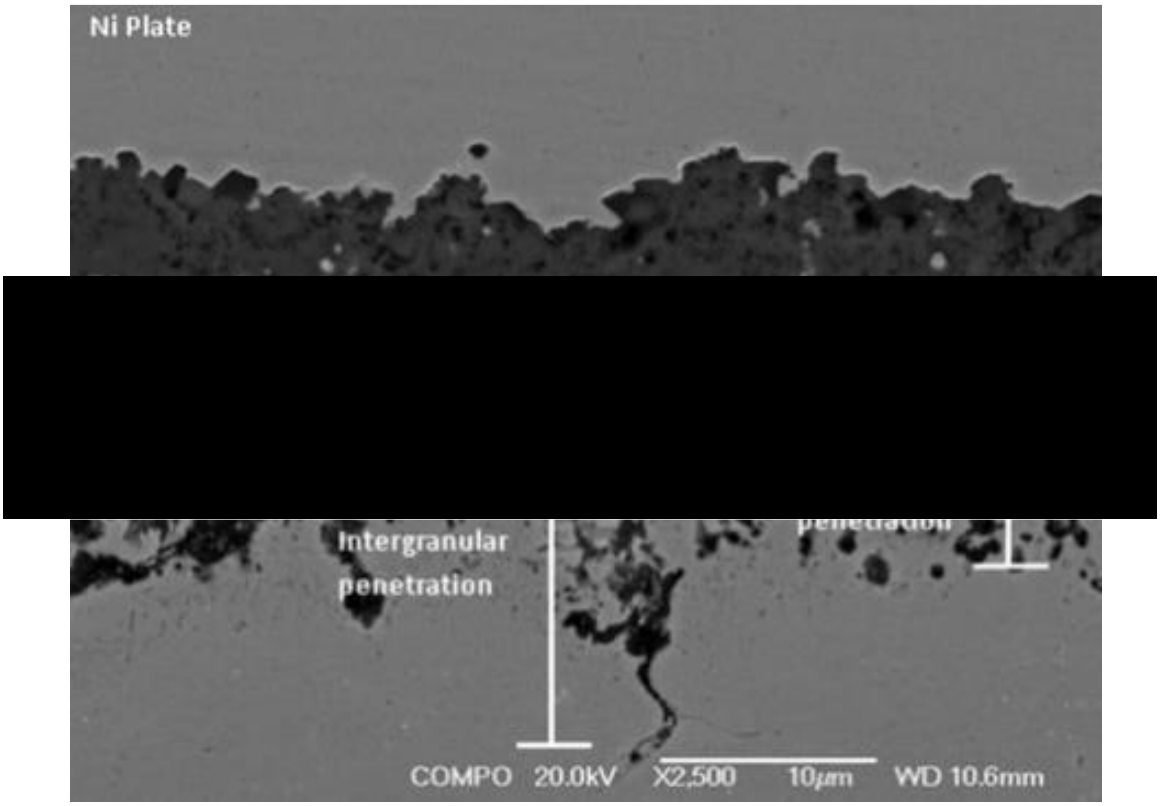

Figure 28: Cross sectional analysis of RR1000 [46]

2.3.5 Effect of Surface Condition on Oxidation

Surface condition and the associated sub-surface residual stress are important factors in the consideration of oxidation due to the fact that service components undergo a peening process. Studies have been conducted across a number of materials to determine the effect of shot peening and machining on the growth of oxides compared to polished conditions [116]–[124], and it has been found that the more damaged conditions lead to a faster oxide growth rate but no noticeable change on the morphology of the oxides. This is at least in part due to the increase in nucleation sites created by the peening process [111], [116], [125]. Another factor is the increased presence of dislocations imparted on the material by the peening process leading to an increase in the rate of the 'short circuit' diffusion mechanism of pipe diffusion as discussed in Section 2.3.1. Interestingly, whilst conducting investigations it was also found that materials that have some residual stress in the surface, when oxidised led to a small recrystallized layer forming below the surface oxides, and as such will have altered mechanical properties [91], [106], [117], [126]; this was found to be more prevalent in coarse grain materials. It can be seen from the literature that even though it is a widely investigated area, there is little research into the effects of peening on oxide growth for the nickel based superalloys.

As part of a study conducted by Li et al. 2008 [127], on high purity nickel, it was found that oxidation of damaged surfaces acted to lower the roughness of the surface, whereas oxidation for polished surfaces usually acts to induce damage. This is shown in Figure 29, in which S is a polished surface, R1 is a lightly damaged surface and R2 is a highly damaged surface.

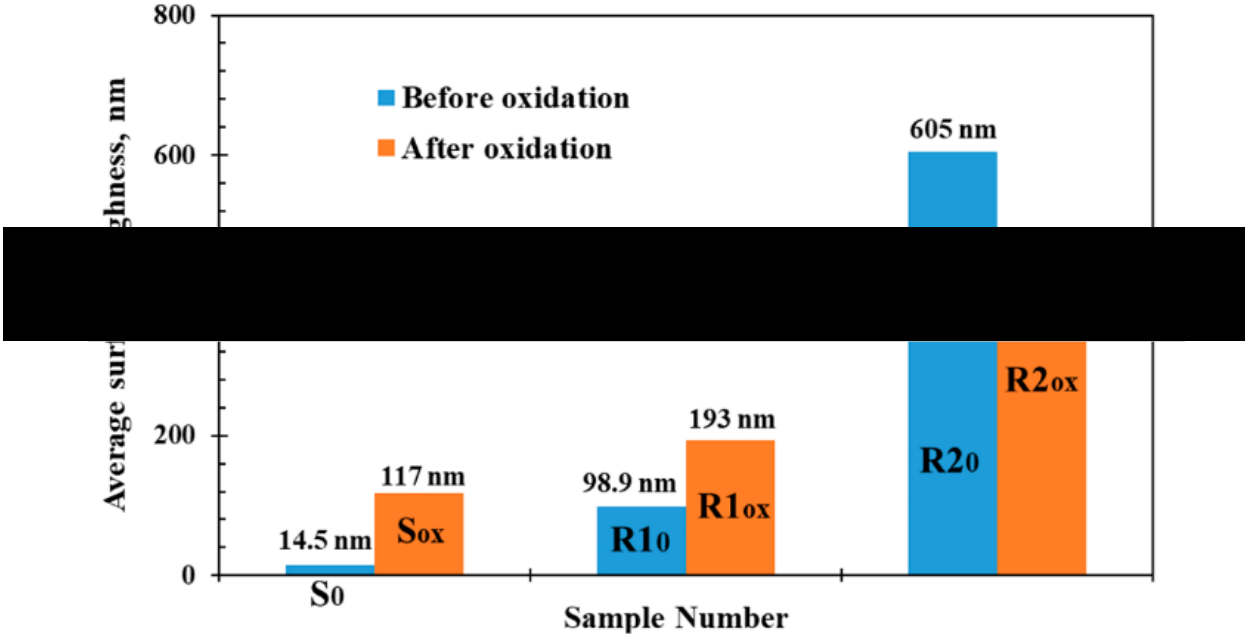

Figure 29: Average surface roughness values of the nickel samples before and after oxidation for 60 min [127]

2.3.6 Effect of Temperature on Oxidation of RR1000

A great deal of work has been conducted to determine the effect of temperature on the rate of oxide growth in RR1000. A larger focus of the work has been based around the coarse grain variant of the alloy [45], [47], [83] or has focussed on TGA [45], [47], [103] rather than oxide depth measurements. Where measurements have been taken only the chromium oxide layer has been measured [45], or measurements were taken after Focussed Ion Beam (FIB) milling into the surface of the specimen [49], [83], [84], [103], [114], and there are not enough measurements taken to be statistically comprehensive. It can be understood from these examples however, that there is a pattern of dramatically increased oxidation damage accumulation rates at temperatures exceeding 700°C, and that the growth is seen to be self-mediating to some extent, leading to a reduction in growth rate over time; parabolic rates are often mentioned [13].

2.3.7 Grain Size and Oxidation

It would seem logical, given the mechanics of short-circuit diffusion, that fine grained variants of alloys would have an increase in oxidation damage compared to their coarser grained counterparts, due to the net reduction in activation energy of diffusion for fine grain alloys. The question of the effect of grain size on oxidation damage accumulation is however far more complicated. The formation of the all-important protective oxide scale varies significantly as a result of the combination of microstructure and composition [128].

Many studies have been conducted into the sensitivity of oxidation to grain size across a range of alloys [75], [104], [108], [109], [129]–[133]. As an example of the complexity of the problem, the work by Trindade et al. [105] shows that for chromium containing iron alloys, as concentration of chromium increased, oxidation resistance decreased with increasing grain size, whereas lower concentrations of chromium exhibited the inverse relationship. The graphic modified from the work presented by Trindade et al. demonstrates this very concisely in Figure 30.

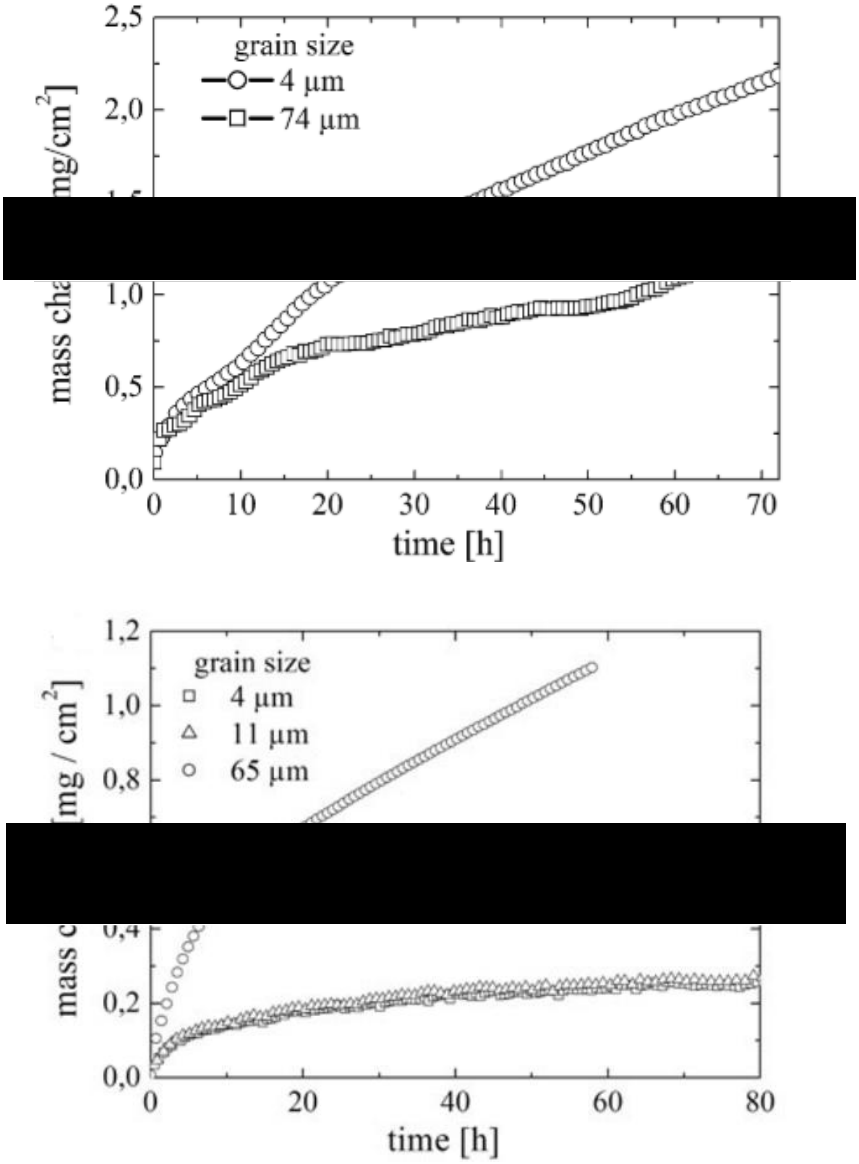

Figure 30: TGA measurement of (top) Cr-2.25 at 550°C (bottom) CrNi-18-8 exposed at 750°C [105]

This work is supported by Chevalier [134] who found there is a critical amount of chromium required in an alloy to form a protective chromium oxide scale. Studies of alloys with sufficiently high chromium content to form protective oxides generally found that coarse grained variants of alloys resulted in increased oxidation [75], [135] due to the increased diffusion rates of the chromium and aluminium [109]. In general it was found that fine grained alloys had greater resistance to spallation which resulted in improved oxidation resistance, however, the opposite has also been established by Strauss et al. (1998) [136].

There is currently very little work dedicated to the effect of grain size on oxidation of the nickel based superalloys, apart from that which has been performed by Wang and Szpunar in 2018 [104] which found that, similar to other alloy systems, it is very material dependant.

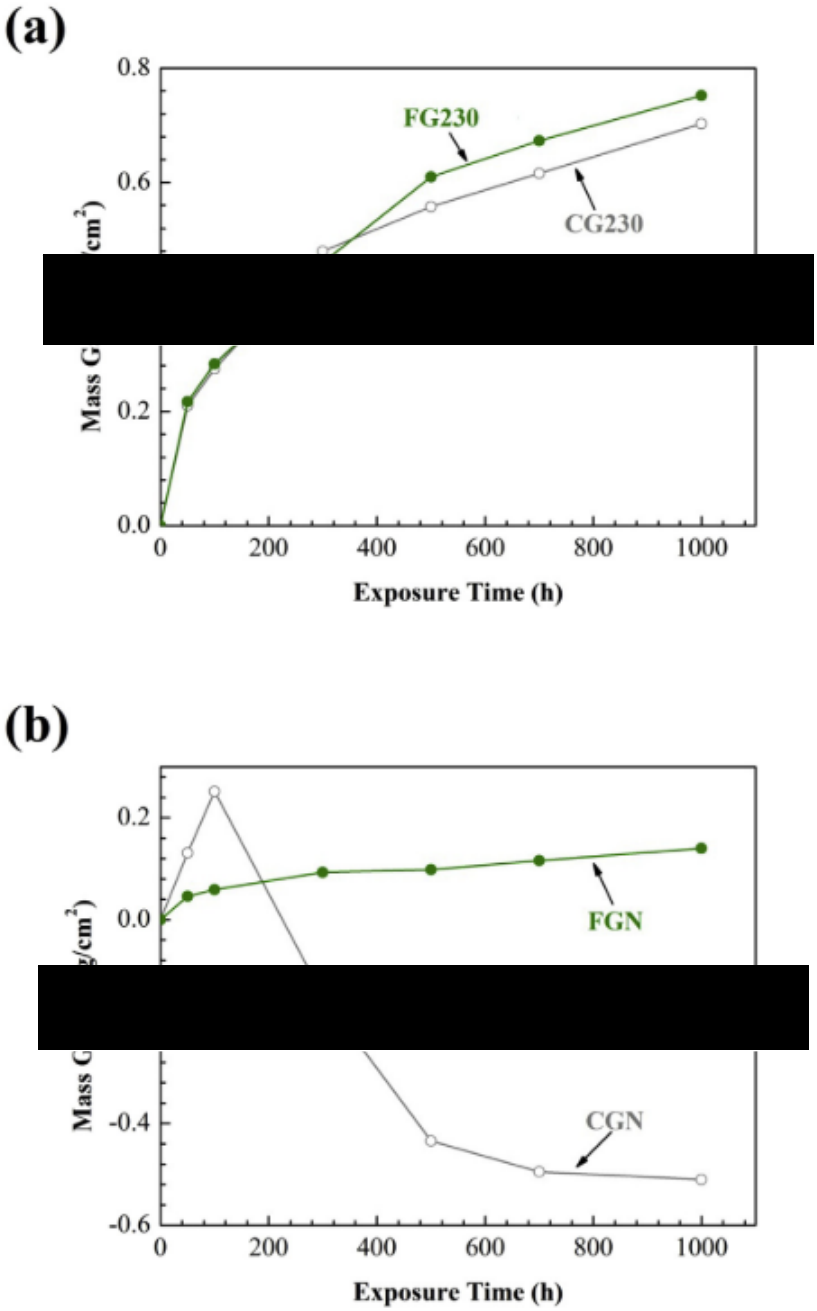

Figure 31: Mass gain after oxidation of fine and coarse grain variants of (a) alloy 230 (b) alloy N [104]

Figure 31 shows the very different oxidation characteristics of two superalloys, with alloy 230 showing similar oxidation rates in both grain size variants with coarse grain performing slightly better, and alloy N which shows rapid oxidation in the coarse grain variant compared to the fine grain, quickly leading to a mass loss due to spallation.

The conclusion to be drawn from the study of grain size is that it is very complicated and alloy dependent. It would therefore be important for any oxidising alloys to have oxidation analyses performed for all variants rather than making assumptions based on data from an analysis of only one grain size.

2.3.8 Oxidation Modelling

In order to quantify the oxidation reaction across a range of materials and alloys, activation energy has been utilised, similar to the method employed by Kofstad [137]. Activation energy is the amount of energy that is required to initiate a reaction or in other words, it is the amount of energy available in a system for a reaction to occur. The theory of activation energy was first presented by Savante Arrhenius, in which he defined the Arrhenius equation shown in Equation 2.

$$k = Ae^{-\frac{E_A}{RT}} \qquad 2$$

Where:
k = rate constant
A = frequency factor
E_A = activation energy
R = gas constant
T = temperature

The Arrhenius relationship will be well known to materials scientists as it is commonly used in the modelling of the creep behaviour of materials, to determine the amount of energy to initiate creep, and is calculated using the steady state creep rate [11], [138]–[140]

The Arrhenius relationship has found good standing in the area of oxidation analysis and has been conducted as part of a large number of studies investigating thermal oxidation growth [86], [103], [141], [142]. There has been little work performed however into the application of activation energy for thermo-mechanical oxidation.

2.3.9 Thermo-Mechanical Oxidation

Studies of high temperature oxidation have primarily been focussed on the growth of oxides in the absence of an externally applied load. The omission of load from the majority of oxide analyses is not an insignificant one, as most engineering materials will often experience significant mechanical stresses during operating. This is especially true of the nickel based superalloys that are designed to operate as loaded components in the hottest parts of the aero engine. A mechanical stress effecting the nature of a chemical reaction is investigated in the discipline of mechano-chemistry [143]. The phenomenon of mechano-chemistry is not well understood but its effects are abundant throughout engineering.

A specific, widely researched form of thermo-mechanical oxidation interactions is that of stress or strain assisted grain boundary oxidation (SAGBO) also referred to as deformation-assisted oxygen diffusion. It is the process by which oxygen diffusion rates into a material are increased along a grain boundary due to the presence of mechanical loading. The reason SAGBO has been investigated to a greater extent than other thermo-mechanical oxidation mechanisms is because it links heavily to high temperature crack growth [144]–[153].

In more recent years research has increased in an effort to understand SAGBO and the overall thermo-mechanical oxidation mechanisms. Initial studies have aimed to quantify the oxidation kinetics and damage levels for a range of alloy systems. Initially a great deal of research was conducted in tensile loading regimes [154]–[160], and other research into what is occurring under compressive loading [161]–[165] with the majority of the work being completed by the same people. A smaller number of studies have looked at back to back tensile and compressive stress effects on oxidation [84], [107], [166], [167]. It was also found that there is an apparent critical stress that must be applied in order for a thermo-mechanical oxidation reaction to take place [107], [167].

Collectively the research has found that loading has a deleterious effect on the oxidation resistance of high temperature materials by increasing the rate of the oxidation reactions. There is however no consensus as to what the mechanism is that causes this apparent increase. Some studies found that on a microscopic level there were changes in the morphology of the oxides from scale thickness to increased depth

of precipitate depletion, but other studies found little to no difference between thermal and thermo-mechanical oxidation. Even for studies conducted for RR1000 there are contradictory results; O'Hanlon et al. [168] found that oxidation under fatigue loading led to cracking of the protective scale, dramatically increasing the oxidation damage depth at temperatures from 650°C; the scale cracking is supported by work conducted by Berger et al. [169]. Karabela et al. [114] however found that there was little to no effect of fatigue loading on the surface oxide depth compared to the unloaded tests until the test temperature reached 800°C.

Accompanying the formation of the oxide layer, creep deformation will occur during the low stress thermo-mechanical oxidation. Creep is the time dependent mechanism of deformation that occurs in materials under a constant load at elevated temperatures (commonly >50% melting point), which will usually occur at a very slow rate when compared to other damage mechanisms [252]. Creep causes the permanent plastic deformation and eventual creep rupture (failure due to creep) of a material at stresses lower that the yield stress. Creep can often be the main cause of failure within a system such as an industrial power plant, or it can contribute to another mechanism to cause failure e.g. aero engines (where fatigue failure is dominant).

Figure 32 shows a generic creep strain curve (strain against time at constant stress and constant temperature).

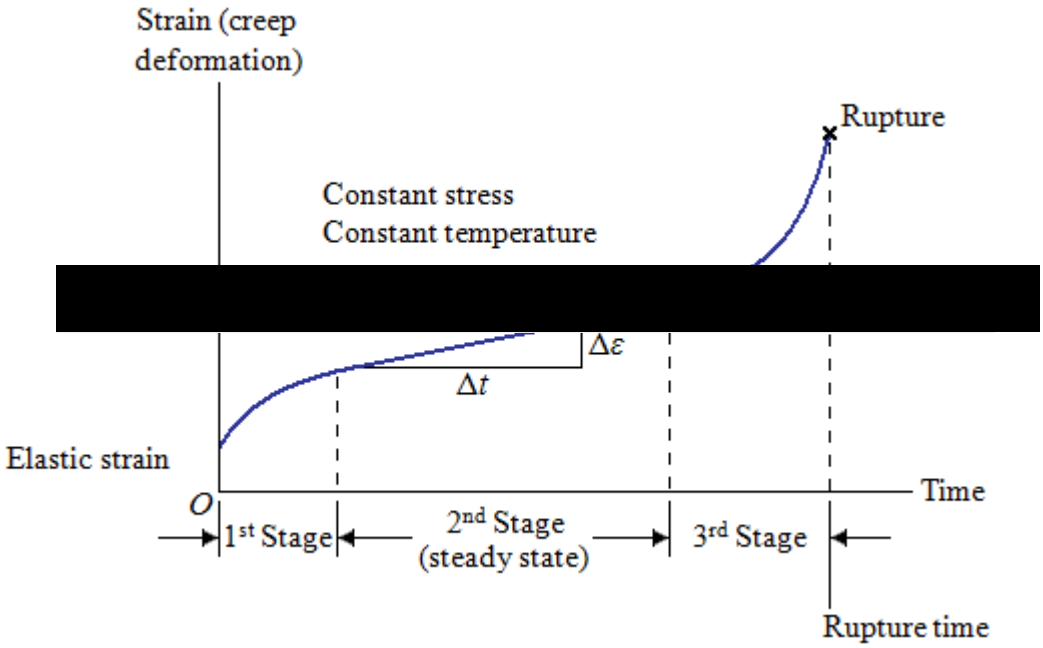

Figure 32: Strain against time curve showing the different stages of creep [170]

Proponents of the power-law theories believe the creep curve can be separated into the sections; primary/transient, secondary/ steady state and tertiary stages. Primary or transient creep sees an initial high creep rate which then decreases; this stage is usually quite short. Secondary or steady state creep displays an almost constant rate of creep; as such, this is the area of most engineering interest, as it is the easiest to predict. The final creep stage is tertiary creep; this stage shows an increase in creep rate until finally rupture occurs. The length of the tertiary creep stage can vary greatly.

Power-law creep theories work on the principal that the process of creep can occur through two main mechanisms, diffusion and dislocation; diffusional creep processes are considered to be the dominant mechanism at low stresses, and the dislocation creep becomes dominant at higher stresses. As previously discussed, diffusion is the process by which the elements involved in the oxidation process move through a material.

2.4 Fatigue

The term fatigue refers to the changes in properties which can occur in materials due to the repeated application of stresses or strains [171]. Although this definition has evolved since its inception in 1964, it is still broadly appropriate. Fatigue failures can result from fluctuating stresses or strains that are significantly smaller than the safe working values determined from a simple tensile test; the initial lack of understanding of this process led to the catastrophic failure of the Comet aircraft in 1953. The term fatigue failure can apply to many forms of failure, and has been split into a number of subgroups; mechanical fatigue, creep-fatigue, thermomechanical fatigue (TMF), corrosion fatigue etc. Fatigue is a significant problem in materials engineering and work to develop the understanding of its effects is very important; "it is often stated that fatigue accounts for at least 90 percent of all service failures" [172]. Fatigue failures occur with no visual changes to the material, which makes it very difficult to monitor, and fracture can occur suddenly, without warning. Fractures are often brittle in appearance, even in usually ductile materials [79].

There are four consecutive and partly overlapping stages to be considered when analysing fatigue failure.

1. Cyclic hardening and / or softening
2. Crack nucleation/ initiation
3. Crack growth
4. Failure/ rupture

The relative effects of the stages of fatigue compared to the overall fatigue life is illustrated by Figure 33.

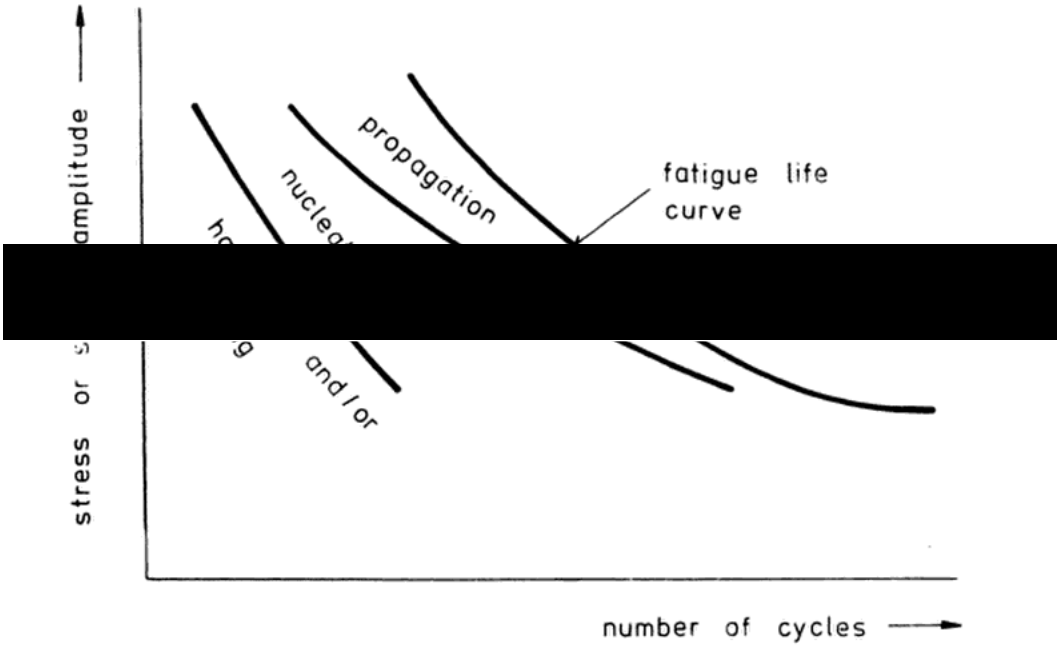

Figure 33: Stress amplitude against number of cycles for the nucleation and propagation stages of fatigue compared to the overall fatigue life [173]

2.4.1 Cyclic hardening and softening

Materials subjected to cyclic loading will exhibit different characteristics based on their initial conditions. It is common for initially very ductile materials, such as those that are in an annealed condition, to cyclically harden before reaching saturation. Counter to this, work hardened or precipitation hardened materials will be more likely to cyclically soften before saturation. For other materials it is more complex, in which some initial hardening may occur followed by a long stretch of cyclic softening, such as nickel chromium martensitic steels [174]. This stage is essentially a deformation process that involves a change in the bulk of the material resulting in strain localisation [175]. Microscopically, this is due to the movement of dislocations within the material; and the formation of more dislocations in initially soft material and the break-up of dislocation barriers and tangles within initially hardened materials [176].

Similar to the nickel chrome martensitic steel mentioned, it is common for the precipitate hardened nickel based superalloys to undergo an initial hardening, followed by a slow cyclic softening stage [177].

2.4.2 Crack Initiation

Crack initiation will often account for as little as 10% [176] but may be as much as 90% [178] of the overall fatigue life so it is vital to understand the mechanism in order to accurately model and understand the fatigue lives of materials. Crack initiation can be considered as occurring in three stages [179], [180]:

1. Crack nucleation
2. Microscopically small crack growth
3. Physically small crack growth

Studies have found that the crack initiation stage is strongly affected by microstructural variability and component geometries for experiments performed under the same conditions [181]. It can therefore be stated that crack initiation will account largely for the substantial scatter that is apparent in the fatigue testing of metallic systems, rather than during the crack propagation stage (large crack growth stage).

Fatigue cracks will nucleate at a point of concentration of plastic strain [176] such as component surfaces and grain boundaries [174], [176], [177], [182].

Figure 34 shows the full range of crack initiation site in polycrystalline materials according to Ellyin:

(i) Transgranular crack
(ii) Intergranular crack
(iii) Surface inclusion/ pore
(iv) Inclusion in the matrix
(v) Grain boundary voids
(vi) Triple point grain boundary intersections

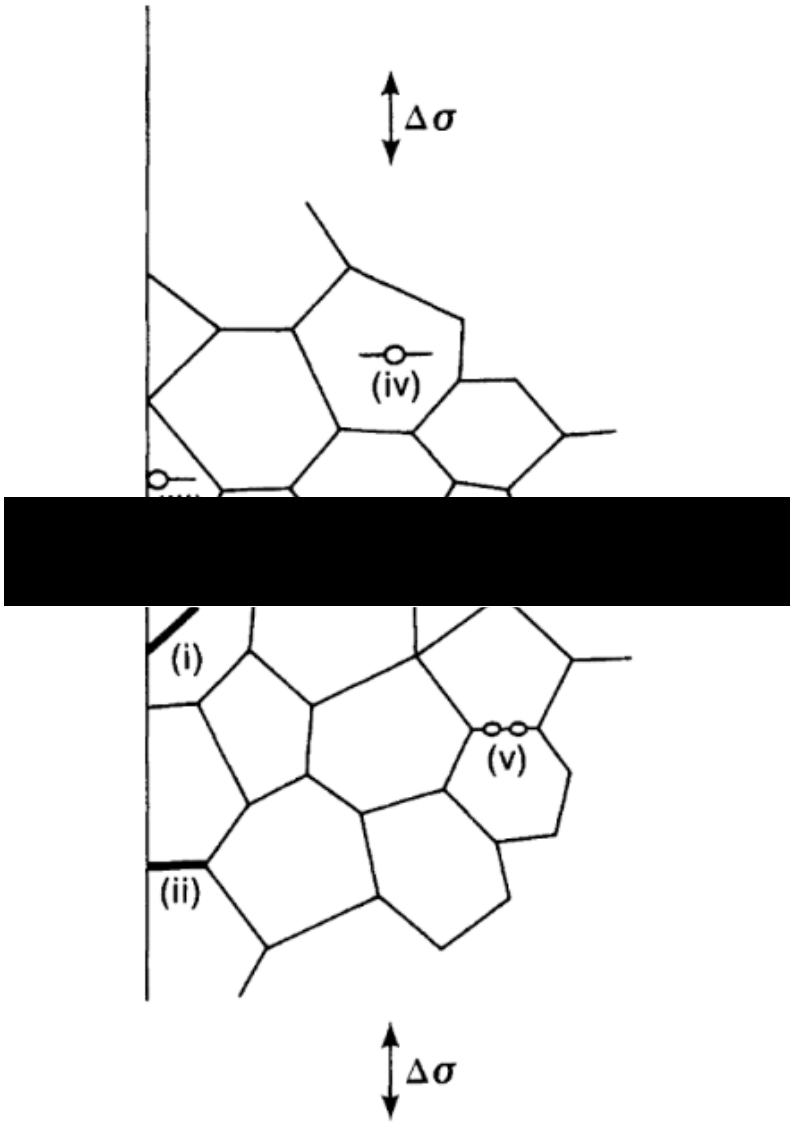

Figure 34: Potential sites for crack initiation in polycrystalline materials [175]

The effect of grain boundary voids and triple points will be more prominent at high temperatures, when creep will become a consideration.

Crack nucleation will occur due to the multiplication and accumulation of dislocations around these features, resulting in a localised increase in dislocation density [183]–[185]. Research first conducted by Ewing [186] discovered the presence of fine, sharp slip bands in favourably oriented crystals of polycrystalline Swedish iron. It was found that as cycle number increased, more specimens presented slip bands and existing bands widened and ultimately developed into small cracks. Investigation into the movement of dislocations was later conducted by Seeger [187] and Friedel [188] in

terms of work hardening of FCC crystals, supporting the theory of slip band formation at the surfaces of components undergoing fatigue loading. The dislocation movement mechanics are highly dependent on a number of factors: temperature, strain amplitude, slip character and stacking fault energy [189]–[191]. The mechanism by which a slip band can initiate damage in the surface of a component can be seen clearly in Figure 35.

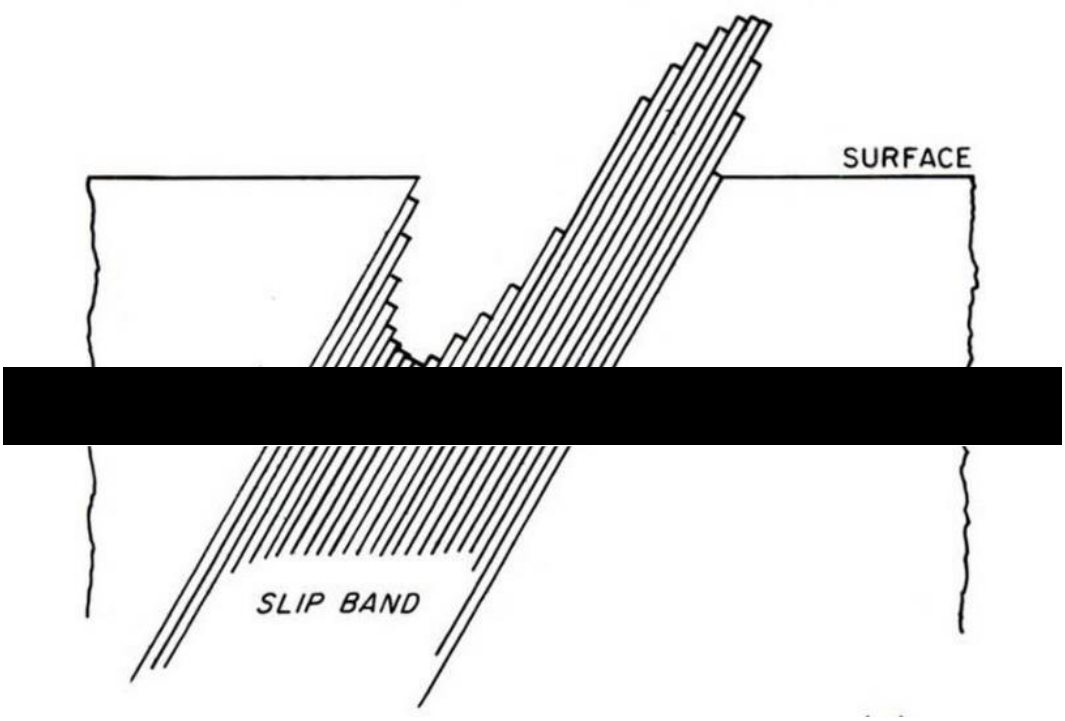

Figure 35: Schematic representation of surface damage caused by slip band [176]

Figure 36 shows a micrograph of the corner of a copper specimen that has undergone a number of fatigue cycles and clearly shows the presence of the slip bands, the scale of which is magnified due to the presence of the acute angle of the specimen.

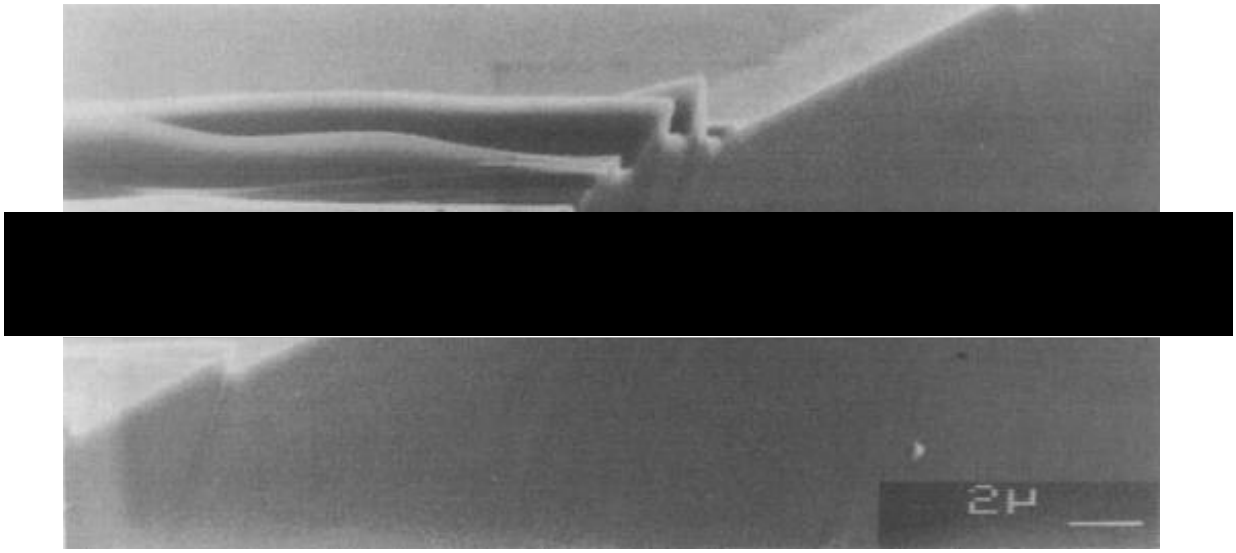

Figure 36: Micrograph of a slip band at the corner of a copper fatigue specimen [192]

The presence of a nucleated fatigue crack is not straight forward to determine as different industries will have a different view of what size of crack represents the onset of fatigue cracking. This will most likely be linked to the resolution of the measurement technique used to determine the presence of a crack [176].

There are a number of factors that will affect how rapidly cracks will nucleate in a component. They are based around the principles that, (i) there is a feature of some sort at the surface or within the component, (ii) there is loss of grain boundary cohesive strength, and (iii) the ability to perform stable dislocation pileups. Furthermore unfavourable geometry and poor surface condition of a component will have the effect of promoting one or more of these mechanisms, as described in Figure 34.

Fatigue crack initiation studies in a range of nickel based superalloys have been performed in order to characterise the method of initiation and the microstructural changes that were presented as a result of the cracks forming. Studies found a range of mechanisms resulted in the initiation of cracks; the formation of slip bands [193], [194], inclusions [195], [196], grain boundaries [196] and facet formation in large grains in the presence of Σ3 grain boundaries [197], [198].

2.4.2.1 Stress Concentration

A large part of the reason why the presence of the slip bands leading to micro-cracking is of importance to fatigue is the fact that the micro-cracks will act as micro-notches, increasing the stress concentration at the notch, creating an inhomogeneous stress distribution throughout a component.

A stress concentration will be caused by a number of features:

- Poor surface condition
- Case hardened layer
- Inclusions/ pores
- Small cracks
- Notches
- Sharp edges
- Threads

The effect of these features is to change the force flux around them, leading to an increase in the density of force lines around the feature; an example of this for a notched specimen is shown in Figure 37.

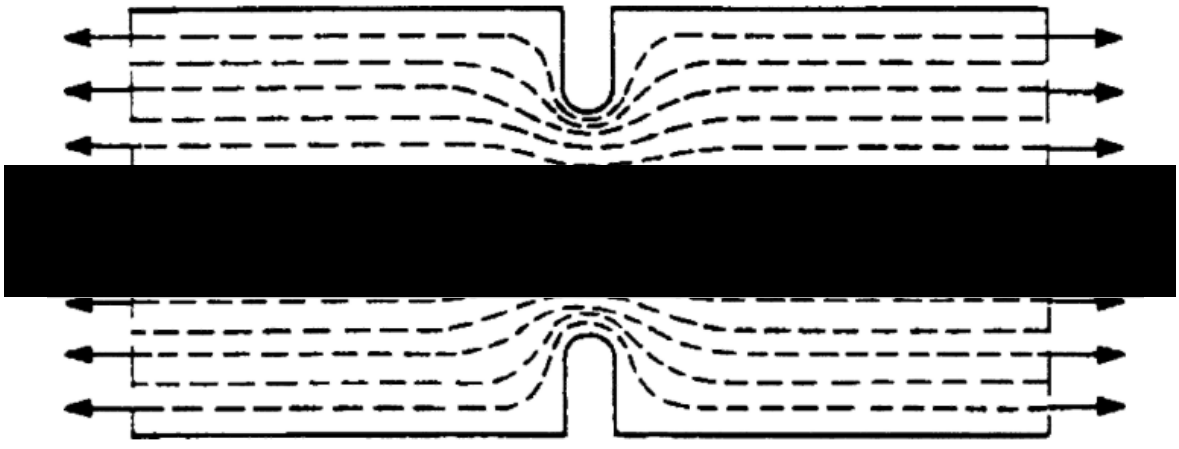

Figure 37: The effect of notches on the main principle stress trajectories [199]

This will lead to an increase in the dislocation density at these features, resulting in an amplified plastic response within the region. These features will also increase the formation of slip bands, which as previously explained will result in stress raisers acting as crack nucleation sites.

The level of elastic stress concentration caused by a certain feature is measured using the stress concentration factor, (k_t) the meaning of which is shown in Equation 3 [200]:

$$k_t = \frac{\sigma_{max}}{\sigma_0} \qquad 3$$

Where:

σ_{max} = peak stress at the root of the stress raising feature

σ_0 = nominal stress that would be present if a stress concentration did not occur

The severity of the stress concentration is dependent upon the geometry of the notch. The higher the k_t the sharper the notch and the more effect it would be expected to have on the resulting fatigue life.

The effect of stress raising features has been widely researched for a range of materials as it is such an important factor in understanding the fatigue resistance of components in service. In mechanical testing it is common to use specialised notch fatigue specimens of known stress concentration factors to determine the notch sensitivity of a material. Current notch fatigue testing is performed to satisfy three questions currently being asked; understanding notch sensitivity, especially under multiaxial loading conditions, the response of notches to temperature and environment, and finally fatigue initiation modelling.

Notch sensitivity analyses are performed for a wide range of materials in order to better understand the crack initiation behaviour [201]–[205]. This is of particular importance for engineering components where it is not possible to avoid stress raising features such as those at the fir tree root of turbine components. An effort has also been made to understand the difference between the fatigue initiation response of notched and un-

notched specimens [206], [207]. Research is also being undertaken into more complex multiaxial loading regimes [208], [209]. The majority of research has been conducted into polycrystalline materials however, research has also been conducted into single crystal components [210]

Through the use of dwell testing and differing test environments an effort has been made to understand the influence of damage mechanisms other than that of fatigue on the crack initiation characteristics of varying materials. This is of particular importance to high temperature engineering components that will experience a wide range of damage mechanisms in operation, including; creep and attack from air, water, sulphurous etc. environments [71], [211]–[215].

A large amount of research has also been performed in more recent years based around efforts to produce models for the prediction of fatigue lives controlled by fatigue crack initiation [216]–[222]. As mentioned previously, there is a great deal of scatter in the fatigue crack initiation lives of components under similar conditions, therefore, modelling is a complex task. However, a promising approach is based around the theory of critical distance. This aims to more accurately model stress at notches during fatigue loading. The theory of critical distance is a complex principle and has found greater use since advancements in FEA software have made it easier to calculate.

Alongside the testing performed on notched fatigue specimens, research has been conducted to understand the effect of smaller, microstructural features on crack initiation in engineering materials. Grain size and texture have been found to have an influence on the initiation rates of nickel superalloys [223], [224]. Also of importance to precipitate hardened alloys such as nickel superalloys, research has been conducted into the effect and method of fatigue crack initiation from inclusions [180], [225]–[227].

2.4.2.2 Surface Effects

The special case of how the surface condition affects crack initiation is to be considered separately as there are many factors that need to be considered.

There are three factors linked to the surface condition that will affect fatigue characteristics [172]:

1. Surface roughness (can act as stress concentrations)
2. Changes in the surface residual stress levels
3. Effects of oxidation and corrosion

Surface roughness can be varied greatly depending on the type of machining operations employed e.g. grinding, milling and polishing [178]. The surface 'valleys' that are created during these operations will act as stress raisers. The friction incurred will also cause areas of heating at the surface of the component that will have an effect on the fatigue properties within a heat affected zone to some depth subsurface. The effects of these techniques can be reduced by simply reducing rate of material removal e.g. slower grinding/ milling velocities. The effect of surface roughness on fatigue life is shown in Figure 38. The component with a gentle grind applied has a markedly longer fatigue life at the same stress.

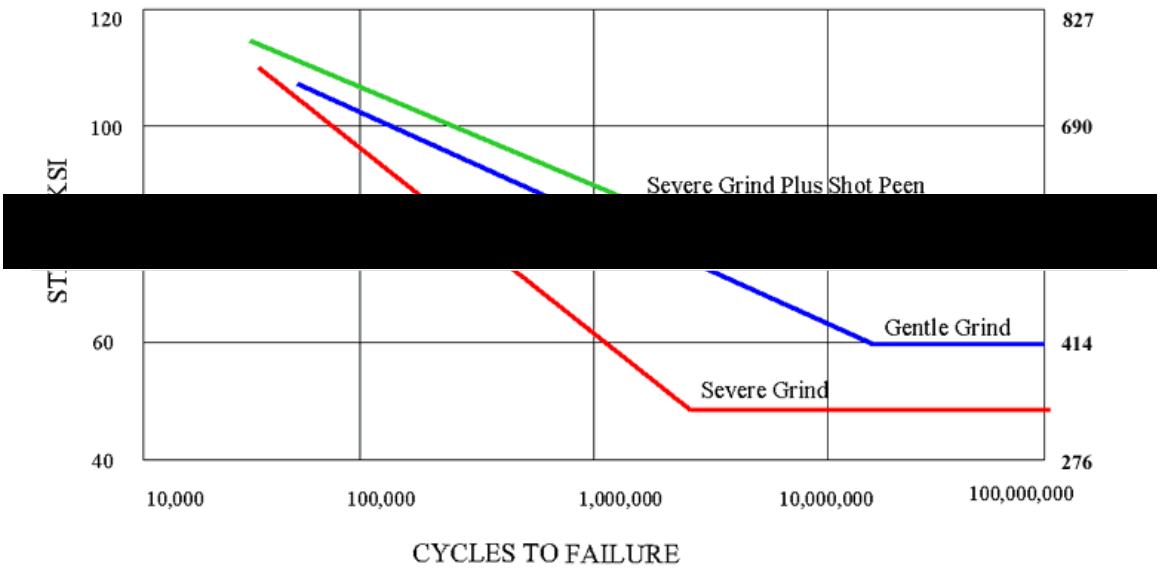

Figure 38: Shot peening & grinding effects on fatigue [228]

As can also be seen in Figure 38 there is a dramatic effect on fatigue resistance from the cold working process of shot peening which is backed up by a great deal of research [229]–[231]. The shot peening process imparts a compressive residual stress near the surface acting to close any short cracks before they have a chance to propagate [232], and will refine the grain size near the surface [233]. A recent study by Messé et al. (2014) has investigated dislocation movement confirming that dislocations form due to plastic deformation induced by peening. The dislocation density is seen to reduce further from the peened surface [234].

For a range of alloys it has been found that thermal and thermomechanical loading will act to remove or reduce the residual stress [43], [235]–[241]. It has also been found that at high stress amplitudes, the compressive residual stresses are depleted especially under a compressive loading regime [230]. With this in mind, the advantages of the compressive stress must be balanced against how damaging to the surface the shot peening process is. The peening process will produce a roughened surface that has many peaks and troughs that can act as stress raising features [242].

2.4.2.3 Oxidation and Initiation

Through a handful of previous studies it has been found that oxidation has a large effect on the fatigue lives of nickel based superalloys, most notably during the crack initiation stage. Many different aspects of the interaction between oxidation and fatigue initiation have been investigated. The effect of cyclic loading on the level of oxidation damage has been investigated for a range of nickel superalloys [92], [114], [168]. Cyclic loading was found to increase the rate of oxidation damage accumulation compared to un-loaded thermal exposures for a range of temperatures from 650°C to 800°C. The effect of prior oxidation on fatigue life was also investigated for plain and notched fatigue specimens at a range of temperatures from 650°C to 800°C and stresses and it was found that there was a notable decrease in the fatigue lives [86], [243]. However, in a study conducted by Cruchley (2015) into as machined coarse grain RR1000 specimens, it was found that there was no life debit after pre-exposure, and at the higher stresses of 900MPa there was actually an improvement in the fatigue life [82]. Finally a study by Jiang in 2015 [50], trying to determine the crack initiation locations for oxidised specimens found that there were a number of different initiation points; grain boundaries, the interface between the γ and the γ' phase due to the formation and cracking of oxides and in some instances cracks initiated from surface pores.

As a point of note, Bílý [174] stated that for non-homogenous bodies, such as those with a hardened surface, micro-cracks can be found below the surface at the interface between the surface layer and the substrate. If considering the hard ceramic oxide layers as a hardened case, this research should be kept in mind.

2.4.3 Propagation

Fatigue crack propagation or growth can occur at stress intensity factors far lower than the fracture toughness of a material. It will be very difficult to remove all stress raisers and surface damage from components meaning crack initiation is inevitable in engineering; therefore, an understanding of the crack propagation rate is vital.

Crack propagation can be thought of as a competition between "intrinsic microstructural damage mechanisms… and extrinsic crack-tip shielding mechanisms" [244]. These mechanisms are apparent in both ductile and brittle materials; however, they will exhibit different levels of prevalence in each. The intrinsic damage mechanisms include dislocation pile-ups and interface decohesion which will lead to cleavage fracture, intergranular cracking and microvoid coalescence. Extrinsic shielding is a complex process and can result from the occurrence of many different mechanisms, some of which will exist only in ductile or brittle materials. An example of some of the shielding processes are crack deflection, crack tip dislocation shielding, crack wake plasticity, bridging, sliding or phase transformation induced closure.

The material being investigated for this analysis can be thought of as a ductile metallic material in the substrate, and a brittle ceramic oxide on the surface.

The rate of fatigue crack growth in metallic materials in relation to the applied stress-intensity range is described in Figure 39. As can be seen there are many factors that influence crack growth rate.

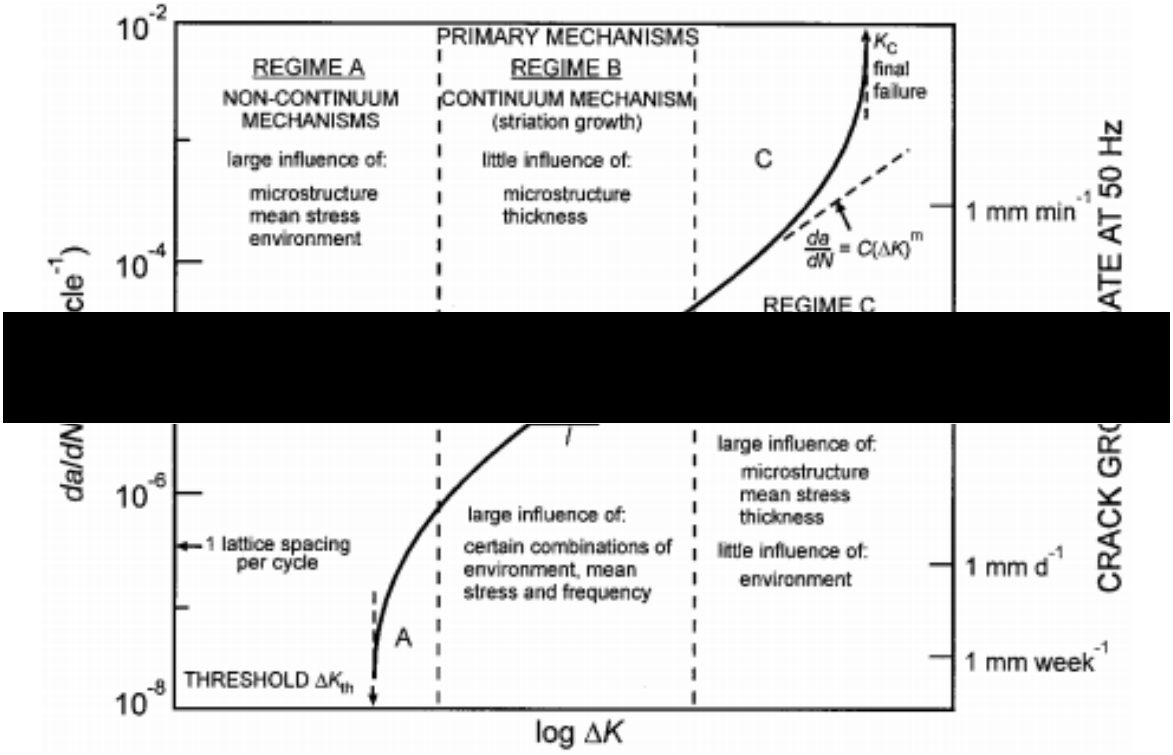

Figure 39: Fatigue-crack growth as a function of applied stress intensity range [245]

Fatigue failure in ductile metals is often characterized by a ductile striation mechanism [244]. Striations represent the advancing distance of a crack front during a single load cycle and are microscopic in size [79]. It has been hypothesised that they are the result of opening and blunting during loading, followed by re-sharpening during unloading of the crack tip, and that this is the primary intrinsic crack growth mechanism in ductile materials [244], the mechanism is moderated primarily by the applied stress intensity range.

The features of fatigue in brittle materials such as the ceramic oxide layer are quite different from those of ductile materials. There will be no striations formed during brittle fatigue, however, the fracture surface will have a very similar appearance to that of a monotonically loaded specimen, but will often present with a greater amount of debris [244]. For brittle materials the extrinsic shielding mechanisms are a great deal more important than for ductile materials. The lack of a plastic zone ahead of the crack tip is detrimental to the fatigue strength of the material; an attempt to promote extrinsic mechanisms within these materials has been investigated with positive results. As an

example, due to the employment of transformation toughening and microcrack toughening, the fracture toughness of zirconia raised from 2 MPa m^{-1} to between 8 and 13 MPa m^{-1} [246].

2.4.3.1 Oxidation and Propagation

At high temperatures, oxidation will occur ahead of the crack tip, leading to a reduction in ductility, increasing crack growth rates [142]; it has been found that the stress assisted grain boundary oxidation (SAGBO) mechanism discussed previously plays an important role in fatigue crack growth for this reason [142], [146], [152].

The effects of temperature on the method of crack growth i.e. intergranular or transgranular was studied for RR1000 by Hyde et al. [247], and it was found that there is a transition temperature range through which one mechanism will become more dominant than the other. The conclusions drawn through examination of fracture surfaces and an understanding of the oxidation mechanism, determined that this transition was due to the oxidation of the material when exposed to high temperatures. It has been found that a crack will grow preferentially along oxidation routes, where the formation and subsequent cracking of chrome or cobalt rich oxides will cause crack initiation and propagation [50]; this will be largely due to the incoherence between the oxide partials and the alloy matrix. This research is supported by the research into another Ni-base superalloy, Waspaloy, which was conducted by Lerch et al. [248].

A study conducted by Kitaguchi et al. [92], investigated the oxidation of a powder metallurgy processed Ni-base superalloy; a micrograph from their work is shown in Figure 40.

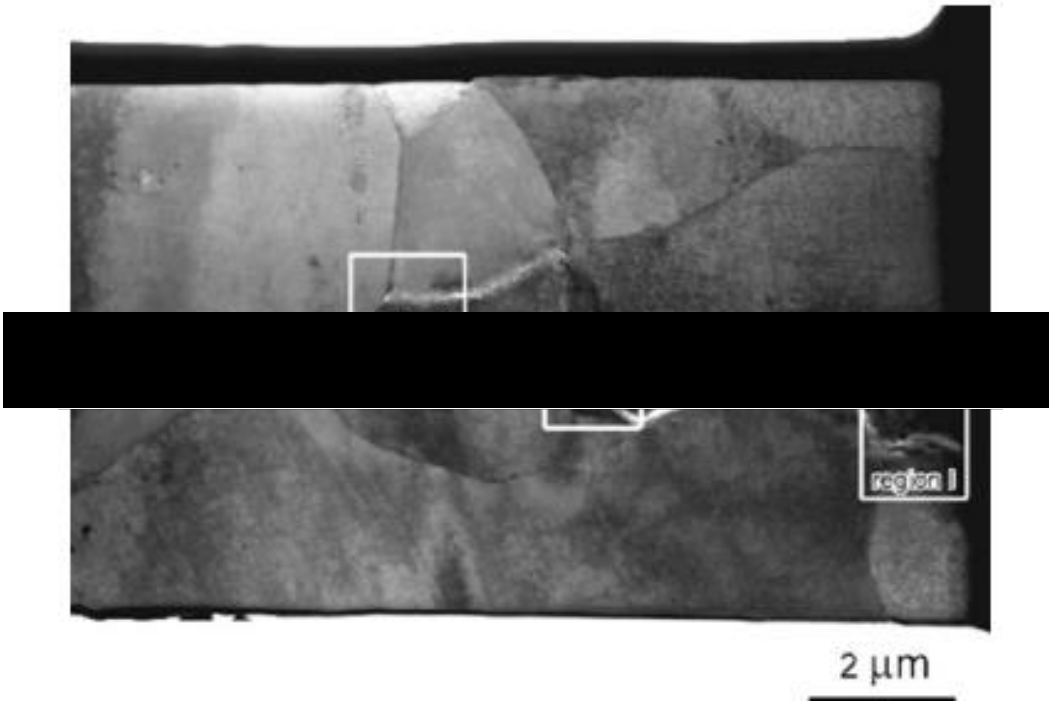

Figure 40: SEM micrograph of oxide intrusion ahead of a crack tip [92]

The oxidation route for this sample can be seen clearly by the white line on the micrograph. The crack tip is to the left of the image, with the oxidation pathway following the grain boundary. The regions labelled in Figure 40 denoted areas which were further studied during the analysis in order to determine how the oxides of the different elements formed at different points along the diffusion pathway. From this study the extent of the oxygen diffusion and subsequent oxidation within the material can be seen. Similar results have been found by Karabela et al. [113].

2.4.4 Temperature

The fatigue properties of metals below room temperature are generally favourable to those at higher temperatures. Although notch sensitivity increases at lower temperatures, fatigue lives have been found to increase [178]. Fatigue strength is then seen to reduce with increasing temperatures. Many factors contribute to this, including an increase in creep-fatigue interaction raising the mean stress level, and increased oxidation along grain boundaries, leading to faster crack growth rates [172]. When recording a high temperature fatigue test, it is customary to note time to failure as well as number of cycles [178].

2.4.5 Fatigue Life

The reason for performing fatigue tests and understanding the effect varying conditions have on the fatigue response of a material is so we can better understand how to utilise the material in service. It is therefore important to understand how the data from fatigue testing will be used in industrial operations. Fatigue component lifing analyses are often conducted in one of two main ways; the total life approach and the defect tolerant approach [244]. The total life method has found favour in ground vehicle design, and the defect tolerant approach has been applied when catastrophic failures are possible, such as the aerospace and nuclear industries.

Total life analysis is the classical method for fatigue design, in which total fatigue life to failure is defined in terms of cyclic stress range or strain range. As the name suggests, the fatigue process from crack nucleation to component failure is analysed. The stress-life approach is used primarily for HCF application; components that will be subjected to low stress amplitude cyclic stresses, where primarily elastic deformation will occur. The *S-N* curve was developed, and the concept of an endurance limit was hypothesised; this is defined as the stress amplitude under which a component will have an infinite fatigue life [178]. For LCF regimes, in which a great deal of plastic deformation is expected, or a component is constrained at some point, strain-life models have been developed [249].

The defect tolerant approach uses fracture mechanics to determine the rates of crack growth; it is predicated on the assumption that all components will contain flaws. The

presence of any crack of critical size will be determined using NDE techniques and if a component is deemed appropriate, it will enter service. A crack growth rate will be applied, assuming there is a crack in the component of a length equal to the resolution limit of the NDE equipment. The component will be allowed to run in service until a time before which the assumed crack would reach an unsafe length, which is termed the critical crack size. The component will then be reanalysed using NDE to determine the presence and nature of any cracks. This process will continue until there is a crack found in the component over which continued service is not allowable. The allowable critical crack size will be determined based on a number of factors including; loading, the strain limit and the material properties e.g. fracture toughness. The crack growth laws used are empirical, and are applicable only for small scale yielding, where the crack tip plastic zone is small in comparison to the geometry of the component, and the loading produces a primarily elastic response [178]. The effects of environment, stress concentration, geometry and mean stresses can be incorporated into the analyses.

3 Experimental Methods

3.1 Oxidation

3.1.1 Specimen Preparation

Due to the brittle nature of the oxides being investigated throughout this project, the development of a specialised specimen preparation procedure was required in order to obtain specimen cross sections suitable for the surface measurements to be taken. The current procedure being used in Swansea University can be found in Appendix III.

3.1.2 Oxide Growth Analyses

The oxidation growth analyses that are being performed as part of this study will come under two categories: thermal exposure and thermo-mechanical oxidation testing. It is important to have an understanding of the oxidation characteristics of a material under purely thermal conditions (at zero applied load). In particular, to understand the oxidation process in an oxidising environment i.e. what oxides will form and at what rates will they grow. Expanding on that knowledge it is important to understand how oxides will grow on components in service. In the case of the turbine disc in an aero engine, high temperatures and stresses will be experienced leading to thermo-mechanical oxidising conditions.

3.1.2.1 Elemental Analysis

The initial stage of the analysis was to determine the composition and morphology of the oxides formed in FG RR1000. A specimen of polished as received material was imaged using light microscopy and then elemental analysis was performed to provide a baseline for the material. The specimen was then exposed in a furnace for 1000 hours at 900°C in order to produce a high level of oxide related damage, to simplify initial investigations. The specimen was then re-imaged using a light microscope and the effect of the thermal exposure on the chemical composition of the alloy was analysed.

3.1.2.2 Thermal Exposures

The initial experimentation phase involved determining the scatter in oxidation behaviour of FG RR1000 under thermal loading. As has been noted by Cottrell, "The rate of oxidation is usually measured by weighing a sample periodically to determine the amount of oxygen taken up" [39], which will usually be performed using a thermogravimetric analysis (TGA). However, it was found that for tests requiring an exposure time over 200 hours, TGA was unsuitable due to the increased chance of spallation, which can result in inaccurate weight measurements.

As such, intermittent furnace exposure with microstructural characterisation has been utilised. After varying time intervals, samples were removed from a furnace and prepared for inspection according to the procedure in Section 3.1.1. For all thermal exposures a SNOL 8,2/1100 furnace has been used with temperature monitored using a fluke meter with a type N thermocouple.

Both shot peened and polished surfaces were investigated; shot peening has previously been shown to have an effect on oxidation rates [43], and it is hoped that this work will further the understanding and provide a robust statistical basis for the scatter in oxidation behaviour previously observed. Specimens were exposed at 700°C, 750°C and 800°C for 24, 100, 250 and 1000 hours with 3 repeats performed for each to provide a sound statistical base. The full test matrix can be found in Appendix I. The method of measuring the oxides can be seen in Appendix III.

The specimens that were used for this initial stage of testing were simple cuboidal plates, 20 x 10 x 2 mm in size, an example of which can be seen in Figure 41. The specimens were sectioned from an unexposed disc forging section provided by Rolls Royce Plc. The specimens were initially removed from the disc using electro discharge machining, as there is minimal waste, to obtain the greatest number of test specimens possible. Where the specimens required further sectioning, a Struers cutting wheel was used, with low cutting speeds (≤0.05mm/min) to limit the depth of the plastic deformation zone. All specimen faces were then ground back to the required dimensions using increasingly fine grit grinding paper, until a final stage of polishing was undertaken to decrease the presence of plasticity and surface roughness at and near the surfaces. Specimens were then shot peened on one face according to the standard RR peening procedure used for nickel turbine discs: 110H/ 200%/ 6-8A. The

peening of only one face allows direct comparison of the oxidation rates of peened and polished surfaces within one specimen.

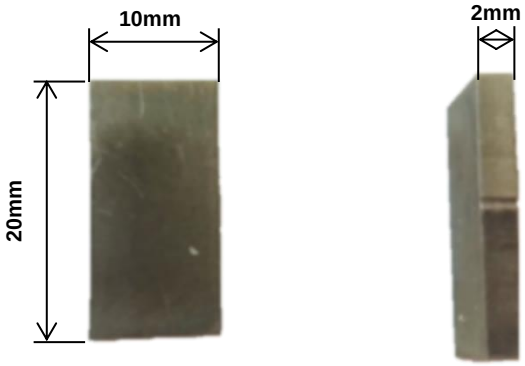

Figure 41: Thermal exposure specimen

3.1.2.3 Thermo-Mechanical Oxidation Testing

It is the purpose of this testing program to determine the extent of oxidation accumulation that occurs across a range of stresses in both tension and compression and compare the results. The stresses analysed were between -600 MPa and 600MPa, for 24, 100 and 250 hour exposure times, with 2 repeats for each. The maximum exposure time of 250 hours was chosen as it was the longest time that could be guaranteed not to result in a creep failure.

After the testing had been conducted, the specimens were prepared according to the procedure in Section 3.1.1, then analysed in the scanning electron microscopy in accordance with section 3.1.4. The full test matrix for the thermo-mechanical oxidation testing program can be seen in Appendix I.

Constant load creep machines with a ratio of 10:1 were utilised initially, according to the SMaRT Standard Test Operating Procedure (STOP) for Constant Load Creep following test standard BS EN ISO 204:2009. This was used purely to assess oxidation damage accumulation within the specimens, not creep damage; the variables were applied load and length of exposure time. The experiments were conducted at a constant temperature.

For the tensile thermo-mechanical loading program RLH10259 specimens were used, which are standard creep specimens. To determine the accuracy of the specimen dimensions after manufacture, each underwent inspection using a shadowgraph prior to testing. The tolerances are set out in the test standards. The specimen drawing can be seen in Appendix II.

As the tensile thermo-mechanical oxidation analysis tests were adopted from tensile creep tests, it was hoped that the compressive thermo-mechanical oxidation tests would be able to be adapted from compressive creep testing methodologies. However, prior to this investigation there was not a test method to perform compressive creep on standard RLH10259 test specimens. The initial compressive test method attempted involved adapting a load reversal cage that was previously developed in SMaRT for a form of miniaturised specimen testing. The purpose of the cage is to adapt a standard constant load creep machine into applying a compressive load uniaxially onto a specimen. An image of the cage can be seen in Figure 42.

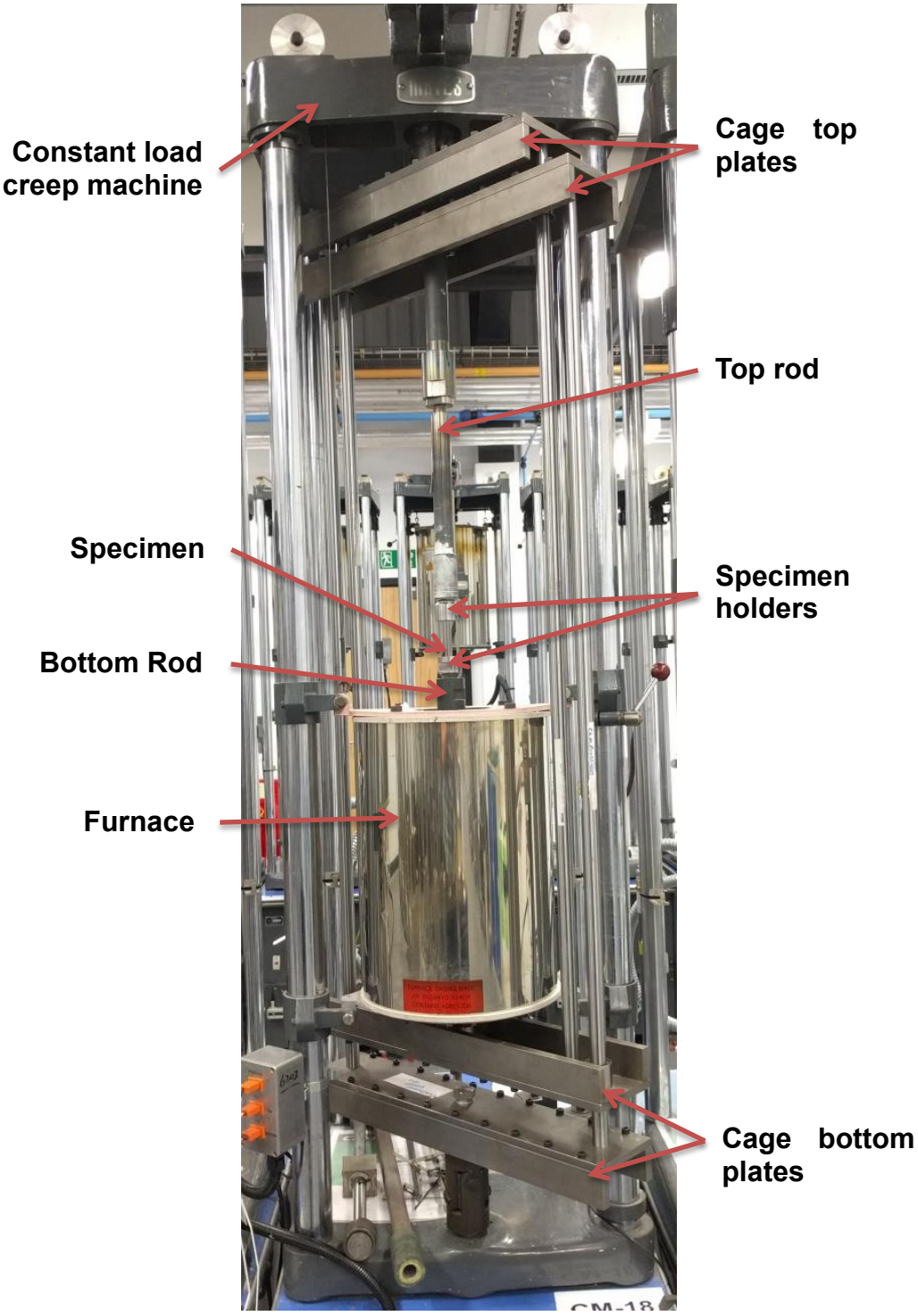

Figure 42: Constant load creep machine with load reversal cage

This method of testing using RLH10259 specimens proved to be unsuccessful during the test development stage. The specimens experienced a great deal of non-uniaxial loading leading to a buckling of the specimen, as can be seen in Figure 43.

Figure 43: RLH10259 specimen that buckled under compressive loading using the load reversal cage

A number of specimens were then designed with differing ratios of cross-sectional area in relation to their gauge length in an attempt to mitigate against the non-uniaxial loading, however, all attempts ended in results similar to those from the RLH10259 investigation.

Following the failed trials an investigation was undertaken into the potential of utilising small compression specimens for the analysis, held under a constant compressive load in an electric screw machine. Using ES-16, an Instron 1361 Electric Screw Test Machine, and the method proved viable and was used throughout the compression thermo-mechanical oxidation programme.

The test machine has a 100kN load cell calibrated down to a load of 1kN making it suitable for this testing program. The testing was performed according to the SMaRT Constant Load Creep STOP based on BS EN ISO 204:2009 to ensure consistency between the compressive and tensile tests. MARM002 nickel superalloy platens were used, with zirconia ceramic disks; the ceramics were used to ensure that during the long thermo-mechanical exposures, the specimens would not indent the platens invalidating the tests.

For the compressive thermo-mechanical oxidation program small compressive specimens were used, which were cylindrical specimens with a diameter of 4.5mm and

a height of 6mm. To determine the accuracy of the dimensions after manufacture, all specimens underwent inspection using a micrometer gauge prior to testing; due to the specimen type it was not possible to use the shadowgraph. The tolerances are set out in the SMaRT Constant Load Creep STOP.

3.1.2.4 Creep Test

In order to determine the potential interaction of creep and oxidation for each of the thermo-mechanical exposures, a strain monitored creep test was performed at the maximum thermo-mechanical exposure stress of 600MPa. The limited testing programme was performed due to a lack of test pieces. The test standard BS EN ISO 204:2009 was followed for the test.

For the creep test a RLH10259 specimen was used, which is a standard creep specimen, the same as was used for the tensile thermo-mechanical oxidation testing. To determine the accuracy of the specimen dimensions after manufacture, it underwent inspection using a shadowgraph prior to testing. The required tolerances are set out in the test standards. The specimen drawing can be seen in Appendix II.

3.1.3 Microhardness Testing

Microhardness tests were performed to determine if the heat treatments changed the plastic response of the material hypothesised through the evolution of the γ' precipitates. Vickers hardness tests were performed at 1kgf with a 10 second dwell on a Struers Duramin 40. Tests were performed initially on the thermal exposure specimens to determine if temperature affected the plastic response of the material, followed by the thermo-mechanical oxidation specimens to investigate if the combination of high temperature and mechanical loading had a different influence than just the high temperature. Due to the statistical variability innate within microhardness testing 20 indentations were performed per specimen.

3.1.4 Microscopy

Using a Jeol 7800F FEG SEM, the wide range of specimens were investigated, and the imaging analyses required for the oxidation damage depth measurements were performed. High magnification energy dispersive x-ray spectroscopy (EDS) was performed on the JEOL 7800F FEGSEM, and the lower magnification EDS was performed on the tungsten filament Hitachi SU3500, both using an Oxford Instruments X-Max^{N}.

High magnification electron backscatter diffraction (EBSD) was performed on the JEOL 7800F FEGSEM with an Oxford Instruments NordlysNano, and the lower magnification EBSD was performed on the Hitachi SU3500 using an Oxford Instruments NordlysMax^{3}.

3.2 Fatigue

3.2.1 Thermally Pre-exposed Fatigue Testing

The issue of fatigue life in the turbine disc design is of great importance. It was hoped that furthering the understanding into the effects of oxidation on the fatigue life of FG RR1000 specimens would aid in the improvement of disc lifing models. For this test program several FG RR1000 specimens underwent load control fatigue testing in accordance with SMaRT Load Control LCF standard test operating procedure (STOP) which is based on BS 3518-1:1993. This was performed in order to determine their life to failure. Specimens were pre-exposed in a SNOL 8,2/1100 furnace with a Fluke 53 II thermometer using an N type thermocouple according to the validated RR oxide growth algorithm to a total damage depth (chromium oxide and aluminium oxide) of 1µm, 3µm or 5µm (the thermal exposures to obtain the damage depths can be seen in Appendix I). The specimens were then tested at a number of different stresses in order to create S-N curves for each damage level. This data was then compared to existing data from undamaged specimens from previous test programs to determine the variation in fatigue life caused by the different damage levels. The full test matrix for this test program can be seen in Appendix I.

The maximum test stress was determined initially from RR load controlled fatigue data, and was then adjusted throughout the test plan in order to get a suitable S-N curve.

To isolate and determine the specific effects of oxidation on the specimen, rather than other effects from extended thermal exposure (e.g. gamma prime coarsening), further load controlled fatigue tests were performed. In this case the specimens underwent vacuum furnace heat treatments, the same as those to produce the required damage depths, in a MTI Corp Ration GSL-1700x with a Pfeiffer HiCube vacuum pump. The full test matrix is shown in Appendix I.

The fatigue tests were performed on SMaRT test machine SH-11; an Instron 2513-501 Hydraulic Testing Machine, which has a 250kN load cell.

Where required, fractography has been performed on these specimens to determine the mode of failure in accordance with section 3.2.8. Also, to determine the effects of

tertiary gamma prime on the fatigue lives of the specimens, microstructural analyses were performed in accordance with the procedure in section 3.2.8.

The specimens used for this section of the testing program are RLH10569, the drawing of which can be seen in Appendix II; the specimens were peened according to the standard conditions used throughout the analysis of 110H/ 125-200%/ 6-8A. To ensure the specimens were in accordance with the tolerances set out in the SMaRT LCF STOP, a shadowgraph was used to take measurements prior to testing.

3.2.2 Notched Fatigue

Notched fatigue testing was performed in order to determine the effect of oxidation on stress raisers similar to those on components in service. Peened specimens with two different notch geometries were chosen in order to determine the level of oxidation on notch sensitivity. Two temperatures were also chosen at which to perform the test in order to determine the effects of oxidation on notches at the temperatures seen by the material in service.

Prior to testing, the majority of the specimens were pre-exposed to an oxide damage depth of 3µm. This damage was chosen as it was the most detrimental to fatigue life from the previous analysis, and it was hoped it would give the greatest contrast to the data for the tests performed on the remainder of the specimens which were left in the as received condition. Data from this analysis was compared to existing data from a previous test programme. The tests were performed on servo-hydraulic rig SH-16

The specimens used for this section of the testing program were RLH10520 for the k_t of 1.55 and RLH8018 for the k_t of 2.29; the drawings of which can be seen in section Appendix II; the specimens were in a peened condition according to the standard conditioned used throughout the analysis: 110H/ 125-200%/ 6-8A. To ensure the specimens were in accordance with the tolerances set out in the SMaRT LCF STOP, a shadowgraph was used to take measurements prior to testing.

3.2.3 Fatigue Crack Propagation Numerical Analysis

It has been hypothesised that oxidation damage will act to affect primarily the initiation stage and not the crack propagation stage of the fatigue damage mechanism. An investigation, using the Paris law relationship based on the effective initial flaw size (EIFS) methodology was used to determine whether the fatigue tests performed consisted purely of crack propagation from the flaws induced within the specimens from the thermal pre-exposures, or whether there was a crack initiation component; the number of cycles of crack propagation to failure was calculated numerically to be compared to the empirical results

The Paris law equation can be seen in Equation 4.

$$\frac{da}{dN} = C\Delta K^m \qquad 4$$

Where:

$\frac{da}{dN}$ = crack growth rate
ΔK = stress intensity range
C & m = constants

To calculate the number of fatigue propagation cycles to failure the Paris law equation is integrated, the result of which can be seen in Equation 5.

$$N_p = \int_{a_0}^{a_f} \frac{da}{C\ \Delta K^m} = \frac{1}{C\left(Y\ \sigma\ \sqrt{\pi}\right)^m} \left[\frac{a_f^{m\prime} - a_0^{m\prime}}{m'}\right] \qquad 5$$

Where:

Y = geometry factor
σ = stress
$m' = 1 - {}^{m}/_{2}$
a_0 = initial flaw size (oxide damage depth)
a_f = flaw size at rupture

3.2.4 Thermo-Mechanical Oxidation Pre-exposed Fatigue

Aero engine HP turbine discs will experience a combination of thermo-mechanical and fatigue damage in operation. To determine how oxidation accumulation under different stresses affects the fatigue life of FG RR1000, a test programme was performed. For this testing programme specimens were initially held under a tensile or compressive stress, and then a low cycle fatigue regime was performed to determine the failure life of the specimens. The test matrix for this stage of the testing is shown in Appendix I. The tests were performed on the electric screw machine ES-16.

Initially, the specimens used in this test regime were RLH10259. These specimens were selected as they are the same as were used in the creep testing regime. It was hoped this would produce consistency in the oxidation growth; however, the initial tests resulted in failure of the specimens at the notches and threads. It is believed that this is due to the similarity of cross sectional area between the gauge and the threaded end, and the stress concentration effect of the threads and notches exacerbated by the fatigue loading. RLH10277 fatigue specimen were therefore used for the analysis; a specimen drawing of which can be seen in Appendix II. To ensure that the tolerances were in line with those required for the SMaRT Constant Load Creep STOP, a shadowgraph was used for measurements prior to testing.

3.2.5 Small Punch Tensile Testing

Small punch tensile testing has found use in mechanical testing as a method of ranking the mechanical properties of materials, with the requirement of very small amounts of material to do a large number of tests compared to conventional tensile testing. The method involves deforming a small cylindrical disc using a hemi-spherical ended punch. The test setup can be seen in Figure 44 [250].

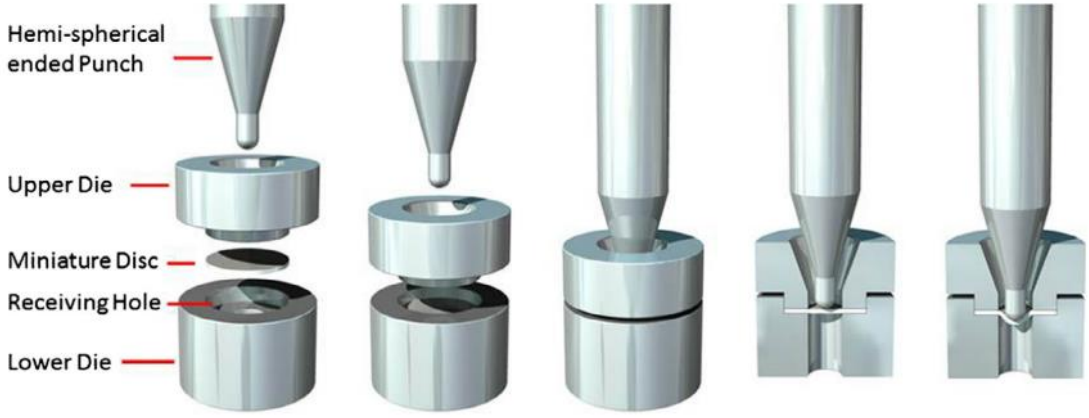

Figure 44: Small punch test apparatus

3 Cylindrical rods were exposed to 1, 3 and 5µm oxidation damage depths, and one was left in the as received condition; small punch specimens were then sectioned from these rods. The tests were performed in order to determine if the heat treatments changed the tensile strength of the bulk material. All the tests were performed under position control at a displacement rate of 0.5 mm/min; testing was performed according to the small punch code of practice [251]. The full test matrix can be seen in Appendix I.

Small punch cylinders of 8mm diameter and a thickness of 500µm +/- 5µm were prepared according to the small punch code of practice [251].

3.2.6 Nanoindentation

Nanoindentation has become a standard technique for characterising the nanomechanical properties of materials. Instead of applying a force and measuring the dimensions of an imprint like the method of microhardness testing, the nanoindentation technique creates an indentation to a required depth and the amount of force that is required to perform the indentation is measured. It is very useful at measuring small changes in microstructures such as welds.

For this analysis, the hardness values of the oxide layers and the gamma prime depleted zone present below the oxides was analysed using accelerated property mapping (XPM) and scanning probe microscopy (SPM). A Bruker Hysitron TI 950 nanoindenter was used to perform the analysis with a Berkovich indenter. A force of 1000µN with a spacing of 1µm was used based on the research by Hintsala et al. [252].

3.2.7 Surface Roughness

It is well known that surface condition can dramatically affect the fatigue initiation properties of a material as discussed in Section 2.4.2.2. It is believed the formation of the oxide scale will affect the surface roughness properties of the alloy and as such a number of methodologies are being investigated to determine the effect of oxidation on the surface roughness of the peened material. For this analysis S_a was used rather than R_a as the measure for surface roughness. S_a is an extension of R_a, the more commonly used linear surface roughness measurement, using areal measurements. This is seen as being a more accurate measure of surface roughness as it works on 3D rather than 2D information and is less likely to miss or conversely be influenced by anomalies within an investigated surface.

50mm x 15mm x 3mm flat plates of peened FG RR1000 were exposed to each of the range of thermal exposures to produce the 1, 3 and 5 µm damage depths and one plate was left in the as received condition. Surface roughness measurements were then performed.

Initially a Nanovea PS50 white light profilometer was used with a 300µm range pen, scanning a 4mm x 4mm area with 1µm step size in both axes. Levelling is performed

using a Gaussian filter according to ISO 16610 and the Sa values are calculated using ISO 25178.

Also used for comparison purposes was an Alicona Infinite Focus using a 10 times magnification lens, with polarised filter to minimise the effects of glare. Levelling was also performed using a Gaussian filter according to ISO 16610 and the S_a values were calculated according to the standard ISO 25178.

3.2.8 Microscopy

The fractographic characterisation of the plain fatigue specimens was performed using a Hitachi SU3500. Fractographic analysis of the small punch specimens was performed using a Keyence VHX-700FE optical microscope. High magnification transmission electron microscopy (TEM) imaging was performed on a FEI Philips TECNAI F20. EDS on the TEM was performed using an Oxford Isis. Transmission Kikuchi diffraction (TKD) also known as transmission electron backscatter diffraction (t-EBSD) was performed on a Jeol 7000F SEM using a Crystal EBSD detector.

4 Results and Discussion

4.1 Oxidation

4.1.1 Thermal Oxidation

4.1.1.1 Elemental Analysis

The etched microstructure of the undamaged parent material is shown in Figure 45; an etch was used to highlight the grain boundaries.

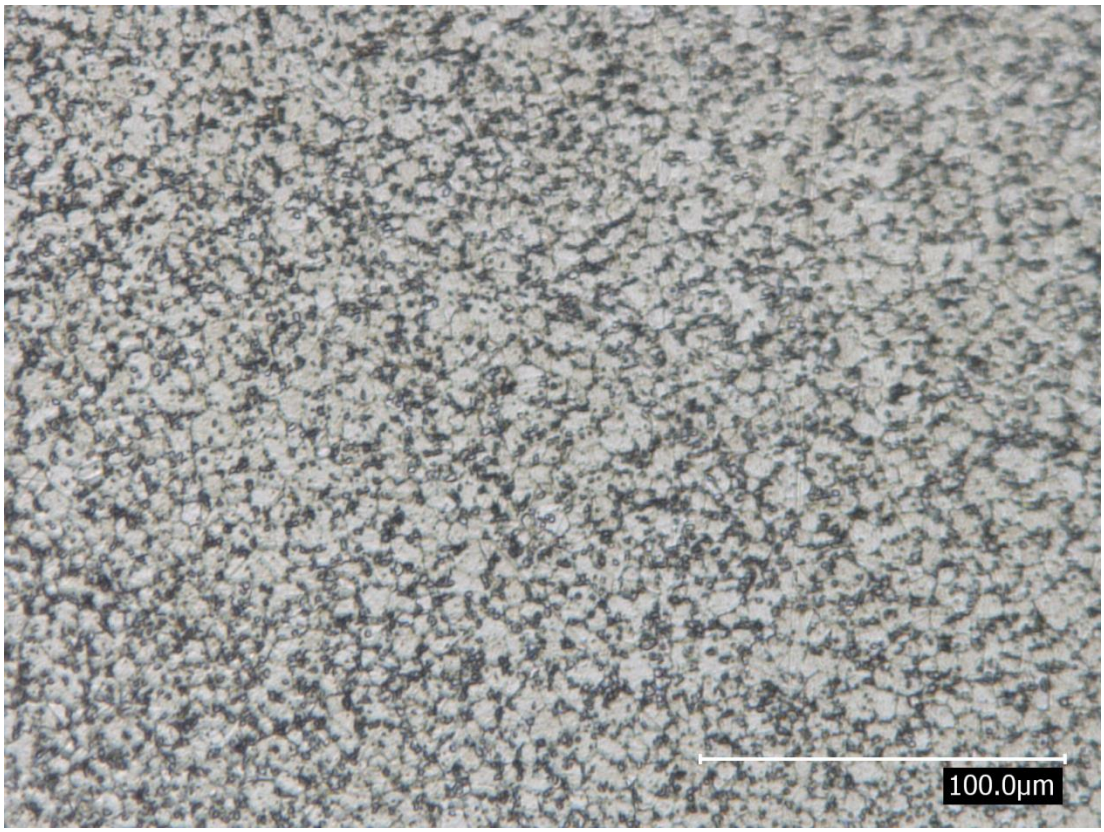

Figure 45: Light micrograph of parent material

The dark particles are the primary γ' at the grain boundaries and the lighter areas characterise the γ matrix. The composition of the parent material for the all the elements within the alloy is shown in Figure 46.

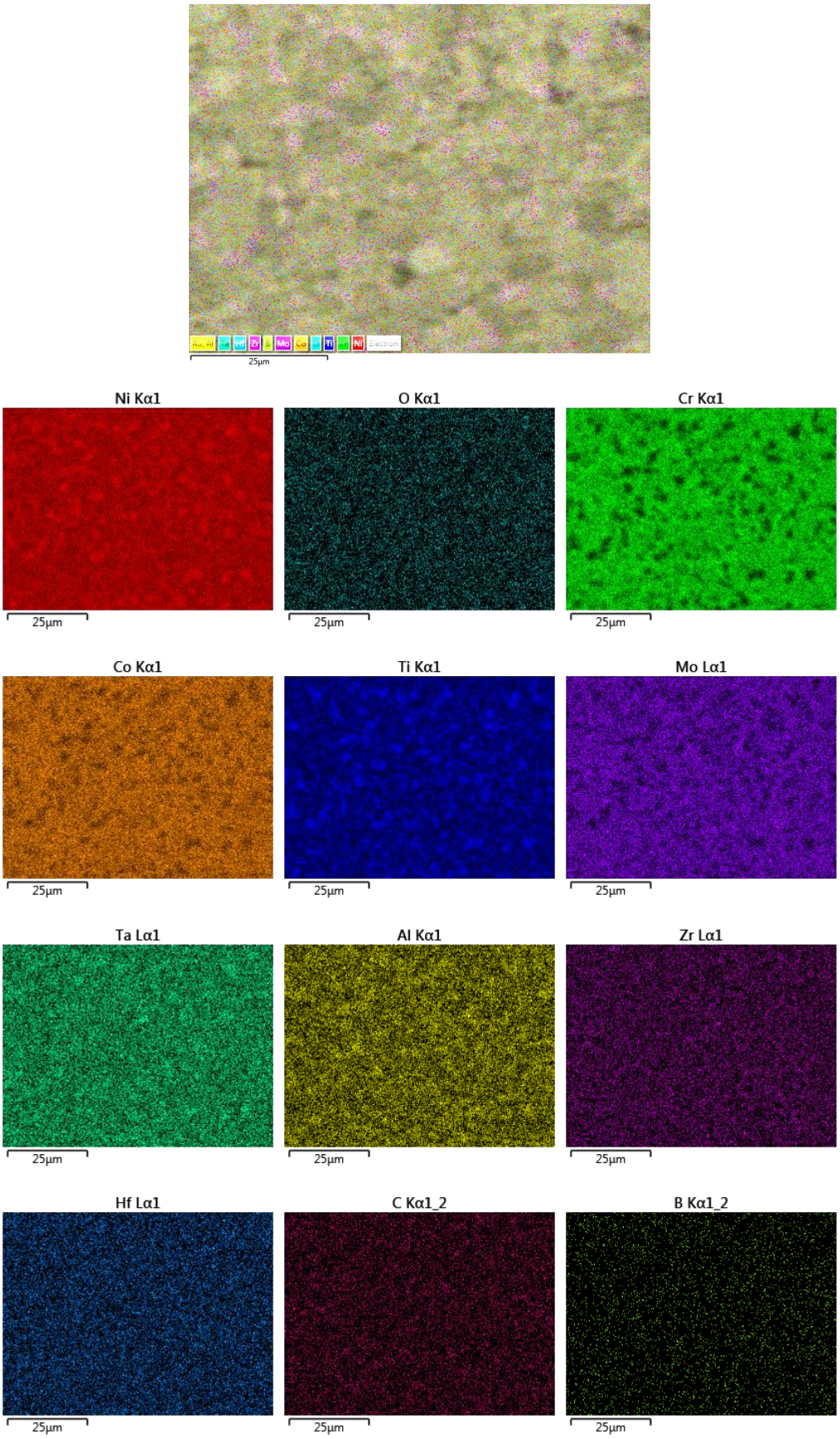

Figure 46 - EDS micrographs of parent FG RR1000 for the elements of RR1000 plus oxygen

The only discontinuities in an otherwise homogenous material is the presence of the nickel, titanium, tantalum and aluminium rich γ' phase; the only elements that are not indicated in the scan are oxygen, carbon and boron. The carbon and boron are very light molecules that EDS typically has trouble resolving and the lack of oxygen is as would be expected for the unexposed as received parent material.

The micrographic imaging following the thermal exposure can be seen in Figure 47.

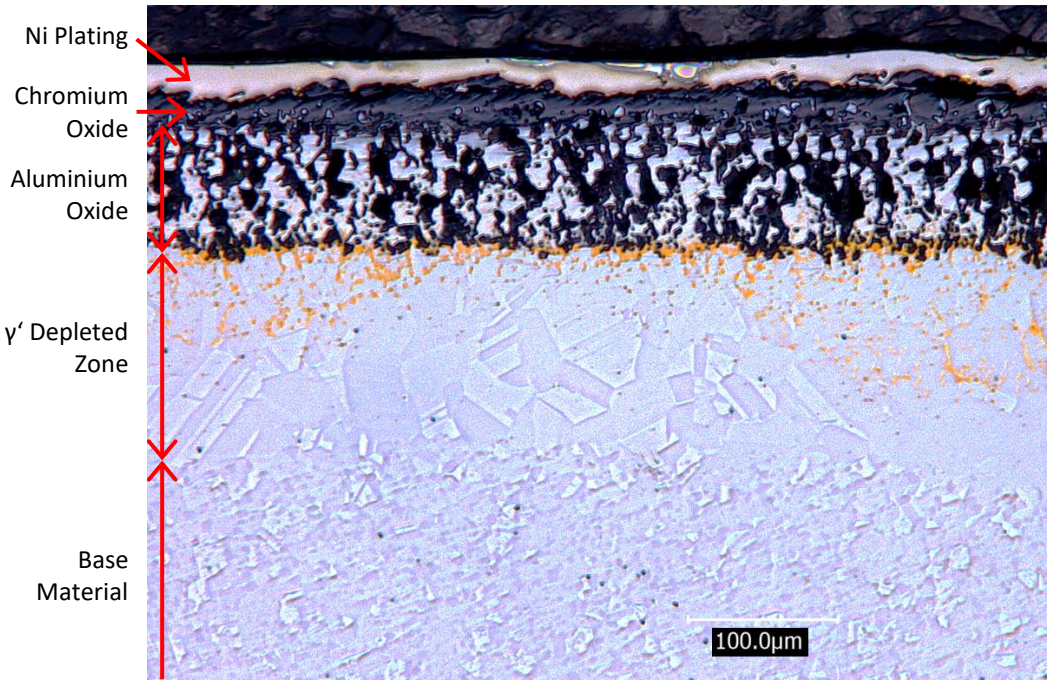

Figure 47: Light micrograph of a thermally exposed surface (polished surface at 900°C for 1000 hours)

As can be seen, there is a continuous scale below the nickel plating and Bakelite layers with protruding growths into the substrate. There is also an apparent γ' depleted zone deeper into the bulk material. Of particular interest is the presence of previously unidentified orange particles throughout the γ' depleted zone that require further analysis using EDS, seen in Figure 48.

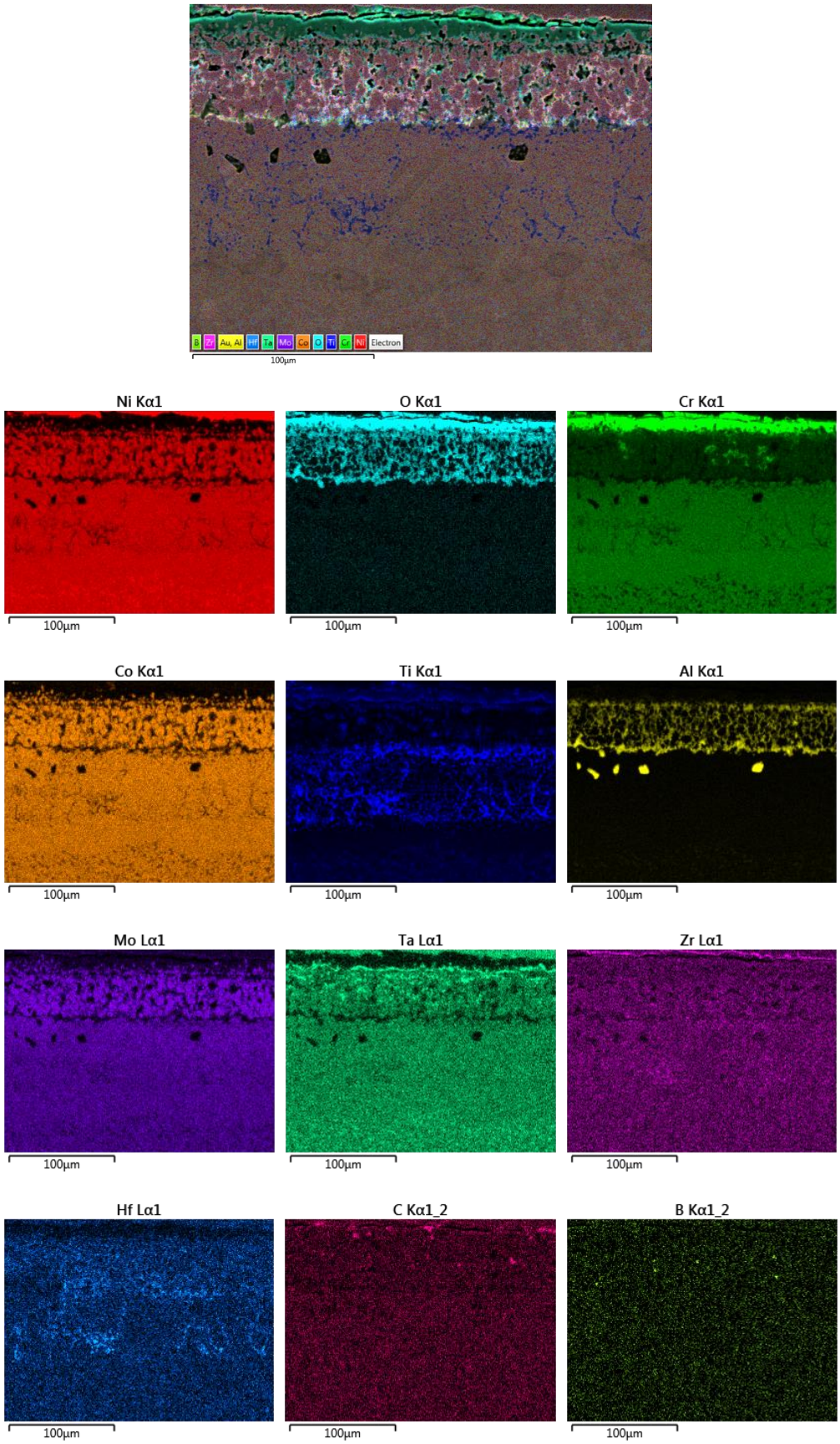

Figure 48: EDS micrographs of thermally oxidised FG RR1000 for the elements of RR1000 plus oxygen

The oxidation map clearly shows the presence of oxygen near the surface. This corresponds clearly to the chromium scale at the surface and aluminium protrusions into the substrate. It is clear to see in the maps for the other elements (Ni, Cr, Co, Ta, Mo, and Zr) that they are depleted in the areas where oxygen is in its highest concentration. The oxide compounds are clearly visible in the micrograph in Figure 47, allowing for easy measurements of the oxide damage levels requiring only high resolution microscopy not continuous EDS mapping.

The orange particles from the micrograph match clearly with titanium elements in the EDS map. This can be assumed to be titanium ions diffusing to the surface to form oxides. It is also evident that there is discontinuous titanium doped within the chromium oxide layer.

Finally, it can be seen, that there is an increased presence of hafnium within the γ' depleted zone, this does not correspond to any oxygen, so it has been assumed that this is present as a result of the oxidation process but is not itself an oxide product.

4.1.1.2 Oxide Characterisation

During the initial high magnification imaging, it became apparent that there was an issue with the nickel plating separating from the oxide, as can be seen in Figure 49. A great deal of effort was made to adapt the mounting procedure to account for this, however, a suitable method was not found during this study. As can be seen in the micrograph however, there is good adherence of the chromium oxide scale to the specimen; the breaking away of the chromium oxide scale is the primary issue faced during oxide preparation procedures. Therefore it has been determined that even though there is separation, the nickel plating is still performing its job of protecting the scale.

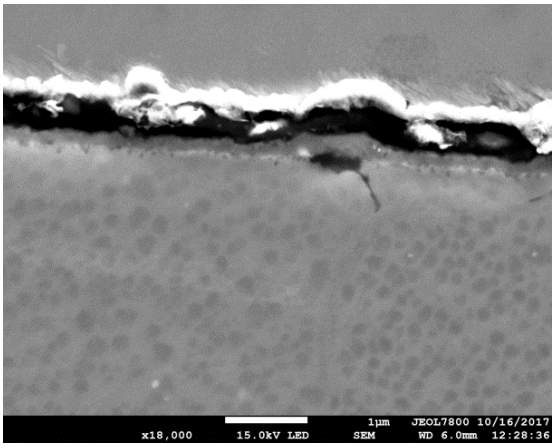

Figure 49: Micrograph of oxidised specimen with separation of the nickel plating (polished surface at 700°C for 100 hours)

Following a range of thermal exposures at different times, temperatures and surface preparation, the oxidation products of the extreme conditions were analysed to see if there was a change in oxide characteristics and morphology. A polished, lower temperature and short exposure specimen is compared directly to a specimen from the most damaging regime of high temperature, peened and longest exposure in Figure 50.

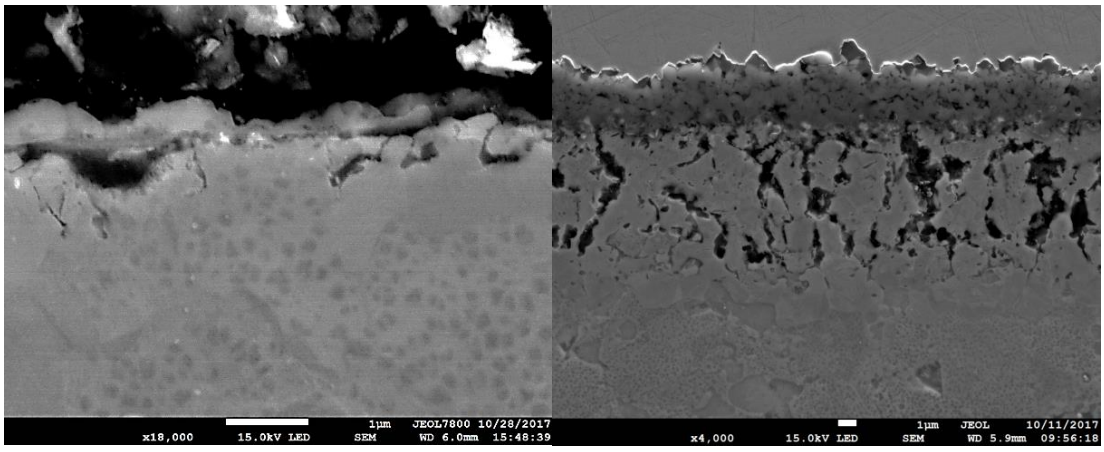

Figure 50: Micrographs of oxides: (left) polished surface at 700°C for 24 hours and (right) peened surface at 800°C for 1000 hours

The damage levels are to greatly different depths, however, the morphologies are essentially the same, and this is true throughout the analysis. There is a continuous chromium scale with varying levels of aluminium oxide intrusion into the substrate.

There are a number of factors previously discussed that will affect oxidation; surface condition, exposure temperature and length of exposure. Some direct comparisons have been performed to determine if there was any difference in the morphologies of the oxides formed; only one variable has been changed for each comparison pair.

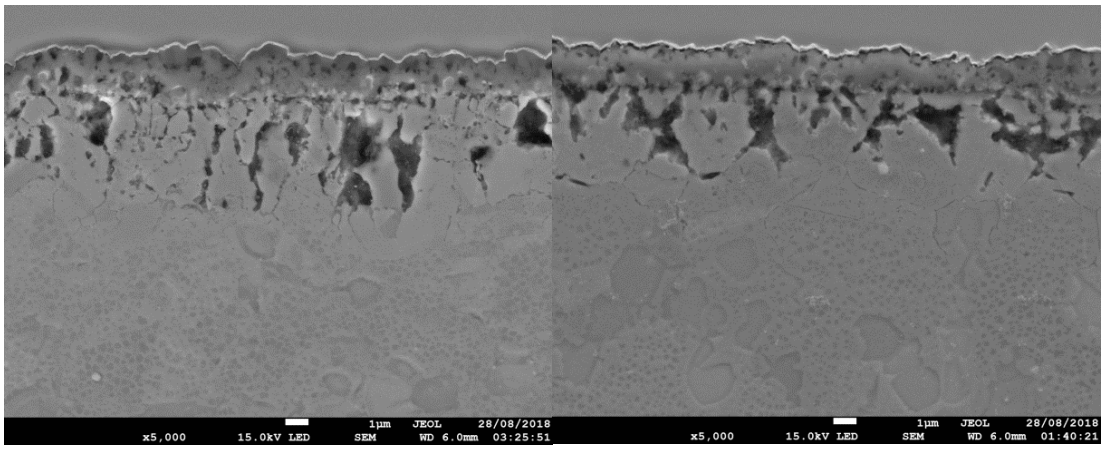

Figure 51: Comparison of thermal exposures on surface condition (750°C for 1000 hours): (left) peened and (right) polished

As can be seen in Figure 51 there is very little difference in the morphology of the oxides. The chromium oxide scale seems more uniform on the polished specimen; this would be due to the smoother surface prior to oxidation. Also, the peened surface has an increased number of aluminium oxide fingers. Most notably, the oxidation on the peened surface is on average 1.4 to 1.5 times deeper than the polished specimen.

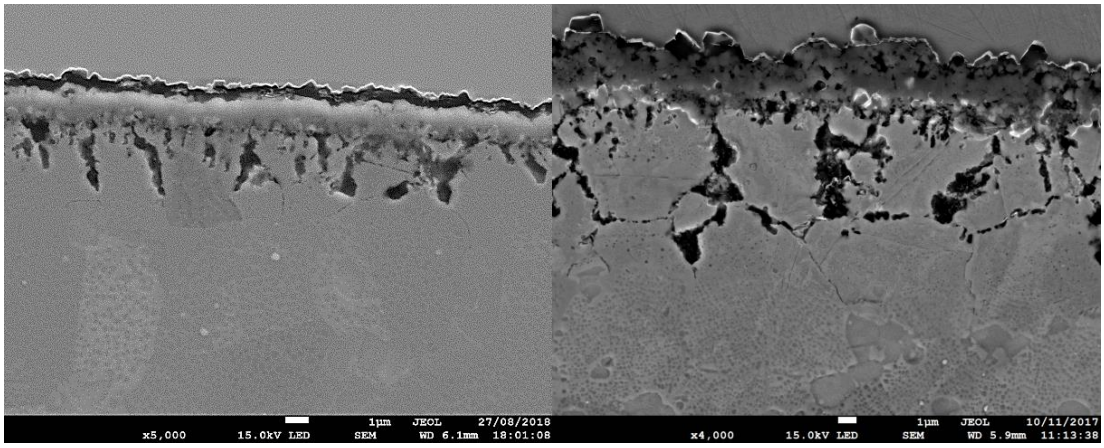

Figure 52: Comparison of exposure time on thermal exposure (polished surfaces at 800°C): (left) 100 hour and (right) 1000 hour

The length of exposure seemed to have no dramatic effect on the morphology of the oxides formed, however, over time, the damage became more pronounced, as can be seen in Figure 52. The scale becomes rougher at the long exposures, and it can be seen that the aluminium fingers start to expand and in some places join up as they grow along the grain boundaries.

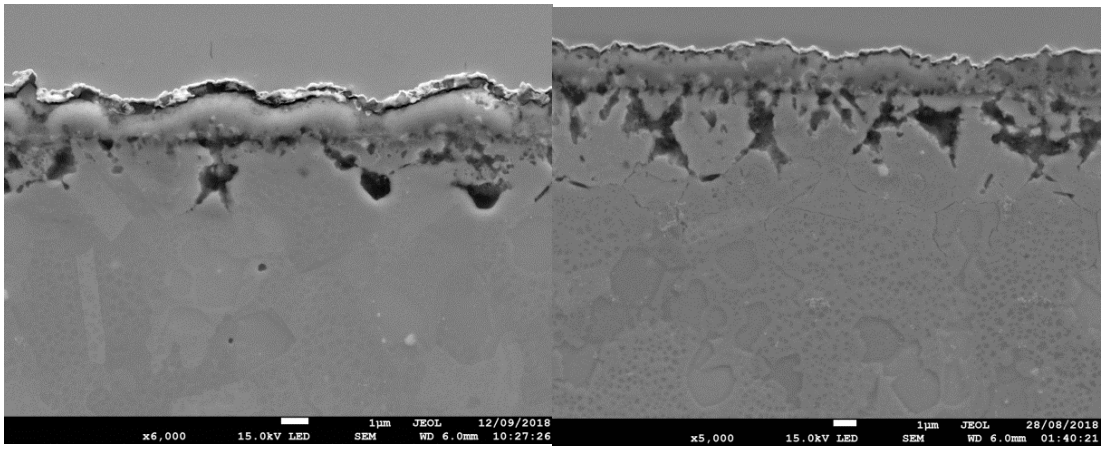

Figure 53: Comparison of temperature on thermal exposure (polished surfaces for 250 hours): (left) 750°C and (right) 800°C

Figure 53 illustrates how temperature difference affects the oxidation; the morphologies are essentially the same, with a minor amount of cracking present in the scale of the 800°C specimen.

As seen in many of the micrographs above, there is an issue of pore formation or cracking in the oxide scale at different points in the thermal exposures of the alloy. Temperature and surface treatment are the controlling factors; the pore formation/ cracking onset temperatures and times for this analysis are shown in Table 3

Table 3: Time to pore formation/ cracking onset

	Time to pore formation / cracking (hours)	
Temperature (°C)	**Peened**	**Polished**
700	1000	None
750	250	None
800	24	100

4.1.1.3 Oxide Damage Depth Measurements

Initial study was undertaken to best determine how to value the oxide damage depth i.e. should the chromium oxide and aluminium oxide be measured together or separately. As such, the oxide depths of the chromium and aluminium were compared to determine if there was a correlation. A graph comparing the ratio of chromium oxide and aluminium oxide depth against the overall damage depth has been plotted in Figure 54.

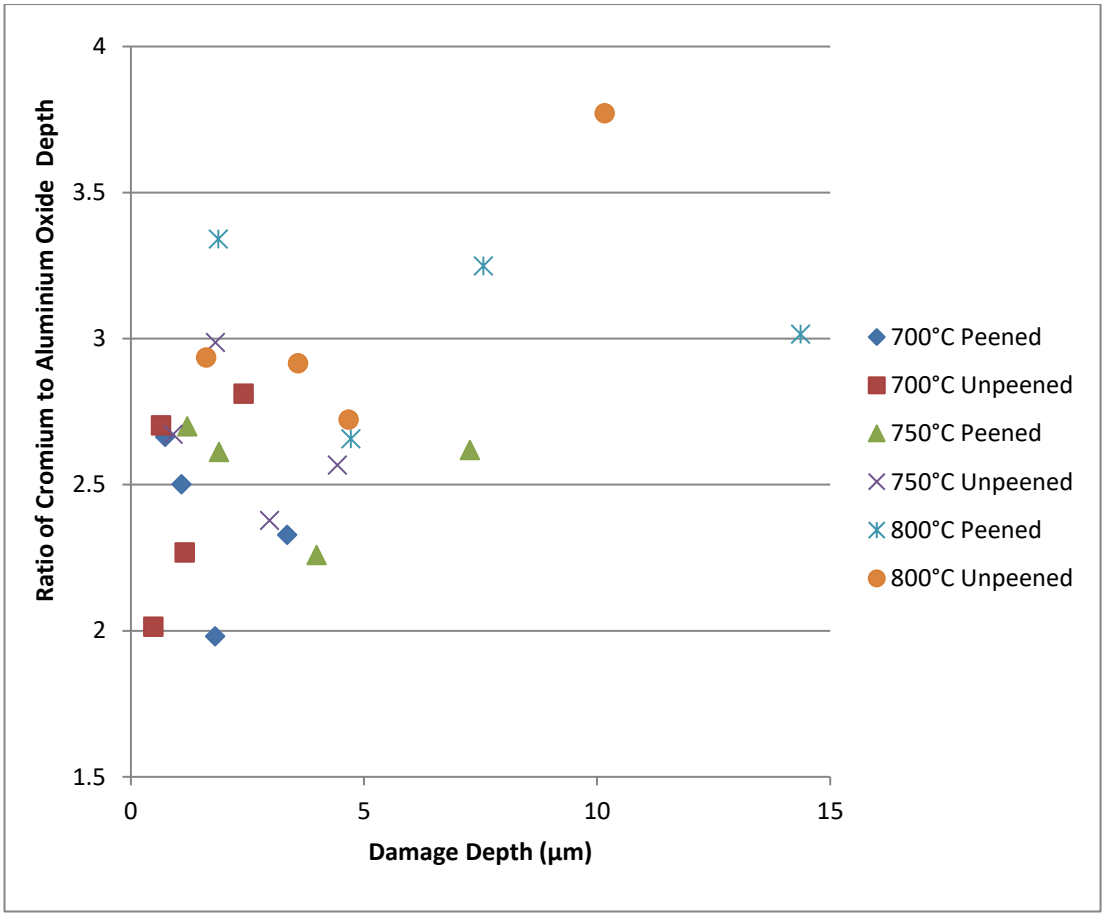

Figure 54: Comparison of the ratio of oxide depths and overall oxide depth

As can be seen, there is no apparent correlation, meaning it would be unwise to consider the chromium and aluminium oxide thicknesses separately throughout the analysis. This is supported by analysis of the micrographs which show areas that present thicker chromium oxide scale tend to have shorter aluminium oxide fingers and vice versa. As such, throughout the analysis, the chromium oxide scale and aluminium oxide fingers will be measured together and from this point on will be referred to as the oxide depth.

The oxide depths of the different thermal exposures can be seen in Figure 55 for the peened and polished specimens.

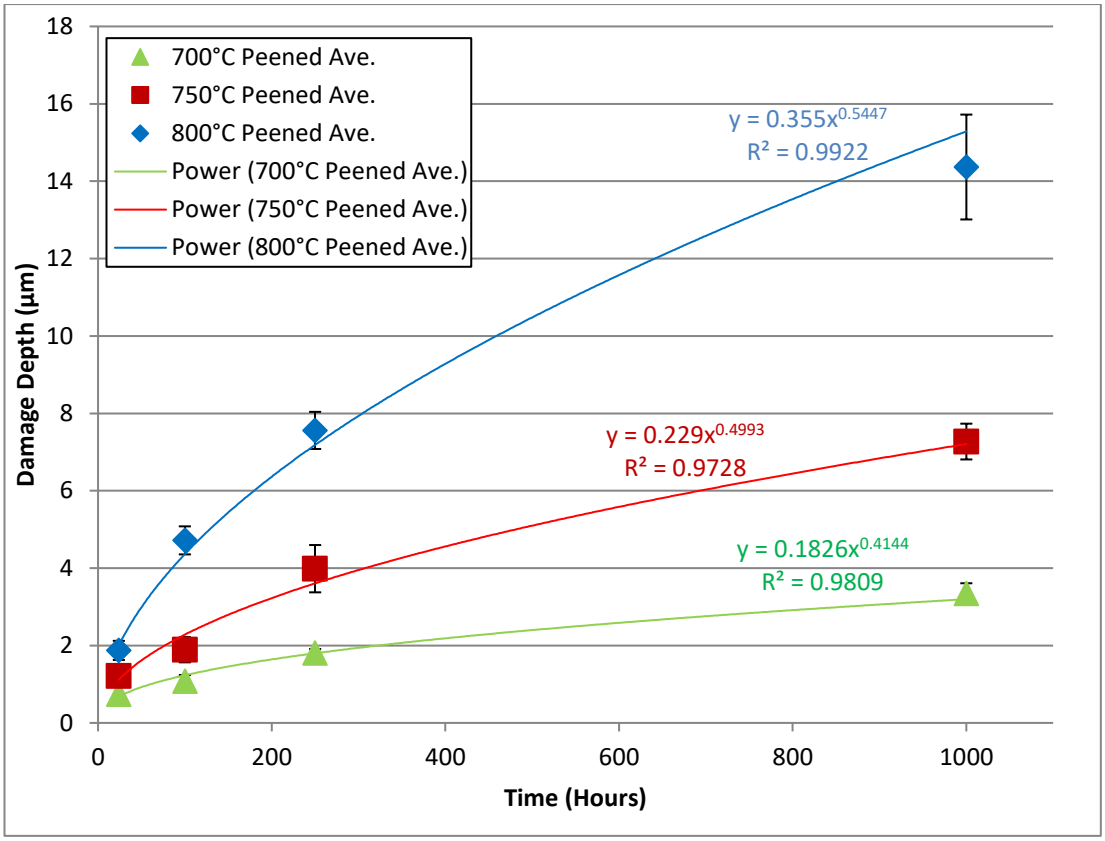

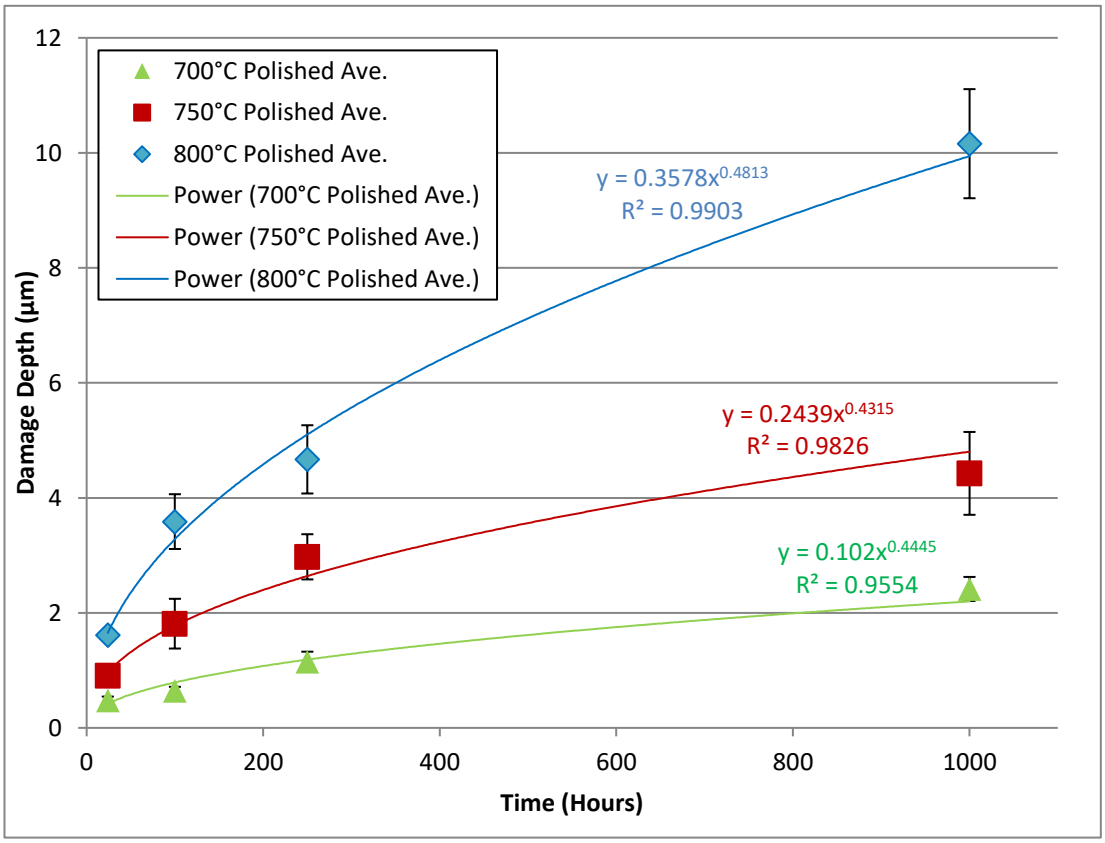

Figure 55: Oxide depth against time for polished specimens in the peened and polished conditions

It can be seen for both the polished and the peened specimens that as the temperature increases the oxide depth increases. The temperature increase of 50°C from 700°C showed an approximate double of the oxide damage depth at all lengths of exposure and the further increase of 50°C to 800°C showed an increase compared to the 700°C of over 4 times at exposure times over 24 hours. A regression analysis of each of the oxidation rates at different temperatures found that power law provided a good fit, with high R^2 values for each. It can also be seen that at longer exposures, the lower temperatures reach a steady state at a shorter exposure than the higher temperatures.

As can clearly be seen when comparing values from the 2 graphs that the peening has a dramatic effect on the rate of oxidation at all temperatures. Peening accounts for an approximately 50% increase in the oxidation rate at each temperature.

To determine if there is a correlation between the oxide depth and the γ' depleted depth a comparison was performed. The result can be seen in Figure 56.

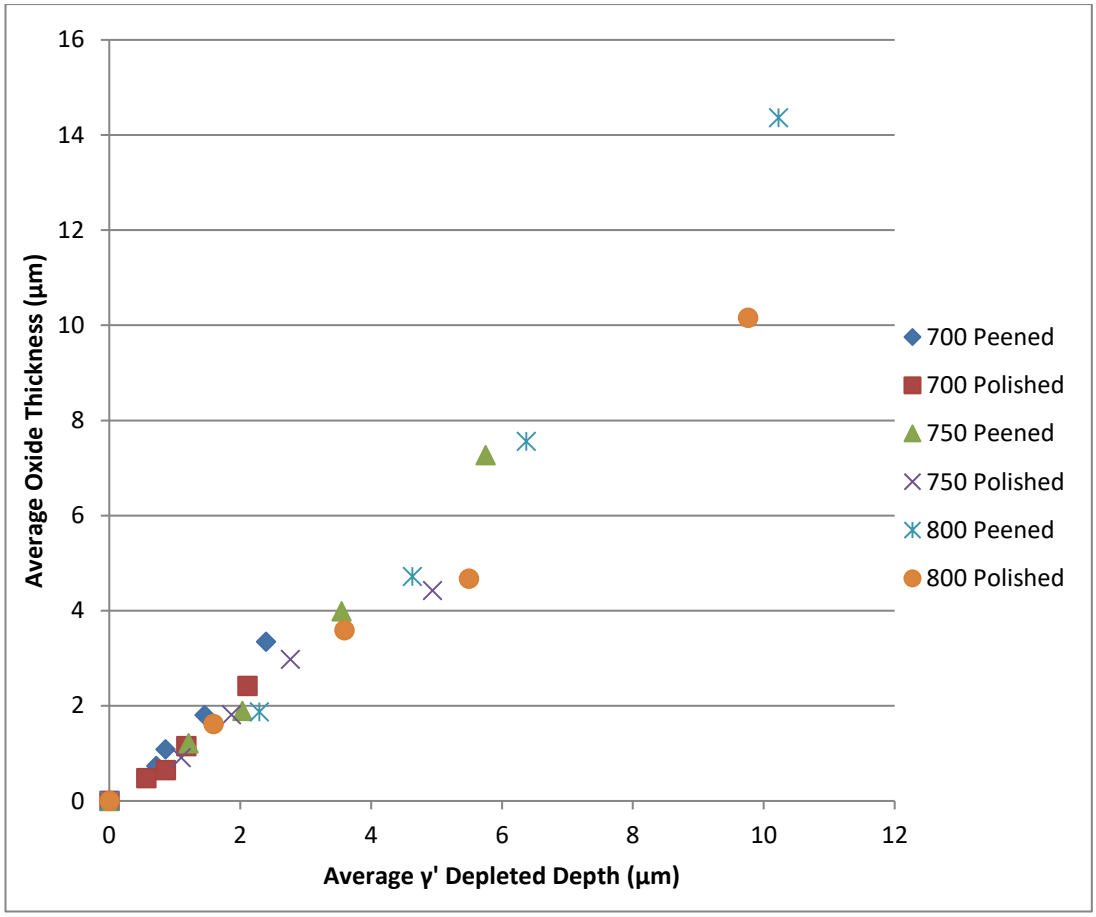

Figure 56: A comparison of average oxide thickness to average γ' depleted depth

As can be seen there is a clear correlation between the oxide depth and the γ' depleted depth. This can be explained by the fact that aluminium oxides will form as a result of the depletion of γ' from the substrate.

4.1.1.4 Hardness Testing

In order to ascertain the effect the thermal heat treatments had on the microstructure of the bulk of the exposed material, the mechanical test of Vickers Hardness was performed. The results can be seen in Figure 57.

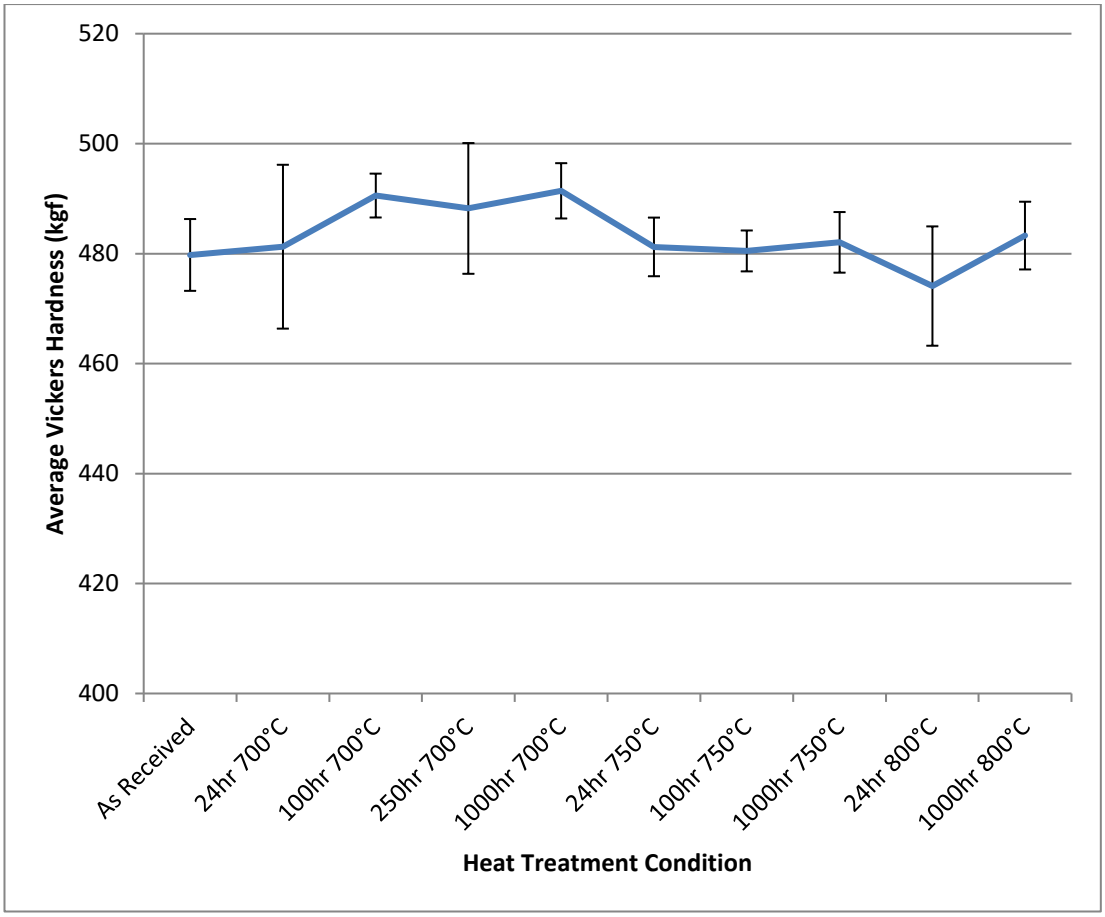

Figure 57: Vickers hardness values of the heat-treated specimens

As can be seen there is statistically no change in the hardness value across all the heat treatments meaning there is no discernible change in the microstructure of the specimens with regard to the plastic response.

4.1.1.5 Thermal Oxidation Modelling

As has been discussed in the literature review, a common method for modelling the oxidation of different materials and material variants is the use of the Arrhenius relationship shown in Equation 2.

Using the Arrhenius equation it can be seen that plotting a graph of the ln k against 1/T will produce a straight line, the gradient of which is the activation energy divided by the gas constant. The reaction rate, k must first be calculated; this can be done using Equation 6.

$$k = \frac{d^n}{t} \qquad 6$$

Where:
k = rate constant
d = thickness of the oxides
n = empirical constant determining the rate law of the reaction
t = time

The value of k must be determined from experimental data. By plotting a graph of the natural log of time against the natural log of the oxide depth, it is possible to find the y intersect at each temperature which provides the natural log of the k value. The graph of this can be seen in Figure 58.

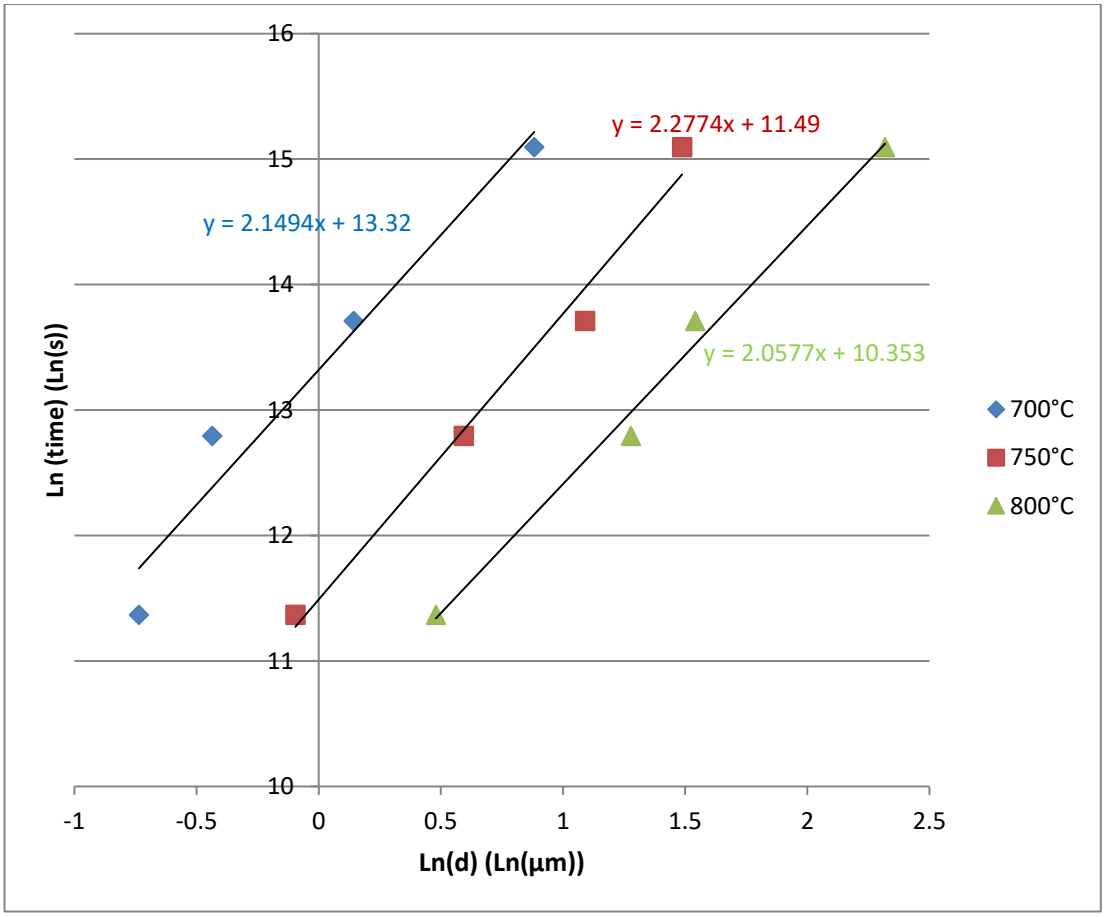

Figure 58: Graph showing the Ln(t) against the Ln(d) to provide the Ln(k) value for the polished specimens

The Ln (k) value can then be plotted against 1/T and the activation energy determined.

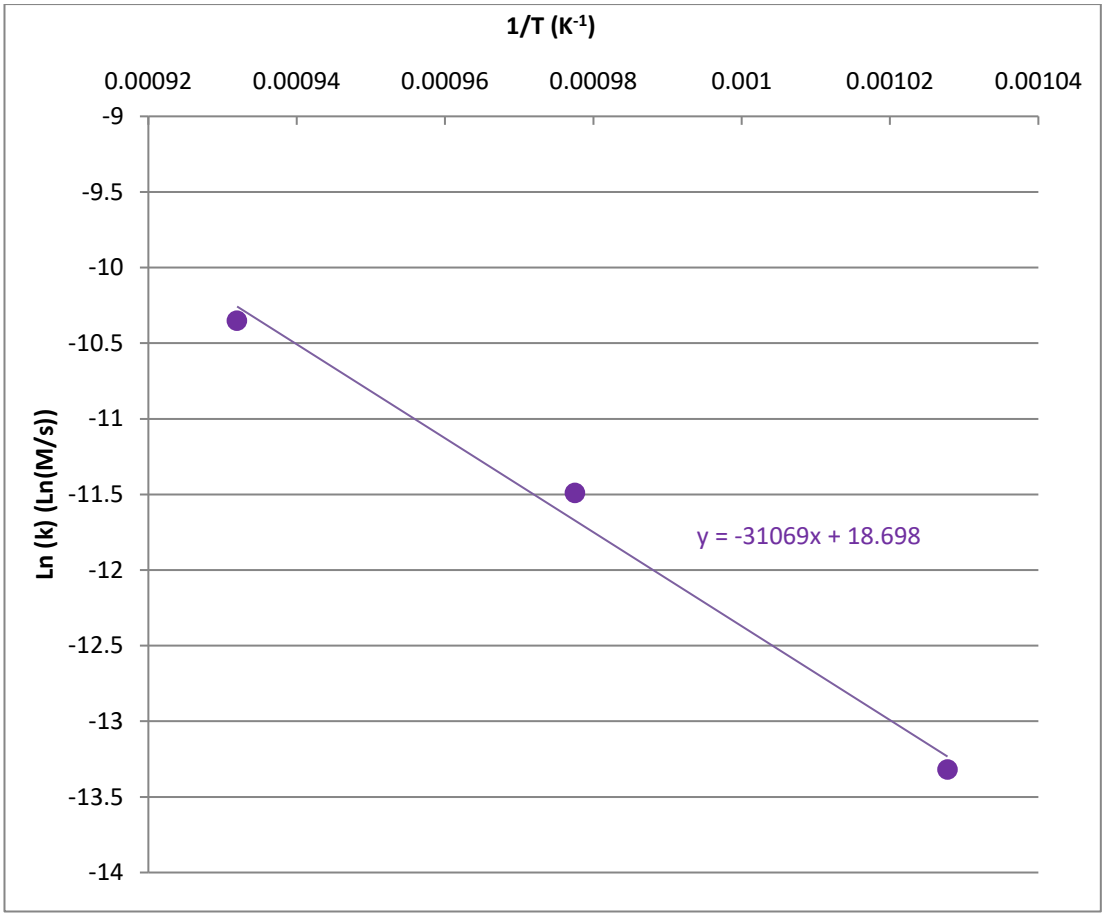

Figure 59: A graph showing the Ln(k) against 1/T to calculate $-E_a/R$

The gradient of the graph provides the negative of the activation energy divided by the gas constant. The activation energy for the polished specimens is 260 kJ/mol, and that provided through the same means for the peened specimens is 190 kJ/mol.

It is believed that the reasoning behind the reduction in the activation energy following peening can be explained by the vacancy diffusion mechanism of short circuit diffusion that was explained in Section 2.3.1. This increase in the rate of pipe diffusion is due to the greatly increased number of dislocation imparted on the material during the highly damaging peening process [253]. Another potential mechanism for the decrease in activation energy is suggested by research conducted by Bertali et al (2016), which suggests that residual stresses in a material will increase the oxidation rate [254].

4.1.2 Thermo-Mechanical Oxidation

4.1.2.1 Oxide Damage Depth Measurements

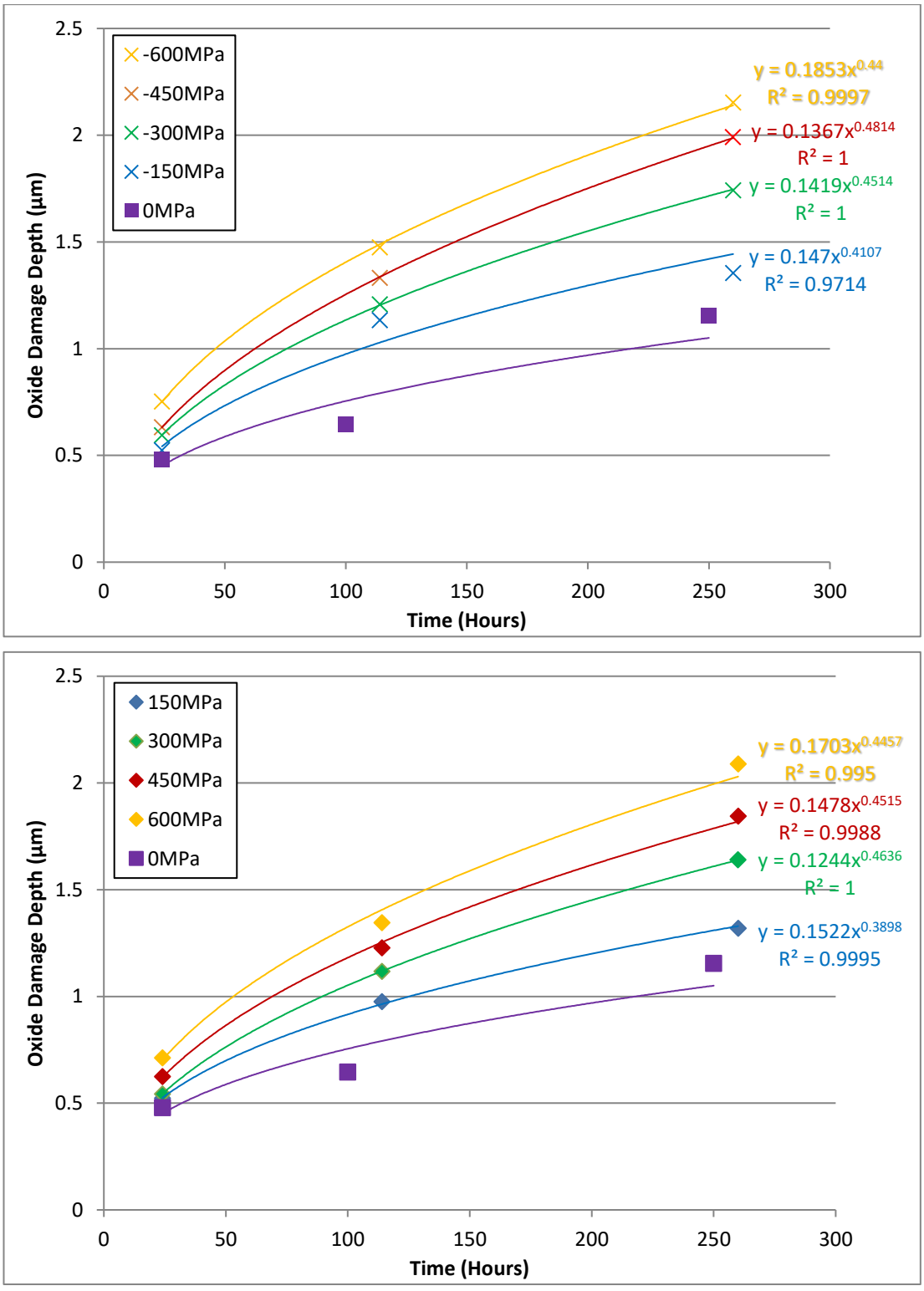

Figure 60: Oxide damage depth measurements for compressive (top) and tensile (bottom) loading at 700°C

As can be seen in Figure 60, the greater the load in both compressive and tensile regimes, the deeper the oxidation depth, up to approximately double the depth at the highest stress experienced. There is a greater effect of increased load at the lower loading regimes i.e. a greater damage depth difference between 150 and 300 MPa than 450 and 600MPa in both compressive and tensile loading. It can also be inferred from the graphs that the compressive regime will result in more damage than the tensile loading; this is similar to results seen for the oxidation of pure nickel [107].

4.1.2.2 Hardness Testing

Similar to the thermal exposure specimens, hardness testing was performed on the thermo-mechanical oxidation specimens in the bulk material away from the oxide product. The Vickers Hardness against time is shown in Figure 61.

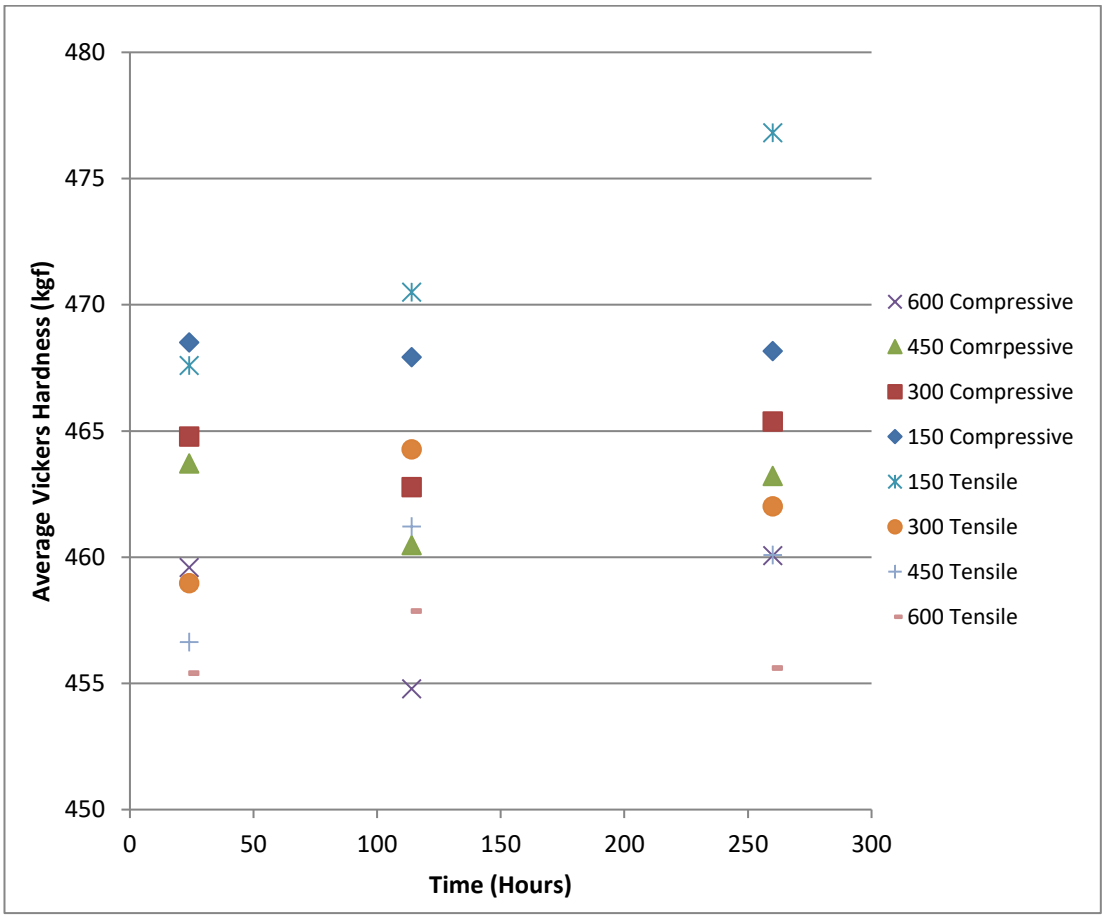

Figure 61: Vickers hardness values of the thermo-mechanical specimens against time

As can be seen from the above graph, there is no discernible correlation between the hardness value and the length of exposure under different loading regimes. It can be inferred that there may be a relationship between the applied stress and the resulting Vickers Hardness i.e. the higher the load in both tensile and compression, the lower the resulting average hardness value however it is not clear; therefore a graph of average Vickers Hardness against stress was plotted in Figure 62.

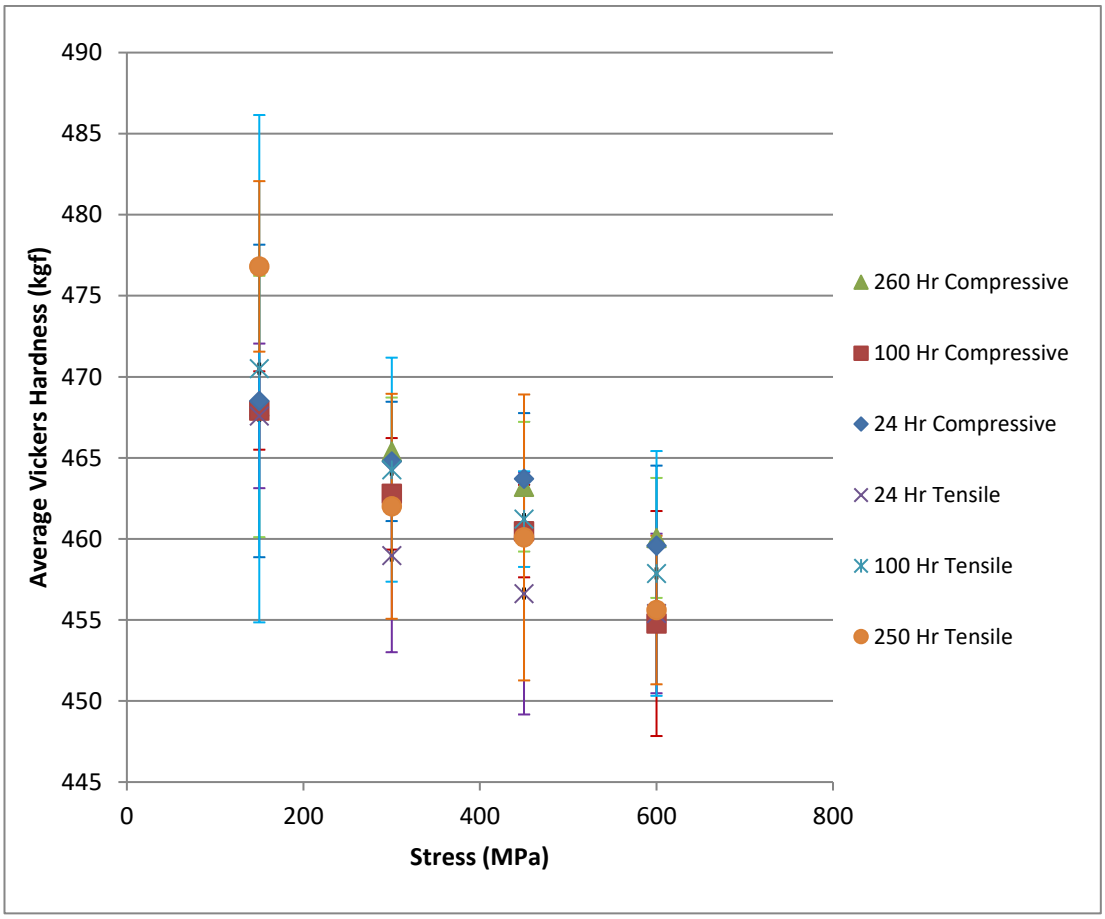

Figure 62: Vickers hardness values of the thermo-mechanical specimens against applies stress with error bars showing a standard deviation

It is clear to see there is a general trend in the data to a reducing hardness as a result of applied load. However, there is a great deal of statistical overlap in the data sets making any firm conclusions unwise.

Even with the statistical uncertainty it is apparent there is a trend in the Vickers Hardness response of the material; the higher the stress, the lower the hardness. Similar to the thermal exposure tests, the length of thermo-mechanical exposure has no apparent effect on the hardness value, suggesting that the change in mechanical properties happens within the first 24 hours (prior to the interruption of the shortest thermo-mechanical exposure performed) and is due only to some form of mechanical damage mechanism.

As discussed in the literature review, creep is the mechanical damage mechanism that will occur during the thermo-mechanical exposures. Therefore, a better understanding of the creep behaviour of the material may assist in the understanding of the change in the hardness values. It may ultimately provide further insight into why thermo-mechanical oxidation is more damaging than thermal oxidation.

The creep response of RR1000 at 600MPa and 700°C can be seen in Figure 63.

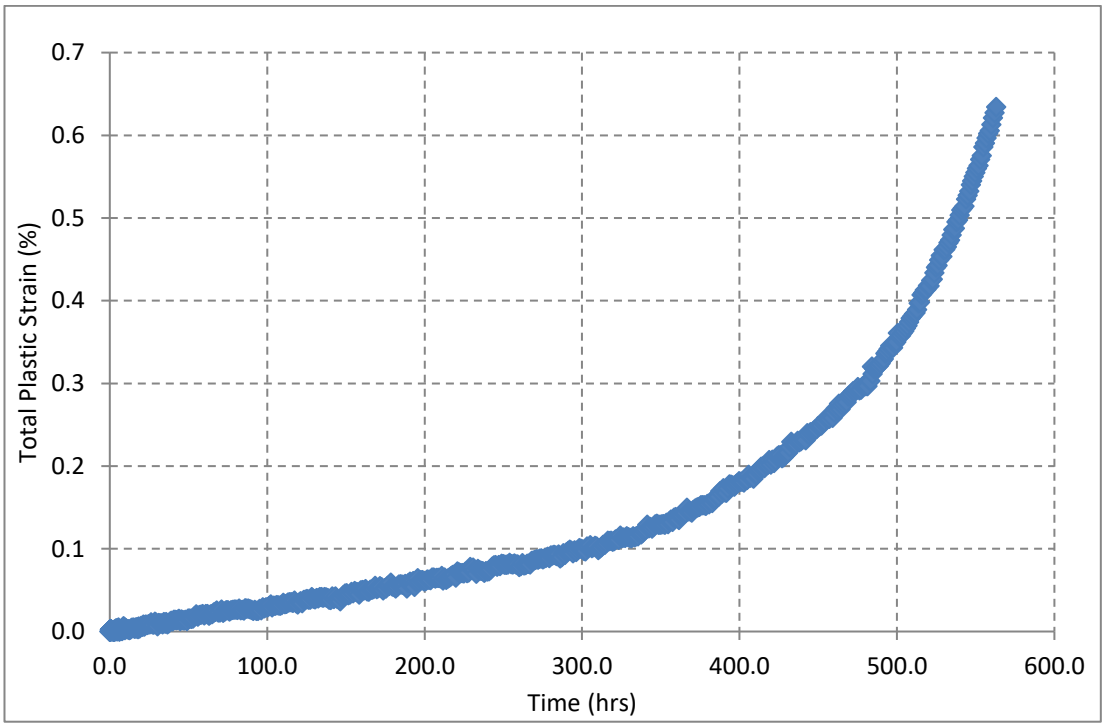

Figure 63: Creep strain against time for FG RR1000 at 600MPa

As can be seen, the total plastic strain accumulation increases noticeably throughout the periods for the thermo-mechanical exposures. This is shown more clearly in Figure 64, which is a cropped version of Figure 63 highlighting the plastic strain accumulation within just this timeframe.

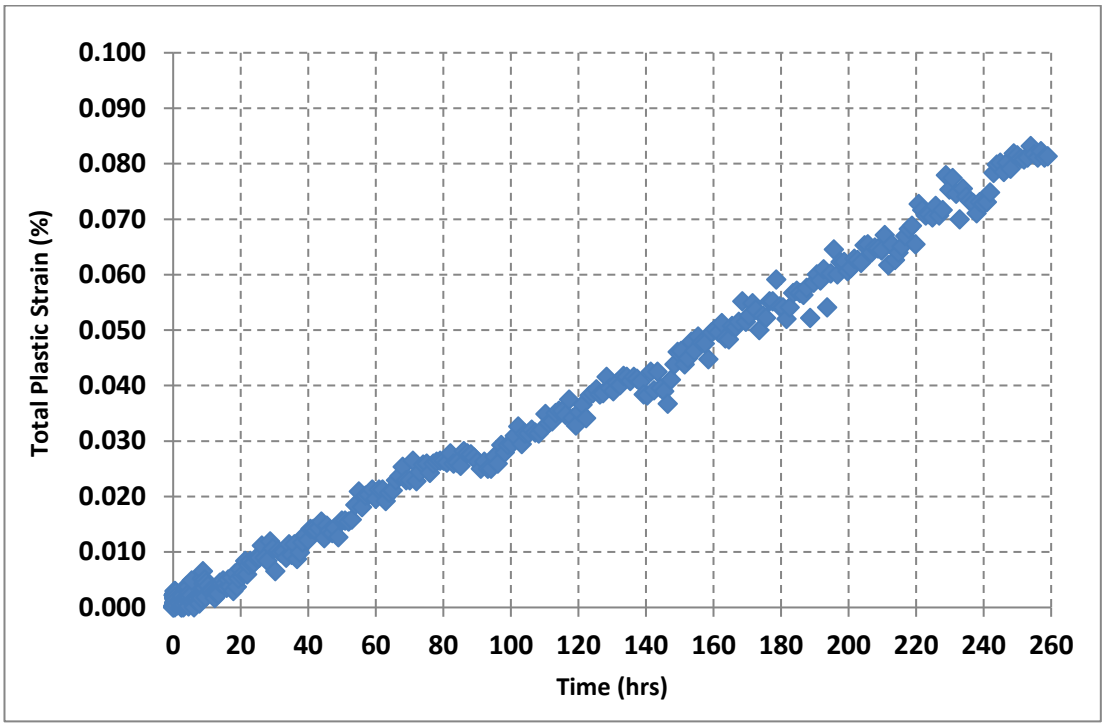

Figure 64: Total plastic strain against time for FG RR1000 at 600MPa (260 hour)

The plastic strain is approximately 0.006% at 24 hours, 0.03% at 114 hours and over 0.08% at 260 hours. It would be assumed that performing plastic deformation on a material would increase its hardness due to the introduction of dislocations; however the opposite has been seen here. It is suggested that this increase in dislocations would lead to an increase in the availability of pipe diffusion pathways which would then increase the rate of dissolution of the tertiary γ' phase, causing the decrease in the hardness of the material.

4.1.2.3 Thermo-Mechanical Oxidation Modelling

The method of modelling thermo-mechanical oxidation is more complicated than that of the thermal oxidation, due to the addition of a mechanical stress. A version of the Arrhenius relationship shown in Equation 7 is commonly used in creep modelling to determine the activation energy for creep, by including a stress component.

$$k = A \cdot \sigma^n e^{-\frac{E_A}{RT}} \quad (7)$$

Where:
k = rate constant
A = frequency factor
σ = stress
n = stress exponent
E_A = activation energy
R = gas constant
T = temperature

This equation has been operated to ascertain its applicability for use in modelling oxide growth.

The stress exponent (n) is provided as the gradient of the plot of the natural log of the reaction rate against the natural log of the stress; this can be seen in Figure 65.

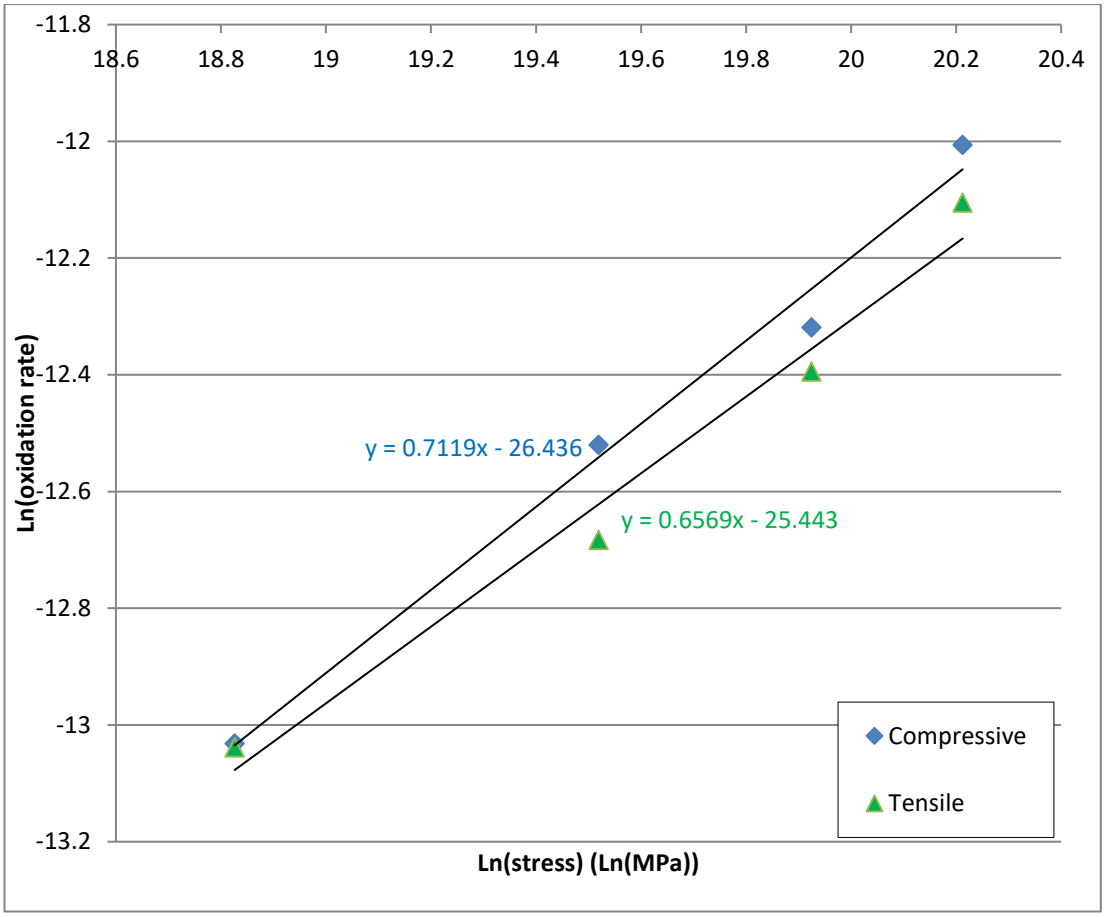

Figure 65: Plot of natural log of oxidation rate against natural log of stress to determine stress exponent

The n value is then input into Equation 7. The value of A is assumed to be the same as that found during the thermal oxidation analysis for the 700°C study, as it is a frequency factor that is temperature dependant.

Table 4: Activation energies for thermo-mechanical tests calculated using the modified Arrhenius equation

Activation energy (kJ/mol)	
Compressive	**Tensile**
365.28	356.96
365.14	357.77
365.84	357.59
364.97	356.78

The values produced through this method shown in Table 4 are considerably larger than that from the thermal oxidation analysis (258.31 kJ/mol) suggesting that the oxidation would be reduced under load, however, as was seen in Figure 60, the application of load acts to raise the oxidation rate in both compression and tension. This method is therefore not viable as a method of calculating thermo-mechanical activation energies.

A different approach was therefore pursued in an attempt to account for the applied stress. A modified version of Equation 7 was developed in order to produce an "apparent activation energy" ($E_A + U_{(r)}\sigma$) which encompasses the fundamental value of activation energy, plus a second term which is now used to determine stress dependence for the analysis; this allows for the same methodology to be used as the thermal oxidation activation energy calculations.

$$k = Ae^{-\frac{E_A + U_{(r)}\sigma}{RT}} \quad 8$$

The equation for the $U_{(r)}$ component can be seen Equation 9.

$$U(r) = U_i - \frac{A}{r^m} + \frac{B}{r^n} \quad 9$$

Where:
$U_{(r)}$ = Potential energy at distance r
U_i = Potential energy related constant
r = distance between bonded atoms
A,B = empirical constants
m,n = empirical constants where m<n

The results produced using this methodology can be seen in Figure 66.

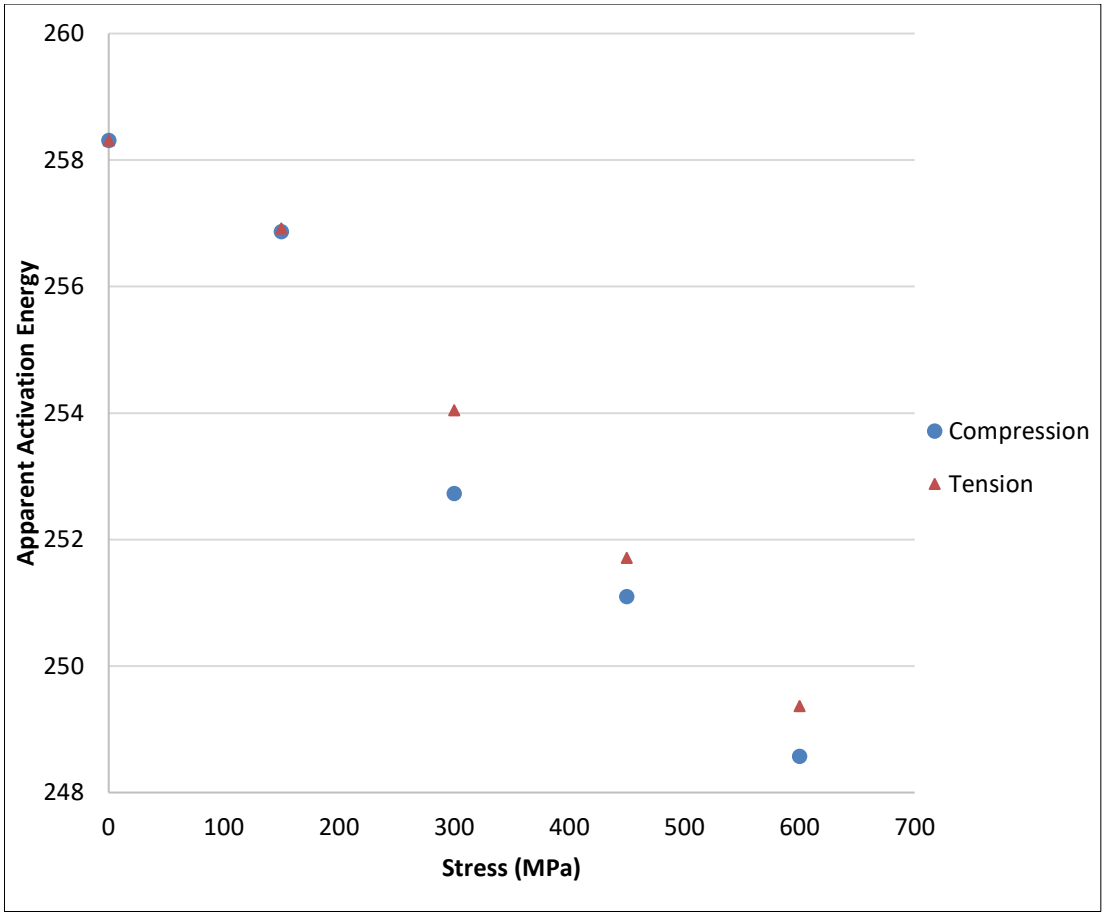

Figure 66: A graph showing the relationship between activation energy and applied stress

As can be seen there is a reduction in the apparent activation energy due to the application of load, which correlates to the increased oxidation damage seen in the specimens; this reduction does however occur over a quite small range. The simplicity of the model provides greater confidence in its applicability for use, of great importance must then be understanding the reasoning behind the change in the apparent activation energy under loading.

A number of different mechanisms studying the mechano-chemical nature of the reaction were investigated in order to determine if they would contribute to the acceleration in oxidation rate under stress and account for the potential compressive and tensile oxidation asymmetry similar to that seen in the oxidation of pure nickel [107].

The initial factor that must be considered to account for the potential oxide growth asymmetry is that there were compressive residual stresses remaining in the test pieces following machining that would act to effectively raise the applied compressive stress. As the full pedigree of these specimens is unknown, and none remain to perform further analyses, this area of investigation cannot be followed.

The next area of investigation is based on the premise that the rate of oxidation reactions is largely controlled by the rate of diffusion of ions in the substrate [14], [53]. Applying a stress to a material is widely known to increase the diffusion rates in engineering materials in the form of diffusional creep processes such as the Nabarro-Herring and Coble creep models. As was discussed in Section 2.3.1, and shown graphically in Figure 13, when the energy barrier Δg_a is met, an atom has sufficient energy to move between lattice locations, distorting the lattice. Under tension, the lattice would be favourably distorted lowering the energy required for diffusion; conversely this model would suggest that applying a compressive stress would act to reduce the rate of diffusion which is contrary to what is observed in the current results. It can therefore be assumed that this is not the rate controlling mechanism.

The area of interest that provides the most compelling evidence to explain the stress effect is that of the internal residual stresses that form in the oxide products. There are a number of theories why residual stresses may form in oxides, two of the most common of which are discussed [255]. The first is the Pilling-Bedworth or volume ratio as explained in Section 2.3.2. The theory states that if an oxide scale was able to form and remain, then it has formed in a compressive condition. If it were in a tensile state, it would have spallated, resulting in more rapid oxidation rates. The second theory is that of a lattice mismatch causing imperfect epitaxy between the oxide and the substrate, resulting in a strain between these regions. A great deal of research has been conducted over the years in order to better understand the effects of these mechanisms [256]–[258]. It has been found for the wide range alloy systems tested, no matter the type of oxide layer that formed, a net compressive stress developed [259]–[262]. This supports the hypothesis that there is an oxide growth asymmetry between the test specimens held under a compressive and a tensile stress, as the residual stress would reduce the effective applied tensile stress and increase the effective applied compressive stress of the test specimens.

An alternative approach proposed by Basoalto is that presented in the Appendix IV, which gives a theoretical analysis for modelling the parabolic growth kinetics during oxidation of this γ′ strengthened nickel-based superalloy. It is proposed that transport of oxygen ions (and therefore oxidation of the alloy) is maintained by the development of an internal stress state at the metal/ oxide interface. These stresses modify the chemical potential of oxygen ions and establish their flux from the free surface to the metal/ oxide interface. An analysis of the mechanical fields is presented that accounts for the viscoplascity of the γ/γ′ alloy as well as differences in the elastic properties of the oxide and metal. The relevant diffusion problem is solved and parabolic growth kinetics with scaling law $h \sim t^{1/2}$ is predicted, where h is the oxide scale thickness and t the elapsed time. Expressions for the apparent activation energy are derived. The applied stress is shown to influence the apparent activation energy. Furthermore, the transformation stress at the metal/oxide interface results in an asymmetric apparent activation energy with respect to loading direction, with lower apparent activation energy under compression than tension.

4.2 Fatigue

4.2.1 Pre-damaged Fatigue Testing

The results from the pre-damaged fatigue testing programme are shown in Figure 67.

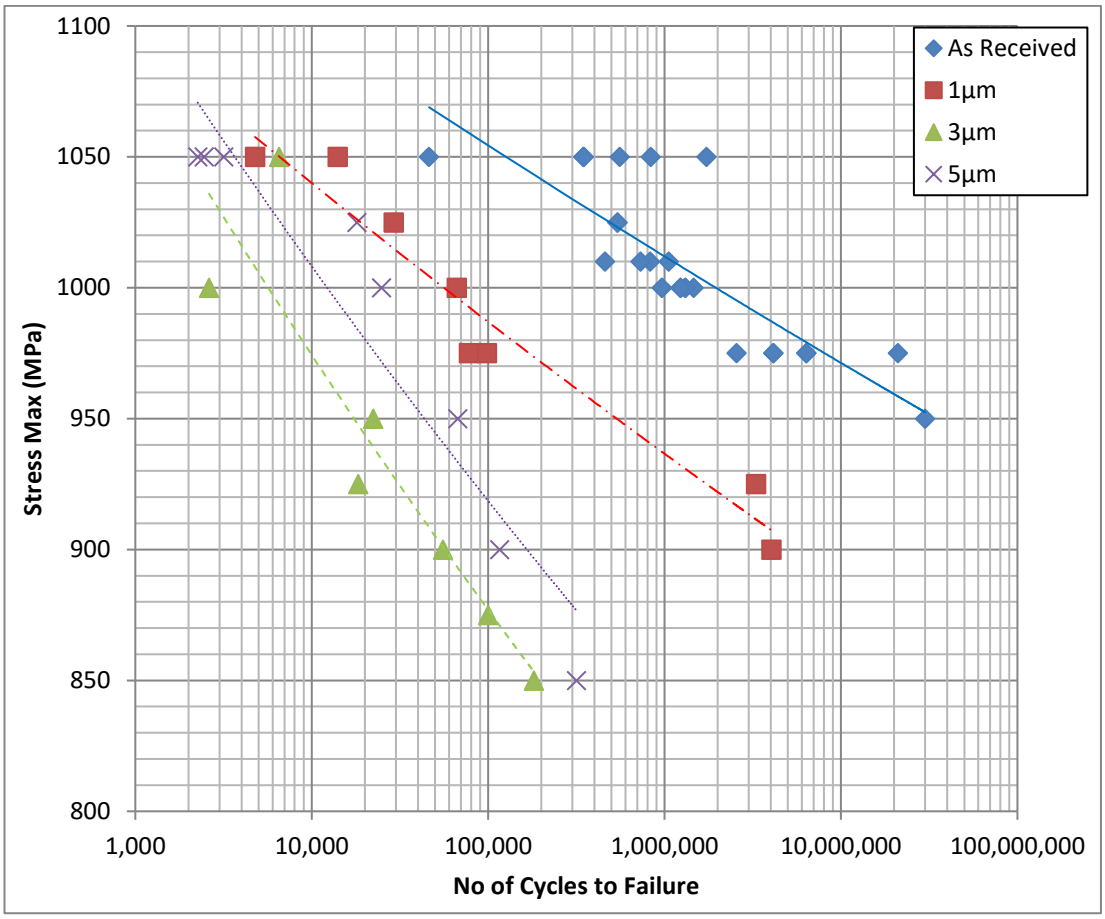

Figure 67: S-N curve for different pre-damaged plane fatigue specimens tested at 700°C

It was observed that overall, the damaging thermal exposures reduced the fatigue lives compared to that of the as received specimens, which was as expected [92], [168]. The maximum stress that was applied during this testing was based on the corresponding 'as received' fatigue testing data from RR. It can be seen however, that there is a great deal of scatter at this stress; upon investigation it was found that this was around the elastic limit of the material at the test temperature as can be seen in the stress strain curve in Figure 68.

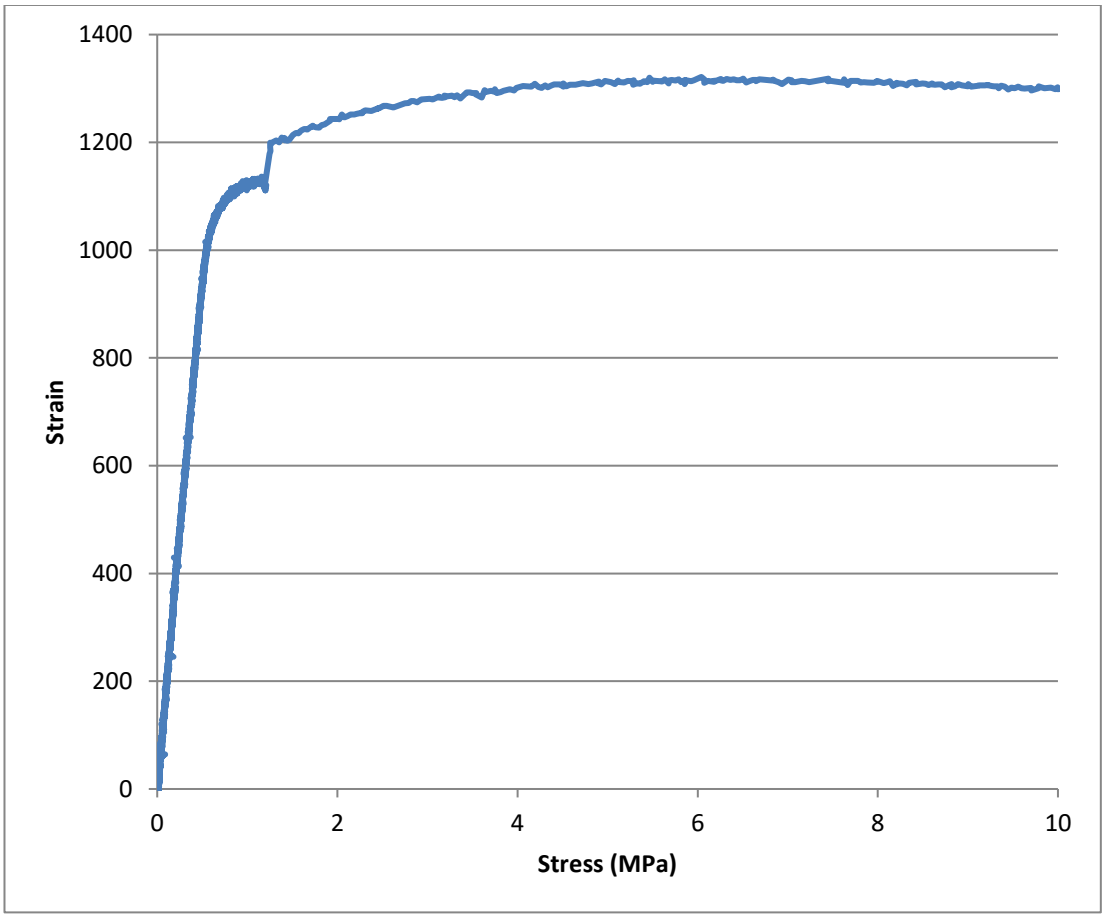

Figure 68: Stress strain response of FG RR1000 at 700°C

Under load control fatigue testing conditions, it is possible to get a large variation in the amount of plastic strain that will be applied to the specimen when loading near the yield stress of the material. This can result in a large variation in the fatigue response, therefore, the data from the fatigue testing programme was replotted without the 1050MPa tests in Figure 69. It can be seen that the data shows a better fit in this form than when the 1050MPa tests were included.

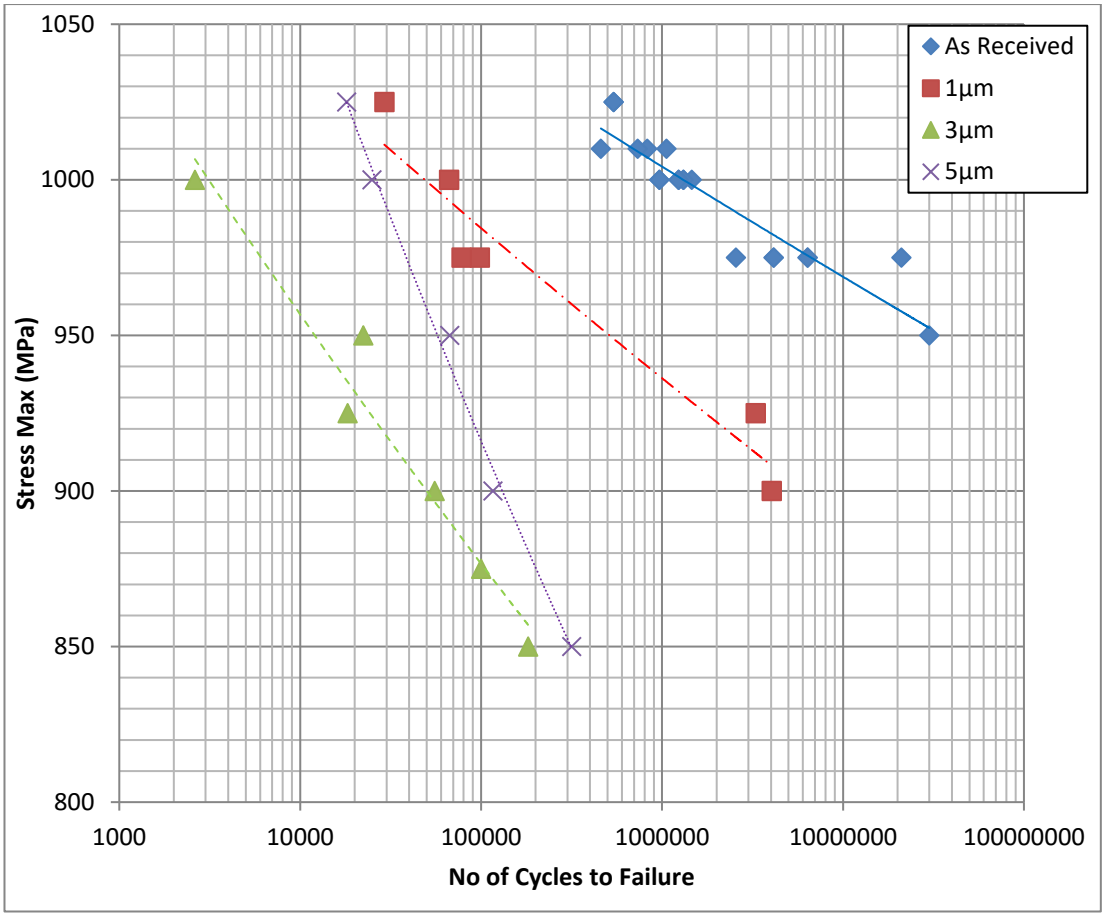

Figure 69: S-N curve for different pre-damaged plane fatigue specimens tested at 700°C without 1050MPa data

The life initially reduced for the 1µm heat treatment by over 90%, with a further drop to the 3µm of approx. 90%. It is however clear that the 5µm heat treatment surprisingly outperformed the 3µm heat treatment, lying between that and the 1µm heat treatment. It would ordinarily be expected that the increase in oxidation damage would lead to a decrease in the number of cycles to failure, as is shown to be the case from the 1µm compared to the 3µm and 5µm heat treatments. Also of interest is the difference in gradient of the S-N curves; the gradients of the S-N response for the as received material, and the 1µm and 3µm heat treatments are comparable suggesting a similar fatigue response/ mechanism. The 5µm heat treatment produced a much steeper gradient with lives at higher stresses similar to those of the 1µm heat treatment and those at the lower stresses closer to those of the 3µm heat treatment suggesting a different mechanistic response.

Investigations were undertaken based on the premise that these changes in mechanistic response and the life improvement were the result of a secondary, complementary mechanism occurring during the crack initiation or propagation stages. A number of potential causes have been investigated to determine the source of the unexpected result:

1. Change in the bulk properties of the alloy
2. Coarsening of the tertiary γ'
3. Plasticity effects due to the γ' depleted zone
4. Surface roughness effects
5. Fatigue crack growth resistance due to subsurface recrystallisation

Prior to the life change analysis, to determine the potential contributions of the initiation and propagation stages an effective initial flaw size analysis was conducted.

4.2.1.1 *Effective Initial Flaw Size Analysis*

For this analysis, crack growth data for FG RR1000 at 700°C and 1050MPa was provided by previous analyses performed by Chris Pretty as part of his doctoral thesis [263]. The data set from this provides the values for C & m for Equation 4 which can be found in Section 3.2.3. The initial flaw size is assumed to be that of the oxidation heat treatment and the final flaw size is measured from the fracture surface of the fractured fatigue specimen; an example can be seen in Figure 70.

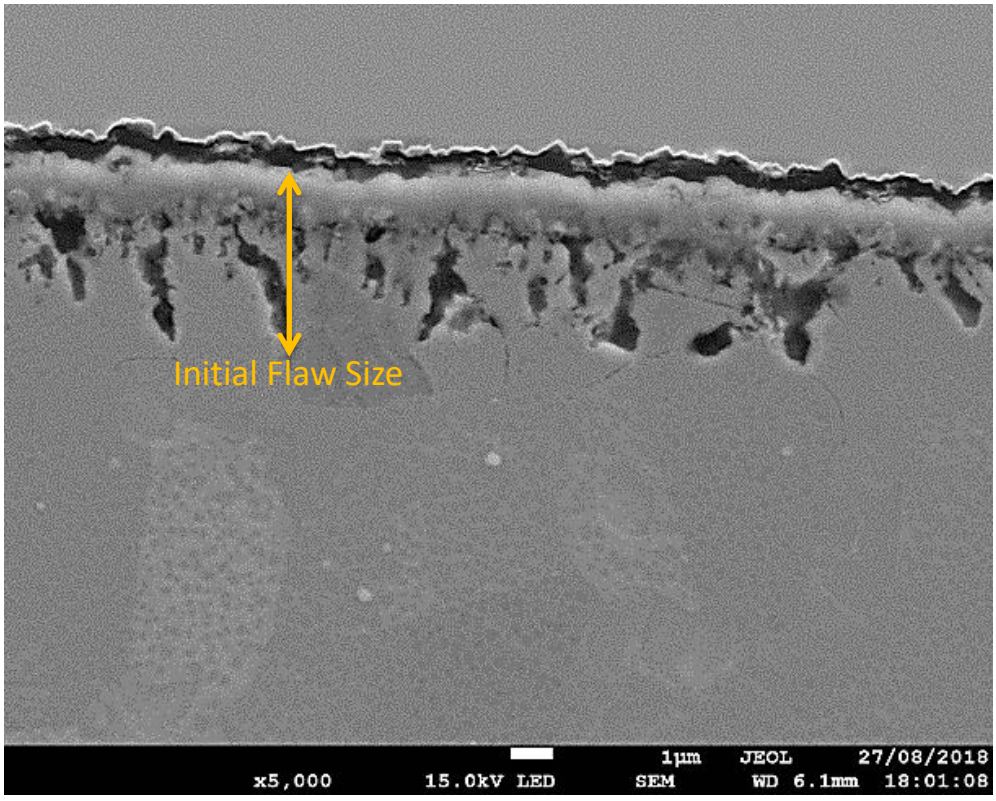

Figure 70: Thermally exposed specimen indicating 5µm oxide flaw used for analysis

The geometry factor can be determined from the experimental data using Equation 10.

$$K_I = Y\,\Delta\sigma\,\sqrt{\pi a} \qquad 10$$

Where:

K_I = stress intensity factor

The results from the effective initial flaw size analysis (EIFS) compared to the actual experimental values can be seen in Table 5.

Table 5: Comparison of actual fatigue lives and predicted lives based on Paris law propagation prediction

Damage Depth (µm)	Actual Life Cycles	Predicted Crack Propagation Cycles	Ratio Predicted: Actual
1	14023	1266	0.09
3	6524	774	0.12
5	3170	622	0.20

For these calculations it can be seen that the actual life cycles data used for the 5µm is lower than that of the 3µm. This is due to the large scatter in the data (explained in Section 4.2.1) when testing near the material yield point. It was necessary to use the data at these test conditions as this was the only crack growth data available from a previous test programme that corresponded to the work completed.

As can be seen there is a considerable disparity between the predicted results and the actual results suggesting that even with the prior oxidation damage, a large portion of the fatigue life is the initiation stage. The ratio of the actual to predicted life decreases as the heat treatment length increases suggesting that as the damage depth increases, fatigue cracks initiate more rapidly as would be expected.

4.2.1.2 Life Change Analyses

Initially, small punch tensile tests were performed to determine if the different heat treatments resulted in a change in the mechanical properties of the bulk material away from any surface effects. The results can be seen in Figure 71.

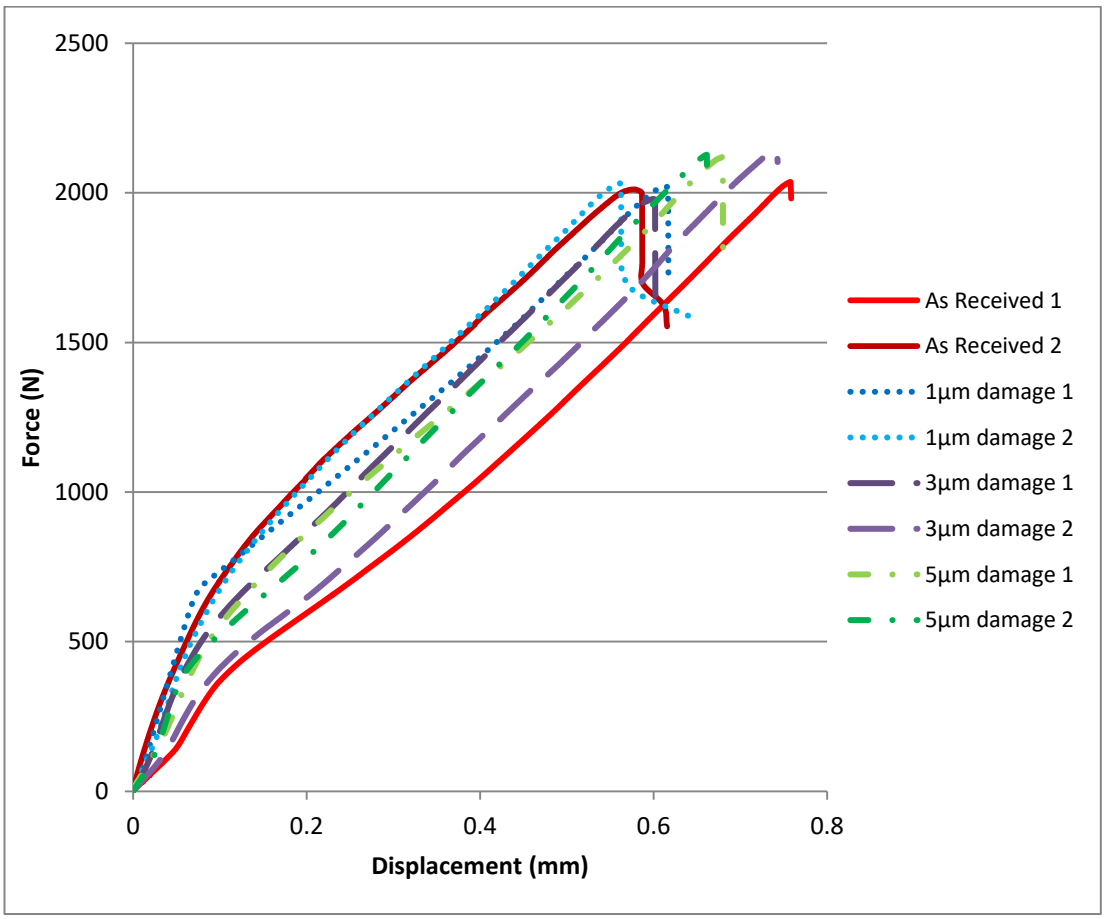

Figure 71: Small punch tensile curve for the heat treated conditions and as received material

As can be seen there is no discernible difference in the small punch tensile response of the material after any of the heat treatments. Fractography was performed on the specimens to determine if there was a difference in the fracture response caused by the heat treatments. The results can be seen in Figure 72.

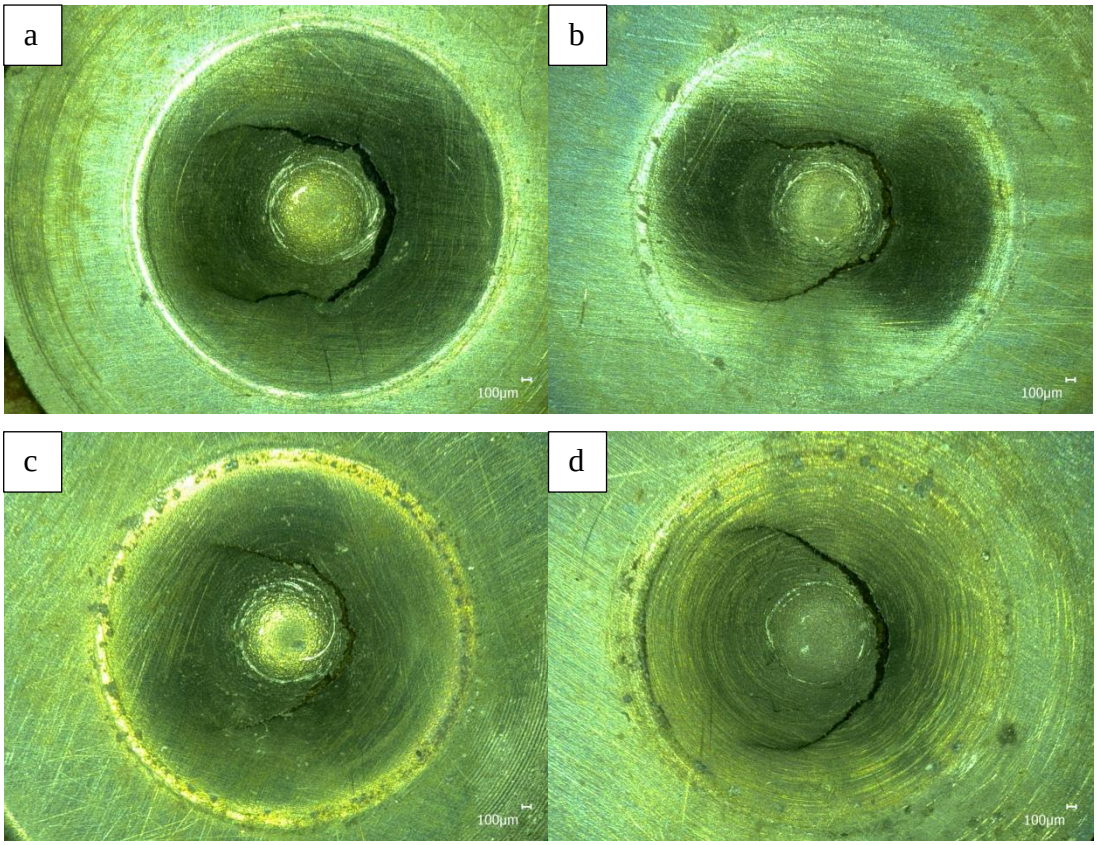

Figure 72: Fractographs of small punch tensile specimens a) as received b) 1µm damage c) 3µm damage and d) 5µm damage

The fractographs show similar fracture responses; there is a ductile response from all heat treatments with a large amount of plastic deformation, with a crack initiating away from the centre of the punch causing tearing and lifting of a flap. This can clearly be seen in the 3D micrograph of an as received specimen post-test shown in Figure 73.

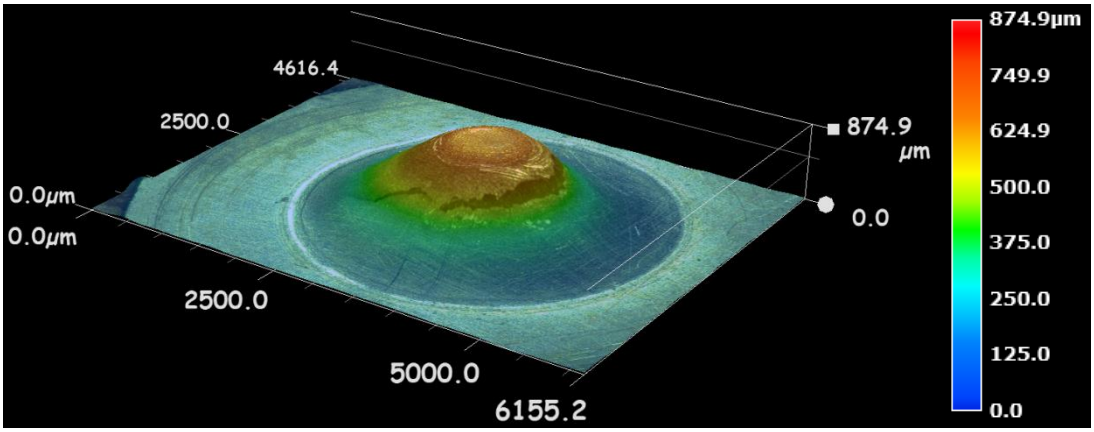

Figure 73: 3D representation of a fractured small punch tensile specimen

The next investigation conducted was into the possibility of coarsening of the tertiary γ' precipitates. As mentioned previously, the alloy contains a high percentage of the γ' phase. Secondary and tertiary γ' act to impede the movement of dislocations and retard fatigue crack growth, improving both the initiation and propagation resistance of a material.

It has been shown by Schulz et al. [264] that at elevated temperatures the small tertiary γ' within the gamma matrix may coarsen; it has long been known that precipitate size has an effect on the fatigue crack growth rates of a material. Two methods were employed to investigate this hypothesis; fatigue tests following vacuum furnace exposures and tertiary γ' measurements using TEM micrographs.

The fatigue tests were performed following thermal exposure using a vacuum furnace according to the heat treatment regimes in Appendix I. It was believed that by using a vacuum furnace, it would be possible to encourage any microstructural changes within the bulk of the specimen while halting the formation of the oxides. Had any discernible level of tertiary γ' coarsening occurred it would be expected that the fatigue lives of the vacuum furnace exposed specimens should have longer lives than the as received specimens, and the specimens that underwent longer heat treatments i.e. 5µm heat treatment specimens should have longer lives compared to the other pre-exposed specimens.

Table 6: A table showing the average fatigue lives of test performed post vacuum heat treatment compared to AR data

DHT	Average no of cycles to failure	SD	Min cycles	Max cycles
As received	426288	261411	46223	835802
1µm	279944	-	-	-
3µm	171102	-	-	-
5µm	193383	-	-	-

At a first glance of Table 6 it would seem as though the average failure lives of the thermally exposed specimens are considerably shorter than the AR specimen, however, all the lives lie within 1 standard deviation of the AR data making it statistically irrelevant. It is believe the large scatter that occurs at the stress is due to the issues when performing fatigue loading close to the yield of a material as discussed in Section 4.2.1. The issues with the test stress being near the yield did not become apparent until after these tests had been completed.

Due to the potential inaccuracies with the previous method and to ensure that any increase in life that may have been produced by tertiary γ' coarsening was not being reduced through some other means i.e. life reduction through another mechanism, transmission electron microscopy (TEM) imaging was conducted to measure the tertiary γ' in an as received specimen and in a specimen that had undergone a 5µm heat treatment. An example of an image used for the measurements can be seen in Figure 74.

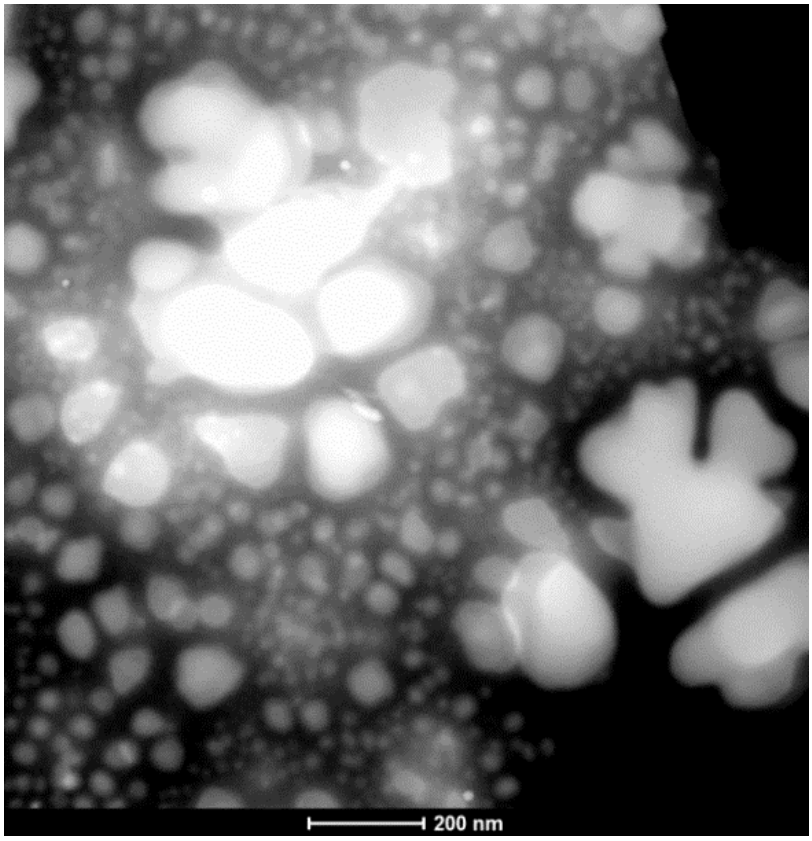

Figure 74: TEM micrograph of secondary and tertiary γ' in an as received specimen

The results from the measurements of the tertiary γ' are shown in Table 7.

Table 7: Tertiary γ' measurements for specimens in 2 heat treatment conditions

	Average Tertiary γ' Size (nm)	Standard Deviation
As received	28	10.1
5µm Heat Treatment	29	9.9

As can be seen, there is no statistical difference between the γ' size values of the 2 heat treatments. Upon further examination, when comparing these values to an existing tertiary γ' growth model from RR is became apparent that the measurements taken were considerably too large and did not conform to a pattern previously seen by RR. This is likely due to a number of factors, firstly, an insufficient number of sample

images were used. Secondly, the resolution was not deemed high enough for this type of analysis. Lastly, there was believed to be a difference in the thresholding values used in the analysis; this is a common issue in the quantification of γ' between 2 different sources. The RR tertiary γ' growth model is a predictive model based on the Ostwald ripening process and was populated with an extensive database of tertiary γ' sizes following exposures at a range of times and temperatures, with imaging performed on a TEM. The output values from the model for average size of tertiary γ' for each of the heat treatment conditions can be seen in Table 8.

Table 8: Tertiary γ' measurements for thermally exposed specimens from RR predictive model

	Average Tertiary γ' Size (nm)
As received	15
1µm Heat Treatment	16
3µm Heat Treatment	30
5µm Heat Treatment	44

These changes in the tertiary γ' size are likely to have dramatically affected the creep response of the alloy, therefore affecting the time dependant fatigue characteristics of the specimens [265], [266]. Furthermore, in the case of the load control tests conducted at stresses near to the yield point of the material, it is also possible that microstructural changes may have altered the yield stress of the material, resulting in reduced plastic strain on loading, and hence increasing fatigue life.

The next area of research interest was highlighted by work performed by Elber [267], [268], which suggests that an increase in the plasticity of a material, can lead to a decrease in the rate of fatigue crack growth due to the mechanism of plasticity-induced crack closure [269]. It is believed that the γ' depleted zone of the alloy after oxidation will have increased ductility, leading to an increase in the plasticity of the region and that this would result in an increase in the effect of plasticity-induced crack closure and therefore an increase in fatigue life. Plasticity induced crack closure may produce

a reduction in the effective stress intensity range during crack growth, hence lowering the crack growth rate and increasing fatigue life. However, as this is a crack propagation mechanism, this may not have a significant contribution on the overall fatigue life, based on the findings of the EIFS calculations. In order to investigate the existence of this plastic zone, Accelerated Property Mapping (XPM) was undertaken in the oxidation region, the benefits of which were explained by Hintsala et al. [252].

A scanning probe micrography (SPM) micrograph of the XPM tested area with the indentations shown can be seen in Figure 75.

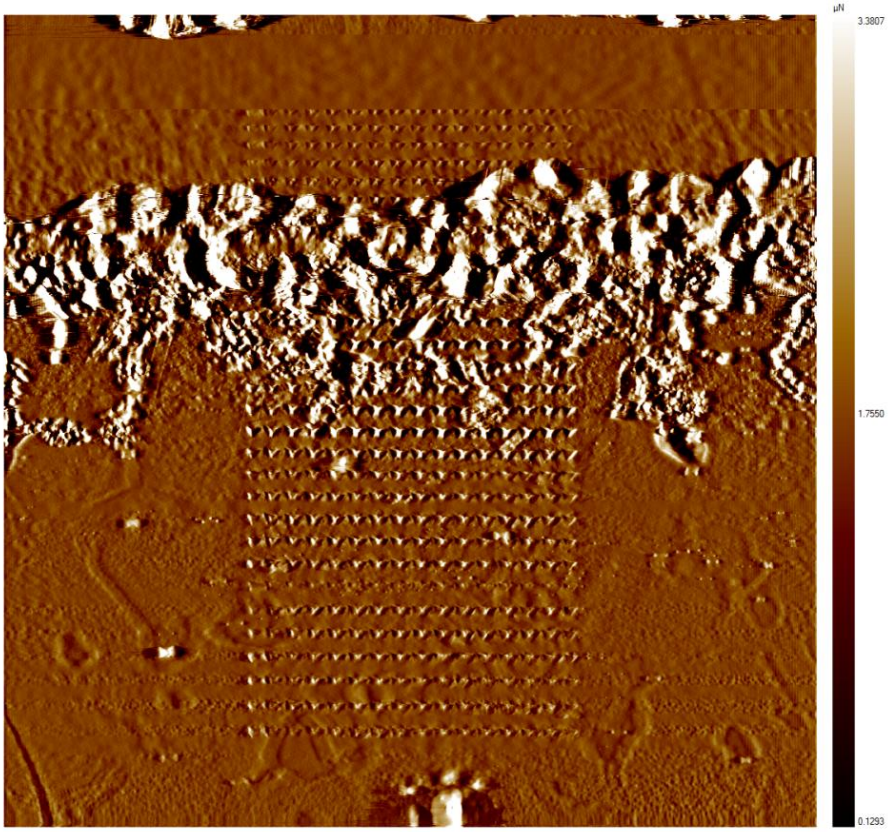

Figure 75: SPM micrograph of the XPM scanned area

The heat map from the XPM analysis can be seen in Figure 76.

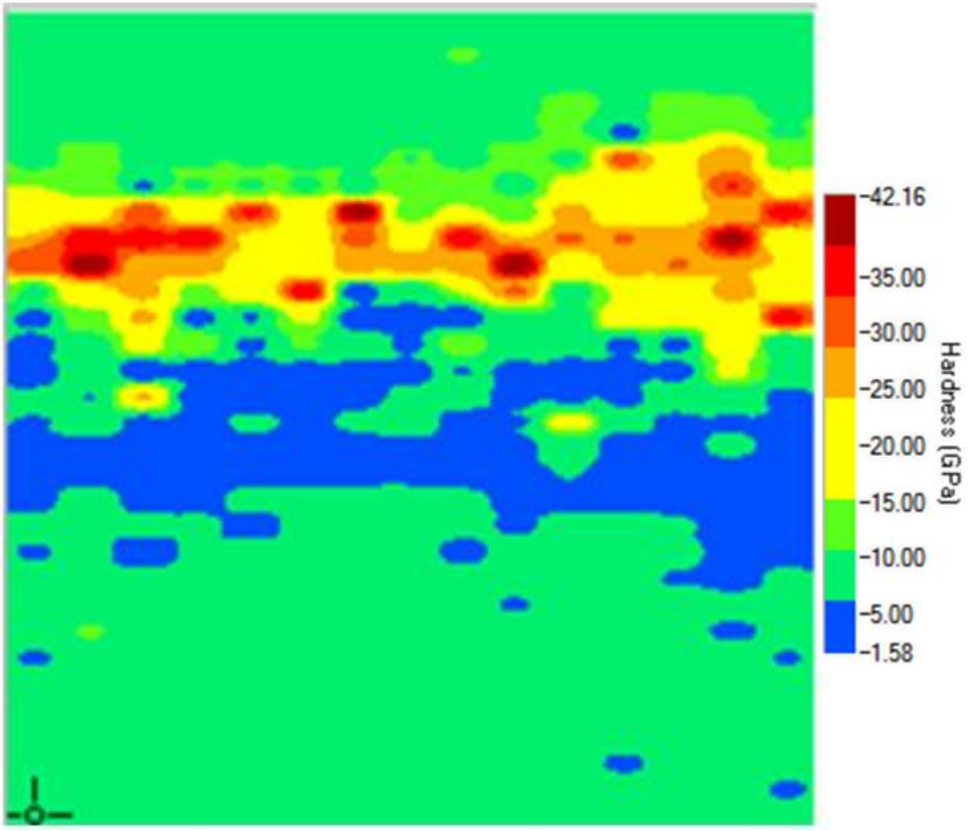

Figure 76: XPM of the oxides, γ' depleted zone and substrate of 5µm thermally exposed specimen with legend

As can be seen there are distinctly different hardness layers across the surface of the specimen. This correlates clearly to the composition that occurs after the oxidation reaction at the surface, as can be seen in the SEM micrograph in Figure 77.

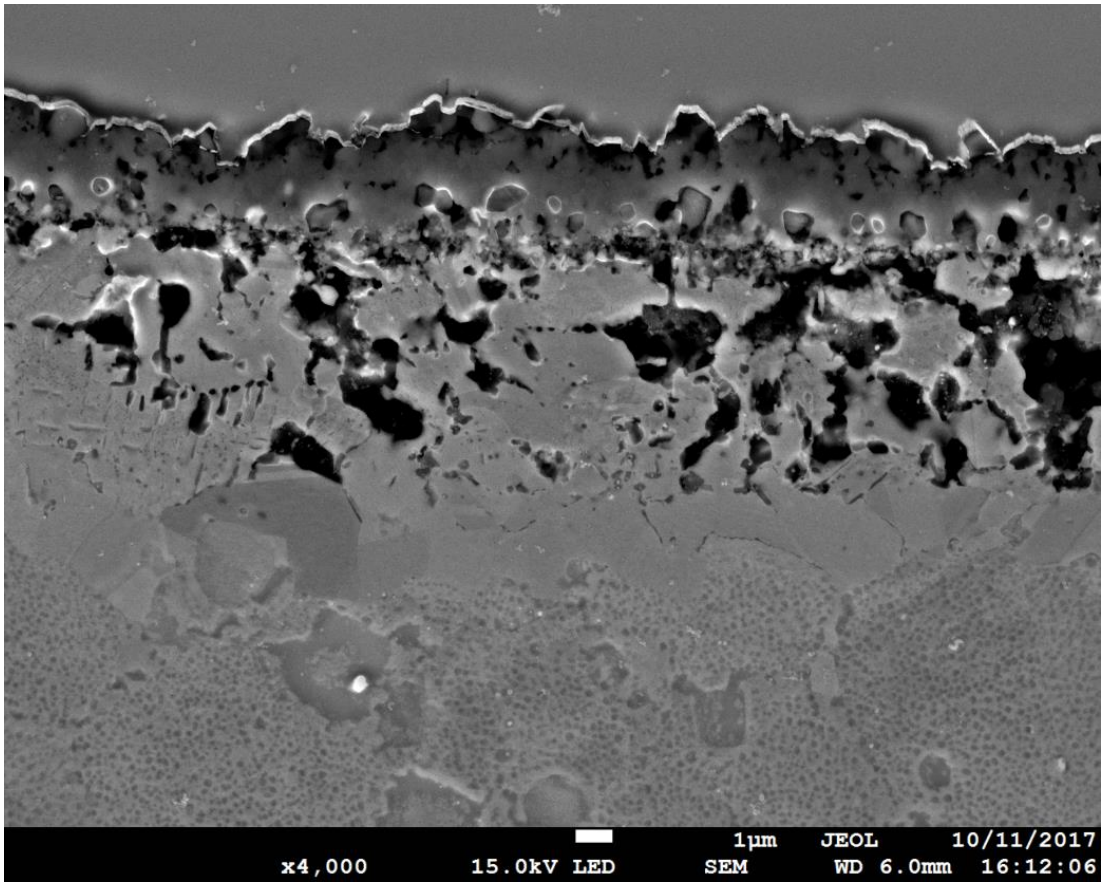

Figure 77: SEM micrograph of surface oxides and evident γ' depleted zone

It is difficult to assign a specific mechanism which results in the increase in fatigue life of the 5µm specimens, compared with 3µm. However, it is possible that the interaction between the alumina fingers and the γ' depleted zone may play a role. As is apparent in Figure 76, there is a dramatic change in the hardness values between the ceramic oxides at the surface and the γ' depleted zone with the base material hardness values sitting between these two extremes. The γ' depleted zone was found to be deeper for longer thermal exposures. It is therefore possible that the reduced hardness of this γ' depleted zone acts to reduce the effectiveness of the crack initiation mechanism from the alumina fingers, hence increasing the fatigue life.

An area of research that shows potential in explaining the increase in fatigue life for the more highly damaged specimens is that of crack tip shielding due to the presence of an interface perpendicular to the direction of growth of the crack. This has been investigated extensively [270]–[272], and it was found that when moving from a

material of lower hardness to a material of greater hardness, there would be a retardation in the crack growth rate [178], [273]. Mechanistically there are three potential events that can lead to an improved fatigue life; 1) crack tip blunting as the crack moves into the γ' depleted zone, 2) relaxation of the crack tip stresses in the γ' depleted zone, and 3) propagation of a crack through the barrier of the γ' depleted zone into the as received material will lead to another barrier to crack growth.

In order to provide meaningful data to the engineering community at large it is important to relate the results from the XPM to a more known method. It is possible to approximate the H_v values from the XPM output using Equation 11.

$$Hardness_{Vickers} \times 0.009807 \approx Hardness\ (GPa) \qquad 11$$

The data from the hardness tests is shown in Table 9. The nanoindentation values are taken from the colour contour brackets on the XPM legend. The formula output represents the values calculated from Equation 11 and some microhardness tests which were performed on the areas that were able to be tested using the microhardness tester in order to validate the equation. As can be seen by the comparison between Equation 11 output and the microhardness values, there is a reasonable correlation, although it should not be relied too greatly upon.

Table 9: Nanohardness, microhardness and calculated values of oxide and sub-oxide regions

Location	**Nanoindentation, GPa**	**Equation 11 Output, H_v**	**Micro hardness, H_v**
Oxides	15 – 42	1529.5 – 4282.7	1652.7 – 3508.2
γ' depleted zone	1 - 5	102.0 – 509.8	-
Base alloy	5-10	509.8 – 1019.7	483.24

As part of another analysis, EDS mapping was performed in a TEM, on the oxide subsurface region, the finding of which further supports the nanoindenter research. Some interesting results were found that were not before evident from EDS scans using either the tungsten filament SEM or FEG SEM. This is believed to be the case due to the higher resolution available by the TEM. The result can be seen in Figure 78.

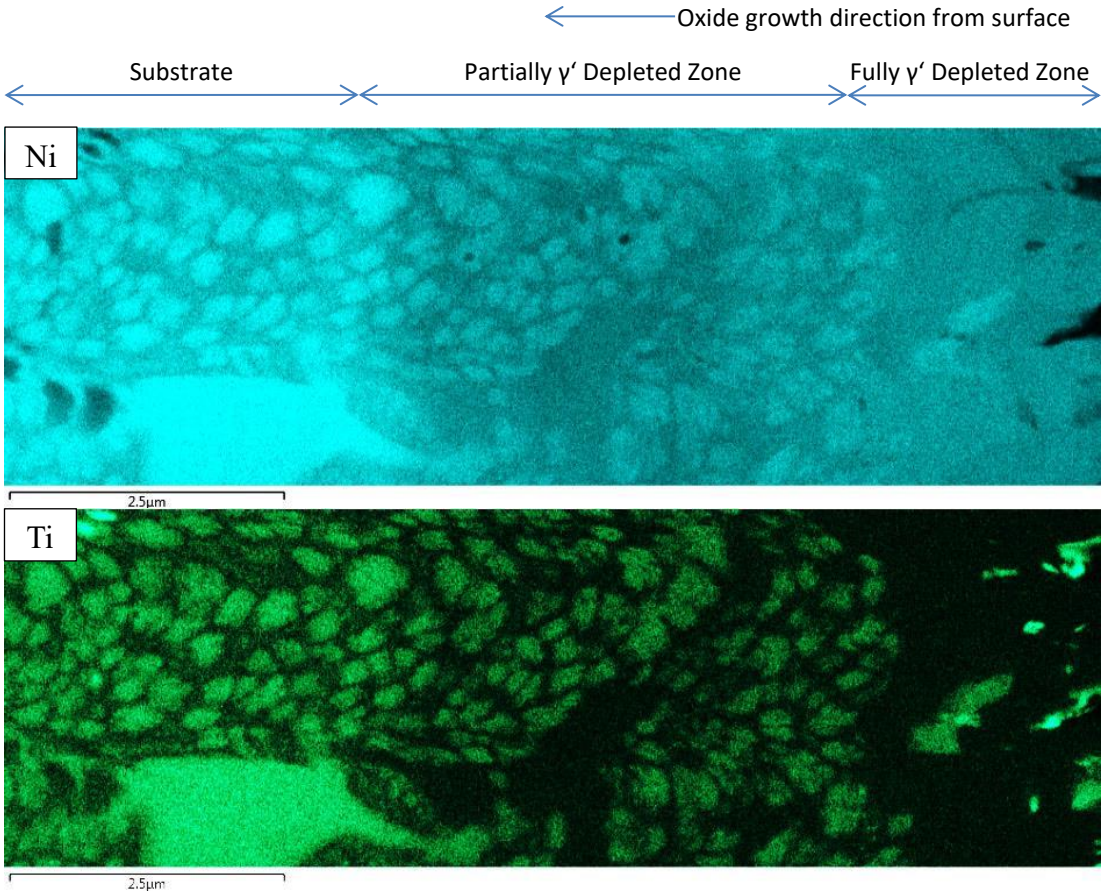

Figure 78: TEM EDS maps of oxide and sub-oxide layers

As is evident from the EDS analysis, there is a fully γ' depleted zone as has been seen in previous research. Of more interest is the apparent presence of a partially γ' depleted zone as is indicated by the change in concentration of the γ' elements at a distance further from the surface. It is evident from the EDS scan that the small tertiary γ' precipitates have been depleted from this region. The earlier dissolution of the tertiary γ' is supported by the precipitation characteristics of tri-modal γ'; tertiary is the last to

form on cooling at around 900°C whilst secondary will precipitate at a substantially higher temperature of approximately 1050°C.

To determine if surface roughness changes due to thermal exposure may play a role in the fatigue lives, heat treatments were conducted on peened flat plates and surface roughness values were measured. A graphical representation of the profilometer data that is used to calculate the S_a value for the as received specimen is shown in Figure 79.

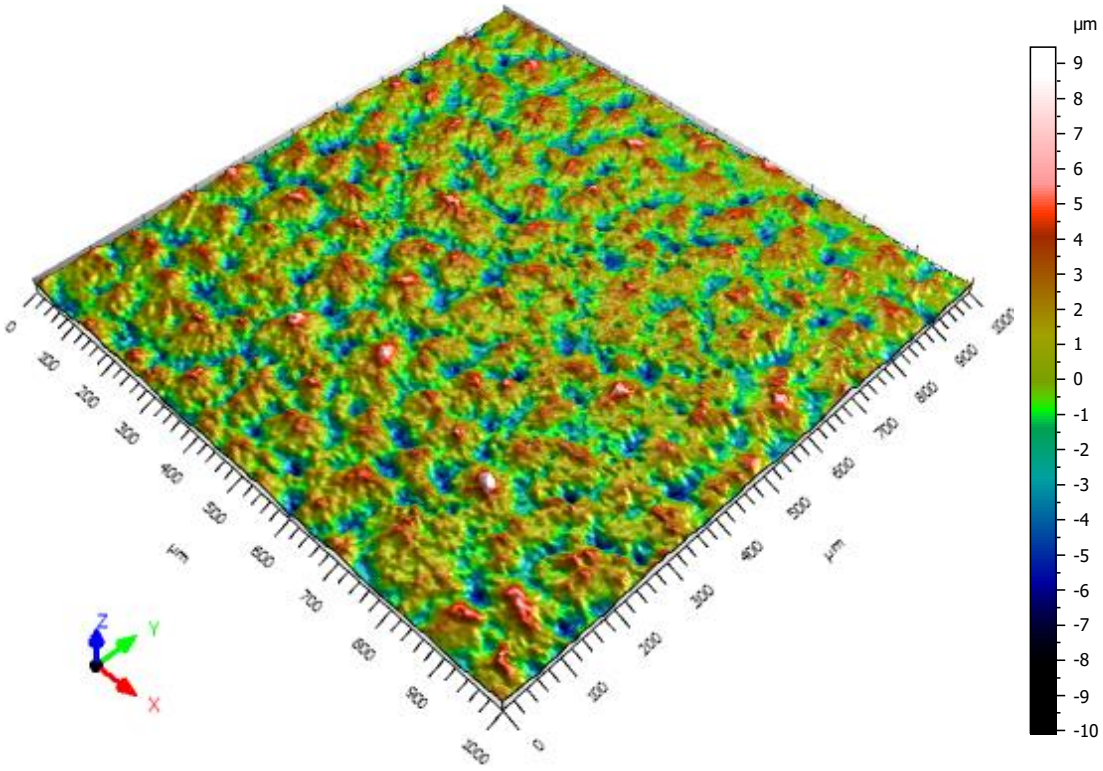

Figure 79: Profilometry map for AR peened specimen from Nanovea

The S_a values for the analysis conducted using the Nanovea are shown in Table 10.

Table 10: S_a surface roughness values produced by the Nanovea

Thermal Exposure	S_a Value (µm)
As Received	1.686
1 µm	0.274
3 µm	0.162
5 µm	0.121

As can be seen this data shows a dramatic change in the S_a between the as received specimen and the heat treated specimens. When investigating the experimental procedure of the Nanovea it became apparent that there were issues with the scan as can be seen in Figure 80.

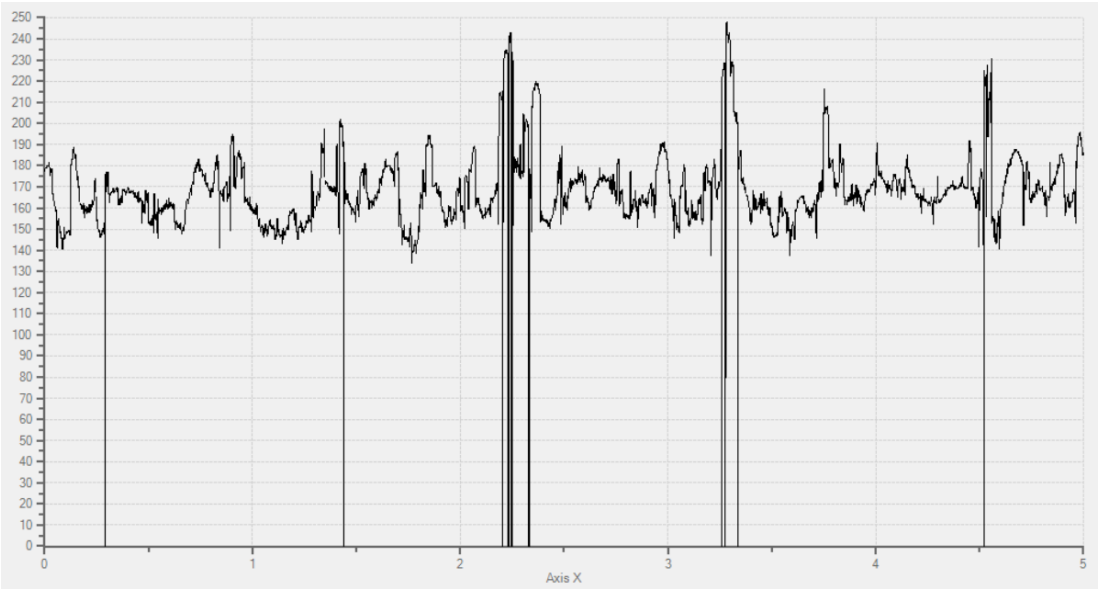

Figure 80: A line of Nanovea profilometer scan data

The Nanovea uses a raster scan system and shown is the output from a single line scan. The y axis shows a measure of the depth measured by the system; as can be seen, in many places the depth reads as 0. This is classed as a ‘dropout’ of the signal and is caused by scatter of the light, meaning no depth is measured for that location on the

specimens. For this reason, another method of surface roughness evaluation was deemed necessary.

The alternative equipment used was an Alicona Infinite Focus microscope; an example of a height profile map that is produced by the equipment is shown in Figure 81.

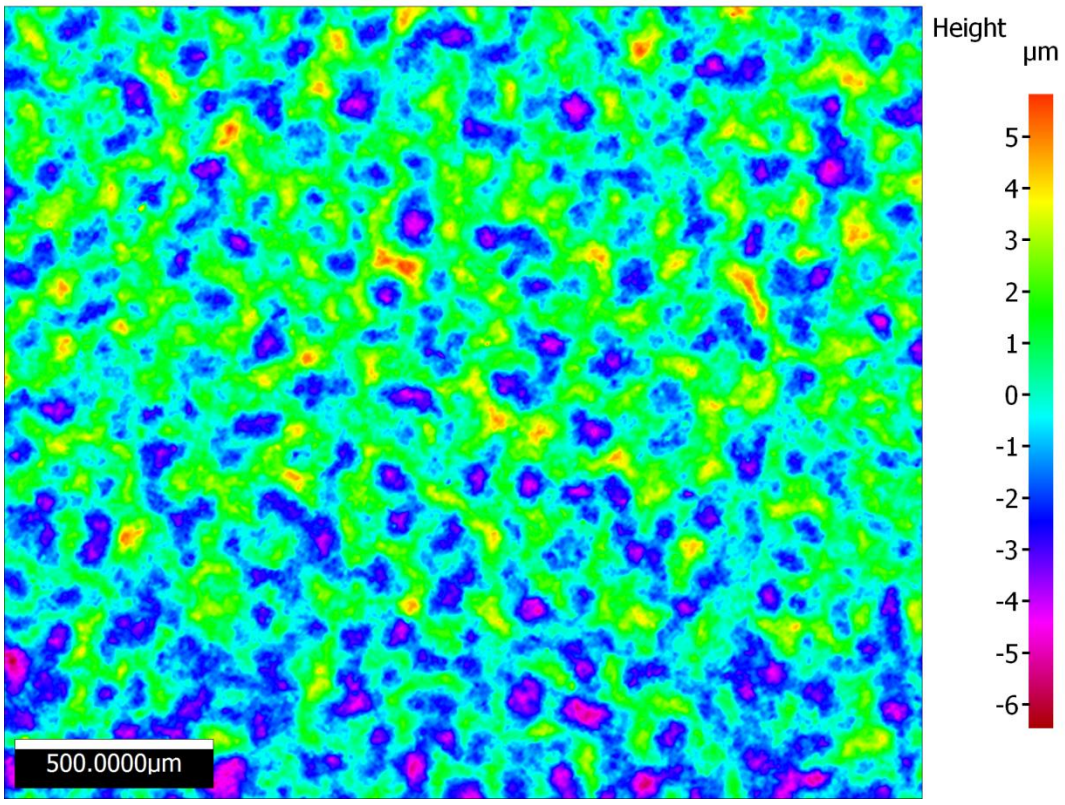

Figure 81: Surface height map for AR peened specimen from Alicona

A useful function of the software that controls the Alicona system, is the presentation of a histogram with the scan data as can be seen in Figure 82. The values presented in the histogram are of little importance, however, the near normal distribution is as would be expected for this kind of data set and provides confidence in the validity of the output.

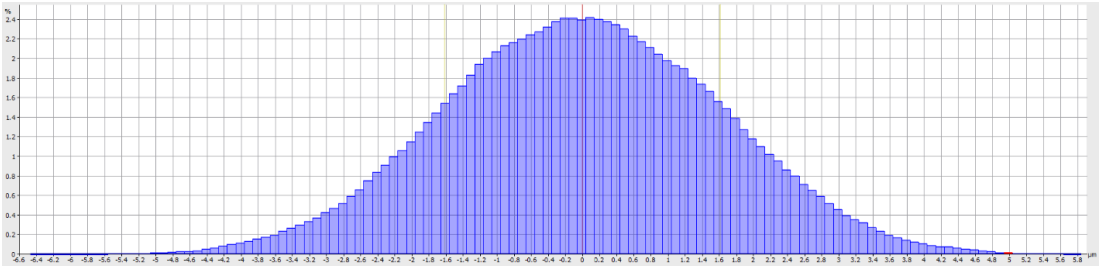

Figure 82: Histogram of data depth readings from Alicona

The S_a surface roughness values for the Alicona are shown in Table 11.

Table 11: S_a surface roughness values produced by the Alicona

Thermal Exposure	S_a Value (µm)
As Received	1.353
1 µm	1.328
3 µm	1.308
5 µm	1.277

As can be seen, the increased oxidation will act to reduce the surface roughness, supporting the hypothesis and the decrease in the S_a may link to the increased fatigue life of the 5µm thermally exposed specimens. However, the reduction in surface roughness corresponds directly to the length of the thermal exposure, suggesting that if an improvement were to occur only as a result of the surface condition it would occur for all the thermal exposure conditions to some extent.

The final area of study undertaken was based on research following a further literature study. In some nickel superalloys a recrystallised zone is present below the oxides formed at peened surfaces; this is especially true in coarse grained materials, but is still true in materials of grain size similar to FG RR1000. To determine if a recrystallised layer is present, initial FEG SEM imaging was conducted as can be seen in Figure 77.

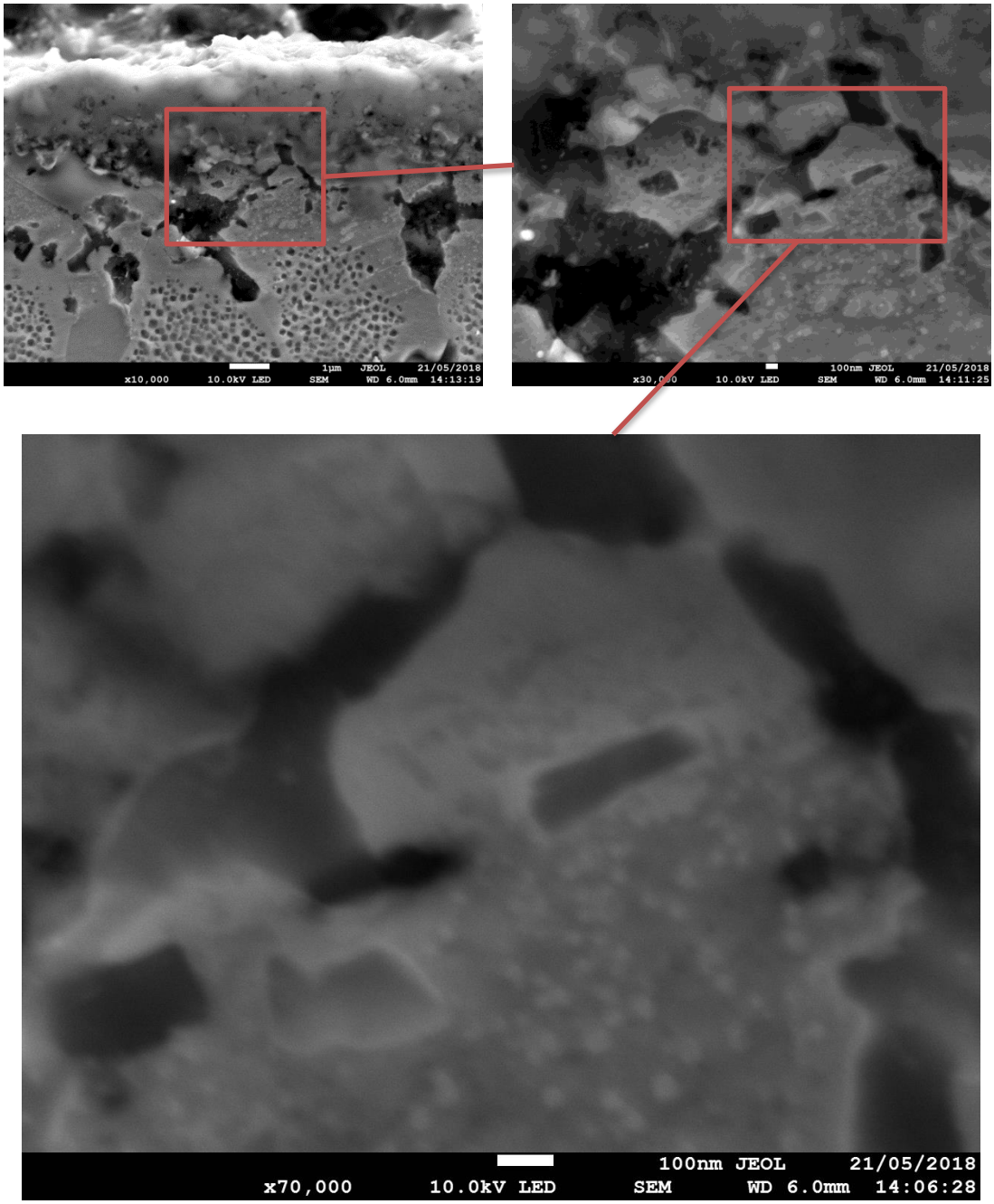

Figure 83: SEM images to determine the presence of a recrystallised zone

As can be seen from this initial analysis, there is some evidence of microstructural change within the area around the aluminium oxide fingers. However, it is difficult to resolve the microstructure without etching, and etching causes too much damage to the oxide and surrounding area, resulting in unusable images. It was however decided from this analysis that there was enough evidence of the potential presence of recrystallisation to warrant further analysis using a higher magnification method; to this end, Transmission Kikuchi Diffraction (TKD) was performed on the area shown as Map Data 3 in the micrograph shown in Figure 84.

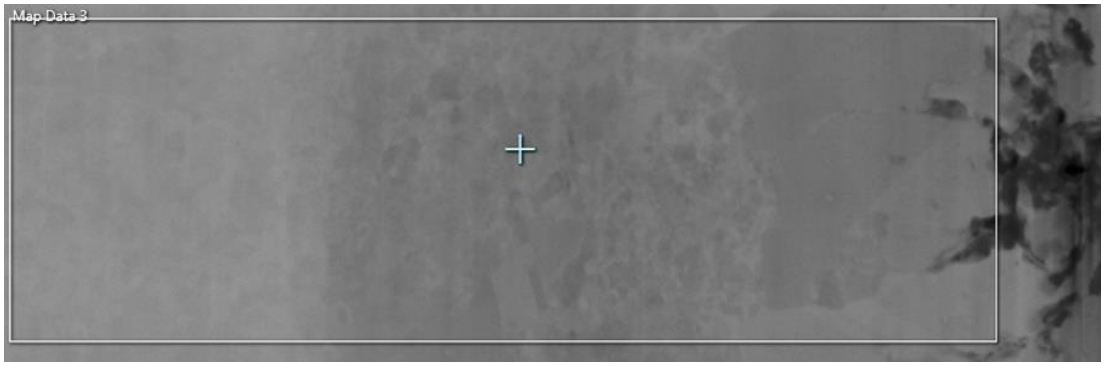

Figure 84: Micrograph showing the location of the TKD scan

The TKD data is shown in Figure 85; band contrast and inverse pole figure (IPF) Z maps have been discussed below.

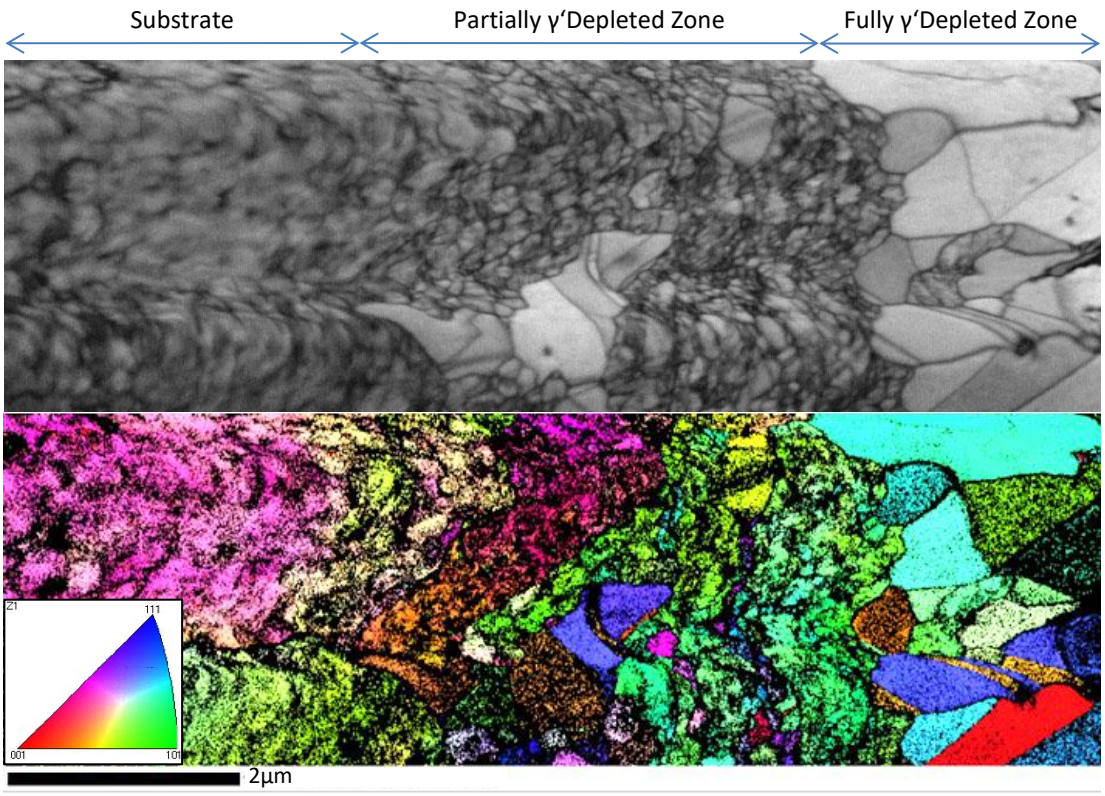

Figure 85: TKD IPF maps data (top) band contrast (bottom) IPF Z

The reason for the low indexing of the TKD scan is because the grains are so small that there is interaction between multiple grains through the thickness of the foil, giving overlapping Kikuchi bands. This means there is not a clear pattern for the system to resolve. The data is however useful, as it is possible to see that there are grains in the partially γ' depleted zone that are clearly smaller than the 4-11µm prior grain size. It would appear that within the partially γ' depleted zone there are a number of very small grains or structures. To support the TKD, high magnification TEM imaging was undertaken in this region in order to more clearly display these small grains/ structures.

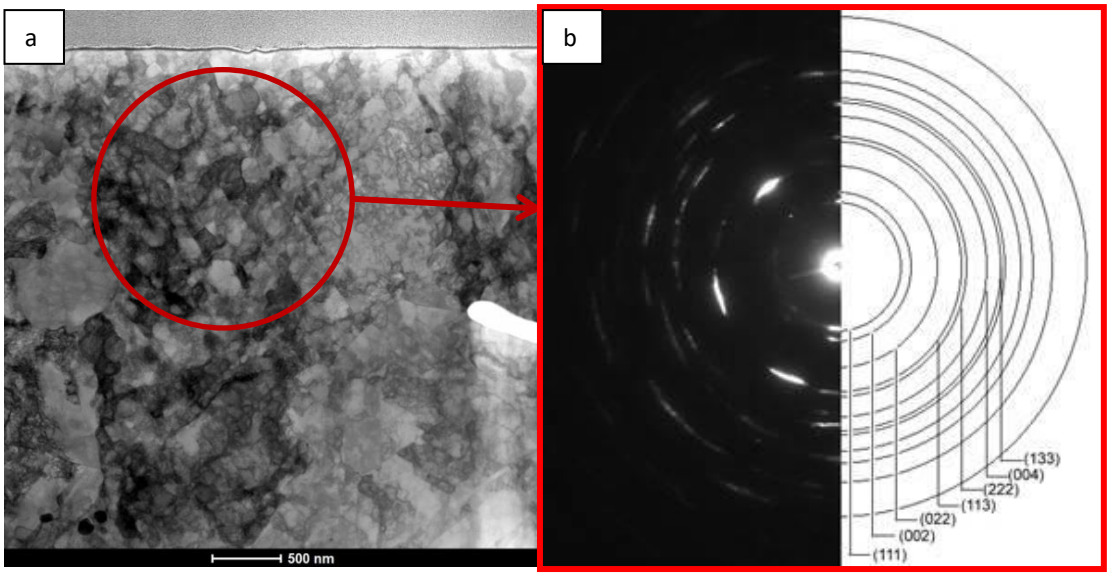

Figure 86: (a) STEM of partially γ' recrystallised zone (b) SAD pattern from the marked area

It can be seen from Figure 86 (a) that there is a very fine grain structure in the partially γ' depleted recrystallised zone. Figure 86 (b) shows a Selected Area Diffraction (SAD) pattern from the circled area shown in Figure 86 (a), this area is polycrystalline with a strong texture (e.g. {011}<211> brass texture). The formation of surface oxides will produce strain subsurface of the alloy, which promotes deformation of the subsurface via dislocation slip and/or twinning. When the deformation is large enough, it may lead to the formation of new grains with a smaller size. If those refined grains were evolved from a prior grain and not completely recrystallized, the grains would show a strong texture which is related to the prior grain. This confirms that there is a complex grain structure of very small grains in this partially γ' recrystallised zone. Research performed by Turnbull and De Los Rios found that reducing the grain size of their material reduced the crack growth rate in the microstructurally small crack regime [274]. They reasoned that this was because the distance a crack extends per cycle is related to the crack tip plastic displacement. By refining the grain size, the slip length ahead of the crack tip is limited, reducing the crack tip plastic displacement accordingly. However, the effect this will have on the fatigue properties of the alloy will be very complex due to the changes in grain size as well as variations in γ' particle size and distribution compared to the bulk material.

The work conducted during the life change analysis can be separated into 2 categories:

- Mechanisms that have no effect:
    - There is no change in the bulk mechanical properties i.e. tensile properties, as a result of the heat treatments.
- Possible life improvement contributing effect:
    - Utilising a tertiary γ' coarsening model developed by RR, it can be determined that coarsening of the tertiary γ' is occurring due to the 3µm thermal exposure and dramatically as a result 5µm thermal exposures. This change in the γ' size will likely have a dramatic effect on the creep response, and as a result, the time dependant fatigue response of the alloy. These microstructural changes will also likely affect the fatigue properties of the tests conducted near the yield point.
    - Nanoindentation found a dramatic change in the plastic properties of the oxide layers, the fully γ' depleted zone and the bulk material. This will likely lead to a mechanism of crack tip shielding as a result of the crack growing perpendicular to a soft-hard interface of the γ' depleted zone and the bulk material.
    - The surface roughness decreases with increasing length of thermal exposure and it is hypothesised that this is due to the effect of the chromium oxide scale 'healing' the peened surface. The extent to which this would affect the crack initiation rates is unclear.
    - There is evidence of recrystallisation of the grains below the chromium oxide scale in the fully γ' depleted zone, and there is some evidence of a very fine grain structure in the partially γ' depleted zone. This may improve fatigue crack growth resistance during the microstructurally small crack stage by reducing the crack tip plastic displacement.

4.2.1.3 Crack Pathway

As previously discussed, Jiang et al. (2015) [50] and Bílý (1993) [174] investigated the crack initiation locations and growth routes of oxidised nickel based superalloy specimens. A microscopic analysis of the cross section of fractured fatigue specimens was undertaken in order to determine the crack initiation location and growth pathway of the oxidised FG RR1000. Specimens in etched and polished conditions were imaged as appropriate for the analysis.

First, the low maximum stress fatigue test specimens were imaged to determine the presence of cracking; example images can be seen in Figure 87. For the purposes of this section of the study, low stress refers to 850MPa and high stress refers to 1050MPa test specimens.

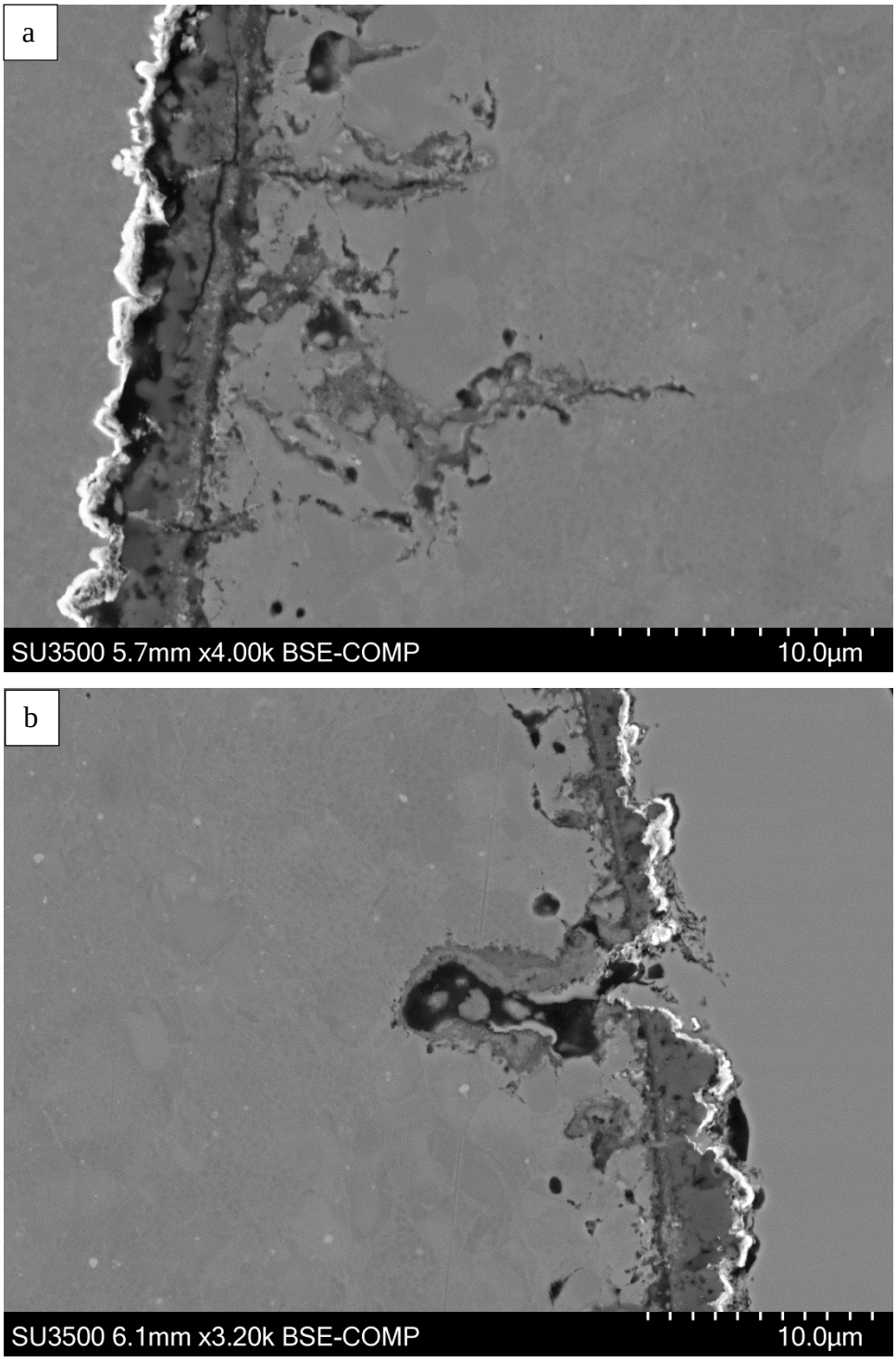

Figure 87: 5µm 850MPa fatigue tested specimen crack pathway image analysis

Figure 87a shows cracking in the chromium oxide scale, which has however, been seen throughout the thermal heat treatments so may be an artefact of the preconditioning heat treatment. Of more interest is the apparent cracking in the aluminium oxide fingers, and possible cracking along the chromium oxide and aluminium oxide interface. This seems to be a very early stage in crack formation and no other cracks of this stage were found during the analysis, suggesting that this stage is very short and once it is initiated it develops quickly to a greater damage as seen in Figure 87b. It is difficult to tell from this image where the crack initiated from and propagated for two reasons. During the process, to protect the oxides, the nickel plate penetrates the crack making it difficult to determine the surface characteristics of the crack, and therefore its initiation. The second reason is the extensive oxidation around the crack, making it difficult to determine the crack propagation path. There were very few other cracks within the lower stress specimens.

High stress specimens were then analysed as can be seen in Figure 88. A greater number of cracks were present throughout the specimens of varying depths; secondary side cracking was also prevalent from these primary cracks at the higher maximum stresses.

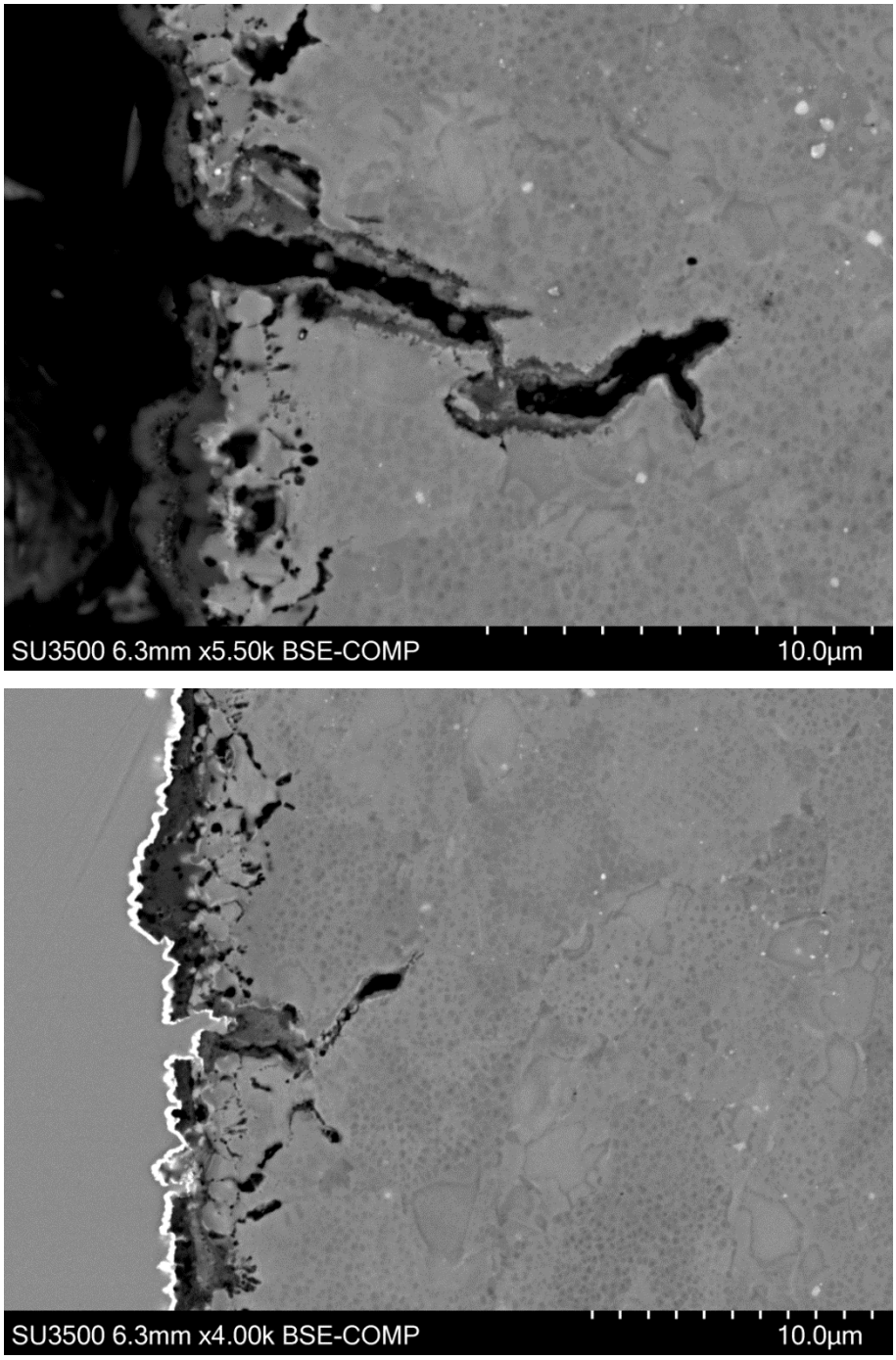

Figure 88: 5µm 1050MPa fatigue test specimen crack pathway image analysis

In order to more clearly determine the crack propagation pathways, the specimens were etched to highlight grain boundaries as shown in Figure 89; it was clear throughout that the cracks commonly followed the grain boundaries, as highlighted by the presence of the primary γ' phase.

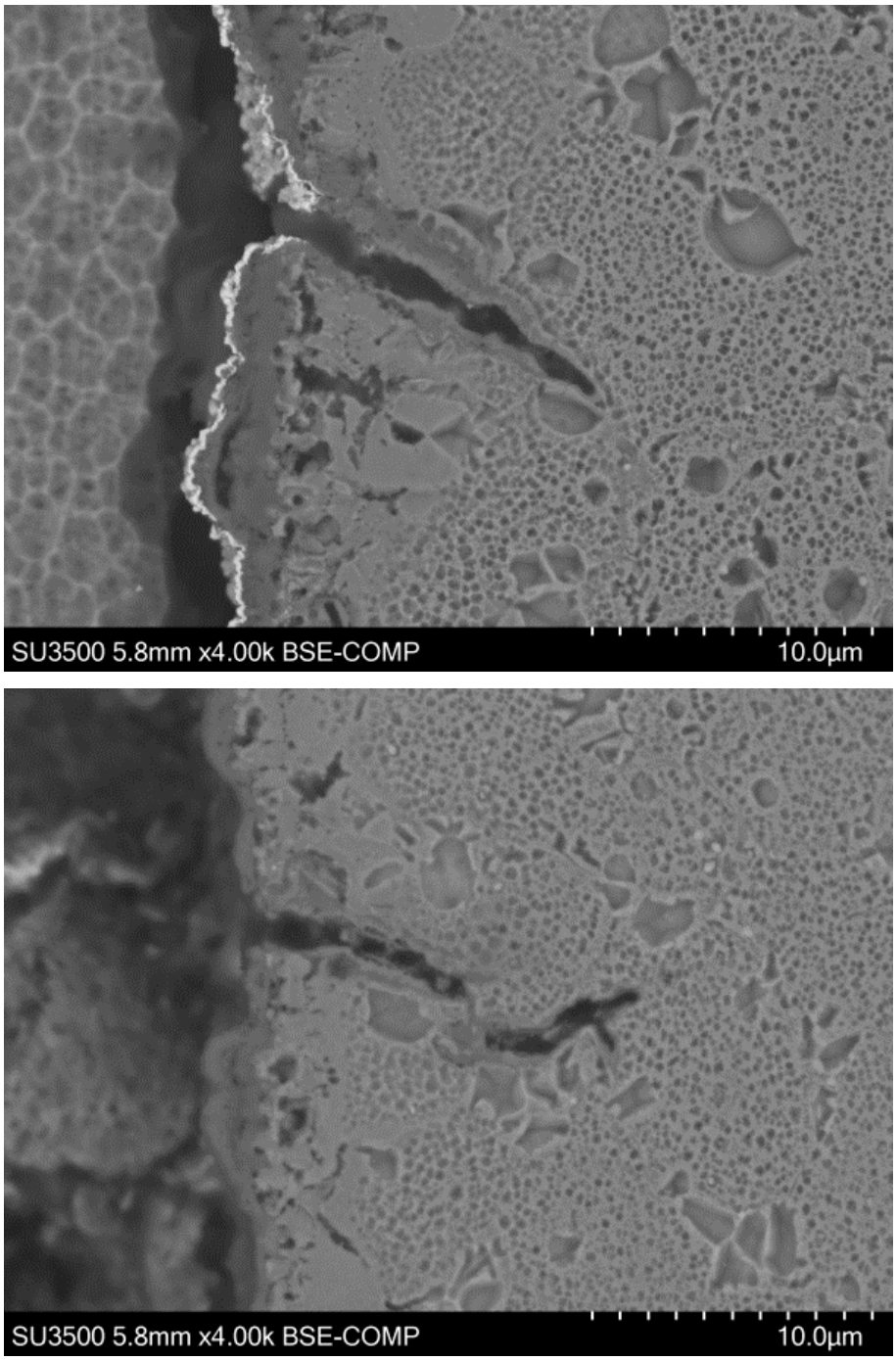

Figure 89: 5µm 1050MPa fatigue test specimen crack pathway etched image analysis

All the cracks from the high stress specimens show considerably less oxidation than that of the lower stress specimen. This aligns to the shorter lives of the higher stress specimens i.e. less time at temperature. The ratio of oxidation depth to crack length

shows how much shorter the crack grew over time compared to the cracks at the higher temperature.

The conclusions from the analysis are therefore:

- Cracks at lower stresses apparently initiate from within the aluminium oxide fingers and the chromium oxide and aluminium oxide interface.
- Cracks initially propagate along grain boundaries i.e. inter-granular.
- Higher stress specimens have greater amounts of cracking throughout the specimen.
- Cracks propagate quicker at higher stresses.

4.2.2 Notch Fatigue

As can be seen from the plain fatigue data in Figure 90, the life reduction caused by the 3µm heat treatment resulted in a reduction in life compared to the as received material of approximately 99.7%.

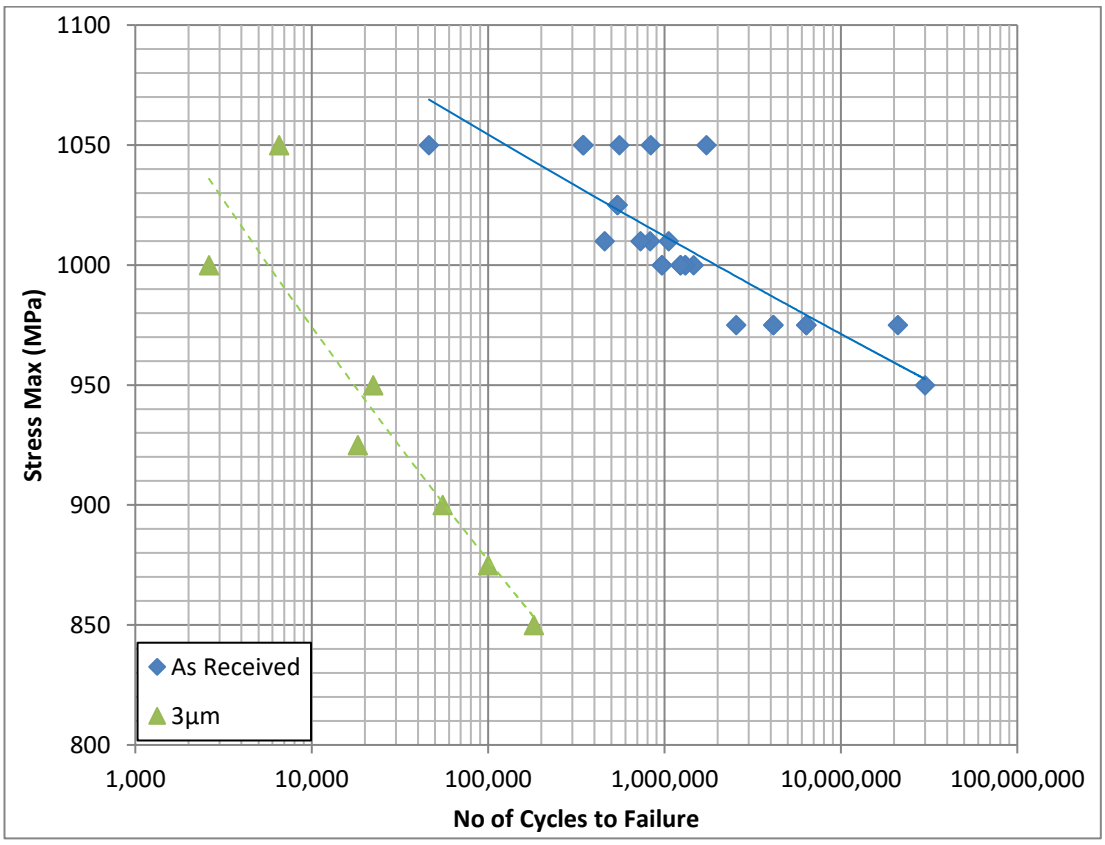

Figure 90: S-N data for as received and 3µm pre-exposed plain fatigue specimens

The S-N curves for the as received and 3µm 1.55 k_t notched specimen can be seen in Figure 91.

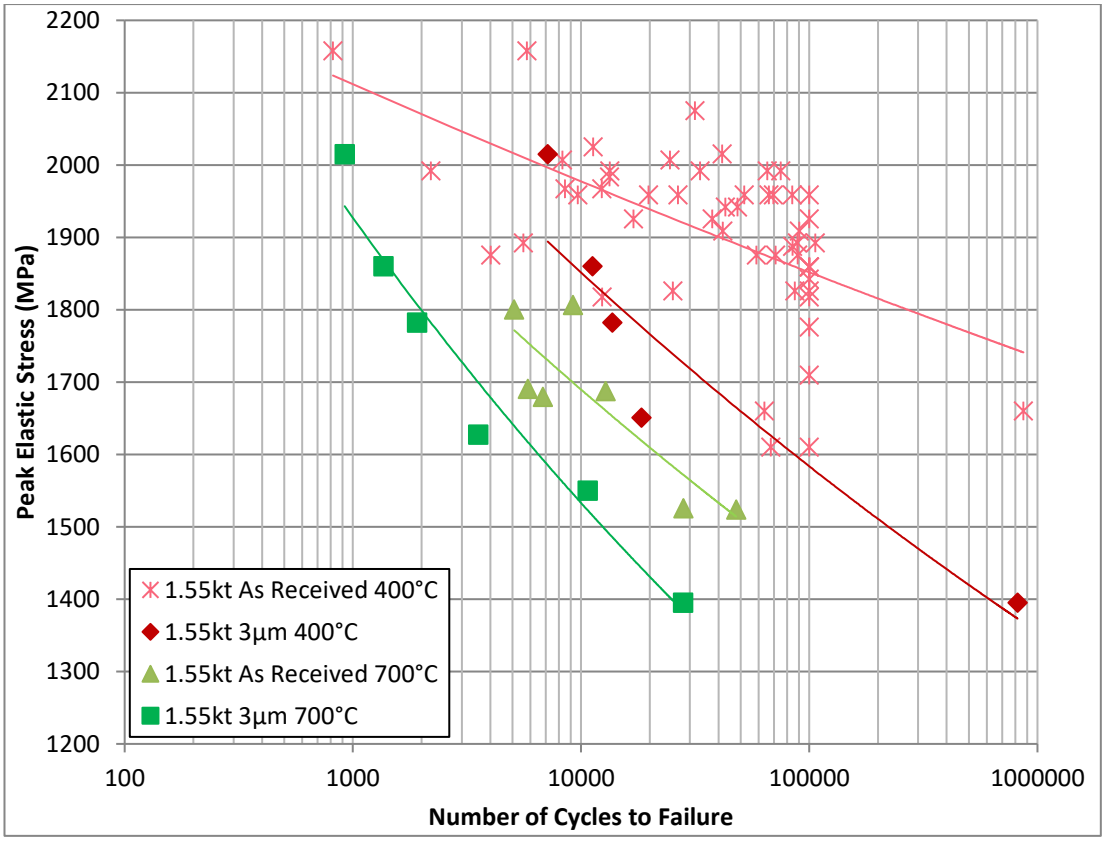

Figure 91: S-N curves for shallower notches at 2 temperatures

It can be seen that the shallow notch results in a greatly reduced fatigue sensitivity to oxidation damage when compared to the plain specimens. The same can be seen for the S-N data for the deeper notch in Figure 92.

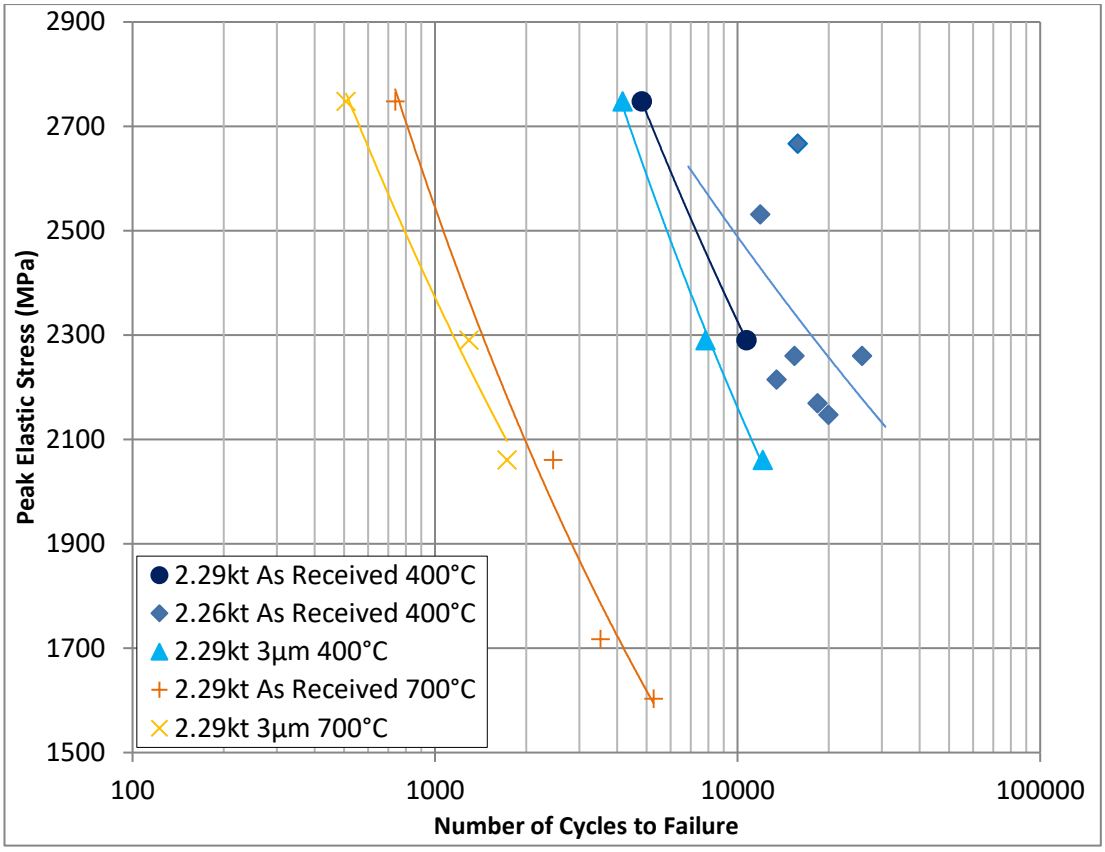

Figure 92: S-N curves for deeper notches at 2 temperatures

It can be seen that the deeper notches show even less sensitivity to oxidation damage than the shallow notch. As previously discussed, oxidation is believed to greatly influence primarily the crack initiation stage of the fatigue process. In notch fatigue, the notch is the primary cause of the initiation by localising the plastic deformation at the stress raiser. Essentially, in the notched specimens it is likely that the notch is acting to initiate the cracks at very low fractions of the total life, prior to the effect any oxide damage would have, resulting in the majority of fatigue life being crack propagation.

This is a very important consideration for turbine disc components, in which there are a great many stress raising features; the initially dramatic results found during the plain fatigue pre-exposure testing will not be as detrimental as initially indicated.

4.2.3 Thermo-Mechanical Oxidation Pre-exposed Fatigue

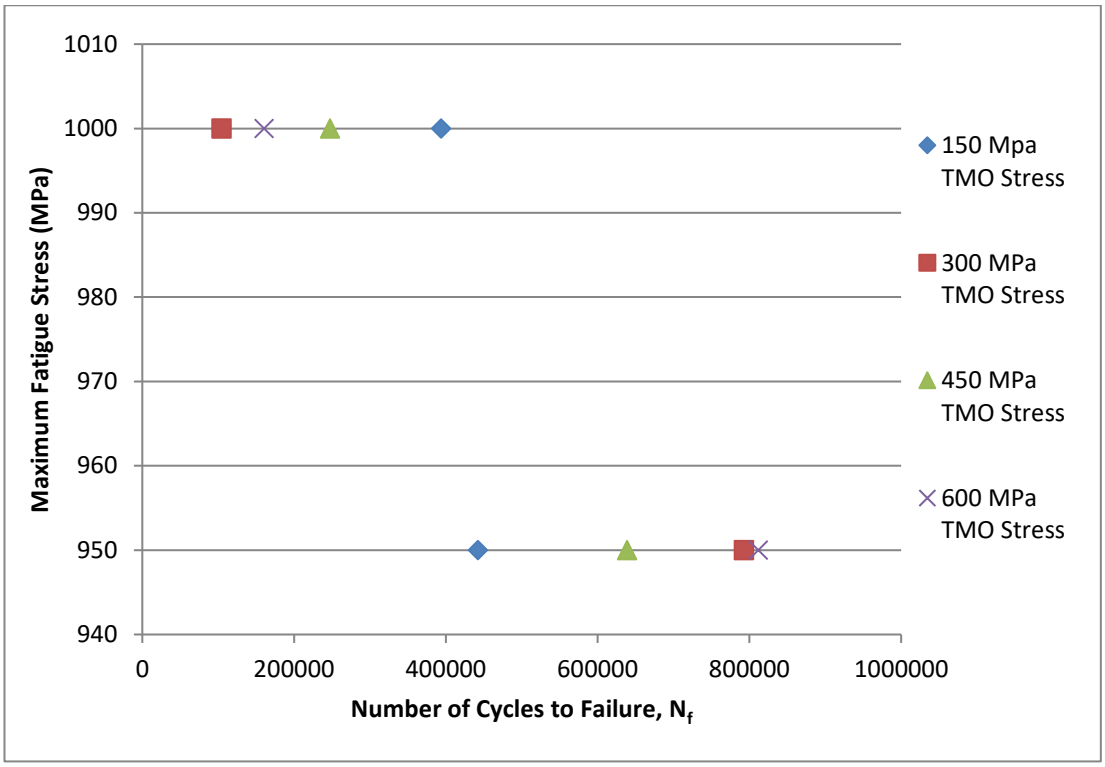

Figure 93: Maximum fatigue stress against number of cycles to failure

As can be seen from Figure 93 the higher the applied stress, the lower the fatigue life; however it does not seem to be clear when plotted in this way if there is a relationship for how the thermo-mechanical oxidation pre-fatigue damage affects the S-N response of FG RR1000.

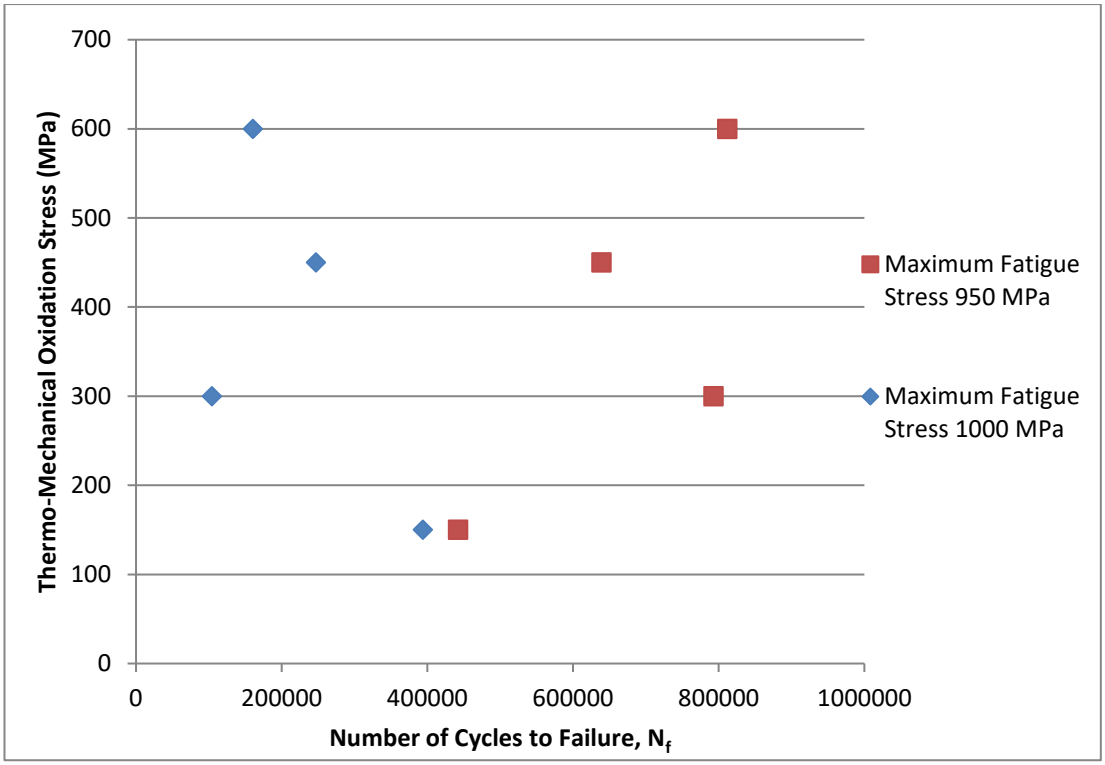

Figure 94: Thermo-mechanical oxidation stress against number of cycles to failure

It can be seen that the specimens tested at 1000MPa had shorter lives than those tested at 950MPa, which is as would be expected. For the 1000MPa fatigue tested specimens, it can generally be seen that as the load during the thermo-mechanical oxidation exposure increases, the life to failure decreases. Of particular interest is how this relationship seems to be inverted for the 950MPa specimens. The reasoning behind this is unclear and it is highly possible that it may be a result of the scatter that is a characteristic of fatigue testing. Due to a limitation in test specimens it has not been possible to investigate further.

5 Discussion

As mentioned in the introduction, a common discussion section has been written to draw together the key findings of the two research areas into one section.

Initially the elemental analysis of the oxidation products of fine grain RR1000 was conducted and it was found that chromium oxide scale and aluminium oxide fingers are the primary oxide formers. Titanium oxide was also found doped throughout the chromium oxide scale; a literature search has found that titanium oxide doping is detrimental to oxidation rates in nickel superalloys.

This then led onto an extensive study of the oxides formed under a range of different conditions. This was performed in order to understand the effect on the overall oxidation rate and morphology as surface condition, exposure time and temperature were varied. It was found that any combination of increasing temperature, increasing surface roughness and increasing exposure time led to more extensive oxidation damage. Pores and cracking were also found to occur in the chromium oxide scale, more prominently in the peened specimens at lower temperatures and shorter exposure times.

Another key finding of this initial analysis was the mechanistically linked nature of the formation of the chromium oxide and aluminium oxide i.e. areas where the chromium oxide scale is thicker the aluminium oxide fingers are shallower and vice versa, the ‘oxide damage depth’ throughout the analysis is considered as the combined depth of the chromium oxide and aluminium oxide. Oxidation of FG RR1000 is found to be a self-mediating process. At all temperatures and surface conditions investigated, a regression analysis was performed and a power law relationship found excellent fit. There is also a clear linear correlation between the γ’ depletion depth and the oxidation damage depth.

A study using Vickers hardness testing approach found that the thermal oxidation heat treatments had no effect on the hardness properties of the bulk material which is as would be hoped at these temperatures. This suggests no change in the bulk properties of the substrate alloy due to the thermal exposures.

In an effort to quantify the oxidation reaction, and allow for numerical comparison between different conditions, a methodology for using the Arrhenius equation to

determine the activation energy for the oxidation reaction was undertaken for the alloy in the peened and polished conditions. The activation energy for the peened specimens was lower than that of the polished specimens. This was most likely due to increased surface area and the effect of compressive residual stresses input into the surface region during the peening process increasing oxidation rates similar to the mechanism seen in the thermo-mechanical oxidation analysis.

Following the experimentation using thermal only heat treatments, the testing was then expanded to include the application of load to the thermal exposure profiles. It was found that oxidation accumulation rates under thermo-mechanical conditions were accelerated by approximately 2 times at the highest stress condition compared to the no load condition. It was also found that compressive stress resulted in a greater damage depth of oxidation than an equal and opposite tensile stress at all stresses and temperatures tested.

Vickers hardness testing was also undertaken following the thermo-mechanical oxidation exposures and they were found to have an effect on the hardness properties of the alloy. The higher the applied load during the exposure, the greater the reduction in hardness value. This is seemingly independent of exposure time and is therefore believed to be as a result of damage imparted on the specimens during the primary creep loading stage.

In an attempt to provide comparable results to the thermal only exposures, the Arrhenius methodology was adapted to produce an ‘apparent activation energy’ value encompassing a component of applied stress and inter-nuclear spacing to more accurately model the tensile and compressive stress oxidation asymmetry. The values calculated during the analysis fit well with what is understood of the thermo-mechanical oxidation characteristics of the alloy and provide confidence in the validity of the approach. In order to better understand what was occurring during the thermo-mechanical reactions, a theoretical analysis was undertaken. A model for anion movement was produced and found good correlation with the experimental findings.

Using the knowledge gained of the oxide growth characteristic of the alloys, it was then important to understand how this oxidation damage would affect its mechanical properties. As such, an oxidation thermal exposure schedule was outlined in order to

produce damage depths within the material of 1µm, 3µm and 5µm combined chromium and aluminium oxides. Fatigue was the mechanical property investigated throughout as it was deemed most relevant to the alloy in service.

Oxidation heat treatment pre-damaging of plain fatigue specimens causes a reduction in fatigue life compared to as received specimens. The 3µm oxide depth pre-exposed fatigue specimens had considerably shorter lives than the 1µm damaged specimen. There was a surprising improvement of the life of the 5µm damaged plane fatigue specimen compared to the 3µm specimen, with the S-N curve lying between the 1µm and 3µm curves. The reasons for the life improvement were investigated and those found to possibly contribute are; coarsening of the tertiary γ', the presence of a sub-surface plastic zone, a surface healing chromium oxide scale and the presence of recrystallised grains which are all believed to affect the fatigue initiation and propagation characteristics of the material.

Tertiary γ' size was found to increase dramatically as a result of the thermal exposures undertaken throughout the study. This change in microstructure will affect the fatigue life in a couple of ways; firstly, during fatigue tests in which creep will also occur, the tertiary γ' size will have a large effect as these particles are an important factor in controlling diffusional creep rates. Secondly, the fatigue response near the yield point will likely be altered as a result of these changes, changing the elastic and plastic properties of the material.

Nanoindentation found a dramatic change in the plastic properties of the oxide layers and the fully γ' depleted zone. The complex relationship between the increasing depth of ductile material and very hard, brittle ceramic like oxides are believed to contribute to variations in crack initiation rates; however more research is required to understand the mechanism. The interaction between the soft γ' depleted zone and the harder bulk material is believed to result in a mechanism of crack tip shielding due to plastic zone interactions ahead of the crack tip. This would lead to a reduction of crack growth rates.

As the level of oxidation damage increases, the areal surface roughness, S_a value decreases due to the 'healing' effect of the surface chromium oxide scale. Fatigue cracks initiate from surface defects; it is therefore hypothesised that the reduction in

surface roughness will decrease crack initiation between the 3µm and 5µm specimens. If this was the only mechanism there would be a life improvement throughout all the increasing oxide damage levels so it is suggested this mechanism is complimentary to another.

There is evidence of recrystallisation of the grains below the chromium oxide scale in the fully γ' depleted zone, and there is some evidence of a very fine grain structure in the partially γ' depleted zone. This may improve fatigue crack growth resistance due to increased crack deviation, however, this is a complex mechanism and requires further analysis to determine if it is beneficial.

An Effective Initial Flaw Size (EIFS) numerical analysis was also conducted to determine if the oxidation damage would lead to purely crack propagation or if there would still be a crack initiation component to the fatigue failure. It was found that there was a big difference between the predicted and the actual values suggesting is still a large initiation stage; the difference between the predicted and actual values for the higher damage specimens reduced suggesting a reduction in the initiation life; this is as would be expected.

To support the findings of the EIFS calculations a microscopy analysis was undertaken in an effort to determine the location of any crack initiation sites and propagation pathways. It was found that at low stresses, few crack formed along the specimen surface and propagation rates were slower, and at higher stresses many more cracks formed and propagated faster. Etched specimens highlighted the crack propagation pathways along the grain boundaries (intergranular). It was possible to see from limited data that cracks formed from within the aluminium oxide fingers and at the chromium oxide and aluminium oxide interface; however, due to the sparsity of this data it is unwise to overstate the conclusions without more supporting research.

In an effort to better emulate the characteristics of components that experience fatigue in service, notch fatigue tests were then performed on specimens of 2 different size notches at 2 temperatures on pre-exposed and as received conditions. Specimens were pre-oxidised to the most damaging level from the plane fatigue testing programme i.e. 3µm. The oxidation damage was found to have a greatly reduced effect on the fatigue life when compared to the plane specimens. This is advantageous as components in

service are more similar to the notch specimens than the plane specimens and notches tend to be the life limiting factor independent of the oxidation damage.

In an effort to determine if there was a link between the thermo-mechanical heat treatment and fatigue life, a small testing programme was undertaken to close out the project. It was found that a higher pre-exposure stress results in a reduction in the fatigue life of the alloy. There is however, no apparent correlation between the lower and higher stress data sets beyond this. It is believed this may be a result of the scatter innate within fatigue testing and with the limited number of test specimens available it has not been possible to investigate this suitably.

6 Conclusion

- Fine grain RR1000 oxidation results in the formation of chromium oxide diffusing from carbides and aluminium oxide fingers and island diffused from γ'. Titanium oxide (also from γ') will also irregularly dope the chromium oxide scale.
- Increased temperature, increased exposure time, increased surface roughness led to greater oxidation damage.
- Chromium oxide and aluminium oxide growth is linked and has been considered together throughout the analysis when determining oxide damage.
- Applied stress during thermal exposure has been found to markedly increase the oxidation rates within the alloy.
- An Arrhenius approach was utilised for the oxidation reaction to quantify the reaction rates:
    - Activation energy was calculated for the thermal exposure tests
        - Peened specimens had a lower activation energy than the polished specimens
    - A method for determining the 'apparent activation energy' was proposed and found good correlation with the data
        - Application of load resulted in a decrease in the apparent activation energy required to initiate the oxidation reaction
        - Compressive loading resulted in a greater reduction in activation energy than applied tensile loads
        - A model based on the effect internal residual stresses have on the rate of anion diffusion has been proposed, and has found good correlation with the experimental results.
- A study was conducted into the hardness properties of the alloy following the thermal and thermo-mechanical exposures:
    - The thermal exposures showed no change in the hardness properties of the substrate material
    - The thermo-mechanical exposures resulted in a reduction in the hardness properties of the alloy. This seems to be a result of the loading magnitude and independent of the exposure time and is likely linked to increased diffusion of γ'.

- Fatigue testing of thermally exposed plane specimens found that there was a reduction in fatigue life compared to as received specimens.
- There was however an unexpected improvement in fatigue life for specimens damaged to 5µm, which S-N data lay between that of specimens damaged to 1µm and 3µm. There are a number of potential reasons for this:
    - γ' coarsening following thermal exposure changing the properties of the material
    - Sub-surface/ sub-oxide soft zone formed by the depletion of γ' resulting in a crack tip shielding mechanism
    - Reduction in surface roughness caused by 'healing' by the chromium oxide scale
    - Recrystallisation in the sub-oxide scale region and very fine grain structure in the partially γ' depleted region
- Effective Initial Flaw Size (EIFS) found that the ratio of initiation to propagation life at all damage levels is highly geared towards initiation suggesting a life improvement mechanism that effects initiation is more likely to be life affecting.
- Microscopy analysis of the fatigued specimens found that at lower stresses less cracks formed and cracks propagated slower than in the higher stress specimens. Cracks were found to initiate within the aluminium oxide fingers and along the chromium oxide and aluminium oxide interface.
- Notched fatigue tests found that the effect of oxidation on the fatigue properties of service components would likely be minimal compared to the harsh geometries imposed on the components themselves.
- Thermo-mechanical heat treatments may have an effect on fatigue life; however, without a more thorough analysis i.e. a larger test matrix, it is not possible to draw any significant conclusions.

7 Further Work

- There are a number of different thermal oxidation experiments using a simple desktop furnace that would be interesting to perform in order to better understand their effect on the oxidation reaction rate:
    - Lower temperatures
    - Higher temperatures
    - 2 stage temperatures: High to low
    - 2 stage temperatures: Low to high

- In this study the effect of only one peening condition on the rate of oxidation was analysed. As different peening options are considered for future rotative parts, an understanding of how the oxidation characteristics may be affected is very important.

- Determine if there is a method of comparing activation energies calculated using oxide thickness measurements and activation energies using thermo-gravimetric analysis. It would also be of great interest to determine if oxide thickness is a suitable means of calculating the activation energy for other alloys, and for those that it is, produce a database.

- With a greater number of plain fatigue specimens it would have been desirable to determine the oxide damage depth at which the increase in life occurs and then at what point the mechanism peaks, and reverses again. This may also ultimately aid in the explanation of why this mechanism occurs.

- It would also be of great interest to see if the mechanism repeats in the coarse grain variant of RR1000, and then ultimately repeat the tests on a wide range of nickel superalloys with large ranges of γ' contents to see if this is a factor. It could be determined if life improvement was potentially related to precipitate size/ volume fraction or grain size.

- An interesting follow on from the thermo-mechanical oxidation analysis was a question raised with regards to creep damage. Is the increase in oxidation

caused as a result of only the plastic damage to the specimen or also some effects from the elastic loading. Would the increased rate of oxidation continue if the load was removed after plastic damage was imparted or is the oxidation rate only increased while the mechanical loading is present. Testing could be performed after a number of specimens have been loaded through a primary creep stage for up to approximately an hour then removed from load and left to oxidise under thermal only conditions and the results could be compared to standard thermo-mechanical oxidation tests.

- The engine conditions in operation are far more complex than those studied throughout this analysis. Thermo-mechanical fatigue (TMF) is being studied broadly for aero-engine materials as it is more representative of an engine in operation. It would be very interesting to measure the oxidation damage accumulation rates during the various TMF interactions, from in phase, out of phase, 90° clockwise and anticlockwise and also at 135° clockwise, the TMF phase angle most representative of the flight cycle. The phase angle referred to in TMF is the phase time difference between the stress cycle and the thermal cycle and is most easy described by Figure 95 [275].

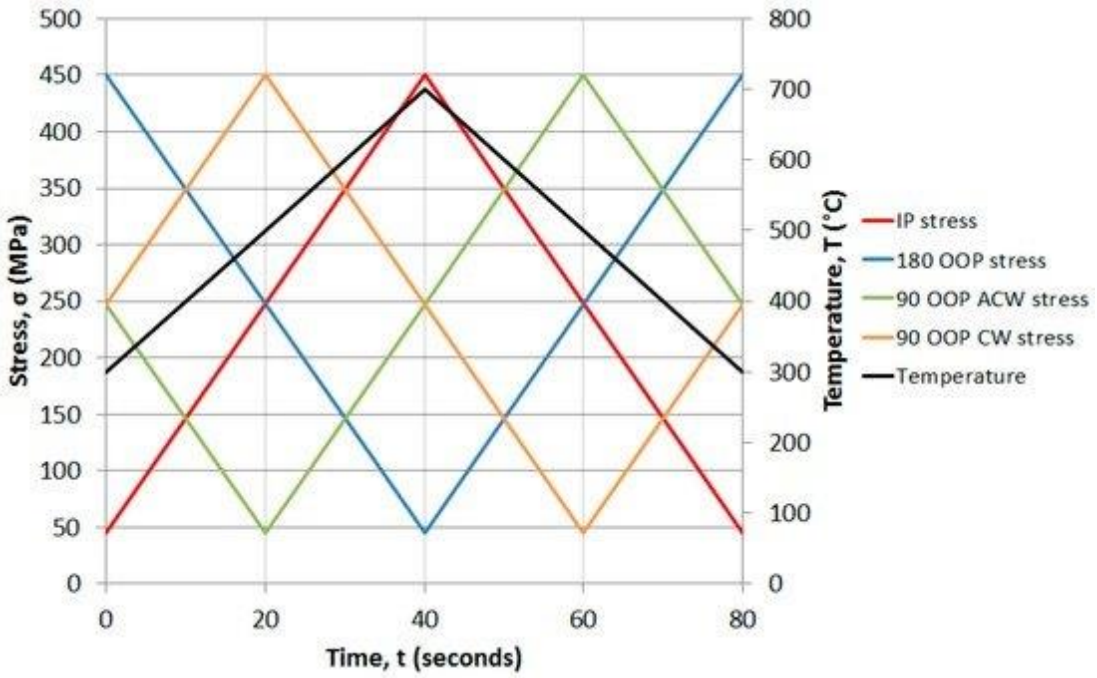

Figure 95: Thermo-Mechanical Fatigue Phase Angle Schematic

- Another analysis should be undertaken to link the current study with the proposed TMF study. Cyclic thermal oxidation testing is suggested as it would allow for comparisons to the thermal oxidation tests to understand the effects of fluctuating temperature, and also to the TMF to isolate what proportion of oxidation is caused by the fluctuating temperature and what is the due to loading effects.

References

[1] H. Fecht and D. Furrer, “Processing of nickel-base superalloys for turbine disc applications,” *Adv. Eng. Mater.*, vol. 2, no. 12, pp. 777–787, 2000.

[2] J. Dahl, “Jet Engine,” *Wikipedia Commons*, 2007. [Online]. Available: http://en.wikipedia.org/wiki/File:Jet_engine.svg. [Accessed: 10-Jul-2015].

[3] Federal Aviation Administration, “Daigram of a turbofan. sic,” *Citizendium*, 2004. [Online]. Available: http://en.citizendium.org/wiki/File:Turbofan.png. [Accessed: 10-Jul-2015].

[4] R. D. Archer and M. Saarlas, *An Introduction To Aerospace Propulsion*. Upper Sadle River: Prentice-Hall, Inc., 1996.

[5] Rolls Royce, *The Jet Engine*, 6th ed. London: Rolls Royce Plc., 2005.

[6] S. Everitt, M. J. Starink, H. T. Pang, I. M. Wilcock, M. B. Henderson, and P. A. . Reed, “A comparison of high temperature fatigue crack propagation in various sub-solvus heat treated turbine disc alloys,” vol. 23, no. 12, pp. 1419–1423, 2007.

[7] R. Haugsrud, “On the high-temperature oxidation of nickel,” *Corros. Sci.*, vol. 45, pp. 211–235, 2003.

[8] W. Betteridge, *Nickel and its Alloys*. Plymouth: MacDonald and Evans Limited, 1977.

[9] R. Bowman, “Superalloys: A Primer and History,” in *9th International Symposium on Superalloys*, 2000.

[10] Y. M. Wang-Koh, “Understanding the yield behaviour of L12-ordered alloys,” *Materials Science and Technology (United Kingdom)*, vol. 33, no. 8. pp. 934–943, 2017.

[11] R. C. Reed, “The Superalloys, Fundamentals and Applications,” in *The Superalloys*, 2006, p. various.

[12] P. Cutler, “Nickel, Nickel Everywhere,” *Materials World*, vol. September, Sep-1998.

[13] S. Cruchley, M. P. Taylor, and H. E. Evans, “Role of Ti on the Oxidation of RR1000 – With and Without Shot-peening,” in *Strategic Partnership Conference*, 2014.

[14] D. J. Young, “The Nature of High Temperature Oxidation,” in *High Temperature Oxidation and Corrosion of Metals*, Elsevier, 2016, pp. 1–30.

[15] B. Lin, L. G. Zhao, J. Tong, and H. J. Christ, “Crystal plasticity modeling of cyclic deformation for a polycrystalline nickel-based superalloy at high temperature,” *Mater. Sci. Eng. A*, vol. 527, no. 15, pp. 3581–3587, 2010.

[16] C. Stöcker *et al.*, “Microstructural characterisation and constitutive behaviour of alloy RR1000 under fatigue and creep-fatigue loading conditions,” *Mater. Sci. Eng. A*, vol. 518, pp. 27–34, 2009.

[17] Y. Q. Chen *et al.*, “Measurement of size-dependent composition variations for gamma prime (γ’) precipitates in an advanced nickel-based superalloy,” *Ultramicroscopy*, vol. 144, pp. 1–8, 2014.

[18] R. J. Mitchell, M. C. Hardy, M. Preuss, and S. Tin, “Development of γ’ morphology in P/M rotor disc alloys during heat treatment,” in *Proceedings of the International Symposium on Superalloys*, 2004, pp. 361–370.

[19] M. R. Jahangiri, H. Arabi, and S. M. A. Boutorabi, “Development of wrought precipitation strengthened IN939 superalloy,” *Mater. Sci. Technol.*, vol. 28, no. 12, pp. 1470–1478, 2012.

[20] H. Z. Li and X. Q. Chen, “Tool Condition Monitoring in Machining Superalloys,” in *Aerospace Materials Handbook*, S. Zhang and D. Zhao, Eds. Boca Raton: CRC Press, 2012, pp. 77–108.

[21] M. Hardy, “The Effect of Microstructure on High Temperature Intergranular Crack Growth in Nickel-Base Superalloys for Disc Applications.” Rolls Royce Plc., Derby, 2011.

[22] Y. Q. Chen, E. Francis, J. Robson, M. Preuss, and S. J. Haigh, “Compositional variations for small-scale gamma prime (γ’) precipitates formed at different cooling rates in an advanced Ni-based superalloy,” *Acta Mater.*, vol. 85, pp. 199–206, 2015.

[23] D. M. Collins, R. K. Heenan, and H. J. Stone, “Characterization of gamma prime (γ) precipitates in a polycrystalline nickel-base superalloy using small-angle neutron scattering,” *Metall. Mater. Trans. A Phys. Metall. Mater. Sci.*, vol. 42, no. 1, pp. 49–59, 2011.

[24] R. A. Ricks, A. J. Porter, and R. C. Ecob, “The growth of γ’ precipitates in nickel-base superalloys,” *Acta Metall.*, vol. 31, no. 1, pp. 43–53, Jan. 1983.

[25] P. A. J. Bagot *et al.*, “An Atom Probe Tomography study of site preference and partitioning in a nickel-based superalloy,” *Acta Mater.*, vol. 125, pp. 156–165, Feb. 2017.

[26] D. M. Collins, B. D. Conduit, H. J. Stone, M. C. Hardy, G. J. Conduit, and R. J. Mitchell, “Grain growth behaviour during near-γ’ solvus thermal exposures in a polycrystalline nickel-base superalloy,” *Acta Mater.*, vol. 61, no. 9, pp. 3378–3391, 2013.

[27] B. Du, L. Sheng, C. Cui, J. Yang, and X. Sun, “Precipitation and evolution of grain boundary boride in a nickel-based superalloy during thermal exposure,” *Mater. Charact.*, vol. 128, pp. 109–114, Jun. 2017.

[28] M. G. Benz, *Preparation of Clean Superalloys*. New York: Marcel Dekker Inc, 1999.

[29] ASM, "Vacuum Induction Melting," *ASM Handb.*, vol. 15, 2008.

[30] British Powder Metal Federation, *Powder Metallurgy: The Process and its Products*. Shrewsbury: MPR Publishing Services Ltd, 1990.

[31] A. D. Boyd-Lee, "Fatigue crack growth resistant microstructures in polycrystalline Ni-base superalloys for aeroengines," *Int. J. Fatigue*, vol. 21, pp. 393–405, 1999.

[32] The Library of Manufacturing, "Metal Forging," *The Library of Manufacturing*. [Online]. Available: http://thelibraryofmanufacturing.com/forging.html. [Accessed: 26-Aug-2015].

[33] ASM, "Casting, Forming and Forging," in *Gear Materials, Properties and Manufacture*, ASM International, 2005, pp. 129–137.

[34] E. Maleki, O. Unal, and A. Amanov, "Novel Experimental Methods for the Determination of the Boundaries Between Conventional, Severe and Over Shot Peening Processes," *Surfaces and Interfaces*, vol. 13, pp. 233–254, Dec. 2018.

[35] M. P. Nascimento, M. a. S. Torres, R. C. Souza, and H. J. C. Voorwald, "Effect of a Shot Peening Pre Treatment on the Fatigue Behaviour of Hard Chromium on Electroless Nickel Interlayer Coated AISI 4340 Aeronautical Steel," *Mater. Res.*, vol. 5, no. 2, pp. 95–100, 2002.

[36] J. Johnson, A. Whetstone, and J. Johnson, "Shot Peening," *Shot Peening*. [Online]. Available: https://www.webpages.uidaho.edu/mindworks/Machine_Design/Posters/PDF/Peening_Poster.pdf. [Accessed: 15-Aug-2015].

[37] R. Fathallah, G. Inglebert, and L. Castex, "Modelling of shot peening residual stresses and plastic deformation induced in metallic parts," in *Sixth International Conference on Shot Peening*, 1996, pp. 464–473.

[38] G. Tamman, "Über Anlauffarben von Metallen," *Zeitschrift fur Anorg. und Allg. Chemie*, vol. 111, p. 78, 1920.

[39] A. Cottrell, *An Introduction to Metallurgy*, 2nd ed. Cambridge: Edward Arnold, 1975.

[40] G. Renaud, "Oxide surfaces and metal/oxide interfaces studied by grazing incidence X-ray scattering," *Surf. Sci. Rep.*, vol. 32, no. 1, pp. 5–90, 1998.

[41] M. R. Bache, J. P. Jones, G. L. Drew, M. C. Hardy, and N. Fox, "Environment and time dependent effects on the fatigue response of an advanced nickel based superalloy," *Int. J. Fatigue*, vol. 31, no. 11–12, pp. 1719–1723, 2009.

[42] A. C. Karaoglanli, K. M. Doleker, B. Demirel, A. Turk, and R. Varol, “Effect of shot peening on the oxidation behavior of thermal barrier coatings,” *Appl. Surf. Sci.*, vol. 354, pp. 314–322, 2015.

[43] B. J. Foss, S. Gray, M. C. Hardy, S. Stekovic, D. S. McPhail, and B. A. Shollock, “Analysis of shot-peening and residual stress relaxation in the nickel-based superalloy RR1000,” *Acta Mater.*, vol. 61, pp. 2548–2559, 2013.

[44] G. A. Greene and C. C. Finfrock, “Oxidation of Inconel 718 in Air at High Temperatures,” *Oxid. Met.*, vol. 55, no. 5–6, pp. 505–521, 2001.

[45] S. Cruchley, H. E. Evans, M. P. Taylor, M. C. Hardy, and S. Stekovic, “Chromia layer growth on a Ni-based superalloy: Sub-parabolic kinetics and the role of titanium,” *Corros. Sci.*, vol. 75, pp. 58–66, 2013.

[46] S. Cruchley, M. P. Taylor, H. E. Evans, M. C. Hardy, and D. J. Child, “Characterisation of subsurface oxidation damage in Ni based superalloy, RR1000,” *Mater. Sci. Technol. (United Kingdom)*, vol. 30, no. 15, 2014.

[47] M. P. Taylor, H. E. Evans, S. Stekovic, and M. C. Hardy, “The Oxidation Characteristics of the Nickel-based Superalloy, RR1000, at Temperatures of 700 - 900°C,” *Mater. High Temp.*, vol. 29, no. 2, pp. 145–150, 2012.

[48] D. M. Knowles and D. W. Hunt, “The influence of microstructure and environment on the crack growth behavior of powder metallurgy nickel superalloy RR1000,” *Metall. Mater. Trans. A Phys. Metall. Mater. Sci.*, vol. 33, no. 10, pp. 3165–3172, 2002.

[49] S. Cruchley *et al.*, “Effect of prior oxidation on high cycle fatigue performance of RR1000 and role of oxidation in fatigue crack initiation,” *Mater. High Temp.*, vol. 32, no. 1–2, 2015.

[50] R. Jiang, S. Everitt, N. Gao, K. Soady, J. W. Brooks, and P. A. . Reed, “Influence of oxidation on fatigue crack initiation and propagation in turbine disc alloy N18,” *Int. J. Fatigue*, vol. 75, pp. 89–99, 2015.

[51] C. J. Smithells and C. E. Ransley, “The diffusion of gases through metals - IV—The diffusion of oxygen and of hydrogen through nickel at very high pressures,” *Proc. R. Soc. A*, vol. 157, no. 891, 1936.

[52] J. R. Davis, *ASM Specialty Handbook: Heat-Resistant Materials*. 1997.

[53] D. J. Young, “Enabling Theory,” in *High Temperature Oxidation and Corrosion of Metals*, Elsevier, 2016, pp. 31–84.

[54] F. C. Campbell, “Elements of Metallurgy and Engineering Alloys,” *ASM Int.*, 2008.

[55] A. Paul, T. Laurila, V. Vuorinen, and S. V. Divinski, “Atomic Mechanism of Diffusion,” in *Thermodynamics, Diffusion and the Kirkendall Effect in Solids*, 2014.

[56] T. Ohashi, “Generation and accumulation of atomic vacancies due to dislocation movement and pair annihilation,” *Philos. Mag.*, vol. 98, no. 25, pp. 2275–2295, 2018.

[57] A. Paul, T. Laurila, V. Vuorinen, and S. V. Divinski, “Short-Circuit Diffusion,” in *Thermodynamics, Diffusion and the Kirkendall Effect in Solids*, 2014.

[58] J. G. M. Becht, F. J. J. van Loo, and R. Metselaar, “The solid state reaction between Cu3P and silicon or germanium,” *React. Solids*, vol. 6, no. 2–3, pp. 157–172, Dec. 1988.

[59] S. J. Rothman, N. L. Peterson, and J. T. Robinson, “Isotope Effect for Self-Diffusion in Single Crystals of Silver,” *Phys. status solidi*, vol. 39, no. 2, pp. 635–645, 1970.

[60] J. Sommer and C. Herzig, “Direct determination of grain-boundary and dislocation self-diffusion coefficients in silver from experiments in type-C kinetics,” *J. Appl. Phys.*, vol. 72, no. 7, pp. 2758–2766, 1992.

[61] A. A. Alibhai, R. J. Chater, D. S. McPhail, and B. A. Shollock, “Use of isotopic tracers and SIMS analysis for evaluating the oxidation behaviour of protective coatings on nickel based superalloys,” *Appl. Surf. Sci.*, vol. 203–204, pp. 630–633, Jan. 2003.

[62] S. Chevalier, F. Desserrey, and J. P. Larpin, “Oxygen transport during the high temperature oxidation of pure nickel,” *Oxid. Met.*, vol. 64, pp. 219–234, 2005.

[63] A. Atkinson, R. I. Taylor, and A. E. Hughes, “A Quantitative Demonstration of the Grain Boundary Diffusion Mechanism for the Oxidation of Metals,” *Philos. Mag. A Phys. Condens. Matter, Struct. Defects Mech. Prop.*, vol. 45, no. 2, pp. 823–833, 1982.

[64] A. Atkinson and R. I. Taylor, “The Diffusion of 63Ni Along Grain Boundaries in Nickel Oxide,” *Philos. Mag. A Phys. Condens. Matter, Struct. Defects Mech. Prop.*, vol. 43, no. 4, pp. 979–998, 1981.

[65] S. C. Tsai, A. M. Huntz, and C. Dolin, “Growth mechanism of Cr2O3 scales: oxygen and chromium diffusion, oxidation kinetics and effect of yttrium,” *Mater. Sci. Eng. A*, vol. 212, no. 1, pp. 6–13, Jul. 1996.

[66] T. N. Ooi, D. S. Mcphail, R. J. Chater, and B. A. Shollock, “Isotope exchange studies of oxidation mechanisms in nickel-base superalloys using FIB-SIMS techniques,” *Surf. Coatings Technol.*, vol. 201, no. 7, pp. 3885–3888, Dec. 2006.

[67] H. T. Mallikarjuna, N. L. Richards, and W. F. Caley, “Effect of alloying elements and microstructure on the cyclic oxidation performance of three nickel-based superalloys,” *Materialia*, vol. 4, pp. 487–499, Dec. 2018.

[68] S. Pedrazzini *et al.*, “Oxidation behaviour of a next generation polycrystalline Mn containing Ni-based superalloy,” *Scr. Mater.*, vol. 113, pp. 51–54, Mar.

2016.

[69] N. Madern, J. Monnier, R. Baddour-Hadjean, A. Steckmeyer, and J.-M. Joubert, “Characterization of refractory steel oxidation at high temperature,” *Corros. Sci.*, vol. 132, pp. 223–233, Mar. 2018.

[70] G. Ouyang *et al.*, “Oxidation resistance of a Mo-W-Si-B alloy at 1000–1300 °C: The effect of a multicomponent Mo-Si-B coating,” *Appl. Surf. Sci.*, vol. 470, pp. 289–295, Mar. 2019.

[71] M. R. Bache *et al.*, “High temperature fatigue behaviour in an advanced nickel based superalloy: The effects of oxidation and stress relaxation at notches,” *Theor. Appl. Fract. Mech.*, vol. 84, pp. 64–71, Aug. 2015.

[72] W. J. Quadakkers and J. Żurek, “Oxidation in Steam and Steam/Hydrogen Environments,” in Shreir’s Corrosion, Elsevier, 2010, pp. 407–456.

[73] D. J. Young, “Oxidation of Pure Metals,” *High Temp. Oxid. Corros. Met.*, pp. 85–144, Jan. 2016.

[74] J. M. Perrow, W. W. Smeltzer, and J. D. Embury, “The role of structural defects in the growth of nickel oxide films,” *Acta Metall.*, vol. 16, no. 10, pp. 1209–1218, 1968.

[75] J. H. Kim, D. I. Kim, S. Suwas, E. Fleury, and K. W. Yi, “Grain-size Effects on the High-Temperature Oxidation of Modified 304 Austenitic Stainless Steel,” *Oxid. Met.*, vol. 79, pp. 239–247, 2013.

[76] E. McCafferty, *Introduction to Corrosion Science*. 2010.

[77] R. W. Revie and H. H. Uhlig, *Corrosion and Corrosion Control: An Introduction to Corrosion Science and Engineering*, Fourth. John Wiley & Sons, Inc., 2008.

[78] N. B. Pilling and R. E. Bedworth, “The oxidation of metals at high tempertures,” *J. Inst. Met.*, vol. 29, p. 529, 1923.

[79] W. D. Callister, *Fundementals of Material Science and Engineering*, 5th ed. New York: John Wiley & Sons, Inc., 2001.

[80] L. García *et al.*, “Evidence for artificial magnetite coating on Iberian armoury,” *Rev. Metal.*, vol. 47, no. 2, pp. 101–111, 2011.

[81] A. S. Khanna, *Introduction to High Temperature Oxidation and Corrosion*. Dehli: ASM International, 2002.

[82] S. Cruchley, H. Y. Li, H. E. Evans, P. Bowen, D. J. Child, and M. C. Hardy, “The role of oxidation damage in fatigue crack initiation of an advanced Ni-based superalloy,” *Int. J. Fatigue*, vol. 81, pp. 265–274, 2015.

[83] S. Cruchley, H. Evans, and M. Taylor, “An overview of the oxidation of Ni-based superalloys for turbine disc applications: surface condition, applied load and

mechanical performance," *Mater. High Temp.*, vol. 33, no. 4–5, pp. 465–475, 2016.

[84] B. J. Foss, M. C. Hardy, D. J. Child, D. S. McPhail, and B. A. Shollock, "Oxidation of a Commercial Nickel-Based Superalloy under Static Loading," *JOM*, vol. 66, no. 12, 2014.

[85] A. J. Manning, D. Knowles, and C. J. Small, "Nickel Based Superalloy," US 7,208,116 B2, 2007.

[86] C. K. Sudbrack, S. L. Draper, T. T. Gorman, J. Telesman, T. P. Gabb, and D. R. Hull, "Oxidation and the effects of high temperature exposures on notched fatigue life of an advanced powder metallurgy disk superalloy," in *Superalloys 2012*, 2012, pp. 863–872.

[87] D. J. Young and D. J. Young, "Alloy Oxidation II: Internal Oxidation," in *High Temperature Oxidation and Corrosion of Metals*, Elsevier, 2016, pp. 261–333.

[88] F. Rhines, "A Metallographic Study of Internal Oxidation in the α-Solid Solutions of Copper," *Trans. AIME*, vol. 137, p. 246.

[89] J. L. Meijering and M. J. Druyvesteyn, "Hardening of Metals by Internal Oxidation," *Philips Res. Rep.*, vol. 2, pp. 81–102.

[90] J. L. Meijering and M. J. Druyvesteyn, "Metals by Internal Oxidation, Part II," *Philips Res. Rep.*, vol. 2, pp. 260–280.

[91] S. Cruchley, M. P. Taylor, R. Ding, H. E. Evans, D. J. Child, and M. C. Hardy, "Comparison of Chromia Growth Kinetics in a Ni-based Superalloy, with and without Shot-peening," *Corros. Sci.*, vol. 100, pp. 242–252, 2015.

[92] H. S. Kitaguchi *et al.*, "Oxidation ahead of a crack tip in an advanced Ni-based superalloy," *Acta Mater.*, vol. 61, pp. 1968–1981, 2013.

[93] B. Pieraggi, "Defects and transport in oxides and oxide scales," in Shreir's *Corrosion*, 2010.

[94] G. M. Kim, E. A. Gulbranson, and G. H. Meier, "Corrosion Mechanisms of Coal Combustion Products on Alloys and Coatings," in *Conf. Fossil Energy Materials Program*, 1987, p. 343.

[95] H. Nagai and M. Okabayashi, "Deleterious Effect of Ti Addition on the Oxidation Resistance of Ni-20Cr Alloy," *Trans. Japan Inst. Met.*, vol. 22, no. 10, pp. 691–698, 2014.

[96] S. W. Yang, "Effect of Ti and Ta on the oxidation of a complex superalloy," *Oxid. Met.*, vol. 15, pp. 375–397, 1981.

[97] C. Qiu, "Net-Shape Hot Isostatic Pressing of a Nickel-Based Powder Superalloy," Birmingham, 2010.

[98] J. L. Smialek and G. H. Meier, “High-Temperature Oxidation,” *Superalloys II*, pp. 293–326, 1987.

[99] D. C. Murray, “On Improving the Oxidation Resistance of a Nickel-Based Superalloy Produced by Powder Metallurgy,” Dalhousie University, 2012.

[100] M. J. Donachie and S. J. Donachie, *Superalloys: A Technical Guide, 2nd Edition*. 2002.

[101] R. H. Bricknell and D. A. Woodford, “The Mechanism of Cavity Formation During High Temperature Oxidation of Nickel,” *Acta Metall.*, vol. 30, no. 1, pp. 257–264, 1982.

[102] R. H. Bricknell and D. A. Woodford, “Embrittlement of Nickel Following High Temperature Air Exposure.,” *Metall. Trans. A, Phys. Metall. Mater. Sci.*, vol. 12 A, no. 3, pp. 425–433, 1981.

[103] A. Encinas-Oropesa, N. J. Simms, J. R. Nicholls, G. L. Drew, J. Leggett, and M. C. Hardy, “Evaluation of Oxidation Related Damage Caused to a Gas Turbine Disc Alloy Between 700 and 800°C,” *Mater. High Temp.*, vol. 26, no. 3, pp. 241–249, 2009.

[104] X. Wang and J. A. Szpunar, “Effects of grain sizes on the oxidation behavior of Ni-based alloy 230 and N,” *J. Alloys Compd.*, vol. 752, pp. 40–52, Jul. 2018.

[105] V. Trindade, H. J. Christ, and U. Krupp, “Grain-Size Effects on the High-Temperature Oxidation Behaviour of Chromium Steels,” *Oxid. Met.*, vol. 73, pp. 551–563, 2010.

[106] A. Kanjer *et al.*, “Effect of Laser Shock Peening on the High Temperature Oxidation Resistance of Titanium,” *Surf. Coatings Technol.*, vol. 326 A, pp. 146–155, 2017.

[107] C. H. Zhou, H. T. Ma, and L. Wang, “Comparative study of oxidation kinetics for pure nickel oxidized under tensile and compressive stress,” *Corros. Sci.*, vol. 52, no. 1, pp. 210–215, Jan. 2010.

[108] X. Peng, J. Yan, Y. Zhou, and F. Wang, “Effect of Grain Refinement on the Resistance of 304 Stainless Steel to Breakaway Oxidation in Wet Air,” *Acta Mater.*, vol. 53, no. 19, pp. 5079–5088, Nov. 2005.

[109] L. Liu, Z. Yang, C. Zhang, M. Ueda, K. Kawamura, and T. Maruyama, “Effect of grain size on the oxidation of Fe–13Cr–5Ni alloy at 973 K in Ar–21 vol%O2,” *Corros. Sci.*, vol. 91, pp. 195–202, Feb. 2015.

[110] E.-G. Wagenhuber, V. B. Trindade, and U. Krupp, “The role of oxygen-grain-boundary diffusion during intercrystalline oxidation and intergranular fatigue crack propagation in alloy 718,” in *Proceedings of the International Symposium on Superalloys and Various Derivatives*, 2005, pp. 591–600.

[111] R. Naraparaju, V. B. Trindade, H.-J. Christ, and U. Krupp, “Effect of shot peening

on high temperature oxidation behaviour of boiler steel: experimental results and simulation," *Corros. Eng. Sci. Technol.*, vol. 44, no. 3, pp. 211–217, 2009.

[112] K. Hoque, "Ionic conducting oxide materials for clean energy applications: synthesis, structure and conductivity," Chalmers University, 2012.

[113] A. Karabela, L. G. Zhao, B. Lin, J. Tong, and M. C. Hardy, "Oxygen diffusion and crack growth for a nickel-based superalloy under fatigue-oxidation conditions," *Mater. Sci. Eng. A*, vol. 567, pp. 46–57, 2013.

[114] A. Karabela, L. G. Zhao, J. Tong, N. J. Simms, J. R. Nicholls, and M. C. Hardy, "Effects of cyclic stress and temperature on oxidation damage of a nickel-based superalloy," *Mater. Sci. Eng. A*, vol. 528, no. 19–20, pp. 6194–6202, 2011.

[115] J. Cao, J. Zhang, Y. Hua, R. Chen, Z. Li, and Y. Ye, "Microstructure and hot corrosion behavior of the Ni-based superalloy GH202 treated by laser shock processing," *Mater. Charact.*, vol. 125, pp. 67–75, 2017.

[116] L. Tan, X. Ren, K. Sridharan, and T. R. Allen, "Effect of Shot-Peening on the Oxidation of Alloy 800H Exposed to Supercritical Water and Cyclic Oxidation," *Corros. Sci.*, vol. 50, no. 7, pp. 2040–2046, 2008.

[117] N. Sheng, K. Horke, A. Meyer, M. R. Gotterbarm, R. Rettig, and R. F. Singer, "Surface recrystallization and its effect on oxidation of superalloy C263," *Corros. Sci.*, vol. 128, no. April, pp. 186–197, 2017.

[118] R. Naraparaju, H. J. Christ, F. U. Renner, and A. Kostka, "Effect of shot-peening on the oxidation behaviour of boiler steels," *Oxid. Met.*, vol. 76, pp. 233–245, 2011.

[119] R. Naraparaju, H. J. Christ, F. U. Renner, and A. Kostka, "Dislocation engineering and its effect on the oxidation behaviour," *Mater. High Temp.*, vol. 29, no. 2, pp. 116–122, 2012.

[120] J. C. Rosser *et al.*, "Steam oxidation of Super 304H and shot-peened Super 304H," *Mater. High Temp.*, vol. 29, no. 2, pp. 95–106, 2012.

[121] Z. Yue, M. Fu, X. Wang, and X. Li, "Effect of shot peening on the oxidation resistance of TP304H and HR3C steels in water vapor," *Oxid. Met.*, vol. 77, pp. 17–26, 2012.

[122] A. M. Huntz, B. Lefevre, and F. Cassino, "Roughness and oxidation: Application to NiO growth on Ni at 800°C," *Mater. Sci. Eng. A*, vol. 290, pp. 190–197, 2000.

[123] S. Uran, B. Veal, M. Grimsditch, J. Pearson, and A. Berger, "Effect of Surface Roughness on Oxidation : Changes in Scale Thickness , Composition , and Residual Stress," *Oxid. Met.*, vol. 54, pp. 73–85, 2000.

[124] Z. G. Zhang, P. Y. Hou, F. Gesmundo, and Y. Niu, "Effect of surface roughness on the development of protective Al2O3 on Fe-10Al (at.%) alloys containing 0-

10 at.% Cr," *Appl. Surf. Sci.*, vol. 253, pp. 881–888, 2006.

[125] B. G. Cade, W. F. Caley, and N. L. Richards, "Comparison of oxidation performance of two nickel base superalloys for turbine applications," *Can. Metall. Q.*, vol. 53, no. 4, pp. 460–468, 2014.

[126] H. Ma, Y. He, S.-Y. Bae, and K. Shin, "Effect of Shot Peening on Oxidation Behavior of SS304H Upon Long Term Steam Exposure," *J. Nanosci. Nanotechnol.*, vol. 18, pp. 6167–6472, 2018.

[127] B. Li, T. Fu, and C. Shi, "Correlations Between High-Temperature Oxidation Kinetics and Thermal Radiation Characteristics of Micro-Structured Nickel Surfaces Oxidized at 1173 K," *Metals (Basel).*, vol. 9, no. 1, p. 17, 2018.

[128] D. R. Baer and M. D. Merz, "Differences in oxides on large-and small-grained 304 stainless steel," *Metall. Trans. A*, vol. 11, no. 12, pp. 1973–1980, 1980.

[129] H. Fujikawa and Y. Iijima, "Effect of Grain Size on the High Temperature Oxidation Behaviour of Austenitic Stainless Steels," *Defect Diffus. Forum*, vol. 333, pp. 149–155, 2013.

[130] S. Samal and S. K. Mitra, "Influence of Grain Shape, Size, and Grain Boundary Diffusion on High-Temperature Oxidation of Pure Metal Fe, Cu, and Zn," *Metall. Mater. Trans. A Phys. Metall. Mater. Sci.*, vol. 46, no. 8, pp. 3324–3332, 2015.

[131] Z. Q. Cao, H. J. Sun, J. Lu, K. Zhang, and Y. Sun, "High temperature corrosion behavior of Cu–20Co–30Cr alloys with different grain size," *Corros. Sci.*, vol. 80, pp. 184–190, Mar. 2014.

[132] P. Pérez, "Influence of the alloy grain size on the oxidation behaviour of PM2000 alloy," *Corros. Sci.*, vol. 44, no. 8, pp. 1793–1808, Aug. 2002.

[133] H. Z. Zheng, S. Q. Lu, and Y. Huang, "Influence of grain size on the oxidation behavior of NbCr2 alloys at 950–1200 °C," *Corros. Sci.*, vol. 51, no. 2, pp. 434–438, Feb. 2009.

[134] S. Chevalier, "What did we learn on the reactive element effect in chromia scale since Pfeil's patent?," *Mater. Corros.*, vol. 65, no. 2, pp. 109–115, 2014.

[135] T. S. Jo, S. H. Kim, D.-G. Kim, J. Y. Park, and Y. Do Kim, "Effects of grain refinement on internal oxidation of Alloy 617," *J. Nucl. Mater.*, vol. 402, no. 2–3, pp. 162–166, Jul. 2010.

[136] S. Strauss, E. Pippel, and J. Woltersdorf, "Effects of Grain Size Cold Working and Surface Finish on the Metal-Dusting Resistance of Steels," *Oxid. Met.*, vol. 50, no. 3/4, pp. 241–254, 1998.

[137] P. Kofstad, "Protective properties of chromia and alumina scales," in *Materials Science Forum*, 1994, vol. 154, pp. 99–108.

[138] F. Dobeš and K. Milička, “Application of creep small punch testing in assessment of creep lifetime,” *Mater. Sci. Eng. A*, vol. 510–511, no. C, pp. 440–443, 2009.

[139] P. Feltham, “On the activation energy of high temperature creep in metals,” *Philos. Mag.*, vol. 2, no. 17, pp. 584–588, May 1957.

[140] W. J. M. Tegart and O. D. Sherby, “Activation energies for high temperature creep of polycrstalline zinc,” *Philos. Mag.*, vol. 3, no. 35, pp. 1287–1296, Nov. 1958.

[141] P. Berthod, “Kinetics of high temperature oxidation and chromia volatilization for a binary Ni-Cr alloy,” *Oxid. Met.*, vol. 64, pp. 235–252, 2005.

[142] H. E. Evans, H. Y. Li, and P. Bowen, “A mechanism for stress-aided grain boundary oxidation ahead of cracks,” *Scr. Mater.*, vol. 69, pp. 179–182, 2013.

[143] L. Takacs, “The Historical Development of Mechanochemistry,” *Chem. Soc. Rev.*, vol. 42, pp. 7649–7659, 2013.

[144] L. G. Zhao, J. Tong, and M. C. Hardy, “Prediction of crack growth in a nickel-based superalloy under fatigue-oxidation conditions,” *Eng. Fract. Mech.*, vol. 77, no. 6, pp. 925–938, 2010.

[145] H. T. Pang and P. A. . Reed, “Microstructure effects on high temperature fatigue crack initiation and short crack growth in turbine disc nickel-base superalloy Udimet 720Li,” *Mater. Sci. Eng. A*, vol. 448, pp. 67–79, 2007.

[146] R. Jiang *et al.*, “Role of oxygen in enhanced fatigue cracking in a PM Ni-based superalloy: Stress assisted grain boundary oxidation or dynamic embrittlment?,” *Corros. Sci.*, vol. 139, pp. 141–154, Jul. 2018.

[147] M. Schlesinger, T. Seifert, and J. Preussner, “Experimental investigation of the time and temperature dependent growth of fatigue cracks in Inconel 718 and mechanism based lifetime prediction,” *Int. J. Fatigue*, vol. 99, pp. 242–249, Jun. 2017.

[148] B. Kang, X. Liu, C. Cisloiu, and K.-M. Chang, “High temperature moiré interferometry investigation of creep crack growth of inconel 783—environment and β-phase effects,” *Mater. Sci. Eng. A*, vol. 347, no. 1–2, pp. 205–213, Apr. 2003.

[149] M. Hörnqvist, L. Viskari, K. L. Moore, and K. Stiller, “High-temperature crack growth in a Ni-base superalloy during sustained load,” *Mater. Sci. Eng. A*, vol. 609, pp. 131–140, Jul. 2014.

[150] E. Storgärds, K. Simonsson, and S. Sjöström, “Three-dimensional crack growth modelling of a Ni-based superalloy at elevated temperature and sustained loading,” *Theor. Appl. Fract. Mech.*, vol. 81, pp. 2–10, Feb. 2016.

[151] A. H. S. Iyer, K. Stiller, G. Leijon, H. C. M. Andersson-Östling, and M. Hörnqvist

Colliander, “Influence of dwell time on fatigue crack propagation in Alloy 718 laser welds,” *Mater. Sci. Eng. A*, vol. 704, pp. 440–447, Sep. 2017.

[152] E. Fessler, E. Andrieu, V. Bonnand, V. Chiaruttini, and S. Pierret, “Relation between crack growth behaviour and crack front morphology under hold-time conditions in DA Inconel 718,” *Int. J. Fatigue*, vol. 96, pp. 17–27, Mar. 2017.

[153] L. Ma and K.-M. Chang, “Identification of SAGBO-induced damage zone ahead of crack tip to characterize sustained loading crack growth in alloy 783,” *Scr. Mater.*, vol. 48, no. 9, pp. 1271–1276, May 2003.

[154] G. Amiri, B. Lesage, A. M. Huntz, and R. Molins, “Effect of a Tensile Load on the Oxide Growth Rate on Ni20Cr Alloy,” *Defect Diffus. Forum*, vol. 194–199, pp. 1695–1700, 2001.

[155] Y. Chen, X. Fan, Y. Sun, and W. Zhang, “Effect of Tensile Load on High Temperature Oxidation of CoNiCrAlY Coating,” *Surf. Coatings Technol.*, vol. 352, no. August, pp. 399–405, 2018.

[156] G. Moulin, P. Arevalo, and A. Salleo, “Influence of External Mechanical Loadings (Creep, Fatigue) on Oxygen Diffusion During Nickel Oxidation,” *Oxidation of Metals*, vol. 45, no. 1–2. pp. 153–181, 1996.

[157] G. Calvarin-Amiri, A. M. Huntz, and R. Molins, “Effect of an applied stress on the growth kinetics of oxide scales formed on Ni-20Cr alloys,” *Mater. High Temp.*, vol. 18, no. 2, pp. 91–99, 2014.

[158] H. Y. Qi, X. B. Liang, S. L. Li, and X. G. Yang, “High-temperature oxidation behavior of DZ125 Ni-based superalloy under tensile stress,” *Rare Met.*, pp. 1–6, 2016.

[159] B. R. Barnard, P. K. Liaw, R. A. Buchanan, and D. L. Klarstrom, “Affects of applied stresses on the isothermal and cyclic high-temperature oxidation behavior of superalloys,” *Mater. Sci. Eng. A*, vol. 527, no. 16–17, pp. 3813–3821, Jun. 2010.

[160] P. Berger, G. Moulin, and M. Viennot, “Nuclear microprobe study of stress-oxidation of nickel,” *Nucl. Instruments Methods Phys. Res. Sect. B Beam Interact. with Mater. Atoms*, vol. 130, no. 1–4, pp. 717–721, Jul. 1997.

[161] C.-H. Zhou, H. Ma, and L. Wang, “Compressive Stress Effects on Oxide-Scale Growth and Failure of Fe-20Cr Alloys During High Temperature Oxidation,” *J. Harbin Eng. Univ.*, vol. 31, no. 4, pp. 537–541, 2010.

[162] C. H. Zhou, H. Zhang, X. G. Guan, R. Y. Pan, F. J. Sun, and N. N. Mao, “High temperature oxidation of Ni-20Cr alloy under compressive stress,” *IOP Conf. Ser. Earth Environ. Sci.*, vol. 233, p. 032005, 2019.

[163] C. H. Zhou *et al.*, “Oxidation Kinetics Researches under the Condition of Compressive Loading,” in *IOP Conference Series: Materials Science and Engineering*, 2018, vol. 389, no. 1.

[164] C. H. Zhou, R. Y. Pan, H. Zhang, and X. G. Guan, “Oxidation Behavior of Ni-10Cr Alloy under the Compressive Stress at 900 °Ç” in *2018 3rd Asia-Pacific Electronics and Electrical Engineering Conference (EEEC 2018)*, 2019, pp. 270–277.

[165] C. H. Zhou, R. Y. Pan, and H. T. Ma, “Effect of Compressive Stress on the High-Temperature Oxidation Behavior of a Fe-20Ni Alloy in Air,” *Mater. Sci. Forum*, vol. 921, pp. 168–176, 2018.

[166] M. M. Nagl and W. T. Evans, “The Mechanical Failure of Oxide Scales Under Tensile or Compressive Load,” *J. Mater. Sci.*, vol. 28, no. 23, pp. 6247–6260, 1993.

[167] C. H. Zhou, H. T. Ma, and L. Wang, “Effect of Mechanical Loading on the Oxidation Kinetics and Oxide-Scale Failure of Pure Ni,” *Oxid. Met.*, vol. 72, no. 1–2, pp. 125–126, 2009.

[168] J. H. O’Hanlon, M. C. Hardy, D. J. Child, B. Foss, P. J. Withers, and M. R. Bache, “The effect of minimum dwell cycles on the environmental and fatigue response of RR1000,” in *MATEC Web of Conferences*, 2014, vol. 14.

[169] P. Berger, L. Gaillet, R. El Tahhann, G. Moulin, and M. Viennot, “Oxygen diffusion studies in oxide scales thermally grown or deposited on mechanically loaded metallic surfaces (MS-P2),” in *Nuclear Instruments and Methods in Physics Research, Section B: Beam Interactions with Materials and Atoms*, 2001, vol. 181, no. 1–4, pp. 382–388.

[170] EngineeringArchives, “Creep,” *2012*. [Online]. Available: http://www.engineeringarchives.com/les_matsci_creep.html. [Accessed: 27-Mar-2015].

[171] ISO, “ISO/R 373:1964 General principles for fatigue testing of metals,” 1964.

[172] G. Dieter and D. Bacon, *Mechanical Metallurgy. SI Metric Edition*. 1988.

[173] M. Klesnil and P. Lukaš, *Fatigue of Metallic Materials*. Elsevier, 1980.

[174] M. Bílý, *Cyclic Deformation and Fatigue of Metals*. Bratislava: Elsevier, 1993.

[175] F. Ellyin, *Fatigue Damage, Crack Growth and Life Prediction*. 2011.

[176] J. C. Grosskreutz, “Fatigue Mechanisms in the Sub-Creep Range,” in *Metal Fatigue Damage: Mechanism, Detection, Avoidance and Repair*, S. S. Manson, Ed. Philadelphia, 1971, pp. 5–60.

[177] D. Lambert, “Fatigue Damage Accumulation in Nickel Base Superalloys,” University of Sheffield, 1994.

[178] S. Suresh, *Fatigue of Materials*, 2nd ed. Cambridge: Cambridge University Press, 1998.

[179] D. L. McDowell, “Multiaxial small fatigue crack growth in metals,” *Int. J. Fatigue*, vol. 19, pp. 127–135, 1997.

[180] D. L. McDowell, K. Gall, M. F. Horstemeyer, and J. Fan, “Microstructure-based fatigue modeling of cast A356-T6 alloy,” *Eng. Fract. Mech.*, vol. 70, no. 1, pp. 49–80, Jan. 2003.

[181] L. Zambrano *et al.*, *Engineering Design Reliability*. Boca Raton: CRC Press, Taylor & Francis Group, 2005.

[182] W. H. Kim and C. Laird, “Crack Nucleation And Stage I Propagation in High Strain Fatigue-II. Mechanism,” *Acta Metall.*, vol. 26, pp. 789–799, 1977.

[183] J. Polák, “Resistivity of fatigued copper single crystals,” *Mater. Sci. Eng.*, vol. 89, pp. 35–43, May 1987.

[184] J. Polák, “On the role of point defects in fatigue crack initiation,” *Mater. Sci. Eng.*, vol. 92, pp. 71–80, Aug. 1987.

[185] J. Polák, “The effect of intermediate annealing on the electrical resistivity and shear stress of fatigued copper,” *Scr. Metall.*, vol. 4, no. 10, pp. 761–764, Oct. 1970.

[186] J. A. Ewing and J. C. W. Humfrey, “The Fracture of Metals under Repeated Alternations of Stress,” *Philos. Trans. R. Soc. A Math. Phys. Eng. Sci.*, vol. 200, pp. 241–253, 1902.

[187] A. Seeger, J. Diehl, S. Mader, and H. Rebstock, “Work-Hardening and Work-Softening of Face-Centred Cubic Metal Crystals,” *Philos. Mag.*, vol. 2, no. 15, pp. 323–350, 1957.

[188] J. Friedel, “A Discussion on Work-Hardening and Fatigue in Metals,” *Math. Phys. Sci.*, vol. 242, p. 145, 1957.

[189] L. F. Coffin, “Annual Review of Materials Science,” *Annu. Rev. Inc.*, vol. 2, p. 313, 1972.

[190] H. J. Christ and H. Mughrabi, “Cyclic stress-strain response and microstructure under variable amplitude loading,” *Fatigue Fract. Eng. Mater. Struct.*, vol. 19, no. 2–3, pp. 335–348, 1996.

[191] Z. S. Basinski, A. S. Korbel, and S. J. Basinski, “The temperature dependence of the saturation stress and dislocation substructure in fatigued copper single crystals,” *Acta Metall.*, vol. 28, no. 2, pp. 191–207, Feb. 1980.

[192] Z. S. Basinski and S. J. Basinski, “Fundamental aspects of low amplitude cyclic deformation in face-centred cubic crystals,” *Prog. Mater. Sci.*, vol. 36, no. C, pp. 89–148, 1992.

[193] M. Fried *et al.*, “Fatigue crack initiation in nickel-based superalloys studied by microstructure-based FE modeling and scanning electron microscopy,” *MATEC*

Web Conf., vol. 14, p. 16001, 2014.

[194] Z. Alam, D. Eastman, G. Weber, S. Ghosh, S. Ghosh, and K. Hemker, “Microstructural Aspects of Fatigue Crack Initiation and Short Crack Growth in René 88DT,” *Superalloys 2016*, pp. 561–568, 2016.

[195] G.-J. Deng *et al.*, “Small fatigue crack initiation and growth mechanisms of nickel-based superalloy GH4169 at 650 °C in air,” *Eng. Fract. Mech.*, vol. 153, pp. 35–49, Mar. 2016.

[196] L. Zhu, Z. R. Wu, X. T. Hu, and Y. D. Song, “Investigation of small fatigue crack initiation and growth behaviour of nickel base superalloy GH4169,” *Fatigue Fract. Eng. Mater. Struct.*, vol. 39, no. 9, pp. 1150–1160, 2016.

[197] J. Miao, T. M. Pollock, and J. Wayne Jones, “Crystallographic fatigue crack initiation in nickel-based superalloy René 88DT at elevated temperature,” *Acta Mater.*, vol. 57, no. 20, pp. 5964–5974, Dec. 2009.

[198] J. Miao, T. M. Pollock, and J. W. Jones, “Fatigue Crack Initiation in Nickel-Based Superalloy René 88 DT at 593°C,” in *Superalloys 2008*, 2008, pp. 589–597.

[199] J. Schijve, Ed., “Stress Concentration at Notches,” in *Fatigue of Structures and Materials*, Dordrecht: Springer, 2009, pp. 53–88.

[200] Y. Murakami, *Theory of Elasticity and Stress Concentration*. 2016.

[201] M. Shenoy, J. Zhang, and D. L. McDowell, “Estimating fatigue sensitivity to polycrystalline Ni-base superalloy microstructures using a computational approach,” *Fatigue Fract. Eng. Mater. Struct.*, vol. 30, no. 10, pp. 889–904, 2007.

[202] G. M. Castelluccio, W. D. Musinski, and D. L. McDowell, “Recent developments in assessing microstructure-sensitive early stage fatigue of polycrystals,” *Curr. Opin. Solid State Mater. Sci.*, vol. 18, no. 4, pp. 180–187, Aug. 2014.

[203] C. Stöcker, M. Zimmermann, and H.-J. Christ, “Localized cyclic deformation and corresponding dislocation arrangements of polycrystalline Ni-base superalloys and pure Nickel in the VHCF regime,” *Int. J. Fatigue*, vol. 33, no. 1, pp. 2–9, Jan. 2011.

[204] N. Kawagoishi, H. Tachiya, Q. Chen, H. Nisitani, M. Goto, and E. Kondo, “Notch Sensitivity in Fatigue of Nickel-Base Superalloy at Elevated Temperatures,” *Nihon Kikai Gakkai Ronbunshu, A Hen/Transactions Japan Soc. Mech. Eng. Part A*, vol. 64, no. 627, pp. 2869–2875, 1998.

[205] G. K. Haritos, T. Nicholas, and D. B. Lanning, “Notch size effects in HCF behavior of Ti–6Al–4V,” *Int. J. Fatigue*, vol. 21, no. 7, pp. 643–652, Aug. 1999.

[206] C. Santus, D. Taylor, and M. Benedetti, “Sensibility analysis of the fatigue critical distance values assessed by combining plain and notched cylindrical specimens,” *Procedia Struct. Integr.*, vol. 8, pp. 67–74, Jan. 2018.

[207] F. Berto, P. Gallo, and P. Lazzarin, “High temperature fatigue tests of un-notched and notched specimens made of 40CrMoV13.9 steel,” *Mater. Des.*, vol. 63, pp. 609–619, Nov. 2014.

[208] G. Matsubara and K. Nishio, “Multiaxial high-cycle fatigue criterion for notches and superficial small holes from considerations of crack initiation and non-propagation,” *Int. J. Fatigue*, vol. 67, pp. 28–37, Oct. 2014.

[209] N. R. Gates and A. Fatemi, “Multiaxial variable amplitude fatigue life analysis using the critical plane approach, Part II: Notched specimen experiments and life estimations,” *Int. J. Fatigue*, vol. 106, pp. 56–69, Jan. 2018.

[210] D. Leidermark, J. Moverare, M. Segersäll, K. Simonsson, S. Sjöström, and S. Johansson, “Evaluation of fatigue crack initiation in a notched single-crystal superalloy component,” *Procedia Eng.*, vol. 10, pp. 619–624, Jan. 2011.

[211] T. P. Gabb, J. Gayda, J. Telesman, L. J. Ghosn, and A. Garg, “Factors influencing dwell fatigue life in notches of a powder metallurgy superalloy,” *Int. J. Fatigue*, vol. 48, pp. 55–67, 2013.

[212] J. Telesman, T. P. Gabb, L. J. Ghosn, and J. Gayda, “Effect of notches on creep-fatigue behavior of a P/M nickel-based superalloy,” *Int. J. Fatigue*, vol. 87, pp. 311–325, 2016.

[213] J. Liao, J. Tan, X. Wu, D. Ning, G. Xue, and W. Yao, “Corrosion fatigue behavior of 304 stainless steel notched specimen in high-temperature pressurized water,” *Mater. Sci. Eng. A*, vol. 748, pp. 137–145, Mar. 2019.

[214] D. Wan, Y. Deng, J. I. H. Meling, A. Alvaro, and A. Barnoush, “Hydrogen-enhanced fatigue crack growth in a single-edge notched tensile specimen under in-situ hydrogen charging inside an environmental scanning electron microscope,” *Acta Mater.*, vol. 170, pp. 87–99, May 2019.

[215] D. Gustafsson *et al.*, “Fatigue crack growth behaviour of Inconel 718 – the concept of a damaged zone caused by high temperature hold times,” *Procedia Eng.*, vol. 10, pp. 2821–2826, Jan. 2011.

[216] G. M. Owolabi, R. Prasannavenkatesan, and D. L. McDowell, “Probabilistic framework for a microstructure-sensitive fatigue notch factor,” *Int. J. Fatigue*, vol. 32, no. 8, pp. 1378–1388, Aug. 2010.

[217] W. D. Musinski and D. L. McDowell, “Microstructure-sensitive probabilistic modeling of HCF crack initiation and early crack growth in Ni-base superalloy IN100 notched components,” *Int. J. Fatigue*, vol. 37, pp. 41–53, Apr. 2012.

[218] G. M. Owolabi and H. A. Whitworth, “Modeling and Simulation of Microstructurally Small Crack Formation and Growth in Notched Nickel-base Superalloy Component,” *J. Mater. Sci. Technol.*, vol. 30, no. 3, pp. 203–212, Mar. 2014.

[219] Y. Yamashita, Y. Ueda, H. Kuroki, and M. Shinozaki, “Fatigue life prediction of small notched Ti–6Al–4V specimens using critical distance,” *Eng. Fract. Mech.*, vol. 77, no. 9, pp. 1439–1453, Jun. 2010.

[220] G. Owolabi, O. Okeyoyin, O. Bamiduro, A. Olasumboye, and H. Whitworth, “The effects of notch size and material microstructure on the notch sensitivity factor for notched components,” *Eng. Fract. Mech.*, vol. 145, pp. 181–196, Aug. 2015.

[221] A. Spaggiari, D. Castagnetti, E. Dragoni, and S. Bulleri, “Fatigue life prediction of notched components: a comparison between the theory of critical distance and the classical stress-gradient approach,” *Procedia Eng.*, vol. 10, pp. 2755–2767, Jan. 2011.

[222] J. Wang and X. Yang, “HCF strength estimation of notched Ti–6Al–4V specimens considering the critical distance size effect,” *Int. J. Fatigue*, vol. 40, pp. 97–104, Jul. 2012.

[223] S. Birosca, F. Di Gioacchino, S. Stekovic, and M. Hardy, “A quantitative approach to studying the effect of local texture and heterogeneous plastic strain on the deformation micromechanism in RR1000 nickel-based superalloy,” *Acta Mater.*, vol. 74, pp. 110–124, Aug. 2014.

[224] R. Jiang, N. Karpasitis, N. Gao, and P. A. S. Reed, “Effects of microstructures on fatigue crack initiation and short crack propagation at room temperature in an advanced disc superalloy,” *Mater. Sci. Eng. A*, vol. 641, pp. 148–159, Aug. 2015.

[225] A. Pineau and S. D. Antolovich, “Probabilistic approaches to fatigue with special emphasis on initiation from inclusions,” *Int. J. Fatigue*, vol. 93, pp. 422–434, Dec. 2016.

[226] J. Jiang, J. Yang, T. Zhang, F. P. E. Dunne, and T. Ben Britton, “On the mechanistic basis of fatigue crack nucleation in Ni superalloy containing inclusions using high resolution electron backscatter diffraction,” *Acta Mater.*, vol. 97, pp. 367–379, Sep. 2015.

[227] G. Owolabi, O. Okeyoyin, O. Bamiduro, and H. Whitworth., “Fatigue Strength Reduction Factor for Polycrystalline Nickel Base Superalloy with and without Non-Metallic Inclusions,” *Procedia Eng.*, vol. 74, pp. 297–302, Jan. 2014.

[228] Metal Improvement Company, “Shot Peening,” *Job Shop*, 2015. [Online]. Available: http://www.jobshop.com/techinfo/papers/reasonstoshotpeen.shtml. [Accessed: 14-Jul-2015].

[229] Z. Y. Wang, Q. Y. Wang, and M. Cao, “Experimental study on fatigue behaviour of shot-peened open-hole steel plates,” *Materials (Basel).*, vol. 10, no. 9, 2017.

[230] E. R. R. de los Rios, A. Walley, M. T. T. Milan, and G. Hammersley, “Fatigue crack initiation and propagation on shot-peened surfaces in A316 stainless steel,”

Int. J. Fatigue, vol. 17, no. 7, pp. 493–499, Oct. 1995.

[231] W. Li and B. Liu, "Experimental investigation on the effect of shot peening on contact fatigue strength for carburized and quenched gears," *Int. J. Fatigue*, vol. 106, pp. 103–113, Jan. 2018.

[232] Y. Ochi, K. Masaki, T. Matsumura, and T. Sekino, "Effect of shot-peening treatment on high cycle fatigue property of ductile cast iron," *Int. J. Fatigue*, vol. 23, no. 5, pp. 441–448, May 2001.

[233] L. Trško, O. Bokůvka, F. Nový, and M. Guagliano, "Effect of severe shot peening on ultra-high-cycle fatigue of a low-alloy steel," *Mater. Des.*, vol. 57, pp. 103–113, May 2014.

[234] O. M. D. M. Messé, S. Stekovic, M. C. Hardy, and C. M. F. Rae, "Characterization of Plastic Deformation Induced by Shot-Peening in a Ni-Base Superalloy," *Jom*, vol. 66, no. 12, pp. 2502–2515, 2014.

[235] M. Khadhraoui, W. Cao, L. Castex, and J. Y. Guédou, "Experimental investigations and modelling of relaxation behaviour of shot peening residual stresses at high temperature for nickel base superalloys," *Mater. Sci. Technol.*, vol. 13, pp. 360–367, 1997.

[236] S. B. Kim, A. Evans, J. Shackleton, G. Bruno, M. Preuss, and P. J. Withers, "Stress relaxation of shot-peened UDIMET 720Li under solely elevated-temperature exposure and under isothermal fatigue," *Metall. Mater. Trans. A Phys. Metall. Mater. Sci.*, vol. 36A, pp. 2005–2041, 2005.

[237] W. Cao, M. Khadhraoui, B. Brenier, J. Y. Guedou, and L. Castex, "Thermomechanical relaxation of residual stress in shot peened nickel base superalloy," *Mater. Sci. Technol.*, vol. 10, pp. 947–954, 1994.

[238] A. Evans, S. B. Kim, J. Shackleton, G. Bruno, M. Preuss, and P. J. Withers, "Relaxation of residual stress in shot peened Udimet 720Li under high temperature isothermal fatigue," *Int. J. Fatigue*, vol. 27, no. 10–12, pp. 1530–1534, 2005.

[239] R. John, D. J. Buchanan, M. J. Caton, and S. K. Jha, "Stability of shot peen residual stresses in IN100 subjected to creep and fatigue loading," in *Procedia Engineering*, 2010, vol. 2, no. 1, pp. 1887–1893.

[240] D. J. Buchanan and R. John, "Relaxation of shot-peened residual stresses under creep loading," *Scr. Mater.*, vol. 59, no. 3, pp. 286–289, 2008.

[241] D. J. Buchanan, R. John, and R. A. Brockman, "Relaxation of shot-peened residual stresses under creep loading," *J. Eng. Mater. Technol. Trans. ASME*, vol. 131, no. 3, pp. 0310081–03100810, 2009.

[242] D. J. Child, G. D. West, and R. C. Thomson, "Assessment of surface hardening effects from shot peening on a Ni-based alloy using electron backscatter

diffraction techniques," *Acta Mater.*, vol. 59, no. 12, pp. 4825–4834, Jul. 2011.

[243] T. P. Gabb, C. K. Sudbrack, S. L. Draper, R. A. MacKay, and J. Telesman, "Effects of Long Term Exposures on Fatigue of PM Disk Superalloys," *Mater. Perform. Charact.*, vol. 3, no. 2, pp. 44–67, 2013.

[244] R. O. Ritchie, "Mechanisms of fatigue-crack propagation in ductile and brittle solids," *Int. J. Fract.*, vol. 100, pp. 55–83, 1999.

[245] R. O. O. Ritchie, "Influence of microstructure on near-threshold fatigue-crack propagation in ultra-high strength steel," *Met. Sci.*, vol. 11, no. 8–9, pp. 368–381, 1977.

[246] A. G. Evans, "Perspective on the Development of High-Toughness Ceramics," *J. Am. Ceram. Soc.*, vol. 73, no. 2, pp. 187–206, 1990.

[247] C. J. Hyde, W. Sun, and T. H. Hyde, "An investigation of the failure mechanisms in high temperature materials subjected to isothermal and anisothermal fatigue and creep conditions," *Procedia Eng.*, vol. 10, pp. 1157–1162, 2011.

[248] B. A. Lerch, N. Jayaraman, and S. D. Antolovich, "A study of fatigue damage mechanisms in Waspaloy from 25 to 800°C," *Materials Science and Engineering*, vol. 66, no. 2. pp. 151–166, 1984.

[249] S. S. Manson, "Behaviour of Materials Under Conditions of Thermal Stress," Cleveland, 1954.

[250] R. C. Hurst, R. J. Lancaster, S. P. Jeffs, and M. R. Bache, "The contribution of small punch testing towards the development of materials for aero-engine applications," *Theor. Appl. Fract. Mech.*, vol. 86, pp. 69–77, Dec. 2016.

[251] "CEN Workshop Agreement, CWA 15627: Small Punch Test Method for Metallic Materials," Brussels, Belgium, 2007.

[252] E. D. Hintsala, U. Hangen, and D. D. Stauffer, "High-Throughput Nanoindentation for Statistical and Spatial Property Determination," *JOM*, vol. 70, no. 4. pp. 494–503, 2018.

[253] V. Azar, B. Hashemi, and M. Rezaee Yazdi, "The effect of shot peening on fatigue and corrosion behavior of 316L stainless steel in Ringer's solution," *Surf. Coatings Technol.*, vol. 204, no. 21–22, pp. 3546–3551, Aug. 2010.

[254] G. Bertali, F. Scenini, and M. G. Burke, "The effect of residual stress on the Preferential Intergranular Oxidation of Alloy 600," *Corros. Sci.*, vol. 111, pp. 494–507, Oct. 2016.

[255] S. Taniguchi, "Stresses Developed During The Oxidation Of Metals And Alloys," *Trans. Iron Steel Inst. Japan*, vol. 25, 1985.

[256] J. L. Ruan, Y. Pei, and D. Fang, "Residual stress analysis in the oxide scale/metal substrate system due to oxidation growth strain and creep deformation," *Acta*

Mech., 2012.

[257] Z. Tao *et al.*, “Modelling of the Mechanical Behaviour of a Chromia Forming Alloy Under Thermal Loading,” *Oxid. Met.*, vol. 88, no. 1–2, pp. 15–27, 2017.

[258] H. E. Evans, “Stress effects in high temperature oxidation of metals,” *Int. Mater. Rev.*, vol. 40, pp. 1–40, 1995.

[259] S. R. J. Saunders, H. E. Evans, M. Li, D. D. Gohil, and S. Osgerby, “Oxidation growth stresses in an alumina-forming ferritic steel measured by creep deflection,” *Oxid. Met.*, vol. 48, no. 3–4, pp. 189–200, 1997.

[260] A. M. Huntz, G. Calvarin Amiri, H. E. Evans, and G. Cailletaud, “Comparison of oxidation-growth stresses in NiO film measured by deflection and calculated using creep analysis or finite-element modeling,” *Oxid. Met.*, vol. 57, no. 5–6, pp. 499–521, 2002.

[261] M. Li, T. Li, W. Gao, and Z. Liu, “Determination of oxide growth stress by a novel deflection method,” *Oxid. Met.*, vol. 51, no. 5, pp. 333–351, 1999.

[262] S. Maharjan, X. Zhang, and Z. Wang, “Effect of oxide growth strain in residual stresses for the deflection test of single surface oxidation of alloys,” *Oxid. Met.*, vol. 77, pp. 93–106, 2012.

[263] C. J. Pretty, “Thermo-Mechanical Fatigue Crack Growth Of A Polycrystalline Nickel Alloy,” Thesis for Doctor of Engineering, Swansea University, 2014.

[264] F. Schulz, H. Y. Li, H. Kitaguchi, D. Child, S. Williams, and P. Bowen, “Influence of Tertiary Gamma Prime (γ′) Size Evolution on Dwell Fatigue Crack Growth Behavior in CG RR1000,” *Metall. Mater. Trans. A Phys. Metall. Mater. Sci.*, vol. 49, pp. 3874–3884, 2018.

[265] M. C. Chaturvedi and Y. Han, “Effect of particle size on the creep rate of superalloy Inconel 718,” *Mater. Sci. Eng.*, vol. 89, pp. L7–L10, 1987.

[266] P. L. Threadgill and B. B. Wilshire, “The Effect of Particle Size and Spacing on Creep of Two-Phase Copper–Cobalt Alloys,” *Met. Sci.*, vol. 8, pp. 117–124, 1974.

[267] W. Elber, “Fatigue crack closure under cyclic tension,” *Eng. Fract. Mech.*, vol. 2, no. 1, pp. 37–44, 1970.

[268] W. Elber, “The Significance of Fatigue Crack Closure,” in *Damage Tolerance in Aircraft Structures*, ASTM International, 1971, pp. 230–242.

[269] C. S. Lee, C. G. Park, and Y. W. Chang, “Precise determination of fatigue crack closure in Al alloys,” *Mater. Sci. Eng. A*, vol. 216, no. 1–2, pp. 131–138, Oct. 1996.

[270] X. X. Song, Y. B. Shang, H. J. Shi, L. S. Niu, and Z. X. Wang, “Plastic mismatch effect on plasticity induced crack closure: Fatigue crack propagation

perpendicularly across a plastically mismatched interface," *Fatigue Fract. Eng. Mater. Struct.*, pp. 1–15, 2018.

[271] F. Jiang, Z. L. Deng, K. Zhao, and J. Sun, "Fatigue crack propagation normal to a plasticity mismatched bimaterial interface," *Mater. Sci. Eng. A*, vol. 356, no. 1, pp. 258–266, 2003.

[272] T. S. Cook and F. Erdogan, "Stresses in bonded materials with a crack perpendicular to the interface," *Int. J. Eng. Sci.*, vol. 10, pp. 677–697, 1972.

[273] S. Suresh, Y. Sugimura, and E. K. Tschegg, "The growth of a fatigue crack approaching a perpendicularly-oriented, bimaterial interface," *Scr. Metall. Mater.*, vol. 27, no. 9, pp. 1189–1194, 1992.

[274] A. Turnbull and E. R. De Los Rios, "The effect of grain size on fatigue crack growth in an aluminium magnesium alloy," *Fatigue Fract. Eng. Mater. Struct.*, vol. 18, no. 11, pp. 1355–1366, 1995.

[275] C. J. Pretty, M. T. Whitaker, and S. J. Williams, "Thermo-mechanical fatigue crack growth of RR1000," *Materials (Basel).*, vol. 10, no. 34, pp. 1–20, 2017.

Appendix I

Appendix I: Table 1 - Test matrix for thermal exposure tests

Temperature (°C)	Hold (hrs)	Repeats
700	24	3
	100	
	250	
	1000	
750	24	
	100	
	250	
	1000	
800	24	
	100	
	250	
	1000	

Appendix I: Table 2 - Thermo-mechanical oxidation test matrix

Stress (MPa)	Temperature (°C)	Hold (hrs)	Test frame type	Repeats
-600	700	24	Electric Screw	2
		100		
		250		
-450		24		
		100		
		250		
-300		24		
		100		
		250		
-150		24		
		100		
		250		
0		24	Furnace	
		100		
		250		
+150		24	10:1 Constant Load Creep	
		100		
		250		
+300		24		
		100		
		250		
+450		24		
		100		
		250		
+600		24		
		100		
		250		

Appendix I: Table 3 – Thermally pre-exposed fatigue test matrix

Max Stress (MPa)	Damage Depth (µm)	Test Temperature (°C)	Waveform	Frequency (Hz)	R ratio
1050	1	700	Trap	0.25	0.05
1050					
1025					
1000					
975					
975					
925					
900					
1050	3				
1000					
950					
925					
900					
875					
850					
1050	5				
1050					
1025					
1000					
975					
975					
950					
900					
850					

Appendix I: Table 4 - Thermal pre-exposures

Damage Depth (µm)	Time (hours)	Temperature (°C)
1	72	700
3	211	740
5	310	762

Appendix I: Table 5 – Vacuum furnace thermally pre-exposed fatigue test matrix

Max Stress (MPa)	Damage Depth Heat Treatment (µm)	Repeats	Test Temperature (°C)	Waveform	Frequency (Hz)	R ratio
1050	1	2	700	Trap (24 hours) / Sine (remainder)	0.25(24 hours) / 1 (remainder)	0.05
	3	2				
	5	2				

Appendix I: Table 6 - Notched fatigue test matrix

Nominal Stress (MPa)	Test Temperature (°C)	Stress Concentration Factor, k_t	Waveform	R ratio	Pre-exposure depth (µm)
900	400	1.55	Sine	0.05	3
1000					
1065					
1150					
1200					
1300					
900	700				
1000					
1050					
1150					
1200					
1300					
1000	400	2.29			As received
1200					
1200	700				
1300					
900	400	2.29			3
1000					
1200					
900	700				
1000					
1200					

Appendix I: Table 7 - Thermo-mechanical oxidation fatigue interaction test matrix

Test Temperature (°C)	Thermo-mechanical oxidation - Stage 1		Fatigue - Stage 2			
	Stress (MPa)	Hold Time (Hrs)	Max Stress (MPa)	R ratio	Frequency	Waveform
700	150	114	950	0.05	0.25(24 hours) / 1 (remainder)	Trap (24 hours) / Sine (remainder)
			1000			
	300		950			
			1000			
	450		950			
			1000			
	600		950			
			1000			

Appendix I: Table 8 - Small punch test matrix

Pre-exposure Depths (µm)	Test Temperature (°C)	Displacement rate (mm/min)	Repeats
As Received	700	0.5	2
1			
3			
5			

Appendix II

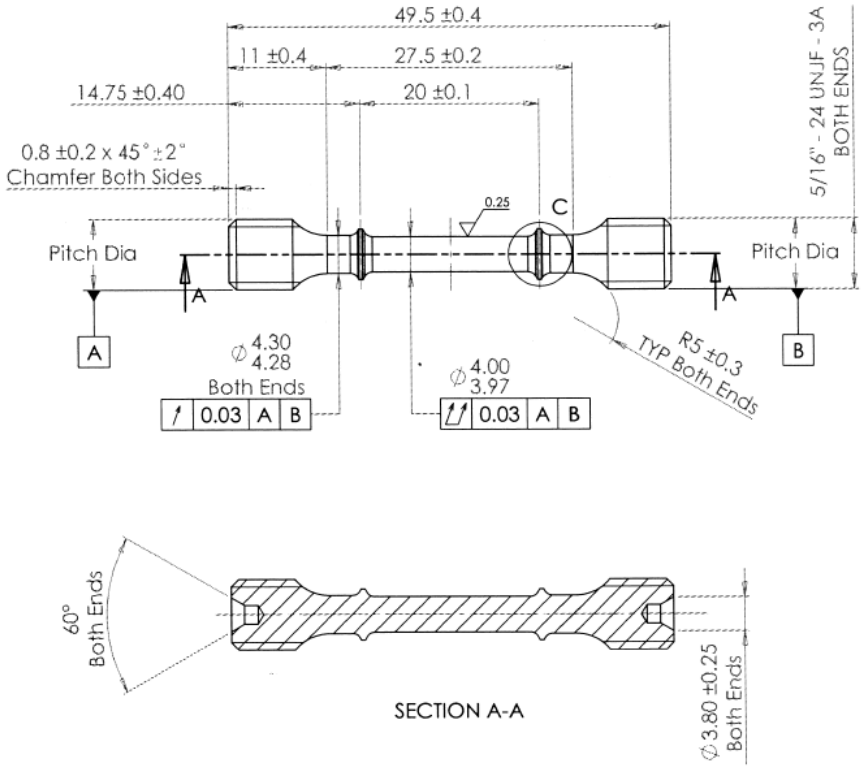

SECTION A-A

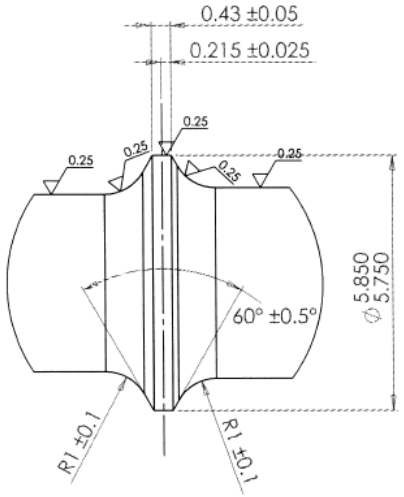

TYP Both Sides

DETAIL C
SCALE 10 : 1

SCALE 1:1

	NAME	SIGNATURES	DATE				
				2nd Issue Re-drawn by P.S.Marsden	D.Koovits	11/01/2013	2
DRAUGHTS PERSON	D.Koovits	[redacted]	11.1.13	1st Issue for Production old drawing by Rolls-Royce	D.Koovits	27-7-2000	1
DRAWING APPROVAL	J.Wardle	[redacted]	11.1.13	Modification	Name	Date	Issue
MACHINING SERVICES	T.Fogden (RR)	[redacted]	11.1.13				
TEST GROUP	N.Clarke (RR)	[redacted]	24/01/13	Rolls-Royce			
CUSTOMER	M.Twite (RR)	[redacted]	28-04-13				

TITLE:

12.5mm² Elevated Temperature Creep / Tensile Test Piece

INTERPRET GEOMETRIC TOLERANCING PER:

MATERIAL: Free Issue

FINISH: **1.6 Microns U.O.S.**

COMMENTS

ALL DIMENSIONS AND TOLERANCES ARE IN mm, EXCEPT WHERE STATED.

MANUFACTURE MUST BE IN ACCORDANCE WITH MSRR9968

DWG. NO. **RLH10259**

SCALE: **DO NOT SCALE DRAWING** SHEET 1 OF 1

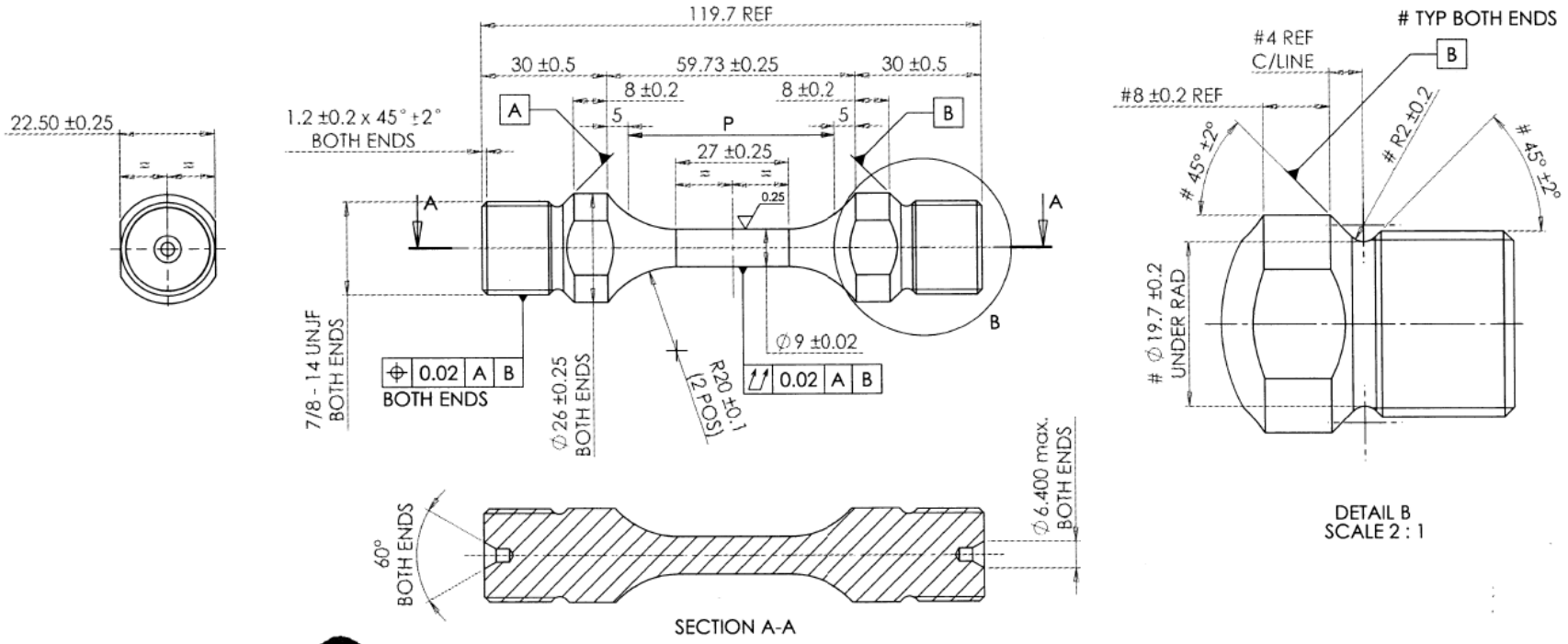

THROAT SECTION TO BE INSPECTED FOR FORM AND DIA
RECORED USING PROTECTION EQUIPMENT TO AVOID SURFACE DAMAGE
TURNED TEST PIECES TO BE LONGITUDINALLY POLISHED TO THE EXTENT OF 'P'

SCREW THREADS TO BS1081

CENTRES REQUIRED FOR INSPECTION PURPOSE

	NAME	SIGNATURES	DATE
DRAUGHTS PERSON	D.Koovits	[redacted]	15/09/2012
DRAWING APPROVAL	J.Wardle	[redacted]	15/09/2012
MACHINING SERVICES	T.Fogden (RR)	[redacted]	21.9.12
TEST GROUP	N.Clarke (RR)	[redacted]	21/09/12
CUSTOMER	T.Jackson (RR)	[redacted]	24/09/12

Modification	Name	Date	Issue
1st Issue for Production Use	D.Koovits		1

Rolls-Royce

TITLE:

STRAIN FATIGUE TEST PIECE

INTERPRET GEOMETRIC TOLERANCING PER:

MATERIAL: Free Issue

FINISH: 1.6 Microns U.O.S.

COMMENTS

ALL DIMENSIONS AND TOLERANCES ARE IN mm, EXCEPT WHERE STATED.

MANUFACTURE MUST BE IN ACCORDANCE WITH MSRR9968

DWG. NO. **RLH10569**

SCALE: **DO NOT SCALE DRAWING**

SHEET 1 OF 1

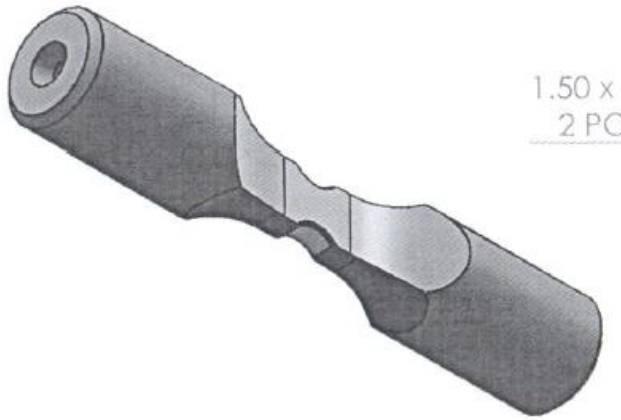

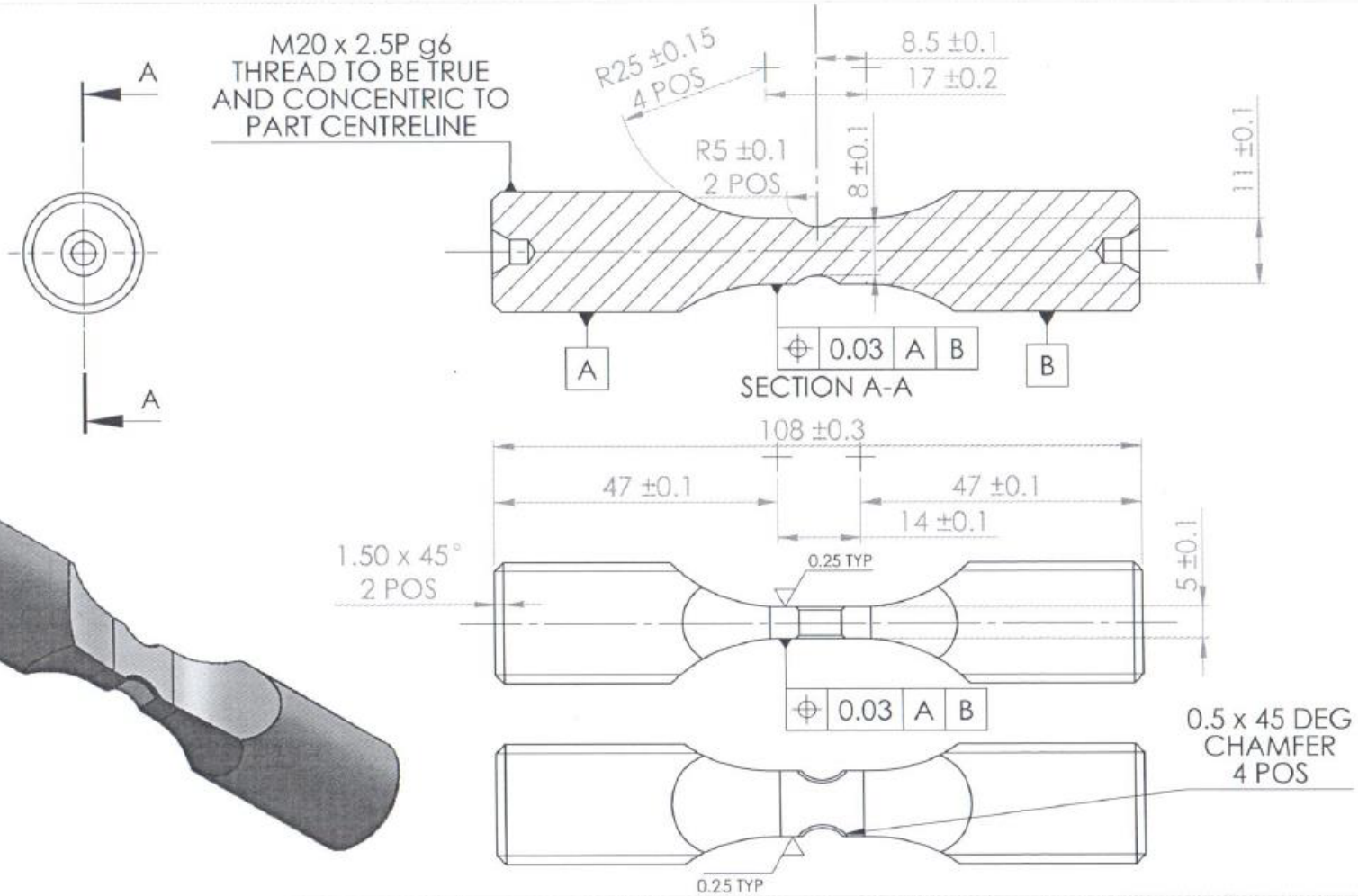

	NAME	SIGNATURES	DATE
DRAWN	D.Koovits	[redacted]	14/02/11
CHECKED	J.Wardle	[redacted]	14/02/11
M/c Service	T.Fogden (RR)	[redacted]	27.3.13
Test Group	N.Clarke (RR)	[redacted]	27/03/13
Support Group	Y. Li (RR)	[redacted]	23/3/13

COMMENTS

Modification	Name	Date	Issue
file was KT2 now KT1.55 ref Rolls-Royce report No EDNS01000171561	D.Koovits	01/03/13	2
1st Issue for Production Use	D.Koovits	25/02/11	1

PSM

TITLE:

AIR HOLE KT1.55
LCF SPECIMEN

DWG. NO. **RLH10520**

SCALE:

SHEET 1 OF 1

ALL DIMENSIONS AND TOLERANCES ARE IN mm, EXCEPT WHERE STATED.
MANUFACTURE MUST BE IN ACCORDANCE WITH MSRR 9968
DO NOT SCALE DRAWING

INTERPRET GEOMETRIC TOLERANCING PER:

MATERIAL: Free Issue

FINISH: 0.8 Microns U.O.S.

DO NOT SCALE DRAWING

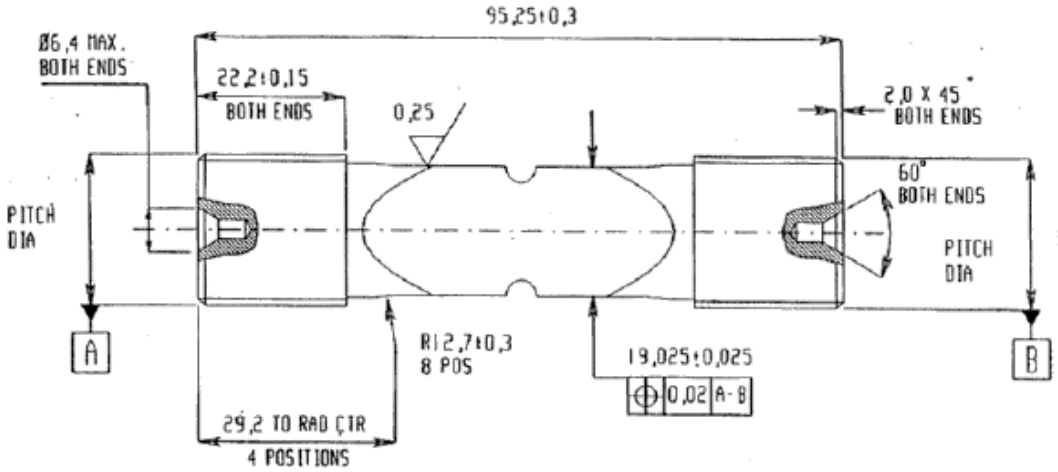

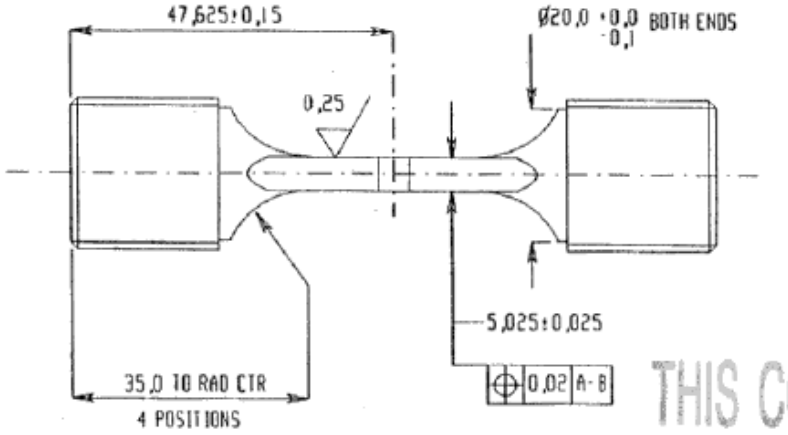

* REMOVE SHARP CORNERS (4 POS) ON NOTCH BY LONGITUDINAL POLISH 0,45±0,05 RAD. DO NOT SCRATCH MACHINED SURFACES

NOTCH DETAIL - ENLARGED VIEW

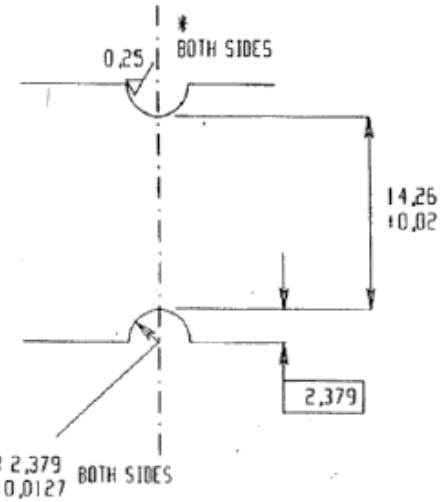

* CENTRES REQUIRED FOR INSPECTION PURPOSES

ALL DIMENSIONS AND TOLERANCES ARE IN mm EXCEPT WHERE STATED

ROUGHNESS VALUES FOR MACHINED SURFACES TO BE 1,6 MICRONS U.O.S THUS $\sqrt{x}$

DRAWN J HUTTON	TITLE LOW CYCLE FATIGUE NOTCH TEST PIECE (KT 2.29)		
DATE MAY 1995			
SCALE NOT TO SCALE	DWG. No. RLH 8018	ISSUE No. 3	

APPROVAL

	TEST GROUP	SUPPORT GROUP
[redacted] 2/11/95	Sig. [redacted] Name [redacted] Date 2/11/95	Sig. [redacted] Name [redacted] Date 6/11/95

NOTE
1 # CENTRES REQUIRED BOTH ENDS FOR INSPECTION PURPOSES
2 TEST PIECE TO LONGITUDINALLY POLISHED TO THE EXTENT OF P
3 DRAWING INTERPRETION TO BS308
4 SCREWTHREADS TO BS4084

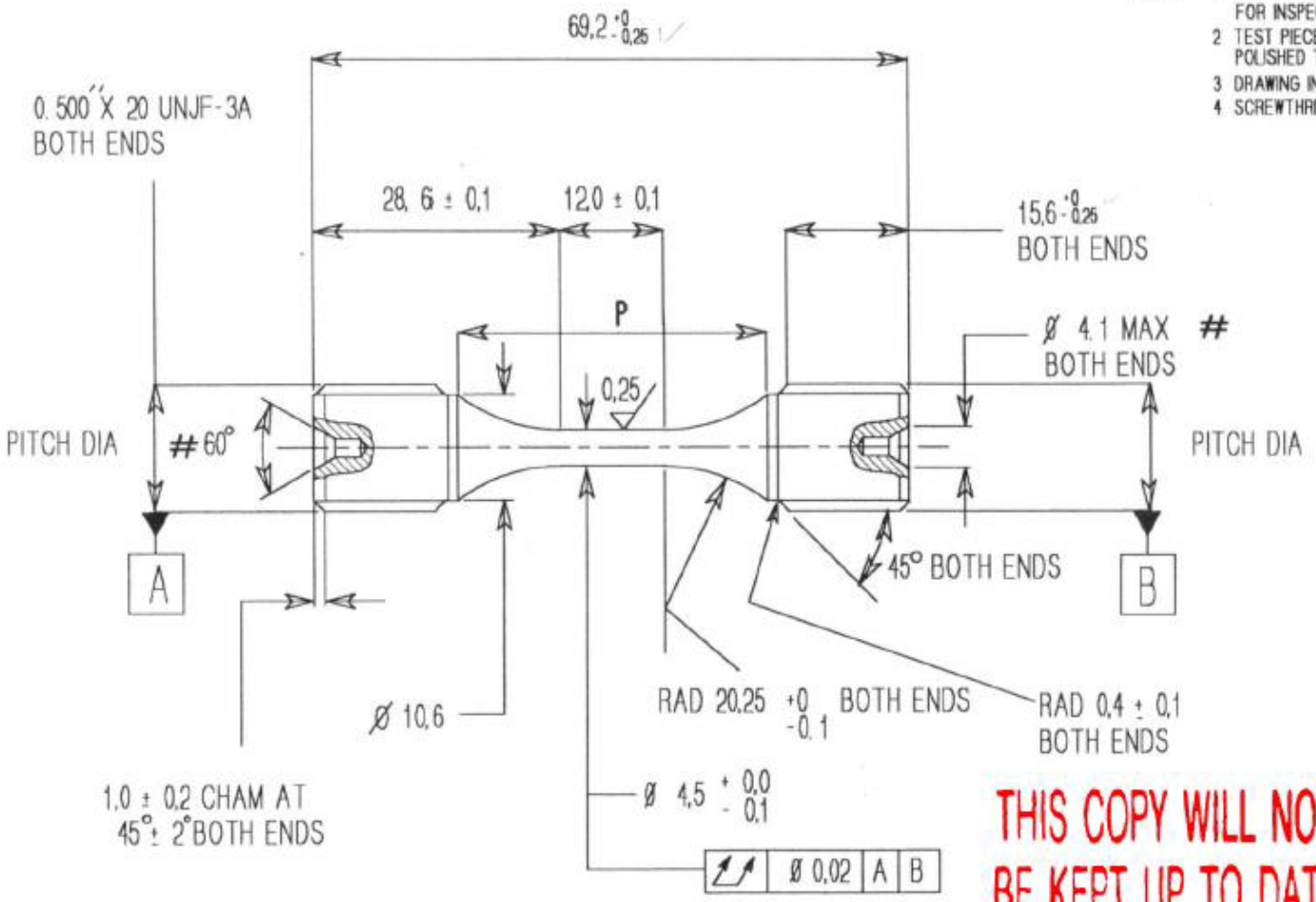

THIS COPY WILL NOT BE KEPT UP TO DATE

ALL DIMENSIONS AND TOLERANCES ARE IN mm EXCEPT WHERE STATED

ROUGHNESS VALUES FOR MACHINED SURFACES TO BE 1,6 MICRONS U C S THUS

DRAWN M J HARRIS

DATE APRIL 2001

SCALE NOT TO SCALE

TITLE
AXIAL HIGH CYCLE FATIGUE
TEST PIECE EXTENDED THREAD

DWG No RLH10277

ISSUE No 1

APPROVAL

MACHINING SERVICES	TEST GROUP	SUPPORT GROUP
Sig [redacted]	Sig [redacted]	Sig [redacted]
Name [redacted] Date 24/04/01	Name [redacted] Date 24/4/01	Name [redacted] 24.04.01

Appendix III

Swansea University
Prifysgol Abertawe

SPECIMEN PREPARATION PROCEDURE FOR OXIDATION ANALYSIS OF Ni-BASED ALLOYS

D Lewis

Created: 27/10/2016
Last Updated: 03/08/2017

1. INTRODUCTION

A standard procedure is required for the assessment of oxidation and corrosion of high temperature nickel based superalloys to ensure the consistency of the data generated, by minimising sources of technical variations.

2. SCOPE

Swansea University oxidation and corrosion damage assessments are currently being performed by observing the cross section of exposed samples to analyse and measure the oxidation/ corrosion scale and subsurface features, in line with that used with Rolls Royce. This document will cover the procedural aspects of this analysis technique with focus on high temperature nickel based superalloys.

3. SPECIMEN PREPARATION BEFORE EXPOSURE

Material should be prepared as small rectangular plates where possible, 20 x 10 x 2 mm in size, using low cutting speeds (<0.05 mm/min) to limit plastic deformation. Oxidation behaviour is surface-finish dependent and so the standardisation of the surface topography is required in all instances where the effect of surface finish is not being studied. All surfaces of any specimen should be ground, with progressively finer SiC grit size finishing with a 1200 grit grind for five minutes duration. Consistent grinding limits differences in residual surface damage and stress concentrations arising from surface topography. Edges and corners should be chamfered at approximately 45 degrees by around 0.5 mm on all edges and corners. Samples should be subsequently polished to a surface finish of R_a between 0.2 and 0.3 μm using progressively finer diamond solution with appropriate lubricant and polishing pads. Samples for furnace exposure should be placed in a clean, contaminant-free alumina boat during exposure.

4. FURNACE EXPOSURE

For these tests it is recommended that an available SNOL 8,2/1100 from the ISM Met Prep room be used. This is a high accuracy electric muffle furnace, with the temperature monitoring undertaken using a suitable thermocouple. A laboratory air environment is suitable in all cases where the atmosphere is not the variable of study, with water vapour levels currently not controlled. At the predetermined time intervals specimens are removed and left to air cool prior to cross sectional analyses. This method assumes that no spallation occurs during the cooling-heating process; if spallation occurs, a lidded alumina boat should be used and the specimen should be weighed with and without the spalled material.

5. SPECIMEN PREPARATION AFTER EXPOSURE

The samples to be analysed using cross-sectional analysis should be gold sputtered and nickel plated prior to mounting in Bakelite. The samples should then be polished to a finish ready for SEM imaging.

a) Gold Sputter Coating

1. Prior to sputter coating, samples should be cleaned using a soft tissue soaked in acetone on each side of the specimen (this stage should be avoided if there is evidence of spallation.
2. Place the sample on the coater sample tray (ensuring acetone has dried prior to placement in chamber).
3. Ensure argon gas supply is open and the regulator gauge is reading approximately 0.3bar.
4. Adjust the coater sample table height, so that the target to sample distance is approximately 35mm (For samples with complicated geometry e.g. porous or finely detailed, see instruction manual section 5.2 for further instruction).
5. Close the top-plate and pump chamber by turning on the sputter unit (if buzzing noise comes from unit ensure top-plate is fully sealed by applying light pressure to top of plate).
6. If the unit has not been used recently or is being used with different conditions, perform stages 6.1 to 6.3. If the unit has been used frequently using the same conditions proceed to stage 7.

6.1. Check the timer value on the digital display. If necessary, press *PAUSE/TEST* and reset the process time (30 secs is often used for ISM applications).

6.2. Check the pre-set sputter current value by pressing *SET mA* and adjust if necessary (30mA is often used for ISM applications).

6.3. Select *MANUAL*, press *FLUSH*, wait for 3 – 5 seconds and press *LEAK*. Wait for the pressure to stabilize, check the pressure and adjust if necessary using the knob on the rear of the sputter unit (0.08mb is often used for ISM applications).

7. Select AUTO and press CYCLE.
8. When the timer resets the coating is complete. Switch of the sputter unit and wait for the chamber to fill, then lift the top-plate and remove the sample.
9. The sputter coater functions by line of site, therefore, the sample should be rotated, and the procedure repeated for each face.

b) Nickel Plating Procedure

Once the samples have been gold coated sputtered, they should be coated using a bright nickel plating solution.

Equipment List

- Power pack
- Hot Plate with magnetic stirring capabilities
- Retort stands with 2 clamps
- 2 off cables
- 2 off crocodile clip
- Magnetic stirring bead
- Anode material (currently using nickel mesh attached using crocodile clip)
- Bright nickel plating solution
- 2 liter beaker
- Type N thermocouple with fluke temperature monitor

Procedure

1) The equipment should be setup as should in figure 1 in a fume cupboard.
2) Approximately 500ml of plating solution should be placed in the beaker.
3) The solution should be heated to 50°C prior to plating and kept at this temperature throughout (the hot plate currently available in the ISM should be set to approx. 125°C to achieve the 50°C required). The solution should be agitated using a magnetic stirrer rotating at approximately 600rpm.
4) The sample surface area should be measured and the current used should be set to achieve an electric current density of 50 mA/cm². This should be kept constant throughout the process.
5) The sample should be held in a crocodile clip (cathode) the connected to the circuit and fully submerged in the plating solution. The current should be applied for 20 minutes.
6) After plating, the sample should be carefully removed and left to air cool at room temperature. When cooled rinse in acetone.

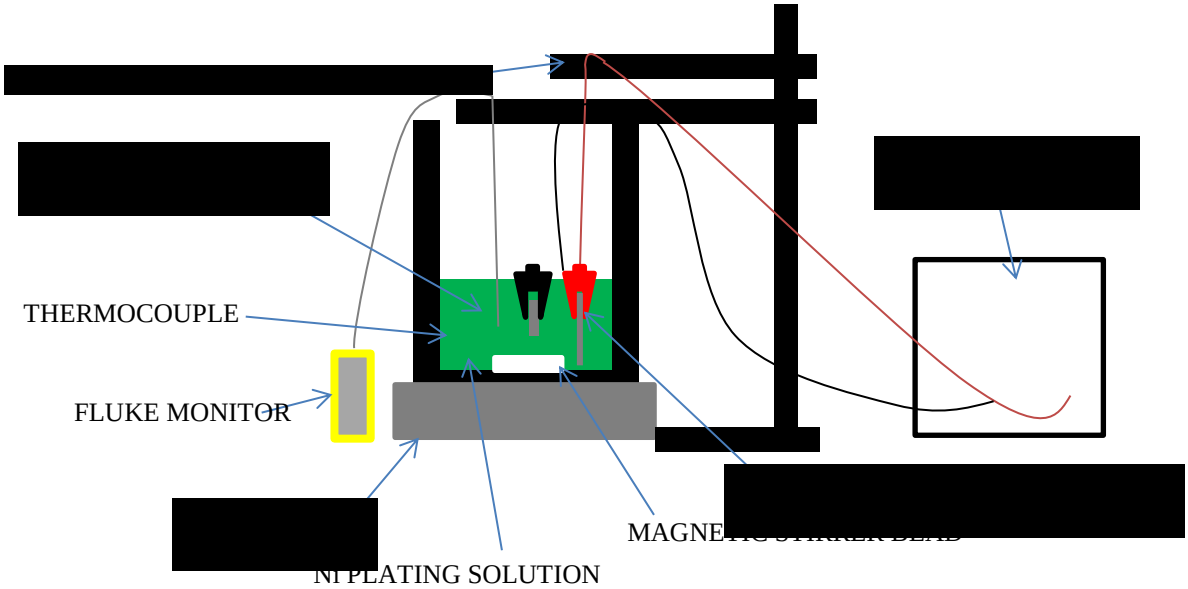

Appendix III: Figure 1– Schematic of Ni plating Setup

c) Mounting Procedure

This procedure has been optimised for the OPAL 410 Hot Mounting Press, with a 32mm mount diameter. The unit should be setup using the values in Appendix III: Table 1.

Appendix III: Table 1 - Mounting press settings

RESIN	PRESSURE	TEMPERATURE (°C)	HEATING TIME (mins)	COOLING TIME (mins)
METPREP CONDUCTO-MOUNT 2	(SETTING 2)	130	10	10

d) Grinding and Polishing Procedure

The grinding and polishing procedure is performed using the procedure in Appendix III: Table 2.

Appendix III: Table 2 – Specialised polishing parameters

	STEP 1 (GRINDING)	STEP 2 (GRINDING)	STEP 3 (POLISHING)	STEP 4 (POLISHING)
BASE	SiC PAPER, #220 GRIT *	SiC PAPER, #320 GRIT - #1200 GRIT PROGRESSIVELY	DAC	MD-CHEM
MEDIA	WATER	WATER	DIAPRO DAC	OP-S (0.04 MICRON)
FORCE (N)	HAND PRESSURE	HAND PRESSURE	25	20
SPEED (RPM)	300	300	150	150
TIME (MINS)	AS REQUIRED	AS REQUIRED	5	8
CLOTH CLEANING	DISPOSE WHEN FINISHED	DISPOSE WHEN FINISHED	WATER RINSE AND AIR DRY	WATER RINSE THOROUGHLY AND AIR DRY **

*This stage is used to remove excess material/ to produce samples of the required thickness.

**Ensure the polishing unit is wiped down thoroughly to avoid cross contamination. If using the auto-doser for OPS, ensure the dowser tube is cleared using water.

After polishing with OP-S, it is advisable to polish the sample on the MD-CHEM base with water media, to remove excess OP-S from the sample.

6. MICROSCOPY

a) Microscopy Features

The features that are to be investigated during a cross sectional analysis can be seen in Appendix III: Figure 2.

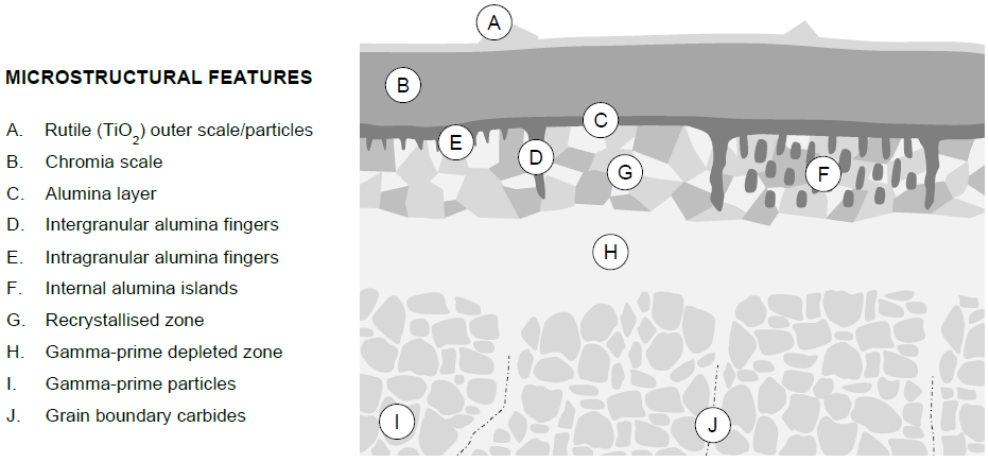

Appendix III: Figure 2 - Schematic of Expected Oxide Morphology After High Temperature Exposure of Ni-based Alloys [84]

For the current analyses, the features labelled C, D and E are the most important variables for analysis.

b) Microscopy Methods

Scanning Electron Microscopy is suitable for imaging of most detail for the cross-sectioned specimens. Back-scatter electron (BSE) microscopy has been found to produce images with good contrast between different elements; however, secondary electron (SE) imaging also will produce reasonable micrographs. Initial BSE setting that will usually produce an image for further manipulation are:

- Working distance – 5-8mm
- Spot size/ probe current – Small e.g. Jeol 7800F 5-8
- Accelerating voltage – 10-15 kV
- Small aperture e.g.3 or 4 on Hitachi SU3500

For quantification of oxide damage, images should be collected such that damage covers 25-75% of the total image height, from 10 randomly selected areas representative of the sample, from around the cross-section.

For elemental differentiation, Energy Dispersive X-Ray Spectroscopy (EDS) has been found to produce good results.

For the study of recrystallized grains Electron Back-Scatter Diffraction (EBSD) is most suitable.

For other features such as Gamma Prime depleted areas and carbide depleted grain boundaries, etching of samples is required. This must be performed after other measurements have been performed as the etchant will cause damage to the oxide scales. Gamma prime distributions are suitably identified by an electrolytic etch (2-3 V for 3 seconds) using a 10% phosphoric acid solution. Also, a 0.06μm colloidal silica preparation (which will lightly etch the surface) can be suitable. For the investigation of carbides on grain boundaries, Kalling's Etch, applied gently using a swab across the surface of interest in 2 perpendicular directions.

It is recognised that projects may require more specific analysis and characterisation of certain features, which may or may not be covered in this procedure.

c) Image Analysis

Collected images can be analysed and measured in computer software such as ImageJ, which allows calibrated point-to-point distance measurement.

In order to calculate average feature depths and standard deviation of these depths, a number of measurements are required. It is recommended that five equally spaced sampling lines are taken on each of the 10 images collected per sample to produce 50 measurements per sample in total. Individual measurements should be recorded in micrometres to two decimal places, with average values quoted to two significant figures.

Total damage depth should be used to describe the total extent of damage to the deepest oxidation-related feature observed. This should be measured from the oxide/air (i.e. outermost) interface. In all cases, it must be stated which features are included in the total damage depth, e.g. Total damage depth = Rutile outer scale to carbide depletion depth. It may be useful to describe the total damage depth using the lettered notations in Appendix III: Figure 3, e.g. Total damage depth = A+B+G (for the example above).

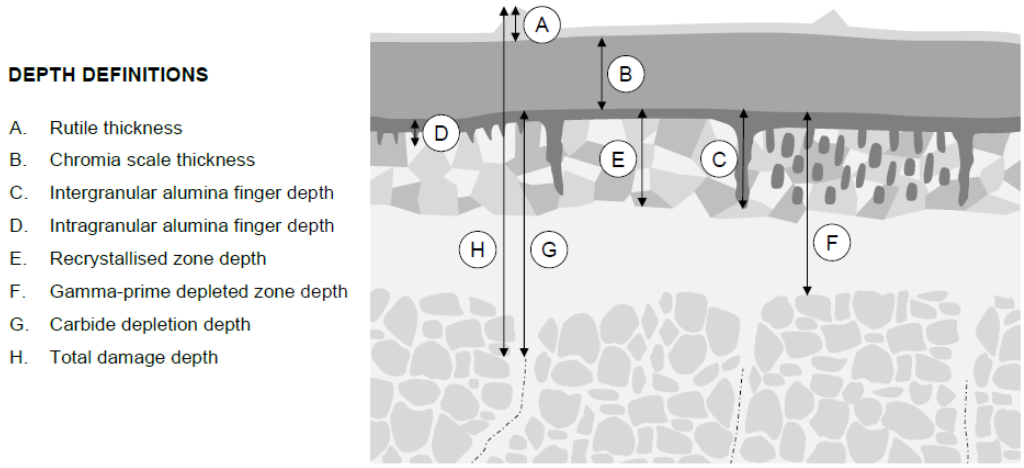

Appendix III: Figure 3 - Schematic to Define the Various Depth Measurements Possible After High Temperature Exposure of Ni-based Alloys

Where the five equally spaced sampling lines do not intersect any intergranular alumina fingers, the sampling lines can be adjusted so they intersect accordingly. Where less than the required 50 measurements have been taken per sample, the value of measurements should be stated. The method is described in Appendix III: Figure 4.

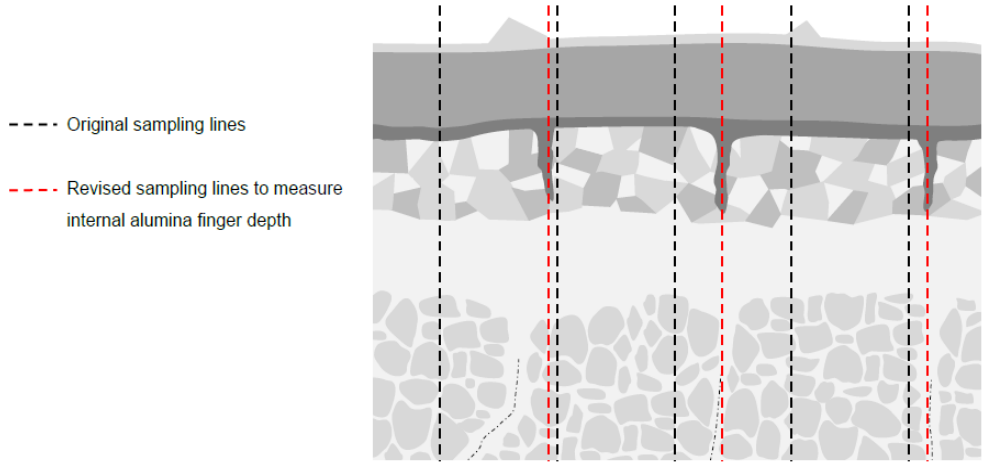

Appendix III: Figure 4 - Schematic of Measurement Methods Where No Sampling Lines Intersect Intergranular Alumina Fingers

For non-linear features e.g. where the alumina fingers do not run parallel to the sampling lines, the method shown in Appendix III: Figure 5 should be used for measuring the damage depth.

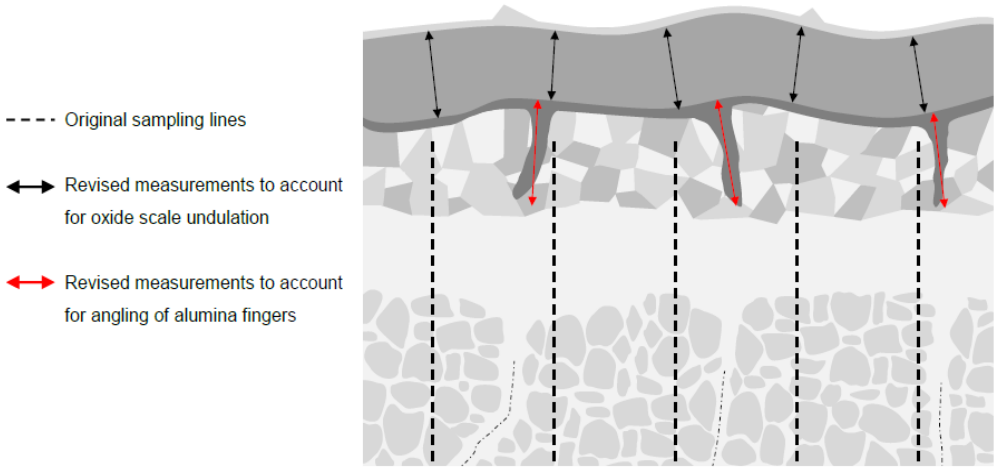

Appendix III: Figure 5 - Schematic of Measurement Methods Where the Features are Non-Parallel to the Sampling Lines

Appendix IV

Modelling Anion Controlled Oxidation In Nickel-based Superalloys

Hector Basoalto

Department of Materials Science and Engineering, University of Sheffield

Summary

A theoretical analysis is presented for modelling the parabolic growth kinetics during oxidation of a γ' strengthened nickel-based superalloys. In particular, it aims to rationalise the experimental observation of Lewis and co-workers [1,2] that the apparent activation energy for oxide growth under compressive applied stresses are smaller than those determined under tensile uniaxial loading conditions. It is proposed that transport of oxygen ions (and therefore oxidation of the alloy) is maintained by the development of an internal stress state at the metal/oxide interface. These stresses modify the chemical potential of oxygen ions and establish their flux from the free surface to the metal/oxide interface. An analysis of the mechanical fields is presented that accounts for the viscoplascity of the γ/γ' alloy as well as differences in the elastic properties of the oxide and metal. The relevant diffusion problem is solved and parabolic growth kinetics with scaling law $h \sim t^{1/2}$ are predicted, where h is the oxide scale thickness and t the elapsed time. Expressions for the apparent activation energy are derived. The applied stress is shown to influence the apparent activation energy. Furthermore, the transformation stress at the metal/oxide interface results in an asymmetric apparent activation energy with respect to loading direction, with lower apparent activation energy under compression than tension.

1 Physical model

This section describes the main aspects of the proposed physical model for anion controlled oxidation in γ′ nickel-based superalloys. Following formation of an initial oxide layer, further development of the oxide layer requires diffusion of oxygen ions to the metal/oxide interface, where they react with available cations (Al^{+2}, Cr^{+2}, Ni^{+2}). This in turn requires that the chemical potential of the diffusing anions at the free surface and the metal/oxide interface be different. This can be achieved through the development of stress variations across the oxide layer, since the pressure is known to modify the chemical potential.

Consider the case of a cylindrical specimen of radius R and gauge length L at some temperature T and zero applied stress, as illustrated in Figure 1a. It is assumed that an initial oxide layer of thickness h at $r = a$ has already formed. Let the material points occupied by the oxide and metal be denoted by $\mathcal{B}^o$ and $\mathcal{B}^m$, respectively (see Figure 1b). Over a time interval δt the oxide advances by an amount δh into the alloy, thereby transforming a domain $\delta\mathcal{B}^*$ into oxide. The volumes of $\delta\mathcal{B}^*$, $\mathcal{B}^o$ and $\mathcal{B}^m$ are denoted by $V(\delta\mathcal{B}^*)$, $V(\mathcal{B}^o)$ and $V(\mathcal{B}^m)$, respectively, and are such $V(\delta\mathcal{B}^*) \ll \delta V(\mathcal{B}^o) \ll V(\mathcal{B}^m)$. The transformation in $\mathcal{B}^*$ is accompanied by a change in volume associated with the replacement of the γ/γ′ lattice cells by that of the oxide, resulting a transformation strain ϵ_o^* in $\delta\mathcal{B}^*$. Compatibility requirements will induce an internal stress state as the material on either side of $\delta\mathcal{B}^*$ will constrain the expansion due to ϵ_o^*. Consequently, the newly formed oxide in $\delta\mathcal{B}^*$ is in under compression. Let this stress be denoted Σ_o^*. Equilibrium of forces demand that tensile stresses, Σ_m^*, ahead of the interface in the alloy must balance the compressive stresses in the transformed region. This tensile stresses exist over a domain $\delta B^{\gamma\prime} \in B^m$ which will be taken to be

γ' depletion zone ahead of the metal/oxide interface. Since $\delta\mathcal{B}^*$ and $\delta B^{\gamma'}$ are relatively small compared with the oxide thickness and assuming Σ_o^* and Σ_m^* uniform within these regions is a good approximation. For an elastically deforming oxide and elasto-viscoplastic metal, evolution relations for Σ_o^* and Σ_m^* are derived in section 2. Rate-dependent plastic deformation in $\mathcal{B}^o$ will result in relaxation of the Σ_o^* and Σ_m^*. Outside these regions, the internal stresses must decay with increasing distance away from the transformation/γ' depletion zones. The stresses in the oxide are approximated by treating $\mathcal{B}^o$ as a cylinder subject to an internal pressure Σ_o^*, from which the hoop and radial stress distributions are obtained. Similarly, the stresses in the alloy can be approximated by solutions to the problem of a solid cylinder subject to an external pressure Σ_m^*.

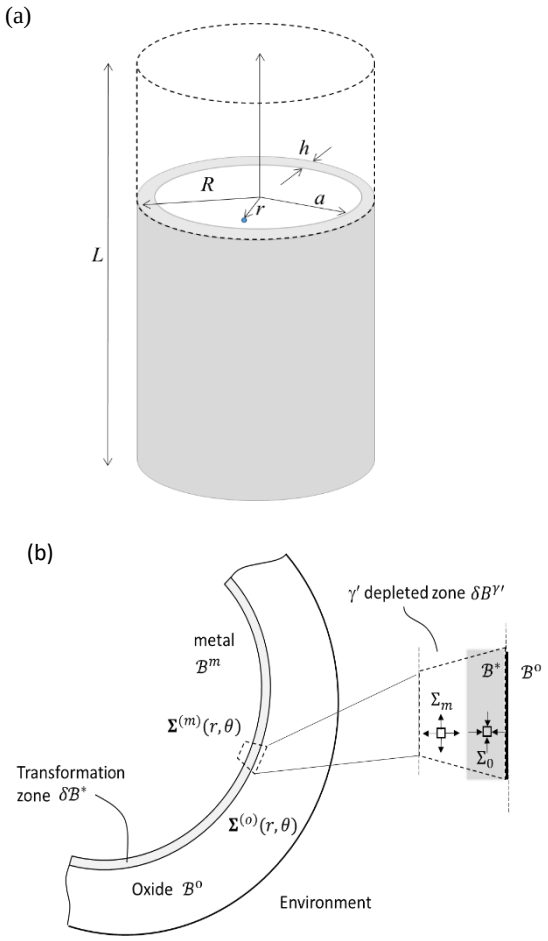

Figure 1 (a) Schematic of basic geometry. (b) Definition of oxide, transformation and metal domains and associated stress states.

The stress Σ_o^* in $\delta\mathcal{B}^*$ will modify the oxygen anion chemical potential from that at the free surface. This difference in the chemical potential will result in the diffusion of oxygen ions from the surface to the metal/oxide interface. In section 3, it is shown that the approximated stress field in $\mathcal{B}^o$ (the oxide) does not lead to stress-assisted diffusion, thereby, simplifying diffusion problem considerably. The predicted concentration fields are used to calculate the flux of oxygen ions arriving at the metal/oxide interface. From the flux the oxide growth rate is derived.

2 Transformation induced stresses

Consider a cylindrical uniaxial test piece of length L and radius R as shown in Figure 1. For anion controlled oxidation the oxide grows inwards from the surface into the metal through diffusion of oxygen ions. Reactions between oxygen anions and metal cations occur at the metal/oxide interface located at $r = a = (R - h)$, where h is the thickness of the oxide. Suppose the interface advances by δh inwards. Let $\delta\phi_o = V(\delta\mathcal{B}^*)/(\pi R^2 L) = 2\,a\,\delta h/R^2$ be the volume fraction of the newly formed oxide. Let ϵ_o^* be the eigenstrain associated with the change in volume as metal is transformed to oxide. This eigestrain is determined by the Pilling-Bedworth ratio Π_{PB} of the alloy and is given by

$$\epsilon_o^* = \frac{1}{3}\ln \Pi_{PB} \tag{2.1}$$

Differences in thermal expansion between the newly formed oxide and metal substrate will contribute to the Eigenstrain. This contribution will not be considered further; however, the theory can easily be extended to account for such effects. The transformation strain ϵ_o^* will induce a redistribution of stress in the vicinity of the oxide/metal interface. The situation is schematically illustrated in Figure 2. The stress in the transformed volume is

$$\Sigma_o^* = E_o \epsilon_o^* \tag{2.2}$$

where E_o is the Young's modulus of the oxide. Imposing equilibrium, will induce a stress Σ_m on the metal substrate side of the interface, so that locally these stresses satisfy the condition

$$\delta\phi_o\,\Sigma_o^* + \delta\phi_m\,\Sigma_m^* = 0 \tag{2.3}$$

where $\delta\phi_m = V(\delta\mathcal{B}^{\gamma'})/(\pi R^2 L)$ is the volume fraction of the γ' depleted zone. Compatibility requirements demand that the deformation rates in $\delta\mathcal{B}^{\gamma'}$ and $\delta\mathcal{B}^*$ be equal, which leads to the following condition on Σ_m and Σ_o:

$$\frac{\Sigma_o^*}{E_o} + \epsilon_o^* = \frac{\Sigma_m^*}{E_m} + \epsilon_m^p \tag{2.4}$$

where E_m is the effective Young's modulus of the metal substrate and ϵ_m^p is the plastic strain on the metal substrate side of the interface. Combining Equations (2.3) and (2.4), the pressure exerted by the transformation zone on the oxide layer is

$$\Sigma_o^* = -\frac{\delta\phi_m \, E_o E_m}{E_m + \delta\phi_o \Delta E}\left(\epsilon_o^* - \epsilon_m^p\right) \tag{2.5}$$

where $\Delta E = E_o - E_m$. It follows from Equation (2.5) that plastic deformation of the metal substrate will relax the transformation stress near the interface. Now that Σ_o^* is known, from Equation (2.3), the stress in $\delta\mathcal{B}^{\gamma'}$ is given by

$$\Sigma_m^* = -\frac{\delta\phi_o}{\delta\phi_m}\Sigma_o^* \tag{2.6}$$

From Equation (2.5), the oxidation process induces a compressive stress in $\delta\mathcal{B}^*$. When $\delta\mathcal{B}^*$ is small compared $\mathcal{B}^o$, the problem resembles that of a cylinder $\mathcal{B}^o$ subject to an internal pressure Σ_o^*. This internal pressure will induce a stress field $\mathbf{\Sigma}^{\mathrm{o}} = (\Sigma_{rr}^o, \Sigma_{\theta\theta}^o, \Sigma_{zz}^o)$ in the oxide. Assuming that this is a reasonable approximation, the stress fields in the oxide are

$$r \in \mathcal{B}^{\mathrm{o}}, \qquad \Sigma_{rr} = \beta(1 - R^2/r^2)\,\Sigma_o^* \tag{2.7}$$

$$r \in \mathcal{B}^{\mathrm{o}}, \qquad \Sigma_{\theta\theta} = \beta(1 + R^2/r^2)\,\Sigma_o^* \tag{2.8}$$

where $q = 1/(R^2/a^2 - 1)$. Under plane strain conditions $\Sigma_{zz} = \nu_o\,(\Sigma_{rr} + \Sigma_{\theta\theta})$ and inserting the last two expressions

$$r \in \mathcal{B}^{\mathrm{o}}, \qquad \Sigma_{zz} = 2\,q\,\nu_o\Sigma_o^* \tag{2.9}$$

From Equations (2.7),(2.8) and (2.9), the hydrostatic stress $P_o = -\,(\Sigma_{rr} + \Sigma_{\theta\theta} + \Sigma_{zz})/3$ in the oxide domain (excluding transformation zone) is

$r \in \mathcal{B}^o$,

$$P_o = -\frac{2}{3}\, q(1+\nu_o)\, \Sigma_o^* \tag{2.10}$$

Equations (2.7) - (2.10) are based on static solutions of a cylinder subject to internal pressure. In reality a mobile metal/oxide interface will modify and translate the stress field away from the static solution. For growth rates that are not too fast, the approximations given by Equations (2.7) - (2.10) should provide a reasonable representation of the stress state in the oxide; this needs to be proved. However, it will be shown in the following sections that these macroscales stresses do not contribute to the diffusion of oxygen ions.

3 Constitutive description of γ/γ′ alloy

A state variable framework is adopted for the constitutive description for the plastic rate of the metal. Key elements of the theory is the evolution of a kinematic back stress σ_k and evolution of the mobile dislocation density ρ_m. The development of the state variable σ_k is associated with stress partitioning between plastically hard domains. An example of such a mechanism is provided by limiting deformation to the γ phase with the γ' precipitate phases undergoing elastic distortion only. A distribution of plastically hard/soft grains will also contribute to the development of a kinematic back stress. A continuity condition is used to model the mobile dislocation density evolution, where competition between generation and annihilation rates gives the net rate of change in mobile dislocations. The generation rate is controlled by the activation of Frank-Read sources while the annihilation rate is linked to the formation of dislocation dipoles. For a precipitate strengthened nickel-based superalloys, it can be shown that $\dot{\epsilon}_m^p$ has the form [**Error! Reference source not found.**]

$$\dot{\epsilon}_m^p = \frac{\rho_m \lambda_p D_v^m c_j}{M\, r_p} \sinh\left(\frac{(\Sigma_m^* - \sigma_k)\, \Delta V^*}{M\, kT}\right) \tag{3.1}$$

$$\dot{\sigma}_k = G\, \phi_p \left(1 - \frac{\sigma_k}{H^*\, \Sigma_m^*}\right) \dot{\epsilon}_m^p \tag{3.2}$$

$$\dot{\rho}_m = \rho_s \Gamma_m^+ - \rho_m^2 \frac{M\, b\, v_g G_m}{4\, \pi (1-\nu) \Sigma_m^*} \tag{3.3}$$

where ρ_m is the mobile scalar dislocation density, ρ_s is the density of dislocation sources, D_v^m the volume diffusivity, c_j jog concentration, ΔV^* an activation volume for dislocation slip, Γ_m^+ is the mean dislocation generation rate, G_m is the shear modulus. The maximum stress transferred to the hard domains is $H^*\, \Sigma_m$. For spherical precipitates, Dyson [4] showed that the parameter H^* is a function of the precipitate volume fraction. The activation volume is taken to be $\Delta V^* = b^2\, \lambda_p$; however, ΔV^* will deviate from this value if the γ′ is fully depleted and the spatial parameter is related to the jog spacing.

4 Oxide growth rate at zero applied stress

At constant temperature and pressure the appropriate free energy is the Gibbs free energy $G = G(F, V, N_1, N_2, \cdots)$ which is defined as

$$\delta G = \delta F - P\delta V + \sum_j \mu_j \, \delta N_j \tag{4.1}$$

where δF is the Helmholtz free energy, P the pressure, μ_j is the chemical potential of chemical species i and δV the change in volume accompanying the process. Suppose that δV is due to transport of some chemical species i. Suppose that for the moment $\delta F = 0$ for a variation in δN_i, then the free energy change associated with transport of chemical species is

$$\delta G = \left(\frac{\partial F}{\partial N_i} - P\frac{\partial V}{\partial N_i} + \mu_i\right)\delta N_i = \left(\mu_i - P\frac{\partial V}{\partial N_i}\right)\delta N_i \tag{4.2}$$

Let $\overline{\Omega}$ is the effective atomic volume of the oxide, the volume of oxide formed is $V = \overline{\Omega}\, N_i$. At equilibrium $\delta G = 0$ and $P = \Sigma^*$ for $r \in \mathcal{B}^*$, so that the chemical potential in the transformation zone is given by

$$\mu^* = P\overline{\Omega} = \overline{\Omega}\, \Sigma_o^* \tag{4.3}$$

using $\mu = kTln\,(c/c_0)$, where c_0 is the equilibrium concentration of oxygen ions in the oxide, it follows that the anion concentration at the interface is

$$c(r = a) = c_0 \exp\left(-\frac{\overline{\Omega}\, \Sigma_o^*}{kT}\right) \tag{4.4}$$

The chemical potential at the free surface is μ_s with concentration c_s of oxygen ions at $r = R$.

Assuming the mass transport of anions reaches steady state relatively quickly; the continuity condition for diffusion becomes

$$\boldsymbol{\nabla} \cdot \boldsymbol{J} = 0 \tag{4.5}$$

where $\boldsymbol{J}$ is the flux of some chemical species. Nickel-based superalloys have complex chemistries and the flux is calculated from the gradients of chemical potential weighted by the Onsager matrix. Fang and co-workers [5,6] have used this approach successfully to model mass transport in RR1000 using a finite element implementation. For the sake of simplicity, the flux of oxygen ions will be assumed to be well characterised by

$$\boldsymbol{J} = \frac{D_v\, c}{kT} \boldsymbol{\nabla} \mu \tag{4.6}$$

where D_v is the diffusivity. Inserting $\mu = kT \ln(c/c_0)$. From Equation (2.10), the pressure in the oxide is constant and will therefore have no contribution to the chemical potential. This simplifies the diffusion problem significantly. Expressing the continuity condition for transport of oxygen ions in polar coordinates:

$$\frac{1}{r}\frac{\partial}{\partial r}\left(r \frac{\partial c}{\partial r}\right) = 0 \tag{4.7}$$

with boundary conditions

$$\begin{aligned} c\ (r = a) &= c_0 \exp\left(\frac{\overline{\Omega}\ \Sigma_o^*}{kT}\right) \\ c\ (r = R) &= c_s \end{aligned} \tag{4.8}$$

This boundary value problem has the solution

$$c\ (r) = c_0 \exp\left(\frac{\overline{\Omega}\ \Sigma_o^*}{kT}\right)\frac{\ln(R/r)}{\ln(R/a)} + c_s \frac{\ln(r/a)}{\ln(R/a)} \tag{4.9}$$

Since the current of oxygen ions is $I(r) = 2\pi\ rL\ J(r)$ and the corresponding volume growth rate of the oxide is $\dot{V} = I(r = a)\ \overline{\Omega}$ and collecting terms

$$\dot{V}(a) = 2\ \pi\ r\ L\ \ D_v\ \frac{\partial(c\ (r) - c_0)}{\partial r}\bigg|_{r=a} \tag{4.10}$$

Inserting solution (4.9) into the last expression gives

$$a\,\dot{a} = \frac{\overline{\Omega}\,D}{\ln(R/a)}\left\{c_s - c_0 \exp\left(\frac{\overline{\Omega}\,\Sigma_o^*}{kT}\right)\right\} \tag{4.11}$$

Taking $R/a = 1/(1-h/R)$ then $\ln(R/a) = -\ln(1-h/R) = h/R + h^2/2R^2 + \cdots = h/R + O(h^2/R^2)$ and to first order in h/R it follows $a\ \ln(R/a) \approx h$. Noting that $\dot{a} = -\dot{h}$ and imposing $c_o = c_s$ Equation (4.11) becomes

$$\dot{h} = \frac{D_v\,c_s}{h}\left[\exp\left(\frac{\overline{\Omega}\,\Sigma_o^*}{kT}\right) - 1\right] \tag{4.12}$$

It follows from the last expression, that the transformation stress Σ_o^* at the oxide/metal interface provides the driving force for oxide growth; setting $\Sigma_o^* = 0$ results in no growth of the oxide layer. The extent of creep in $\mathcal{B}^{\gamma\prime}$ will modify Σ_o^* and in turn will influence the growth rate. Integration of Equation (4.12) implies that the oxide thickness obeys scaling law $h \sim t^{1/2}$.

5 Influence of applied stress field

The equilibrium condition at metal/oxide interface in the presence of an applied stress is

$$\delta\phi_0\,\Sigma_o^* + \delta\phi_m\,\Sigma_m^* = \sigma \tag{5.1}$$

Combining the last expression with the compatibility and inserting Equation (3.1) yields the following expression for the evolution of the stress in $\mathcal{B}^{\gamma\prime}$

$$\dot{\Sigma}_m^* = \frac{E_m}{\bar{E}}\dot{\sigma} - \frac{E_o E_m\,\delta\phi_m}{\bar{E}}\left(\frac{\rho_m\lambda_p D_v^m c_j}{M\,r_p}\sinh\left(\frac{(\Sigma_m^* - \sigma_k)b^2\,\lambda_p}{M\,kT}\right) - \dot{\epsilon}_o^*\right) \tag{5.2}$$

where $\bar{E} = \delta\phi_m E_m + \delta\phi_o E_o$. The last result gives the stress in $\mathcal{B}^{\gamma\prime}$ explicitly in terms of the nickel-based superalloy microstructure. Assuming a lattice square spacing λ_p/r_p is a function of the γ' volume fraction ϕ_p; increasing $\phi_p$results in a decrease in λ_p/r_p and therefore Σ_m^*relaxes at a slower rate. If γ' formers are being depleted as a result of oxidation, then the size r_p and volume fraction ϕ_p of the γ' precipitates will be lower than otherwise would be, leading to an increase in λ_p. According to Equation (5.2), these changes will result in a faster relaxation of Σ_m^*. The stress Σ_o^* in the transformation zone $\mathcal{B}^*$ is determined from rearrangement of Equation (5.1):

$$\Sigma_o^* = \frac{\sigma - \delta\phi_m\Sigma_m^*}{\delta\phi_o} \tag{5.3}$$

Combining Equations (4.12) and (5.3) gives the growth rate of the oxide in the presence of an applied uniaxial stress as

$$\dot{h} = \frac{D_v\,c_s}{h}\left[\exp\left(\frac{\bar{\Omega}}{kT}\left(\frac{\sigma - \delta\phi_m\Sigma_m^*}{\delta\phi_o}\right)\right) - 1\right] \tag{5.8}$$

Setting $\sigma = 0$ the last expression reduces to Equation (4.12).

6 Apparent activation energy

The diffusivity of oxygen ions is usually expressed as $D_v = D_{v,0}\exp(-U_d/kT)$, where U_d is the activation energy for diffusion and $D_{v,0}$ is a pre-exponential parameter. Under zero applied stress, the oxide thickness is obtained by integration of Equation (4.12) and easily shown to be

$$\dot{h} = \frac{D_v\, c_s}{h}\left[\exp\left(\frac{\overline{\Omega}\,\Sigma_o^*}{kT}\right) - 1\right] \tag{6.1}$$

where $\Sigma_o^* = -|\,\Sigma_o^*|$ to emphasise that the transformed region is under compression. In experimental studies, it is common to express the growth rate as

$$\dot{h} = \frac{K}{h}\exp\left(-\frac{Q_{app}}{kT}\right) \tag{6.2}$$

where Q_{app} is an effective or apparent activation energy and K is a model parameter. Comparing Equations (6.1) and (6.2)

$$D_{v,0}\, c_s\left[1 - \exp\left(\frac{\overline{\Omega}|\,\Sigma_o^*|}{kT}\right)\right]\exp\left(-\frac{1}{kT}\left(U_d + \overline{\Omega}|\,\Sigma_o^*|\right)\right) = K\exp\left(-\frac{Q_{app}}{kT}\right) \tag{6.3}$$

and obtain the following expressions for K and the apparent activation energy for zero applied stress conditions

$$K = D_{v,0}\, c_s\left[1 - \exp\left(\frac{\overline{\Omega}|\,\Sigma_o^*|}{kT}\right)\right] \tag{6.4}$$

$$Q_{app} = U_d - \overline{\Omega}|\,\Sigma_o^*| \tag{6.5}$$

Thus, based on Equation (6.2), the development of a transformation stress Σ_o^* modifies the activation energy for the process by $-\overline{\Omega}|\,\Sigma_o^*|$ and as $\Sigma_o^*\,(<0)$ is compressive the apparent activation energy for oxidation is less than that expected from self-diffusion of oxygen anions in the oxide.

Carrying out similar procedure for the oxide growth rate in the presence of an applied stress, the effective growth rate parameters become

$$K = D_{v,0}\, c_0 \left[1 - \exp\left(-\frac{\bar{\Omega}}{kT}\left(\frac{\sigma - \delta\phi_m|\,\Sigma_o^*|}{\delta\phi_o}\right)\right)\right] \tag{6.6}$$

$$Q_{app} = U_d + \frac{\sigma - \delta\phi_m|\,\Sigma_o^*|}{\delta\phi_o} \tag{6.7}$$

Thus, in the presence of an applied stress modifies further the apparent activation energy for the diffusion of oxygen anions. From Equation (4.7), a tensile applied stress ($\sigma > 0$) increases the apparent activation energy, while a compressive stress ($\sigma < 0$) reduces Q_{app}. Furthermore, creep in the metal will relax Σ_o^* resulting in a time dependent apparent activation energy while Σ_o^* is changing. Equation (6.7) predicts an increase in the apparent activation energy as Σ_o^* is relax through creep. It follows that at low stresses creep will fully relax Σ_o^* and no difference between a tensile or compressive stress is predicted. However, at high stresses creep deformation can partially relax Σ_o^* and a lower apparent activation energy is predicted for compressive loads compared to tensile conditions.

7 Conclusions

A macroscopic theoretical treatment of the oxidation growth kinetics in γ′ strengthened nickel-based superalloy has been presented. It is shown that oxygen anion diffusion from the free surface to the metal/oxide interface arises from differences in their chemical potential induced by transformation strains associated with the formation of the oxide. Compressive stresses are established as the metal coverts to oxide, which in turn result in tensile stress in the neighbouring metal (the γ′ depleted zone). Creep in the alloy will relax the compressive stress state on the oxide side of the interface (referred to as the transformation zone). For a given time exposure and temperature, increasing the applied stress will increase the rate of viscoplasticity in the γ′ depletion zone and result in a greater relaxation of the transformation stresses in the formed oxide. This is turn leads to increase differences in the apparent activation energy.

References

1. D.T.S. Lewis, *Oxidation and its effect on the Fatigue Properties of the Nickel Based Superalloy RR1000*, PhD thesis, 2020.
2. D.T.S. Lewis. G. Ding, M.T. Whittaker, P.M. Mignanelli, M.C. Hardy, *The effect of oxidising thermal exposures on the fatigue properties of a polycrystalline powder metallurgy nickel-based superalloy*, Materials and Design 189 (2020) 108529.
3. Basoalto, H.C, Effect of γ′ shearing of creep behaviour, PRISMM Report (2015)
4. Dyson, B, F., Microstructure based creep constitutive model for precipitation strengthened alloys: theory and application, Materials Science and Technology, vol 25 No. 2, 213-220, 2009.
5. C. Fang, *Influence of oxide growth along grain boundaries on the crack growth behaviour of a nickel-based superalloy*, PhD thesis, 2017.
6. C. Fang, H. C. Basoalto, H.Y. Li, S.J. Williams, P. Bowen, *Influence of oxide growth along grain boundaries on the crack growth behaviour of a nickel-based superalloy*, to be published.